Simulation of Volumetrically Heated Pebble Beds in Solid Breeding Blankets for Fusion Reactors: Modelling, Experimental Validation and Sensitivity Studies

Zur Erlangung des akademischen Grades

Doktor der Ingenieurwissenschaften

der Fakultät für Maschinenbau
Karlsruher Institut für Technologie (KIT)

genehmigte

Dissertation

von

Ing. Ind. Francisco Alberto Hernández González

Tag der mündlichen Prüfung: 14. Oktober 2016

Hauptreferent:	Prof. Dr.-Ing. Robert Stieglitz Karlsruher Institut für Technologie (KIT)
Korreferent:	Prof. Dr.-Ing. Marc Kamlah Karlsruher Institut für Technologie (KIT)

Abstract

The Breeder Units are the core components of the so-called Helium Cooled Pebble Bed (HCPB) breeding blanket. These components are responsible for 2 key functions of a nuclear fusion reactor, namely the breeding of the necessary tritium to reach the reactor tritium self-sufficiency and extracting high grade heat to be used for the production of electricity.

The Breeder Units contains pebble beds of lithium orthosilicate (Li_4SiO_4) as tritium breeder material and beryllium as neutron multiplier. One characteristic is the highly nonlinear thermo-mechanical phenomena occurring in these pebble beds under neutron irradiation during the reactor operation. These phenomena is in turn influencing the heat transfer capabilities and therefore of the temperature field in these granular materials. On the other side, the temperature field plays a fundamental role in the 2 aforementioned key functions of the reactor, as the tritium breeding and the heat transfer mostly depends on the thermo-mechanics of these pebble beds. Therefore the correct prediction and control of these thermo-mechanics is a key factor in the feasibility of this breeding blanket concept.

In this dissertation a closed validation strategy for the thermo-mechanical validation of the Breeder Units has been developed. This strategy is based on the development of dedicated testing and modeling tools, which are needed for the qualification of the thermo-mechanical functionality of these components in an out-of-pile experimental campaign.

The neutron flux in the Breeder Units induces a nonhomogeneous volumetric heating in the pebble beds that must be mimicked in an out-of-pile experiment with an external heating system minimizing the intrusion in the pebble beds. Therefore, a heater system that simulates this volumetric heating has been developed. This heater system is based on ohmic heating and linear heater elements, which approximates the point heat sources of the granular material by linear sources. These linear sources represent “linear pebbles” in discrete locations close enough to relatively reproduce the thermal gradients occurring in the functional materials. The heater concept has been developed for the Li_4SiO_4 and it is based on a hexagonal matrix arrangement of linear and parallel heater elements of Ø1 mm separated by 7 mm. The same principle can be applied to reproduce the nuclear heating in the beryllium pebble bed by adjusting the distances and power of the heating elements. A set of uniformly distributed thermocouples in the transversal and longitudinal direction in the pebble bed midplane allows a 2D temperature reconstruction of that measurement plane by means of biharmonic spline interpolation.

This heating system has been implemented in a relevant Breeder Unit region and its proof-of-concept has been tested in a *PRE*-test *M*ock-*U*p e*X*periment (PREMUX) that has been designed and constructed in the frame of this dissertation. The packing factor of the pebble bed with and without the heating system does not show significant differences, giving an indirect evidence of the low intrusion of the system. Such low intrusion has been confirmed by *in-situ*

effective thermal conductivity measurements of the pebble bed at room temperature by hot wire method, showing a good agreement with the available literature. Steady state runs at 5 heating power levels encompassing the highest heat generation to be expected in the BU and relevant transient pulses have been performed, demonstrating the suitability of the concept to mimic the thermal gradients in the pebble beds. The 2D thermal map of the pebble bed at any power level has revealed a mostly symmetric distribution and no significant differences could be observed between the temperature read on the top and bottom surfaces at the interface layer between the pebble bed boundary and the test box of PREMUX. Therefore, no significant effect can be observed in the temperature distribution due to the potential gap formed after successive inelastic compressions of the pebble bed.

As a provision of modeling tools, two complementary approaches have been developed, aiming at giving a comprehensive modeling tool for prediction and validation purposes. The first is a deterministic, simplified thermo-mechanical model implemented in the commercial finite element code ANSYS. This model represents basic phenomena in the pebble beds, namely nonlinear elasticity, Drucker-Prager Cap plasticity, a non-associative flow rule and an isotropic hardening law. Preliminary validation of the model with the available literature on uniaxial compression tests comparing the axial compression stress against pebble bed strain at difference temperatures has shown a good agreement (root mean square errors <10%). The application of the model to PREMUX has shown a good general agreement as well with the temperature distribution dataset obtained during the experimental campaign with PREMUX. The predicted peak hydrostatic pressures are about ~2.1 MPa and are located around the central heaters and thermocouples, while the maximum values for the bulk of the pebble bed are about 1.4 MPa. According to the literature, such hydrostatic stress represents a maximum contact force in the pebbles of 2~3 N, which is lower than the known average crush load for these pebbles. Therefore, a very low cracking amount of the pebbles is to be expected in PREMUX, which has been later confirmed by post-mortem analyses in the decommissioned pebbles from PREMUX.

The second modeling approach is based on a probabilistic finite element method, which takes into account the inherent uncertainties of the model's input parameters and permits running a stochastic sensitivity analysis to obtain statistical information about the model outputs. Such an approach permits a formal validation of the model by defining a metric based on statistical data from both the model and the experiment. This approach has been implemented to a thermal model of PREMUX developed with ANSYS and its DesignXplorer module. After the determination and characterization of the stochastic model input parameters, computational Design of Experiments (DoE) have been run for each power level of the heating system to obtain a set of design points, which are used in a further step to build response surfaces by appropriate interpolation schemes (meta-models) for each model output, corresponding to the temperatures of the pebble bed at the measurement plane of PREMUX. At this point, the meta-models replace the finite element model and thousands of stochastic sampling runs can be performed, obtaining in this way the probabilistic density functions of the model outputs. As validation metric, the slope of a linear regression between the stochastic model outputs and the benchmark values obtained in PREMUX is proposed, which has given a quantitative value of the agreement (1:1) and its statistical significance (95% confidence).

Kurzfassung

Die Bruteinheiten sind die zentralen Komponenten des sogenannten Helium Cooled Pebble Bed (HCPB) Brut Blankets. Diese Komponenten erfüllen zwei Schlüsselfunktionen eines nuklearen Fusionsreaktors: Erbrüten des benötigten Tritiums, um eine Selbstversorgung des Reaktors mit Tritium zu erreichen, und Extrahieren von Wärme, die zur Erzeugung von Elektrizität genutzt werden kann.

Die Bruteinheiten bestehen aus einem Schüttbett aus Lithium-Orthosilikat (Li_4SiO_4) als Tritium-Brutmaterial und einem Beryllium Schüttbett als Neutronen-Multiplikator. Eine Besonderheit, die in den Schüttbetten auftritt, sind stark nichtlineare thermo-mechanische Phänomene unter Neutronenbestrahlung während des Betriebs. Diese Phänomene beeinflussen wiederum die Wärmeübertragungsfähigkeit und somit das Temperaturfeld dieser granularen Materialien. Auf der anderen Seite spielt das Temperaturfeld eine wichtige Rolle bei den zwei vorhergenannten Schlüsselfunktionen des Reaktors, da das Erbrüten von Tritium und die Wärmeübertragung hauptsächlich vom thermo-mechanischen Verhalten dieser Schüttbetten abhängt. Daher ist die korrekte Vorhersage und Kontrolle des thermo-mechanischen Verhaltens ein Schlüsselfaktor für die Umsetzbarkeit dieses Brut Blanket Konzepts.

In dieser Dissertation wurde eine geschlossene Validierungsstrategie zur thermo-mechanischen Validierung der Bruteinheiten entwickelt. Diese Strategie basiert auf der Entwicklung von speziellen Test- und Modellierungswerkzeugen, die zur Qualifikation der thermo-mechanischen Funktionalität dieser Komponenten in einer Out-of-pile Versuchsreihe benötigt werden.

Der Neutronenfluss in den Bruteinheiten erzeugt eine nichthomogene Erwärmung der Schüttbetten, der bei einem Out-of-pile Experiment durch ein externes Heizsystem ersetzt werden muss, wobei die Störung des Schüttbetts möglichst gering zu halten ist. Aus diesem Grund wurde ein Heizsystem entwickelt, das diese volumetrische Heizung simuliert. Dieses Heizsystem basiert auf ohmscher Heizung und linienförmigen Heizelementen, die die punktförmigen Wärmequellen des granularen Materials durch linienförmige Wärmequellen annähern. Diese linienförmigen Wärmequellen repräsentieren „längliche Kügelchen“ in diskreten Positionen, die nahe genug angeordnet sind, um die im funktionalen Material auftretenden thermischen Gradienten zu reproduzieren. Das Heizerkonzept wurde für Li_4SiO_4 entwickelt und basiert auf einer hexagonalen Matrix-Anordnung von linienförmigen und parallelen Heizelementen mit einem Durchmesser von 1 mm und einem Abstand von jeweils 7 mm. Dasselbe Prinzip kann angewandt werden, um die nukleare Erwärmung in Beryllium Schüttbetten zu reproduzieren, indem man die Abstände und Leistung der Heizelemente anpasst. Ein Satz gleichförmig verteilter Thermoelemente in Quer- und Längsrichtung in der Mittelebene des Schüttbetts ermöglichen eine zweidimensionale Temperaturrekonstruktion der Messebene durch biharmonische Spline-Interpolation.

Dieses Heizsystem wurde in einen relevanten Bereich der Bruteinheit eingebaut und der Konzeptnachweis wurde in einem PRE-test Mock-Up eXperiment (PREMUX) erbracht, das im Rahmen dieser Dissertation entwickelt und gebaut wurde. Die Packungsdichte des Schüttbetts mit und ohne Heizsystem zeigt keinen signifikanten Unterschied, was einem indirekten Nachweis der geringen Störung durch das Heizsystem entspricht. Diese geringe Störung wurde durch in-situ Messungen der effektiven thermischen Leitfähigkeit des Schüttbetts bei Raumtemperatur mit der Hot-Wire-Methode bestätigt, die eine gute Übereinstimmung mit der verfügbaren Literatur zeigt. Stationäre Testreihen mit 5 verschiedenen Heizleistungen, die die höchste zu erwartende Wärmeerzeugung sowie relevante transiente Pulse enthalten, wurde durchgeführt und zeigten, dass das Konzept geeignet ist, die thermischen Gradienten innerhalb des Schüttbetts nachzuahmen. Die zweidimensionale Abbildung der Temperaturverteilung zeigt eine fast symmetrische Verteilung bei jedem Leistungsniveau und es konnten keine signifikanten Unterschiede der Temperatur an der oberen und unteren Oberfläche an der Verbindungsschicht zwischen dem Schüttbettrand und der Testbox von PREMUX beobachtet werden. Daher kann kein deutlicher Effekt in der Temperaturverteilung durch die Bildung möglicher Hohlräume nach mehrmaliger nicht-elastischer Kompression des Schüttbetts beobachtet werden.

Zwei sich ergänzende Methoden wurden mit dem Ziel entwickelt, ein umfassendes Modellierungs-Werkzeug für Vorhersage und Validierungszwecken bereitzustellen. Die erste Methode ist ein deterministisches, vereinfachtes thermo-mechanisches Modell, das in dem kommerziellen Finite–Elemente-Code ANSYS implementiert ist. Dieses Modell repräsentiert grundlegende Phänomene innerhalb des Schüttbetts: Nichtlineare Elastizität, Drucker-Prager Cap Plastizität, eine nicht-assoziatives Fließgesetz und ein anisotropes Verfestigungsgesetz. Eine erste Validierung des Modells anhand des Vergleichs der einachsigen Kompressionsspannung von in der Literatur vorhandenen einachsigen Kompressionstests mit der Dehnung des Schüttbetts bei verschiedenen Temperaturen zeigt eine gute Übereinstimmung (root mean square errors (RMSE) $<$ 10%). Die Anwendung des Modells auf PREMUX hat ebenfalls eine im Allgemeinen gute Übereinstimmung der Temperaturverteilungen, die während der Experimentdurchführung mit PREMUX aufgezeichnet wurden, gezeigt. Die vorhergesagten hydrostatischen Spitzendrücke betragen etwa 2,1 MPa und treten um den zentralen Heizer und die Thermoelemente auf, wohingegen im Volumen des Schüttbetts die maximalen Werte bei etwa 1,4 MPa liegen. Laut Literatur entsprechen solche hydrostatischen Drücke einer maximalen Kontaktkraft der Kügelchen von 2-3 N, was unterhalb der bekannten durchschnittlichen Zerdrückungs-Last dieser Kügelchen ist. Daher wird ein geringer Anteil an zerbrochenen Kügelchen in PREMUX erwartet, was später durch eine Analyse der Kügelchen nach Beendigung des Experiments bestätigt wurde.

Der zweite Modellierungs-Ansatz basiert auf einer probabilistischen Finite-Elemente-Methode, die die inhärenten Unsicherheiten der Eingangsparameter des Modells berücksichtigt und erlaubt, eine stochastische Sensitivitätsanalyse durchzuführen, um statistische Informationen über die Ausgänge der Modells zu erhalten. Dieser Ansatz ermöglicht die formale Validierung des Modells durch die Definition eines Kriteriums basierend auf statistischen Daten von Modell und Experiment. Diese Vorgehensweise wurde in einem thermischen Modell von PREMUX in ANSYS und dem DesignXplorer-Modul implementiert. Nach der Bestimmung und Charakterisierung der stochastischen Eingangsparameter des Modells wurde ein Design of Experiments (DoE) für jedes

Leistungs-Level des Heizsystems durchgeführt, um einen Satz von Designpoints zu erhalten, der in einem weiteren Schritt dazu genutzt wurde, ein Response-Surface mithilfe von geeigneten Interpolationsverfahren (Meta-Modelle) für jeden Modellausgang aufzubauen. Ein Modellausgang entspricht dabei jeweils einer Temperatur des Schüttbetts in der Messebene von PREMUX. An diesen Punkten ersetzen die Meta-Modelle das Finite-Elemente-Modell und tausende Berechnungen können durchgeführt werden, um stochastische Stichproben zu erzeugen und auf diese Weise die Wahrscheinlichkeitsdichtefunktionen der Modellausgänge zu erhalten. Als Validierungskriterium wird die Steigung einer linearen Regression zwischen den stochastischen Modellausgängen und den Vergleichswerten aus dem PREMUX Experiment vorgeschlagen, welches einen quantitativen Übereinstimmungswert (1:1) und eine statistische Signifikanz (95 % Konfidenz) gibt.

Contents

List of Symbols

Symbols	Meaning
a	accuracy
c	velocity
$c_{p,air}$	specific heat capacity
d	(1) yield function material parameter
	(2) diameter
f	friction factor
g	(1) gravity
	(2) response surface meta-model
h	(1) fluid enthalpy
	(2) heat transfer coefficient
k	thermal conductivity
k_{eff}	pebble bed effective thermal conductivity
$k_{\%}$	uncertainty coverage factor
l	length
m_0	Rest mass of a particle
$\dot{m}$	mass flow
n	plasma ion density
p	(1) hydrostatic pressure
	(2) significance level (p-value)
$\bar{p}_a$, $\bar{p}_b$	Drucker-Prager Cap model marker points
q	(1) von Mises stress
	(2) physical quantity
	(3) power per unit length
r	(1) radial coordinate in polar axis system
	(2) electric line resistance (per unit length)
r_S	Spearman's rank-order correlation coefficient
r_i	random variable
s	root mean square error
s_i	random variable
s_1, s_2, s_3	principal deviatoric stresses
t	(1) time
	(2) t-Student statistic
u	standard uncertainty
v	particle velocity
x	(1) exponent
	(2) position coordinate

x_i^{det}	deterministic variable
x_i^{sto}	stochastic variable
y	position coordinate
z	position coordinate

$\boldsymbol{x}$	internal variables vector
$\boldsymbol{e}_x$, $\boldsymbol{e}_y$, $\boldsymbol{e}_z$	coordinate system base vectors
$\boldsymbol{n}$	unit normal vector
$\boldsymbol{t}$	tension vector
$\bar{\bar{\boldsymbol{P}}}$	hydrostatic pressure tensor
$\bar{\bar{\boldsymbol{S}}}$	deviatoric stress tensor
$\boldsymbol{x}^{det}$	vector of deterministic variables
$\boldsymbol{x}^{sto}$	vector of stochastic variables

A_c	cross-sectional area
A	yield function material parameter
C_i	curve fitting parameters
C_0	Mohr-Coulomb material parameter
D_h	hydraulic diameter
D_1, D_2	isotropic hardening material parameters
E	(1) particle energy
	(2) Young's modulus
	(3) experimental error
F	plastic flow potential
G	total heating power in pebble bed
H	height
I	current
I_1, I_2, I_3	stress invariants
J_1, J_2, J_3	stress invariants of the deviatoric tensor
K	yield function material parameter
K_0	Drucker-Prager Cap model marker point
L	length
L_{pb}	pebble bed thickness
Nu	Nusselt number
P	power
Pr	Prandlt number
Q	(1) heat
	(2) physical quantity
Q_{gf}	fusion energy gain factor
R	(1) electric resistance
	(2) yield function material parameter
	(3) coefficient of determination of a regression curve
$R\text{-}adj$	adjusted coefficient of determination of a regression curve
R_i	variable rank

R_c^Y	yield function material parameter
R_t^Y	yield function material parameter
R_c^F	plastic flow potential material parameter
R_t^F	plastic flow potential material parameter
Ra	Rayleigh number
Re	Reynolds number
$RMSE$	root mean square error
S_i	variable rank
T	temperature
TCC	thermal contact conductance
W_1	isotropic hardening material parameter
X_0	Drucker-Prager Cap model marker point
Y	yield surface

Greek symbols

α	(1) thermal diffusivity (2) yield function material parameter
α^Y	yield function material parameter
α^F	plastic flow potential material parameter
β	yield function material parameter
β^F	plastic flow potential material parameter
β_L	Lode angle in the Haigh-Westergaard coordinate system
β_{MC}	Mohr-Coulomb friction angle
β_{th}	thermal expansion coefficient
β^Y	yield function material parameter
ε	(1) strain (2) random error
ε_{vol}^{in}	inelastic volumetric strain
θ	meta-model parameter
θ_L	dimensionless temperature
ϑ	angle
λ	proportionality constant
μ	dynamic viscosity
μ_s	pebble bed static friction coefficient
ν	Poisson's ratio
ξ	dimensionless coordinate
ρ	(1) radial coordinate in the Haigh-Westergaard coordinate system (2) mass density
σ	(1) particle cross section (2) standard deviation
σ_Y	yield stress
σ_0	yield function material parameter
σ_1, σ_2, σ_3, σ_I, σ_{II}, σ_{III}	principal stresses

τ_E	plasma confinement time
φ	dilatancy angle
ϕ	relationship between physical quantities
ψ	ratio of triaxial extension to triaxial compression

$\boldsymbol{\theta}$	meta-model parameters vector
$\boldsymbol{\sigma}_1$, $\boldsymbol{\sigma}_2$, $\boldsymbol{\sigma}_3$,	stress tensor eigenvectors
$\overline{\overline{\boldsymbol{\sigma}}}$	stress tensor

Γ	Lode function
$\tilde{\varTheta}$	probabilistic thermal model
$\varTheta$	mechanistic thermal model
Φ	correction factor for the Gnielinski correlation for backward-facing step flows

Index

$\square^{\mathrm{H_i}}_{\mathrm{cold,0}}$	heater i cold part at room temperature
$\square^{\mathrm{H_i}}_{\mathrm{hot,0}}$	heater i hot part at room temperature
$\square^{\mathrm{H_i}}_{\mathrm{tot,0}}$	heater i cold and hot part at room temperature
$\square_{TC}$	thermocouple
$\square_{ini}$	initial
$\square_{Axi}$	axial
$\square_{Lat}$	lateral
$\square_{vM}$	von Mises
Y_{MC}	Mohr-Coulomb
Y_{DP}	Drucker-Prager
Y_{DPC}	Drucker-Prager Cap
$\square^{ABQ}$	formulation in ABAQUS code
$\square^{ANS}$	formulation in ANSYS code
$\square_s$	shear
$\square_c$	compaction cap
$\square_t$	transition shear-to-compaction-cap
$\square^{Gn}$	Gnielinski
$\square^{DB}$	Dittus-Boelter
$\square_{D_h}$	hydraulic diameter
T_{in}	Inlet
T_{out}	outlet

Operators

$\langle\square\rangle$	average between physical fields
$[\square]$	dimension of a physical variable
$\overline{\square}$	(1) negative (2) average

$\widehat{\square}$	estimation
$\mathcal{T}[\square]$	Taylor series expansion
$N(\square)$	normal distribution
$t_{1-\alpha,m-p}$	t-Student distribution with $m-p$ degrees of freedom at a statistical significance of α
$E(\square)$	expected value of random variable
$V(\square)$	variance of random variable
$pdf(\square)$	probability density function
$Cov(\square)$	covariance
$R(\square)$	Gaussian correlation function

Dimensions

$[L]$	length
$[M]$	mass
$[P]$	power
$[T]$	time
$[\boldsymbol{\theta}]$	temperature

Chapter 1

Introduction

Pebble beds are present in many fields of engineering, from hydraulic engineering, to soil mechanics in civil engineering, fluidized beds in chemical rectors and pebble beds for the nuclear industry. In the particular case of the nuclear fusion field, fusion reactors necessitate a so-called *breeding blanket*. This key system of the reactor is mainly aimed at producing tritium, which is one of the two components together with deuterium needed for the nuclear fusion reaction. One of the breeding blanket concepts considered in the European Union is the so-called *Helium Cooled Pebble Bed* breeding blanket. This blanket features *Breeder Units*, containing pebble beds of a ternary lithiated ceramic compound and beryllium. These pebble beds are in charge of the nuclear production of tritium and must work under harsh conditions, e.g. fast neutron flux, temperatures up to ~$900°C$, pulsed conditions and confined thermal expansion. Understanding the thermo-mechanical behavior of the pebble beds and the breeder unit as a whole is fundamental for the development of breeding blanket systems in fusion reactor applications.

In this Chapter, the background of nuclear fusion, the tritium breeding principles and the goal of the breeding blanket system are introduced. The current running programs aimed at developing the necessary scientific knowledge and technology for the realization of a demonstration fusion reactor are thereafter presented. The Chapter concludes by a discussion on the motivation of this work, the goals and the organization of the Chapters in this thesis.

1.1 Background

1.1.1 Thermonuclear reactions and fusion reactors basics

Thermonuclear reaction basics

Early in the 20th century F. W. Aston (Nobel Lectures, 1966) measured the masses of different isotopes, stating the so-called *whole number rule* for isotopes and measuring the masses of different isotopes, being 4 for helium and 1.008 for hydrogen. Motivated by a 0.8% higher than expected mass of hydrogen and taking into account the mass-energy equivalence theorized by A. Einstein (1905), Eddington (1920) suggests that the stars power themselves by fusing 4 hydrogen nuclei to form 1 nuclei of helium, releasing energy in the process due to the excess of mass. This hypothesis, despite oversimplified, put the foundation for the idea of the existence of energy release from thermonuclear fusion (or nuclear fusion).

The fact that the protons, which have a net positive electrical charge, are kept bonded in an atom instead of being expelled due to the electrostatic forces suggested the existence of the so-called *strong interaction* between these nucleons in an atom, acting only at distances of the order of magnitude of the atomic radii. Therefore, according to the Coulomb's law and in order to bring these nuclei together sufficiently close so as to overcome the electrostatic repulsion and allow the strong interaction to take place, two light nuclei like hydrogen would require prohibitively high energies to be produced in a device.

However, the development of the quantum mechanics at that time explained how thermonuclear reactions take place at much lower energies thanks to the existence of the so-called *quantum tunneling* effect. This effect predicts that it exists a non-zero probability of a particle travelling through a barrier such as the one produced by the Coulomb forces. This probability becomes significant enough at high energies to overcome the Coulomb barrier, though these energies are far lower than the ones predicted by the classical electrostatic law.

The probability of a nuclear reaction to occur is characterized by its *cross-section* σ. Figure 1.1-left plots the cross-section of the principal nuclear fusion reactions for different particles' energies. The nuclei involved in these reactions do not have a unique velocity but follow a Maxwellian distribution, which also applies for the relative velocity v of the interacting particles. Thus, an average fusion cross-section $\langle \sigma v \rangle$ over v can be obtained, representing a fusion reaction rate $\left[\frac{m^3}{s}\right]$. The reaction rates for the main nuclear fusion reactions are plotted in Figure 1.1-right.

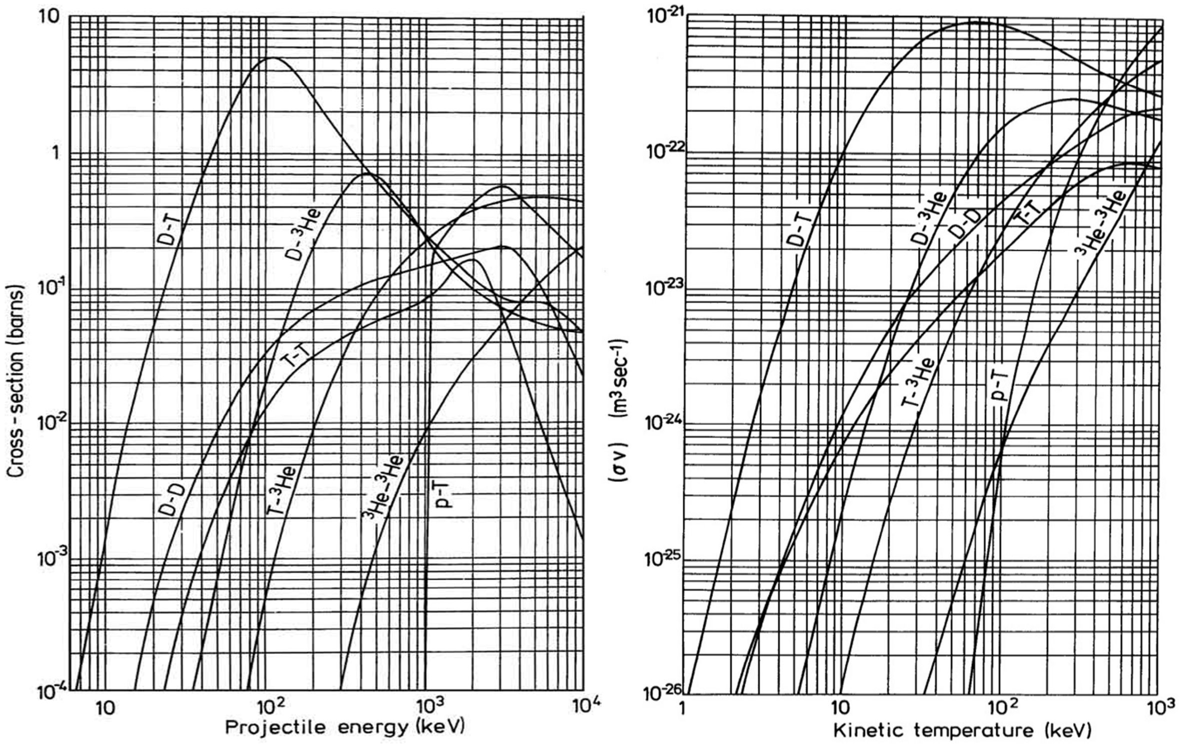

Figure 1.1: Main thermonuclear fusion reactions. Left: nuclear cross-section. Right: reaction rates (National Physical Laboratory, 1995), both as a function of the incident nucleus energy.

In Figure 1.1-right can be noticed that given a $\langle \sigma v \rangle$, the thermonuclear fusion of the hydrogen isotopes deuterium ($^2_1\mathrm{H} \equiv \mathrm{D}$) and tritium ($^3_1\mathrm{H} \equiv \mathrm{T}$) requires lower kinetic energies (up to 550 keV), but always in a range of energies (temperatures) where the reactants are in a plasma state. These characteristics make the D+T reaction as the most promising for demonstrating energy production in a nuclear fusion reactor.

The product of the D+T reaction is then helium, $^4_2\mathrm{He}$ (He), and a neutron, $^1_0\mathrm{n}$ (n). Taking into account that the atomic weight of D, T, He and n are 2.01411 amu, 3.01605 amu, 4.00260 amu and 1.00866 amu respectively[1] and that 1 amu corresponds to $1.66054 \cdot 10^{-27}$ kg (Stieglitz, 2009a), the total mass of the reactants is $(2.01411\ amu + 3.01605\ amu) \cdot 1.66054 \cdot 10^{-27}\ kg/amu = 8.35277 \cdot 10^{-27}\ kg$, while for the products is $(4.00260\ amu + 1.00866\ amu) \cdot 1.66054 \cdot 10^{-27}\ kg/amu = 8.32140 \cdot 10^{-27}\ kg$. The mass defect after the thermonuclear reaction is thus $8.35277 \cdot 10^{-27}\ kg - 8.32140 \cdot 10^{-27}\ kg = 3.13677 \cdot 10^{-29}\ kg$.

According to the mass-energy equivalence equation (Einstein, 1905):

$$E = m_0 c^2 \ , \tag{1.1}$$

where m_0 is a rest mass and $c = 299792458\ m/s$ the speed of light, the mass defect after the thermonuclear fusion is converted into energy as:

$$\begin{aligned} E = m_0 c^2 &= 3.13677 \cdot 10^{-29} \ \cdot 299792458^2 = \\ &= 2.81919 \cdot 10^{-12}\ J \ \cdot \frac{1\ MeV}{1.60218 \cdot 10^{-13}\ J} \approx 17.6\ MeV \ , \end{aligned} \tag{1.2}$$

which relates to the total kinetic energy of the products. As the atomic mass of He is about 4 times that of a neutron, the conservation of momentum indicates that the kinetic energy of the neutron has to be approximately 4 times that of the He, i.e. 14.1 MeV and 3.5 MeV, respectively.

Therefore, the D+T nuclear fusion reaction can be written as:

$$\mathrm{D} + \mathrm{T} \rightarrow \mathrm{He} + \mathrm{n} + 17.6\ \mathrm{MeV} \ . \tag{1.3}$$

Thermonuclear reactor basics

In a thermonuclear reactor, the energy rate associated with the alfa particles produced after the fusion of D and T must be sufficient to maintain the energy of the reactants in the plasma, which suffer mainly of radiation (Bremsstrahlung, synchrotron and line radiation) and diffusion (plasma heat conduction) losses. This self-sustained energy feedback state is referred as *burning* plasma, while the moment when the burn takes place is known as plasma *ignition.* The fusion energy *gain factor* Q_{gf} is then defined as the ratio between the nuclear fusion power P_{fus} and the total plasma heat P_{heat} needed to sustain the thermonuclear fusion reactions:

$$Q_{gf} = \frac{P_{fus}}{P_{heat}} \ . \tag{1.4}$$

---

[1] The unit *amu* stands for "*atomic mass unit*".

The fusion *breakeven* is referred to $Q_{gf} = 1$. However, values of $Q_{gf}\sim 20$ would be required to keep a thermonuclear fusion reactor controllable (Zohm, 2010).

A general condition to achieve a burning plasma in a thermonuclear reactor is given by the so-called *triple product*, which derives from the well-known Lawson criterion (Lawson, 1957). In the triple-product, the condition of burning plasma is achieved when the product defined by the *plasma temperature* T (kinetic energy of the reactants), the *confinement time* τ_E (time required to maintain the plasma above the ignition temperature) and the *ion density* n of the plasma is higher than a certain value, which depends on the reaction type. In the case of the D+T reaction, the triple product $nT\tau_E$ has a minimum of $2.9 \cdot 10^{28} sK/m^3$ at 13 keV (Figure 1.2), representing a temperature of ~150 million $°C$ (Stieglitz, 2009b).

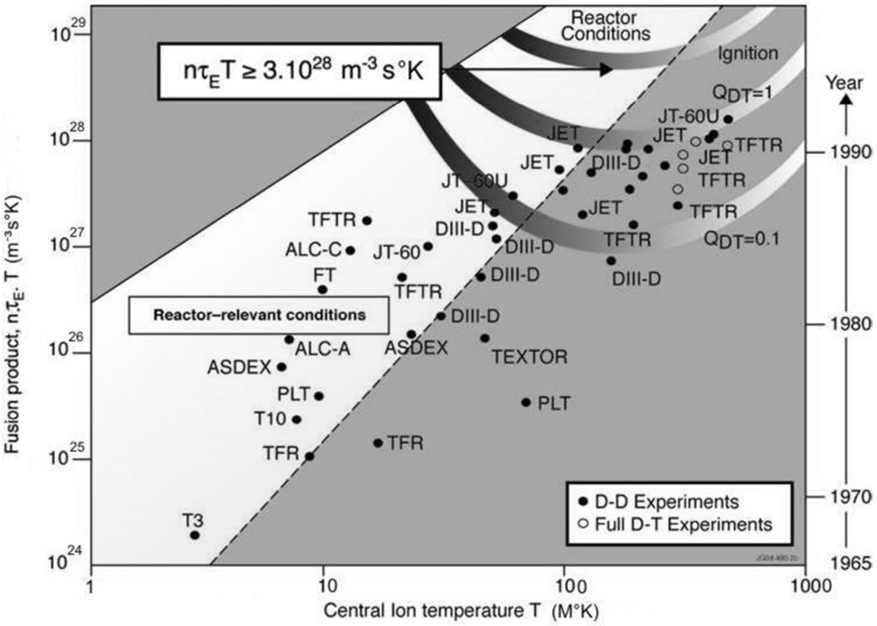

Figure 1.2: Fusion triple product $nT\tau_E$ as a function of the central plasma temperature T. Three isocurves of the $nT\tau_E$ for the cases $Q_{gf} = 0.1$, $Q_{gf} = 1$ and ignition are plotted. The points represents different tokamak devices. Source: https://www.euro-fusion.org.

As there is no known material that can withstand these temperatures in a solid state, two main plasma confinement methods exist: *magnetic confinement* and the *inertial confinement*[2]. The magnetic confinement is based on fact that the particles forming the plasma are ionized, thus having large velocities. Under the presence of magnetic fields these ion particles are to be influenced by Lorenz forces. Therefore, magnetic fields are generated and directed into a vacuum vessel containing the plasma, which is to be confined without reaching the walls of the vessel due to the presence of the magnetic fields. On the other side, in the inertial confinement the D+T reactants are in a pellet-like containment, which is normally heated up by lasers until it implodes, causing the D+T to achieve ignition conditions.

---

[2] Some of the other alternatives to these concepts are reported by Woodruff (2004).

While the scientific and technological level of maturity of the inertial confinement is still in an early stage and does not permit yet to suggest any particular approach for a demonstration reactor (The National Academies, 2011), the magnetic confinement has a broader scientific and technological background, supported already with several devices aimed at demonstrating its technical feasibility. This level of maturity permits to think about a roadmap towards the construction of a DEMOnstration reactor (DEMO) before the mid of the 21st century (Romanelli et al., 2012).

The main fusion reactor concept based on magnetic confinement is the so-called *tokamak*[3] device, which originates from 1950 after Sakharov and Tamm (Azizov, 2012). In a tokamak, the plasma is confined magnetically forming a toroidal shape, as shown in Figure 1.3-left. A central solenoid (or inner poloidal coils) is placed concentrically to the toroid center. This solenoid acts as the primary coil of a transformer inducing a current in the plasma, which acts then here as the "secondary coil", thus producing a poloidal magnetic field. This solenoid also provides for ohmic heating during a start-up phase of the reactor. Toroidal Field (TF) coils are placed around the plasma volume along the toroid centerline and provides for confinement of the plasma particles. The TF coils provides for magnetic flux in the plasma following the toroid annulus. When adding the poloidal magnetic field to the toroidal one, a twisted magnetic field is generated. This magnetic field is necessary in order to compensate the gradient drift that the particles would experience in the case that only a toroidal magnetic field existed. Additionally, poloidal field coils are placed concentrically to the toroid, contributing to the shape and stability of the plasma. The current induced to the plasma is based on a constant increase of the magnetic flux in the central solenoid, which is inherently limited: once the solenoid reaches its magnetic flux limit, the operation must be interrupted (thus terminating the nuclear fusion) and restarted again. This defines the characteristic pulsed operation for this kind of devices. However, a quasi-steady state operation is also possible by using non-inductive current drives (e.g. neutral beam injectors, radio-frequency, etc.)

An alternative magnetic confinement reactor design is based on the so-called *stellarator* concept (Spitzer, 1954; Spitzer, 1958). In this concept, the required twisted magnetic field is generated without the need of inducing plasma current. Instead, the necessary twist to the magnetic field is provided by helical coils placed along the toroid in combination with the TF coils in the case of the *heliotron* concept (Uo, 1961), or by non-planar, modular TF coils in the case of the *helical advanced stellarator* (*helias,* Figure 1.3 bottom) concept (Wobig & Rehker, 1972; Miller & Krakowski, 1981). Contrarily to the tokamak device concept, the fact of not having a central solenoid allows a steady state operation of a reactor based on this concept. However, the stellarator configuration is technically very complex, requiring more precise tolerances than for the tokamak concept, with 3D components (non-planar geometries) and difficult accessibility to the in-vessel components, severely complicating the reactor design.

---

[3] originates from the Russian acronym токамак and stands for "toroidal chamber with magnetic coils".

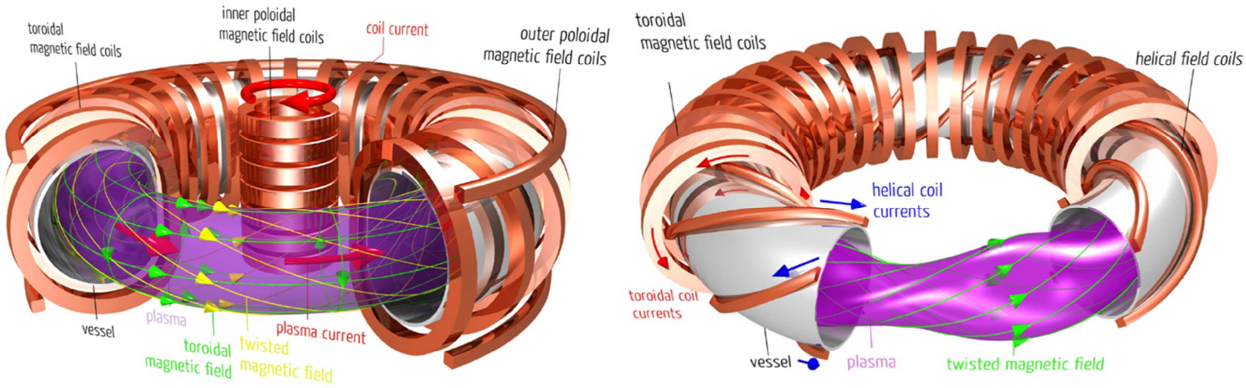

Source: Max-Planck Institut für Plasmaphysik, Abteilung Öffentlichkeitsarbeit

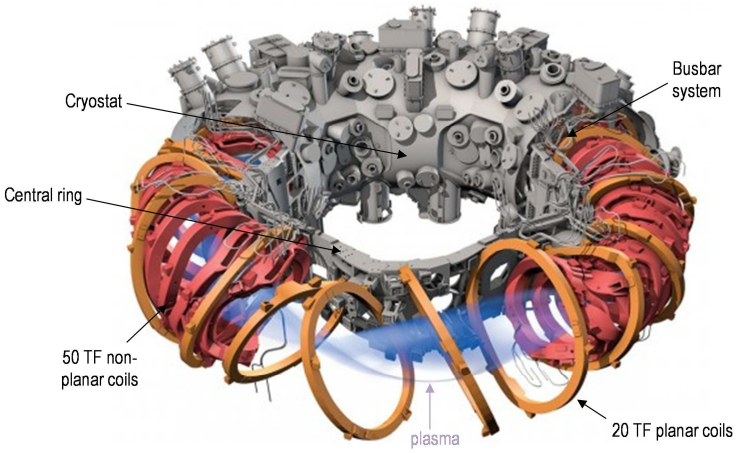

Adapted from: IPP by C. Bickel and A. Cuadra / AAAS Science

Figure 1.3: Conceptual designs of a nuclear reactor based on magnetic confinement. Top-left: tokamak concept. Top-right: heliotron stellarator concept. Bottom: Wendelstein 7-X (heliac stellarator concept)

1.1.2 Thermonuclear reactor core principles: the breeding blanket system

Figure 1.4 left depicts the conceptual schema of a nuclear reactor based on the tokamak device, showing the main functional systems. As mentioned in Section 1.1.1, initial heating is needed to reach the ignition of the plasma. Part of this heating is provided by the ohmic heating of the central solenoid. However, as the plasma increases its temperature, its resistivity decreases, thus limiting the ohmic heating up to 1 keV. The additional temperature is then provided by external heating and a current drive system.

In order to fuel the burning plasma, frozen pellets of D and T are injected directly into the tokamak core, towards the center of the plasma volume. On the one side, D is obtained by Girdler-Sulfid-Process (isotopical exchange), combined with vacuum distillation (Miller, 2001). This hydrogen isotope is found in water in a proportion of 32.5 $mg\ D$ per liter of water (Stieglitz, 2009b), thus being virtually endless. Contrarily, T is a rare isotope, which is radioactive (half-life of 12.3 years) and only present in nature in negligible amounts as a product of the reaction of cosmic rays (high energy neutrons) with the atmosphere' nitrogen (^{14}N) as $^{14}\mathrm{N} + \mathrm{n} \rightarrow\ ^{12}\mathrm{C} + \mathrm{T}$. A certain inventory of T is present as nuclear waste from pressurized heavy-water reactors (Canadian and South-Korean CANDU[4] reactors) as a byproduct of the D reaction with fission neutrons, though being not sufficient to operate a fusion reactor (Federici et al., 2015). Therefore, T must be produced (bred) *in-situ* in the reactor: the function of the tritium breeding is performed by the so-called *breeding blanket system* in a thermonuclear reactor (Figure 1.4).

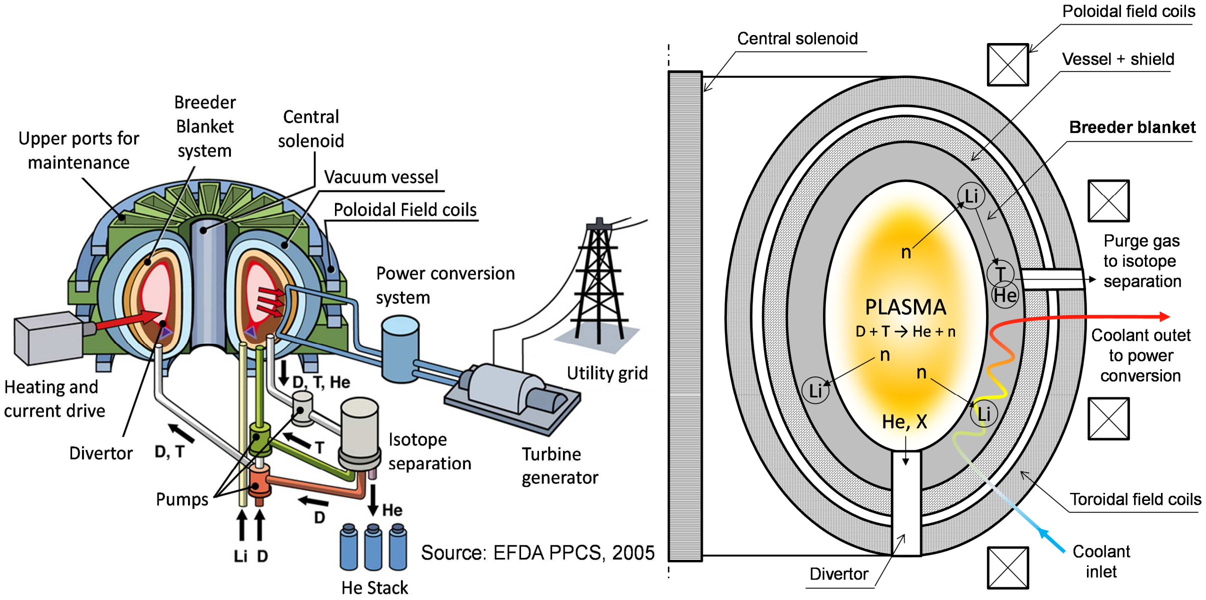

Source: EFDA PPCS, 2005

Figure 1.4: Conceptual representation of a thermonuclear reactor with main systems (left) and section cut view of the reactor core (right).

Once the plasma ignites and burns, 17.6 MeV per reaction are to be released according to Eqn. (1.3). About 80% of this energy originates from the kinetic energy of the fast neutrons and the rest ~20% belong to the He ion “ashes”, a part of it contributing to the plasma heating. As the neutrons are electrically neutral, they are not confined by the magnetic fields and escape the plasma reaching the walls of the tokamak.

The first layer of the tokamak wall facing the plasma is formed by the breeding blanket system (Figure 1.4-right). This system contains ^{6}Li and ^{7}Li in some form of compound which, under the neutron irradiation, reacts to form He and T mostly as an exothermic nuclear reaction. In order to increase the probability of T production, a neutron multiplier material (beryllium or lead) is also inserted in the system. A coolant fluid, normally helium or water at high pressures or a liquid breeder, flows through the inner structures of the breeding blanket, extracting the heat produced by the T breeding and materials activation nuclear reactions. The breeding blanket coolant belongs to the *primary heat transfer system* (PHTS). The power resulting from the temperature increase of the coolant flow in the PHTS is transferred to the secondary coolant of the Balance of Plant (BoP), where the turbine-generator group converts the heat conveyed by the coolant in the BoP into electricity, which is transferred to the utility grid. Therefore, the mission of the breeding blanket is double: to breed T and to extract high grade energy for electricity production, making this component a key performance system in the reactor.

---

[4] acronym for CANada Deuterium Uranium reactor

Two main groups of breeding blanket concepts exist, namely the *solid breeding blankets* and *liquid breeding blankets*. In the solid version, the lithium is placed in the blanket normally in form of a ceramic pebble bed. The lithiated ceramic pebbles remain in the blanket until this is removed at its end of life, which is defined by the maximum allowed radiation damage in the structural steel, degrading its ductility. In order to extract the T produced in the lithiated ceramic pebble beds, a so-called *purge gas* (He) flows through the pebbles, extracting the T contained in them in the process, which is led to an isotope separation facility.

In the liquid version, two variants exist: the liquid metal and the molten salt breeding blanket concepts. In the liquid metal concepts, the lithium (or metallic lithium compound) is in fluid state and continuously flows through the inner structures of the blanket, ensuring a continuous replacement of the breeder material and the purification of T and other transmutation byproduct elements. However, and due to the metallic properties of the fluid, it is influenced by the tokamak magnetic fields, complicating the flow in the breeding blanket. The molten salt variant is not metallic, thus not experiencing magnetohydrodynamic effects, but its low conductivity, higher melting point than liquid metals and very high reactivity (corrosion) complicates the design.

The breeding blanket system is attached to the (vacuum) vessel of the tokamak, which also confers shielding to the magnetic field coils and other sensitive components. The confined He "ashes", as well as impurities that arise from the interaction of the plasma with the breeding blanket plasma facing walls (the so-called *First Wall*, FW), eventually reach the outer part of the plasma. Here, these particles ultimately reach the *divertor* (Figure 1.4-right), which acts as power exhaust for these particles.

1.1.3 ITER and the demonstration fusion reactor DEMO

The International Thermonuclear Experimental Reactor (ITER, later representing the latin word "the way") is the largest experimental fusion reactor of the tokamak type being built up to date. It is an international venture including the European Union (EU), Russia, China, Japan, India, Korea, and the United States (US) aiming at demonstrating technical feasibility of the controlled fusion burning, achieving 500 MW of fusion power with a $Q_{gf} = 10$ (Kaname, 2010).

Despite the technological breakthroughs to be achieved in ITER, the device will not implement a functional breeding blanket but it will implement a blanket that performs the task of a thermal shield instead. ITER will thus not answer the question of the tritium self-sufficiency, as it relies on the external supply of T from the CANDU reactors (~20 kg T for the whole operational time). In a "true" reactor the consumption of T will be about ~153 g in a full power day operation for each GW of installed fusion power for several years (Raeder et al., 2016). The demonstration of the T self-sufficiency, as well as the capability to produce electrical energy at a competitive cost, shall be achieved in a demonstration power plant (DEMO), which is the step after ITER prior to the commercialization of fusion power plants.

In the EU, DEMO is being designed to achieve a fusion power of about 2000 MW (Federici et al., 2015), which contrasts to the 500 MW to be produced in ITER (ITER EDA, 2000).

Therefore, parameters related to the neutron irradiation in ITER are less relevant to DEMO. For instance, while the neutron irradiation on the FW, or *neutron wall load (NWL)*, is 0.57 MW/m^2 on average with peaks of 0.78 MW/m^2, the DEMO blanket will experience peaks about 1.5 MW/m^2. This is translated as well into a higher radiation damage level (measured as displacements per atom, *dpa*) in the structural steel of the FW in DEMO with respect to ITER: while ITER will experience a cumulative damage of about 3 *dpa*, DEMO will experience up to 120 *dpa* at the end of life of the blanket. The surface heat on the FW of the blanket in both devices has also large differences, as well as the duration of the pulsed operation (Figure 1.5): while the former has about 400 s for the flat top, DEMO is intended to reach fat tops of a couple of hours long, having both relevant ramp up and down times of ~30 s and ~60 s respectively. The pulse repetition time in ITER is about 1800 s.

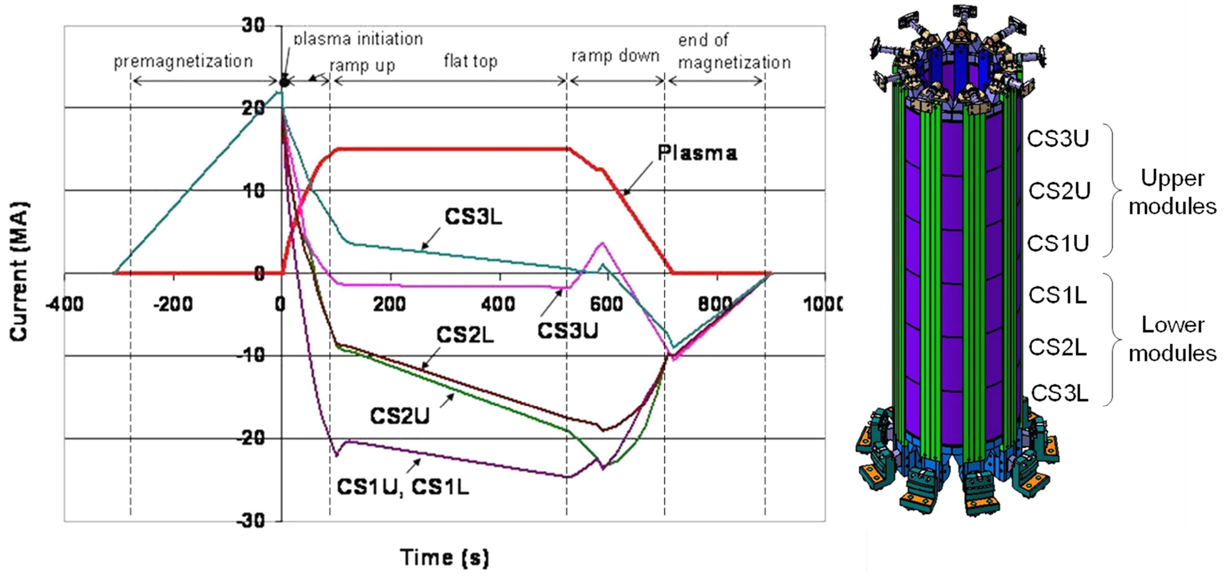

Figure 1.5: Electric current in each of the modules of the central solenoid in ITER. The names of each module of the central solenoid are indicated in the picture at the right. Of especial interest is the plasma current time evolution, which is directly related to the volumetric heating produced at the breeding blanket with the same time evolution (Source: `iter.org`).

1.1.4 The Test Blanket Modules (TBM) and the TBM Breeder Units

Despite not implementing a relevant breeding blanket system, the ITER Test Blanket Working Group (ITER-TBWG) was established in 1994 with the aim at developing a program to test the so-called *Test Blanket Modules* (TBMs), which are blanket modules sharing a degree of relevancy with their respective DEMO concept (Chuyanov & ITER Test Blanket Working Group, 2002).

The TBM program is considered as a key ITER goal and will serve to validate codes used for the design (e.g. T generation rate, T permeation rate to coolant, functional material temperatures and heat extraction capabilities for electricity production), manufacturing and the operation of breeding blanket systems in DEMO (Shatalov, 2001).

Among 11 different TBM versions based on solid and liquid breeding blankets (e.g. see Boccaccini et al., 2006; Ying et al., 2006; Feng et al., 2006; Kirillov et al., 2005; Han et al., 2006; Enoeda et al., 2006; Rajendra Kumar et al., 2008), 6 TBMs have been chosen for their test in ITER. These are: the Helium Cooled Lithium-Lead (HCLL) by the EU, the Helium Cooled Pebble Bed (HCPB) by the EU, the Helium Cooled Ceramic Breeder (HCCB) by China, the Helium Cooled Ceramic Reflector (HCCR) by Korea, the Water Cooled Ceramic Breeder (WCCB) by Japan, the Lithium-Lead Ceramic Breeder (LLCB) by India and Russia and the Dual Coolant Lithium-Lead (DCLL) by the US.

Figure 1.6 shows a section cutoff of the ITER reactor core. The reactor features 18 upper ports, 17 equatorial ports and 9 lower ports that mainly serve for remote handling operations in the reactor core and for the diagnostic, heating and vacuum systems. Though, 3 of these equatorial ports (numbers 2, 16 and 18) are dedicated for the installation of the aforementioned 6 TBMs, 2 in each of these 3 ports, being the port 18 dedicated for the HCPB and HCLL EU-TBMs (augmented detail in Figure 1.6). Both the HCLL and HCPB feature the so-called *Breeder Units*, which are the core part of the TBMs. In particular, the HCPB Breeder Unit is formed by two actively cooled U-shaped steel plates containing the lithium ceramic pebble bed in-between them. The Be pebble bed fills the remaining volume around the Breeder Unit, all forming the so-called *breeder zones* of the HCPB TBM, which are to be relevant to those in DEMO.

The Breeder Units are therefore in charge for the T production in the lithium compound material, its release and transport out of the breeding blanket towards the tritium extraction and removal systems. The T release and its transport through the breeder zone are found to be greatly affected by the temperature of the breeder materials (Federici et al., 1992).

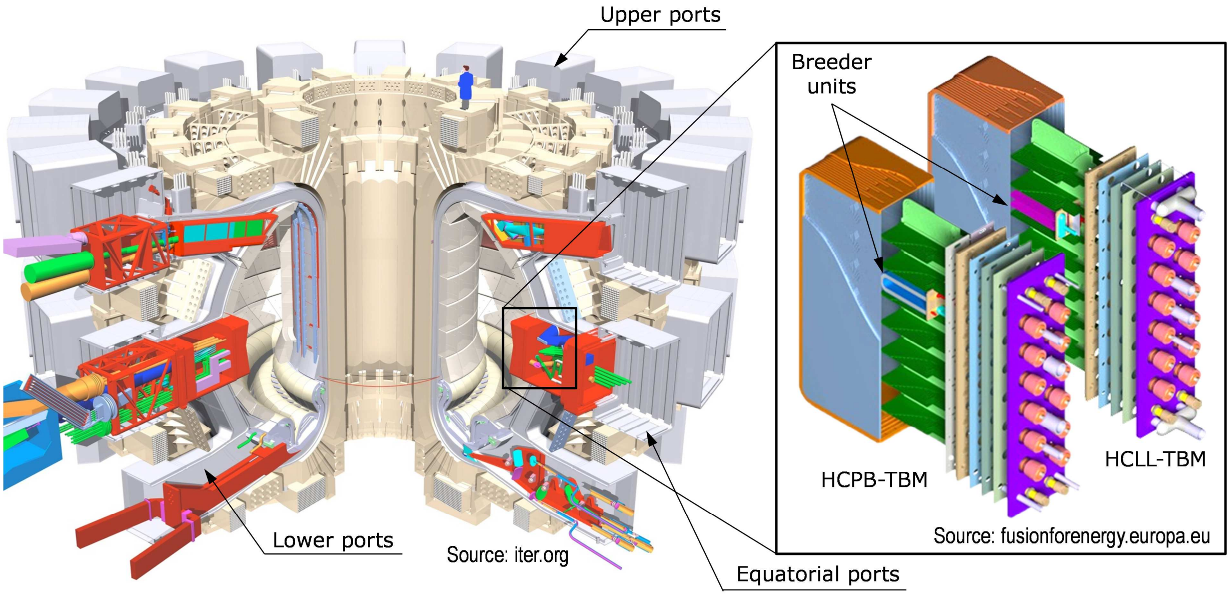

Figure 1.6: Section cutoff of the ITER reactor. In red, some diagnostic systems are highlighted. At the right, an augmented view of the HCPB and HCLL TBMs is ilustrated (Source: `iter.org`).

1.2 Motivation and goal of the Thesis

Due to their location in the reactor, the breeding blankets in fusion reactors and the TBMs in ITER will have to work under severe thermo-mechanical and nuclear conditions, namely high neutron flux decaying along the radial thickness of the component, leading to non-uniform nuclear heating, significant *dpa* damage, He production, swelling and embrittlement; high temperatures, leading to creep and with non-homogeneous distribution and large gradients; cyclic operation, leading to ratcheting and limiting the lifetime of the blanket structural material and high pressure cooling fluids, among others. All these phenomena have an effect in the thermal field of the breeder material. As the figures of merit of T breeding (T release, transport, etc.) are highly dependent on the correct setting of the breeding zone temperature, a good understanding on how the different phenomena acting on the Breeder Units is affecting the temperature distribution and how to maintain a correct thermal control of the breeder zone is essential for a reliable function of the blankets.

Due to this complex behavior of the pebble bed and the whole blanket, experimental validation of the thermo-mechanical performance of breeding blankets in non-nuclear installations (*out-of-pile* testing) and, in particular, of Breeder Unit mock-ups and their associated models is mandatory. However, the out-of-pile tests *"suffer from severe physical and technical restrictions, especially the lack or the non-uniformity of volumetric heating",* as pointed out by Chuyanov et al. (Chuyanov & ITER Test Blanket Working Group, 2002, p.278). This observation is also shared by Abdou et al., who stated that *"the inability to adequately simulate volumetric nuclear heating and its gradients in laboratory experiments represents a serious challenge"* and "*simulating the gradients in the volumetric nuclear heating is essential to discovering new phenomena*" (Abdou et al., 2015, p.24).

Therefore, an advanced heater system concept that accurately reproduces this non-uniform volumetric heating in the pebble beds is required. As additional requirements, this new heater concept must aim at: (1) minimizing its intrusion in the pebble beds, in order to maximize the thermo-mechanical relevancy of an out-of-pile test with respect the respective in-pile test in ITER; and (2) being able to reproduce the ITER power pulses as described in Section 1.1.3. In order to carry out a so-called *proof-of-concept* (Ullman, 2010) of this new heater concept, an experimental mock-up representing a part of a relevant HCPB Breeder Unit needs to be constructed and integrated with the new heater concept.

The aforementioned out-of-pile experiment with a relevant part of a HCPB Breeder Unit will serve as well as benchmark for the validation of finite element models. In this respect, thermo-hydraulic and thermo-mechanical finite element computer codes are applied routinely for the design and development of solid breeding blankets. However, the assessment of the thermo-mechanical performance of the pebble beds of a HCPB breeding blanket requires a complex modeling due to the nonlinear behavior of the pebble beds, mainly nonlinear elasticity, low strain rate (rate-independent) plasticity, thermal creep and swelling. In order to tackle this non-standard thermo-mechanical behavior, different discrete element method, or DEM, (e.g. Gan et al., 2014) and finite element method, FEM (e.g. Di Maio et al., 2010; Gan, 2008) codes have been developed in the last decade. Some of these codes are in an advanced stage and take into account most of the physics involved in the pebble beds for fusion breeding blankets (e.g. Gan, 2008). However, they are computationally expensive, numerically stiff and therefore "*it is needed to consider cost-efficiency of simulations*" and "*a simplified material model may be necessary*" for a practical use of these codes, provided that these simplifications will not alter the basic properties of the original mode (Gan, 2008, p.108). A more pragmatic approach is then required, especially in the early stage of the breeding blanket development, where many design iterations are to be evaluated.

On the other side, a complete and formal validation of computer codes requires the correct quantification of the model output's uncertainties. With this knowledge, statistical metrics can be implemented in order to formally quantify the model's agreement with the experimental results with a certain level of confidence. In order to be able to represent this uncertainty, *probabilistic FEM* analysis is proposed as a complementary approach. Despite probabilistic FEM are being applied in other fields, to the knowledge of the author there has been no attempt to implement this approach to the breeding blanket development up today. As this probabilistic approach requires exhaustive computational runs for the stochastic sampling of the input data and their propagation through the model, the development of a simplified thermo-mechanical model of the pebble beds is again advantageous, but still expensive for today's computational resources. However, the thermo-mechanics of the lithium ceramics of the HCPB can be treated in a decoupled way, therefore the development of the probabilistic modeling approach can be demonstrated in a model of this part of the HCPB Breeder Unit considering only thermal effects.

The goal of this thesis is then to develop a *strategy for the closed validation* of the functionality of a Breeder Unit for solid breeding blankets. This closed validation is performed first by providing a relevant experimental test section of part of a HCPB Breeder Unit, featuring an advanced heater system that accurately mimics the power density existing in this component. Then, a route for the assessment of the thermo-mechanical performance of the device with simplified deterministic and probabilistic finite element models is developed and validated with the aforementioned dedicated experimental set-up. Complementing the experimental and theoretical developments, the validation of a fabrication route of a relevant Breeder Unit mock-up matching nuclear requirements is performed and given in Appendix A. This first of a kind mock-up serves as well to close the gap between the design and development activities completed during the last years and the need for a full-scaled component that is to be tested in an out-of-pile experimental campaign.

1.3 Overview of the Chapters

The organization of the thesis is summarized in the following methodological chart of Figure 1.7. The present work begins with a literature research of related work on HCPB breeding blankets in Chapter 2, from the architecture and functionality to the description of the HCPB TBM and the Breeder Unit for ITER, finishing with a review of past experimental validation of Breeder Units. Chapter 3 describes the design, development and construction of PREMUX, which represents a central part of the present work. The experimental results of PREMUX are compiled and presented thereafter in Chapter 4. Chapters 5 and 6 are dedicated to develop two modeling approaches for the thermo-mechanical assessment of Breeder Units. The first, described in Chapter 5, develops the simplified fully coupled thermo-mechanical model for the pebble beds, where their basic characteristics, namely the nonlinear elasticity and rate-independent plasticity are implemented. Due to the still complex thermo-mechanical model, Chapter 6 describes a strategy to take into account the inherent uncertainty in the model's input data of finite element analyses in order to perform probabilistic thermal analyses. In contrast to the traditional deterministic Finite Element methods, this probabilistic approach allows a formal and quantitative validation route between an experiment and a numerical model. The thesis summary and conclusions are given in Chapter 7, with a proposal for a future work in the field.

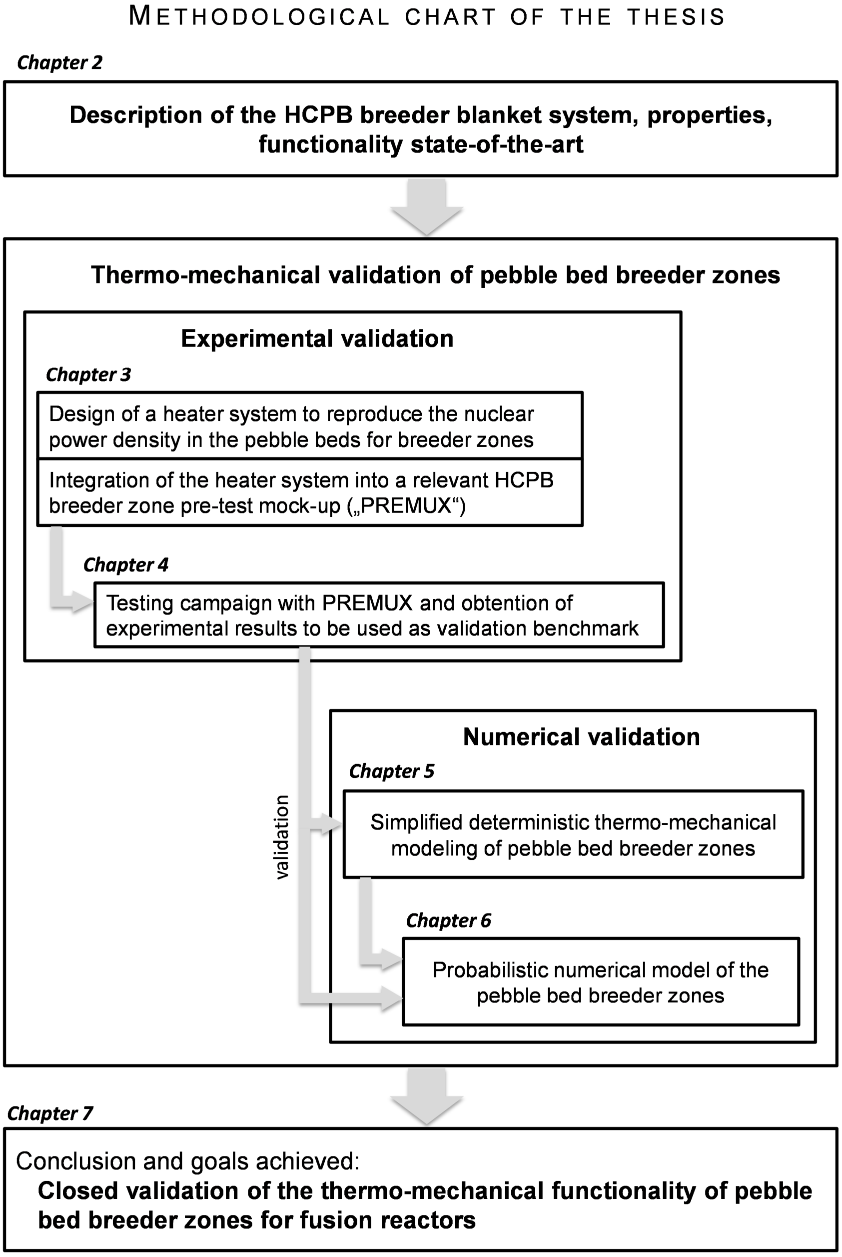

Figure 1.7: Methodological chart describing the organisation of the thesis. After the detailed description of the pebble bed breeder zone architecture and functionality in Chapter 2, the thesis goes through Chapters 3 to 6 developing a closed validation for HCPB Breeder Units.

Chapter 2

The HCPB breeding blanket: related work, state of the art and open issues

Since the establishment of an international collaboration for the development of ITER in the mid-80s, the research and development of a breeding blanket system has been a central and key aspect of a DEMOnstration fusion reactor (DEMO). The R&D activities in this respect have been directed to study several promising concepts for breeding tritium. One of them is the HCPB breeding blanket, featuring the Breeder Units (or more generally, the breeder zone) in its core. In the breeder zone of each HCPB breeding blanket module, a lithium compound-based ceramic pebble bed works as tritium breeder, while a beryllium pebble bed takes the function of a neutron multiplier. Under fusion neutron irradiation, the breeder zone produces enough tritium to self-sustain the tritium consumption rate in the reactor while producing high grade heat that will be extracted for electricity production. A comprehensive description of the functionality of the breeding blanket and a breeder zone is given in this Chapter, together with a literature review of the HCPB breeding blanket concept and the state of the art of the functional materials as well as the available predictive tools for the design and optimization of this component. Issues concerning the close validation of the thermo-mechanical functionality of a HCPB breeding blanket are exposed: firstly, with the problem of the accurate simulation of the nuclear power density in an out-of-pile experiment and secondly with the validation with predictive tools.

2.1 The HCPB breeding blanket: System integration, functionality and architecture

2.1.1 Integration in a fusion reactor

Inside a fusion reactor like DEMO (Figure 2.1), the breeding blanket system is composed of an arrangement of large boxes that fill the place between the plasma and the toroidal-shaped vacuum vessel. The *vacuum vessel* acts as structural support for the different core systems, as well as last shield against the neutron radiation for the superconducting magnets, which are allocated just after the vacuum vessel and provide the magnetic confinement of the plasma.

Starting from the plasma side, several layers can be distinguished. The blanket boxes are the first layer and are considered the plasma facing components, i.e. they are the first component facing the burning plasma volume with a FW that follows the toroidal shape of the tokamak and which covers about 80% of the reactor surface facing the plasma. The remaining 20% is covered by the *divertor system*, which act as power exhaust, diverting the He "ashes" produced by the fusion reaction, as well as impurities raised by the plasma-wall interactions. An inner layer consists of the *breeder zone*, which contains lithium compounds and neutron multipliers necessary to the production of T. Depending on the type of blanket concept and architecture used, several auxiliary structures are present to perform the cooling function, the electrical and thermal insulation and the structural reinforcement of the box. As a final layer before the vacuum vessel, the *back supporting structure* includes the box mechanical support and the attachment system to the vacuum vessel, the manifolds to supply the coolant and to transport the bred T to the fuel cycle system, and a neutron shielding.

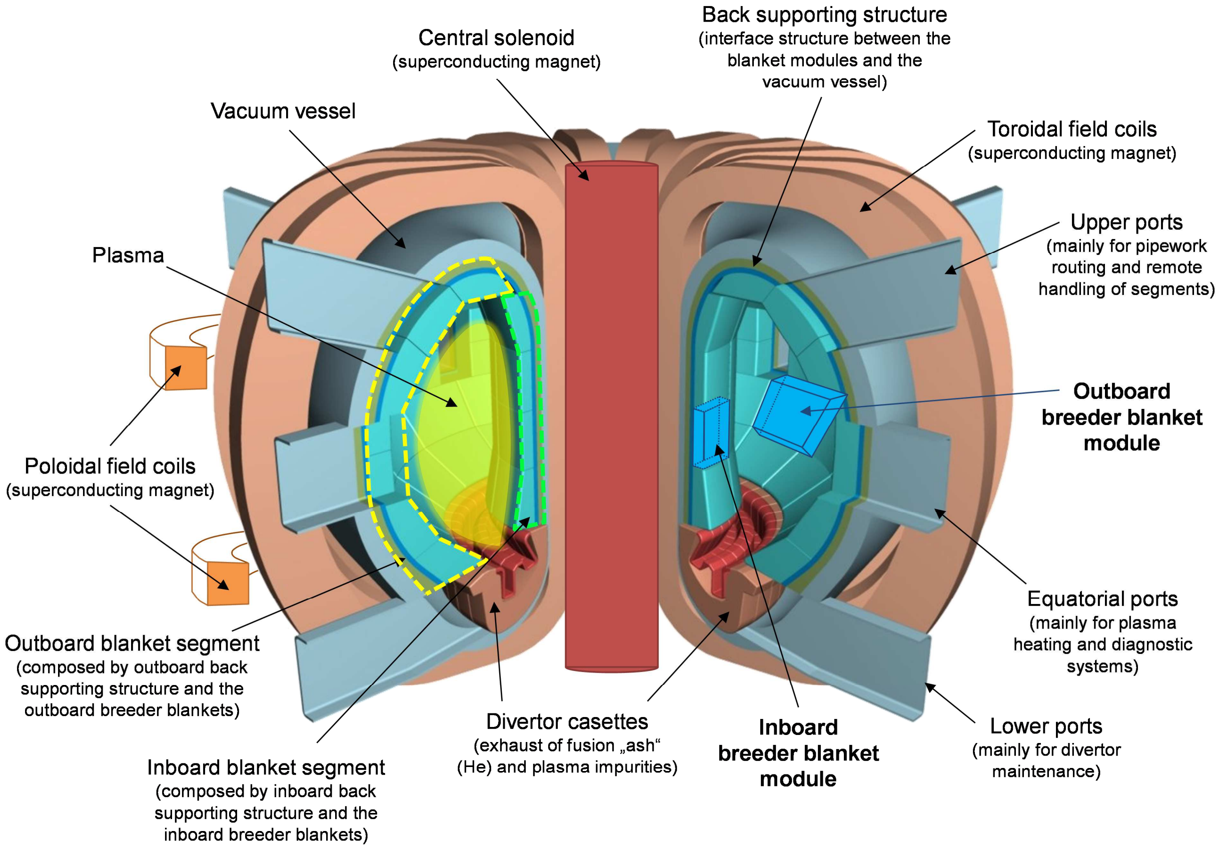

Figure 2.1: Conceptual picture of the tokamak core systems in a DEMO reactor (image adapted from EFDA (2005)).

2.1.2 Breeding blanket functionality

The breeding blanket, without distinction between different possible architectures, is a key system of a nuclear fusion reactor that must achieve 2 basic functions:

1. to breed tritium, in order to supply the fusion reactor of this nuclear fuel, achieving the so-called *tritium self-sufficiency*,

2. to convert the kinetic energy of the neutron flux incident to each breeding blanket, about 80% of the energy released by the fusion reaction in Eqn. (1.3), into heat to be used in an efficient thermodynamic cycle.

This system also contributes indirectly as a shield against the neutron radiation for the vacuum vessel and the superconducting magnets. Despite this contribution, the shielding functionality for the magnet system is nevertheless considered to be demonstrated mainly by the vacuum vessel (Fischer et al., 2015).

The tritium self-sufficiency is measured with the so-called *Tritium Breeding Ratio* (TBR), which is the ratio between the rate of total tritium production in the blanket system and the rate of burning tritium in the plasma due to fusion reactions (Abdou, 1982). While theoretically a TBR = 1 would be enough to ensure the reactor self-sufficiency, a calculated TBR of at least 1.10 is required in order to take into account the different uncertainties in the tritium breeding calculation of the blanket nuclear performances (Fischer et al., 2015) and some authors recommend even a larger value of 1.15 (Abdou et al., 2015).

Tritium breeding function

The tritium breeding principle in a breeding blanket can be accomplished by the nuclear reaction of lithium (Li) with a neutron (n):

$$^{7}\mathrm{Li} + \mathrm{n} + 2.5\ MeV \rightarrow\ ^{4}\mathrm{He} + \mathrm{T} + \mathrm{n}\ , \tag{2.1}$$

$$^{6}\mathrm{Li} + \mathrm{n} \rightarrow\ ^{4}\mathrm{He} + \mathrm{T} + 4.8\ MeV\ . \tag{2.2}$$

Natural lithium is in form of ^{7}Li in 92.5% and ^{6}Li in 7.5%, being both stable. Despite the ability of both Li isotopes to produce T under neutron irradiation, the reaction mechanisms are different. The ^{7}Li absorbs 2.5 MeV of the kinetic energy of the incident neutron (threshold reaction) without consuming that neutron, undergoing a fission to produce ^{4}He, T and gamma radiation. On the other side, ^{6}Li absorbs the incident neutron, increasing the kinetic energy of the reaction products ^{4}He, T and resulting in an exothermic reaction.

From the point of view of the reaction likelihood, both reactions show different behavior. While the probability of a neutron reacting with ^{7}Li is low (see cross-sections in Figure 2.2) and requires fast neutrons (energy threshold about 3 MeV), tritium breeding with ^{6}Li is more efficient, as the activation occurs along the whole neutron energy spectrum, and it is higher than that for the ^{7}Li for neutron energies below ~4 MeV (Figure 2.2), thus being this reaction the main contributor to the tritium breeding.

Tritium breeding suffers of an additional drawback, which is the non-negligible probability (30-35%) of a fusion neutron not being available for tritium production. This can be caused by parasitic absorptions (mainly in the structural materials, about $10\% \div 15\%$), by streaming (through openings, e.g. gaps between breeding blankets, ports for heating and divertor region, about $10\% \div 20\%$) and by leakage of neutrons travelling all through the blanket thickness without reacting (Proust et al., 1991). Therefore, as the ^{6}Li reaction requires one neutron and the availability of the fusion neutron is of about 70% of the time, tritium breeding must be supported in the breeding blanket by a material, the so-called *neutron multiplier* material, able of producing (n,2n) reactions.

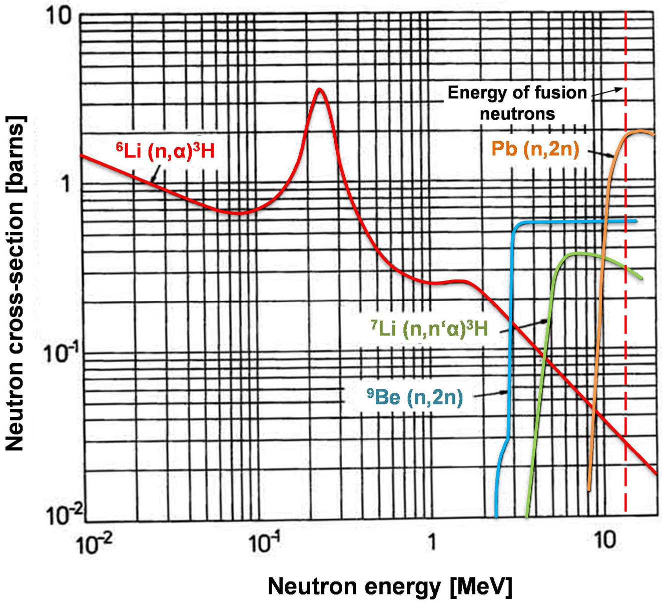

Figure 2.2: Neutron cross-sections of ^{7}Li, ^{6}Li, ^{9}Be and Pb as a function of incident neutron energy (National Physical Laboratory, 1995).

The presence of a multiplication reaction in ^{7}Li is theoretically sufficient to compensate the losses of neutrons with an accurate selection of very low neutron absorber materials in the breeder zone. However the most effective strategy to reach viable TBR levels in blanket concepts is to use more effective neutron multipliers and then replace the ^{7}Li with ^{6}Li with an isotopical enrichment of the ^{6}Li content up to 50% to 90%. This allows the use of Li compounds and structural material as steel in the blanket design.

Candidate materials for neutron multiplier with a relatively large cross-section (Figure 2.2) are lead (Pb) and (Be), being Be the one used in the HCPB breeding blanket. Under fusion neutron radiation, Be undergoes the following threshold (n,2n) reaction:

$$^9\mathrm{Be} + \mathrm{n} + 1.9\ MeV \rightarrow\ 2\ ^4\mathrm{He} + 2\mathrm{n}\ . \tag{2.3}$$

Due to the low energy threshold of the (n,2n) reaction avobe, the energy of the resulting neutrons in Eqn. (2.3) is still high enough to produce further Be activation reactions. As a consequence, a higher neutron multiplication ratio than for Pb multiplier materials is expected (Proust et al., 1991).

On the other side, Be undergoes two additional nuclear reactions under neutron irradiation:

$$^9\mathrm{Be} + \mathrm{n} + 10.5\ MeV \rightarrow\ ^7\mathrm{Li} + \mathrm{T}\ . \tag{2.4}$$

$$^9\mathrm{Be} + \mathrm{n} + 0.6\ MeV \rightarrow\ ^6\mathrm{He} + \mathrm{T}\ . \tag{2.5}$$

The ^{7}Li inside the Be neutron multiplier is prone to be transmuted into T as shown in Eqn. (2.1), while the ^{6}He of Eqn. (2.5) undergoes a beta decay according to:

$$^{6}\mathrm{He} \rightarrow \ ^{6}\mathrm{Li} + {}^{0}_{-1}\mathrm{e}^{-} + \overline{\nu} \ , \tag{2.6}$$

where the ^{6}Li is again prone to produce T as shown in Eqn. (2.2), contributing thus to the nuclear volumetric heating of the Be pebble bed.

High grade heat extraction function

The in-vessel systems are subjected to two main sources of heating, namely: (1) the volumetric source caused by the nuclear interactions of the neutrons from the plasma core and the different breeding blanket materials and (2) the surface heating generated by the the plasma edge and collected by the surfaces of the components facing the plasma. The energy produced by nuclear exothermic reactions in the breeder, multiplier and structural material is known as *energy multiplication*. Typical values are between 1.25 and 1.35 in the case of a HCPB breeding blanket system (Chen et al., 2003; Hermsmeyer et al., 2001; 2003a; 2003b; 2006).

In order to reduce the long term waste, a so-called *Reduced Activation Ferritic Martensitic* (RAFM) steel, namely EUROFER97, has been developed during the last decades in the EU (Tavassoli, 2013). Despite the reduced activation characteristics of this steel, a certain level of neutron activation is still present in this material and therefore its decay heat must be removed by a fluid coolant.

The total nuclear volumetric heating in the blanket is to be extracted by an appropriate coolant flowing through the steel structure of the blanket. This coolant forms the PHTS in the reactor. Helium gas has been traditionally attractive in the field of the breeding blanket development for this purpose, due to its transparency to neutrons, reduced operating pressure (in comparison to a pressurized water system) and its ideal chemical compatibility with the surrounding materials (Proust et al., 1991). Therefore, this gas is the one chosen for the HCPB breeding blanket concept as coolant medium.

The temperature difference between the inlet and outlet of the coolant determines the amount of heat that each blanket module is able to extract and transfer to the coolant in the PHTS. This heat is to be transferred through a heat exchanger to a steam circuit in the BoP, which will power a turbine station for the production of electricity. Therefore, this temperature difference is a crucial performance parameter of the breeding blanket and the reactor itself, as it determines the maximum theoretical thermodynamic efficiency of the reactor. Unfortunately, this temperature difference is limited by the EUROFER97 properties. While the lowest temperature of the steel must be maintained higher than 300 $°C$ in order not to induce a shift in the Ductile to Brittle Transition Temperature (DBTT) of this steel, the highest temperature of the EUROFER97 must be maintained below 550 $°C$ due to the risk of a strong reduction of the creep strength (Lindau et al., 2005; Rieth et al., 2006). This temperature window of 300 $°C -$ 550 $°C$ of the EUROFER is a design limit that imposes an important restriction on the inlet (300 $°C$), as well as on the outlet (500 $°C$) temperatures of the helium coolant, leading to an overall efficiency of the fusion power plant of about 40% (Boccaccini et al., 2004).

2.1.3 HCPB breeding blanket system architecture

Functional materials characteristics

Due to the high temperatures expected in the HCPB breeding blanket and also due to safety, chemical compatibility and industrialization considerations, the most appropriate breeder materials are ternary lithiated ceramic compounds, such as $LiAlO_2$, Li_2ZrO_2, Li_2TiO_3 and Li_4SiO_4 (Proust et al., 1991; Boccaccini et al., 2004). They are utilized in the HCPB blanket in form of polydispersed pebble beds, with quasi-spherical pebbles of sizes between 0.25 *mm* and 0.63 *mm* (Knitter et al., 2007). This granular property of the breeder material has two main goals:

1. to allow a tritium transport carrier gas, so-called *purge gas,* to flow through the voids existing between the pebbles, extracting in the process the tritium generated in the pebbles and transporting it out of the blanket to the Tritium Extraction System,

2. to allow the pebble beds to fill[5] the inner volumes of the breeding blanket designed for them, so as to achieve a good contact between the boundary pebbles and the actively cooled steel walls in the blanket, thus guaranteeing the heat transfer from the pebble to the helium coolant in the steel structures.

Due to the higher concentration of lithium in the Li_4SiO_4 compound when compared to the rest of the options, its good chemical compatibility with EUROFER97, its stability under neutron irradiation and its relatively simpler manufacturing (Boccaccini et al., 2004), it is regarded the first preference for breeder material for the HCPB breeding blanket. In order to ensure a high enough TBR, the natural lithium in the Li_4SiO_4 pebbles is enriched between 30% to 60% with ^{6}Li (Fischer et al., 2015).

Due to the granular nature of the Li_4SiO_4 pebble bed, the temperature along a pebble is homogenized. This topology reduces the thermal stress along the material and the risk of cracking, which contrasts to the case of having a slab of Li_4SiO_4. Moreover, the reduced effective thermal conductivity of the Li_4SiO_4 pebble bed makes the temperature of this material form more predictable against further cracking of the pebbles. On the other side, a certain volume of voids are present after the filling of the HCPB blanket with the pebbles. In order to reach an efficient packing of the pebbles and therefore a high packing factor[6], a mechanical vibration has to be introduced to the blanket module. In this way, packing factors of about 60% to 64% can be achieved (McGeary, 1961; Reimann et al., 2006).

The bulk material of each pebble is also not 100% compact but the fabrication allow a certain degree of porosity. This porosity plays an important role in surface adsorption of the tritium generated in the pebble. This void fraction is utilized to let the helium purge gas to flow through the packed bed, extracting the tritium generated in the pebbles. The mechanism of

---

[5] Assuming a certain void fraction due to the granular nature of the pebble beds.

[6] The packing factor is defined as the ratio of the volume occupied by the pebbles to the total volume of the container where the pebbles are filled in.

tritium extraction from the bulk of each pebble to the helium purge gas (Figure 2.3) is based on a complex mechanism of 4 steps (Federici et al., 1989; Federici et al., 1992):

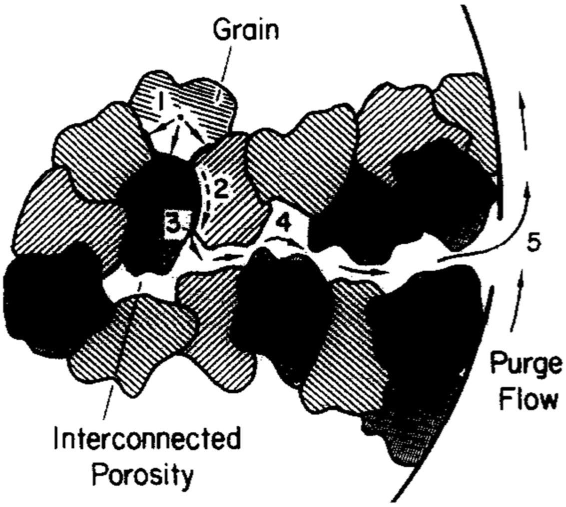

Figure 2.3: Tritium transport mechanisms inside a breeder ceramic pebble. (1) Intragranular diffusion, (2) grain-boundary diffusion, (3) surface adsorption/desorption, (4) pore diffusion and (5) purge flow convection

1. intragranular diffusion, where the tritium atom generated after a $^{6}\mathrm{Li}(\mathrm{n},\mathrm{T})\alpha$ or a $^{7}\mathrm{Li}(\mathrm{n},\mathrm{n}'\mathrm{T})\alpha$ reaction in the grain bulk (being α a ^{4}He particle) diffuses out of the bulk of the grain reaching the grain boundaries,
2. grain-boundary diffusion, where the tritium is transported from the grain boundaries to the pores' boundary surfaces,
3. surface adsorption/desorption, in which the tritium that reached the pores' boundary surface (adsorption) is desorbed into the network of interconnected pores in form of T_2, HT, T_2O and HTO thanks to the presence of the purge gas in the pores of the pebble,
4. pore diffusion, where the tritium molecule diffuses towards the outer surface of the pebble and,
5. purge flow convection, where the tritium molecules being diffused through the network of pores eventually reaches the outer surface of the pebble and it is released into the surrounding purge gas flow.

An additional 0.1% in weight (wt.) of H_2 is added to the He in order to increase the tritium release rate (Kwast et al., 1990; Kwast et al., 1994). A review of the physical properties of Li_4SiO_4 pebbles and pebble beds and their fabrication methods has been compiled by Knitter et al. (2011).

Regarding the beryllium neutron multiplier, its integration in the HCPB blanket is also in form of pebble beds with nearly-spherical pure Be pebbles of 1 *mm* (Proust et al., 1991; Boccaccini et al., 2004). Recently other neutron multiplier materials in form of beryllides such as $Be_{12}V$, $Be_{13}Zr$ and $Be_{12}Mo$ have been gaining momentum due to their improved oxidation resistance, lower swelling and lower T retention, with especial attention to $Be_{12}Ti$ (Kawamura et al., 2004). These neutron multiplier materials are in a R&D development status yet. The packing factors for Be pebble beds are similar as for Li_4SiO_4. Vladimirov (2011) has reviewed and compiled the present status of the Be pebbles and pebble beds characterization, fabrication and properties.

As for the thermo-mechanical properties of the pebble beds for HCPB blankets, their thermal conductivity is coupled with the temperature and stress fields, in particular with the inelastic volumetric strain. The functional relationships of the thermal conductivity with the temperature and the inelastic volumetric strain for Li_4SiO_4 and Be pebble beds are established by Reimann and Hermsmeyer (2002a) and by Reimann et al. (2006b), respectively. While this dependency is not significant for Li_4SiO_4 pebble beds, it is of special importance for the Be pebble beds and can lead to significant deviations in the temperature field in case it is not considered during the design. Moreover, the pulsed operation of the blanket leads to successive compressions and relaxations of the pebble bed due to the differential thermal expansion of the pebble bed itself and the surrounding structural components like the Breeder Unit cooling plates or the TBM stiffening grids. During a compression cycle, e.g. during a power ramp-up and subsequent power flat top phases of a pulse in ITER, the stress in the pebble bed is likely to reach the yield limit, shearing and compacting the pebble bed inelastically. After an expansion, the pebble bed may not recover its original shape due to the inelastic strains and gaps could be formed, thus losing contact with the surrounding cooling plates, with the consequent drop of the local heat transfer and an overall increase of the temperature in the pebble bed.

Generic HCPB breeding blanket architecture

The generic HCPB breeding blanket architecture (Figure 2.4 top-left) is based on alternating layers of Li_4SiO_4 and Be pebble beds, separated by cooling (or stiffening) plates, which are actively cooled by helium at high pressure, usually 8 *MPa* (Boccaccini et al., 2004). The pebble beds, or at least the Li_4SiO_4, are swept by the reference purge gas ($\mathrm{He} + 0.1\mathrm{wt}\%\ \mathrm{H}_2$). In the reference configuration use for the TBM in ITER, the cooling plates used to define the ceramic breeder container form a continuous U-shape, joining both cooling plates by the so-called *ceramic bridge* (dotted shape in Figure 2.4 top-left).

This layered structure of pebble beds and cooling plates is enclosed in a box (Figure 2.4 top-right), formed by an actively cooled U-shaped First Wall (FW) plate facing the plasma volume, caps at the top and bottom side of the blanket box (actively cooled as well) and a backplate. A thin (≈2 *mm*) layer of tungsten on the plasma side of the FW protects the structural steel against plasma-wall interactions (Boccaccini et al., 2004). A system of manifold backplates collects and distributes the helium coolant to the subcomponents in its different cooling stages in the blanket.

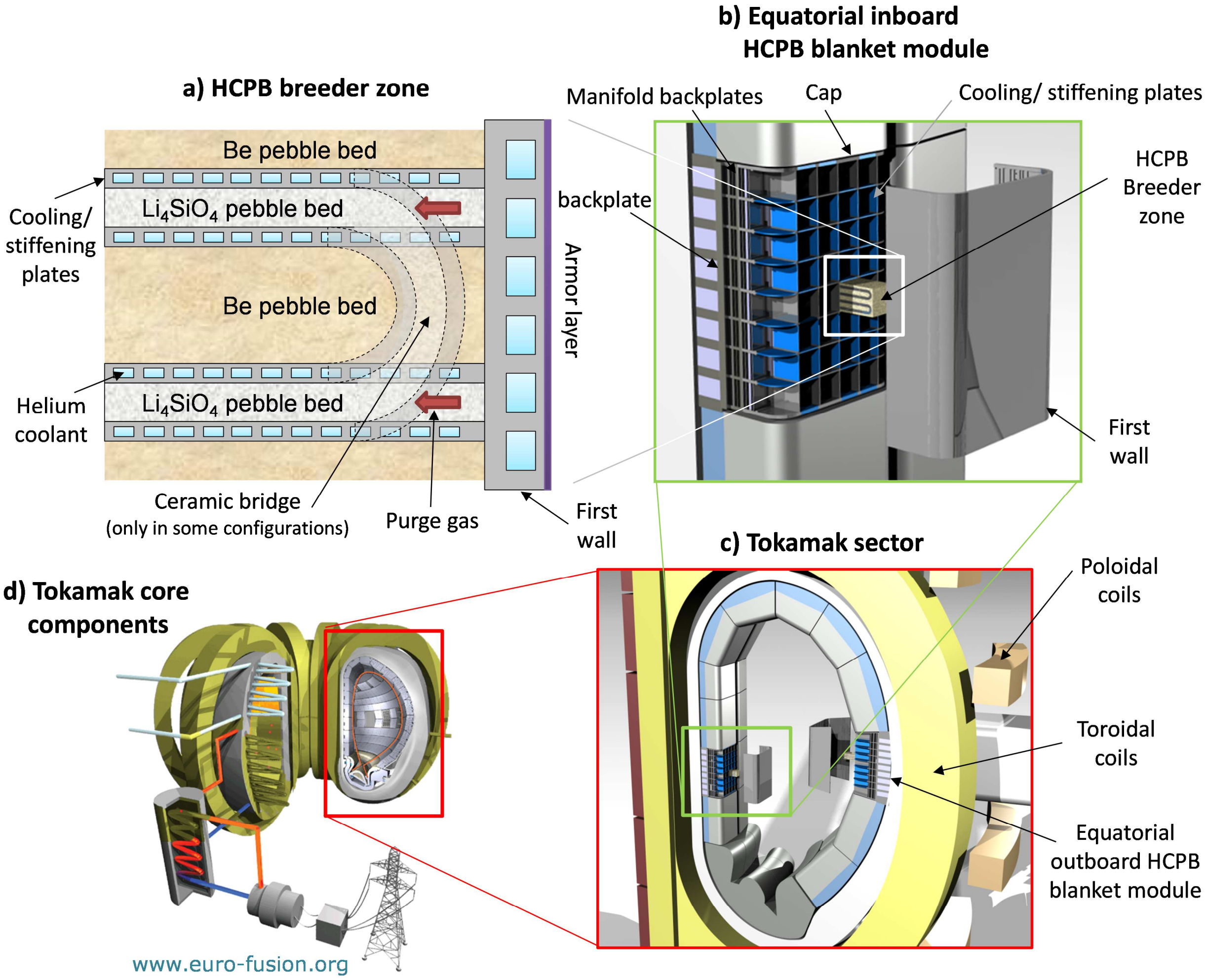

Figure 2.4: Conceptual pictures of a DEMO-like fusion reactor. Top-left: generic breeder zone. Top-right: equatorial inboard HCPB blanket module, with exploded view of its first wall and the breeder zone. Bottom-right: detail of a DEMO sector, composed by 2 inboeard and 3 outboard segments and exploded view of the first wall and breeder zone of the equatorial inboard and outboard blanket modules. Bottom-left: DEMO-like tokamak core components, with indication of the localization of the sector detailed in the bottom-right picture.

2.1.4 DEMO Power Plant Conceptual Study (PPCS)

During the period 2000-2002, the EU executed a DEMO Power Plant Conceptual Study (PPCS), mainly aiming at demonstrating the technical and economic viability of a DEMO nuclear fusion power plant (Maisonnier et al. (2005; 2006), EFDA (2005)). In this study, the HCPB breeding blanket was considered as the breeding blanket for a “near term” (so-called *model B*) DEMO reactor. This HCPB blanket originates from the work of Dalle Donne (1991), which was improved by Hermsmeyer et al. (2001) and revised by Hermsmeyer and Malang (2003b) in the frame of the PPCS. The Hermsmeyer and Malang’s proposal for DEMO blanket in the model B reactor configuration has been further developed by Hermsmeyer et al. (2006) and validated with neutronic, thermo-hydraulic and thermo-mechanical analyses by Chen et al. (2003) and later by Xu et al. (2006).

As reported by Magnani et al. (2009), the DEMO model B HCPB breeding blanket concept is considered to be the most consistent design among the ones analyzed in the EFDA's PPCS. This blanket (Figure 2.5, left), is based on a modular arrangement of breeder zone cuboids defined by horizontal and vertical stiffening grids. In each cuboid, a HCPB Breeder Unit is placed (Figure 2.5, right). Each module is 2000 mm (toroidal) 2000 mm (poloidal) $\times$ 800 mm (radial) and allocates 9 (toroidal) $\times$ 9 (poloidal) Breeder Units. Each of these Breeder Units is formed by horizontal cooling plates, which act as a canister for the solid breeder material. The space between the canisters is filled with a Be pebble bed, with single size pebbles of $\emptyset 1$ mm. The structural material chosen for this blanket is EUROFER97 and the reference breeder material is a polydisperse pebble bed of Li_4SiO_4, with pebble diameters ranging from 0.25 mm to 0.6 mm. The pebble beds are swept with the reference purge gas (He with 0.1wt.% H_2) at a low pressure (0.1 MPa). As for the coolant fluid, He at 8 MPa has been selected.

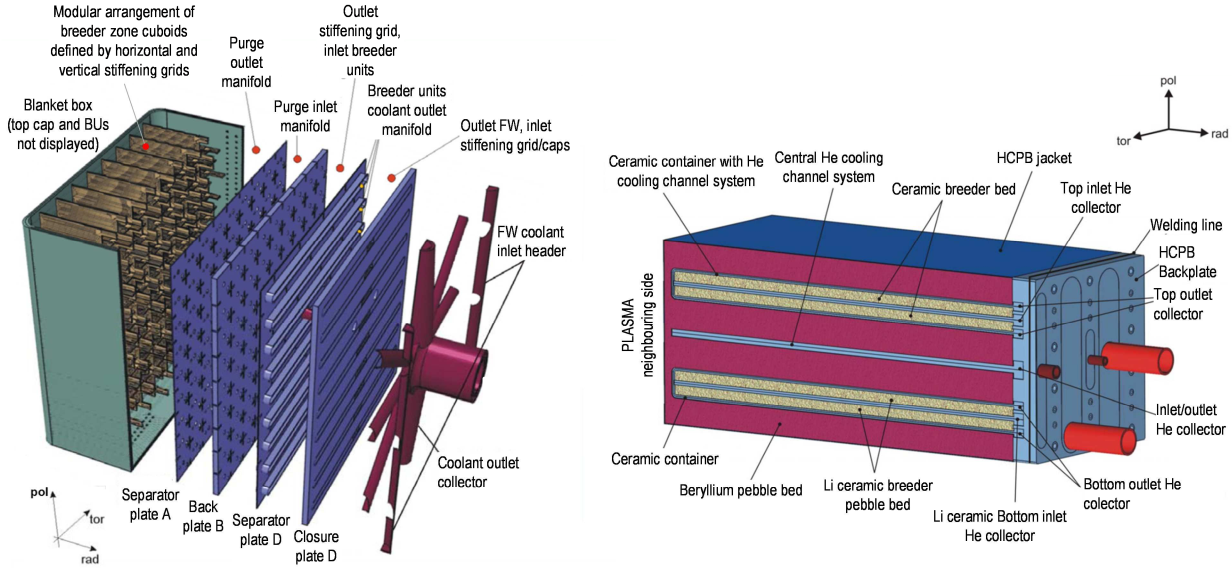

Figure 2.5: The EU DEMO HCPB Breeding blanket reference concept from Hermsmeyer and Malang (Hermsmeyer et al., 2006). Left: exploded view of the this blanket, excluding the Breeder Unit and the pebble beds. Right: detail of one HCPB DEMO Breeder Unit.

These basic characteristics of the HCPB breeding blanket of the PPCS's model B DEMO configuration and its Breeder Unit has been transferred to the conceptual design of the HCPB TBM and the HCPB TBM Breeder Unit for ITER.

2.2 ITER: The HCPB TBM and the HCPB TBM Breeder Unit

2.2.1 Configuration and state-of-the-art

As defined in the ITER TBM Program (Boccaccini et al., 2002; Giancarli et al., 2006; 2012), the HCPB TBM, as well as each of the other 5 TBMs to be tested in ITER, must be representative of its respective Breeding blanket for the DEMO reactor. Therefore, the HCPB TBM design and its HCPB Breeder Units, share many design architecture similarities with the DEMO model B HCPB Breeding blanket in the EFDA's PPCS.

Boccaccini et al. (2005) reported the first design review of the HCPB TBM that included a comprehensive study of the interfaces of this test blanket with the ITER reactor. Here, a so-called *horizontal configuration* of the HCPB TBM was envisaged, which roughly consisted in a module of 1270 mm (toroidal) 740 mm (poloidal) × 800 mm (radial) with an arrangement of 6 (toroidal) × 3 (poloidal) breeder zones. In 2007, a revision of the different TBM designs was requested by the ITER organization so as to allow the installation of a correction coil in the port plug, in order to reduce a distortion in the magnetic field known as *ripple effect*. This design update consisted of a new arrangement from the horizontal to a vertical configuration and a material optimization in order to reduce the amount of RAFM (EUROFER97) steel, which is prone to increase this ripple effect in the plasma (Ruatto & Boccaccini, 1998; Salavy et al., 2009; ITER Documentation, 2004).

The design update of the so-called *HCPB TBM Box* (i.e. the TBM without the Breeder Units) in vertical configuration (Boccaccini et al., 2009; 2011) has been developed by Cismondi et al. (2009; 2010; 2011; 2012). It consists in a module of 484 mm (toroidal) 1660 mm (poloidal) × 710 mm (radial) (Figure 2.6 left) with an arrangement of 2 (toroidal) × 8 (poloidal) breeder zones, where the HCPB Breeder Units are allocated (Figure 2.6 right-top). The reference purge gas flows at a very low velocity in both pebble beds, considering the purge gas normal flow rate (about 4 Nm^3/s and 80 Nm^3/s)[7] proposed for ITER (Ricapito et al., 2008), which corresponds to an order of magnitude of a few mm/s.

Figure 2.6 right-bottom shows the dimensions of the preliminary conceptual design of the HCPB Breeder Unit (Cismondi & Neuberger, 2009). The dimensional parameters have been set to achieve the highest DEMO relevance with the HCPB blanket concept for DEMO. The dimensions in parenthesis indicate the values proposed for the HCPB Breeder Unit for DEMO.

The operational conditions of the conceptual design of the HCPB TBM and the Breeder Units are given by Cismondi et al. (2009). The purge gas enters the Breeder Units at 500 $°C$ and 0.4 MPa and sweeps first the Be pebble bed and thereafter the Li_4SiO_4 pebble bed. The total He coolant mass flow rate in the HCPB TBM is 1.34 kg/s, which enters the TBM at 300 $°C$, 8 MPa and firstly cools the FW, which is considered to receive an homogeneous heat flux of 500 kW/m^2 as conservative assumption. The He is about ~360 $°C$ at the FW outlet and it is collected in a manifold, where 0.58 kg/s are diverted out of the TBM by a bypass pipe. The rest of the He coolant (0.76 kg/s) flows to the vertical and horizontal stiffening plates and the caps. Kiss (2009) reports detailed analyses of the area of the breeder zone for the conceptual design of the vertical HCPB TBM, showing mass flows of the He coolant of ~0.02 kg/s in each cap, horizontal and vertical stiffening plate. After cooling these subcomponents, the He is collected again in a manifold and it is distributed to the cooling plates of the Breeder Units (inlet temperature ~400 $°C$), each being cooled with 0.049 kg/s, flowing through 2 × 30 rectangular channel cross-sections of 4.5 mm × 2.6 mm per cooling plate. The He exiting the Breeder Units is collected at a temperature of ~500 $°C$ in a manifold, where it is routed out of the TBM.

---

[7] Nm^3/s denotes normal m^3/s (DIN Standard 1343:1990-01, 1990).

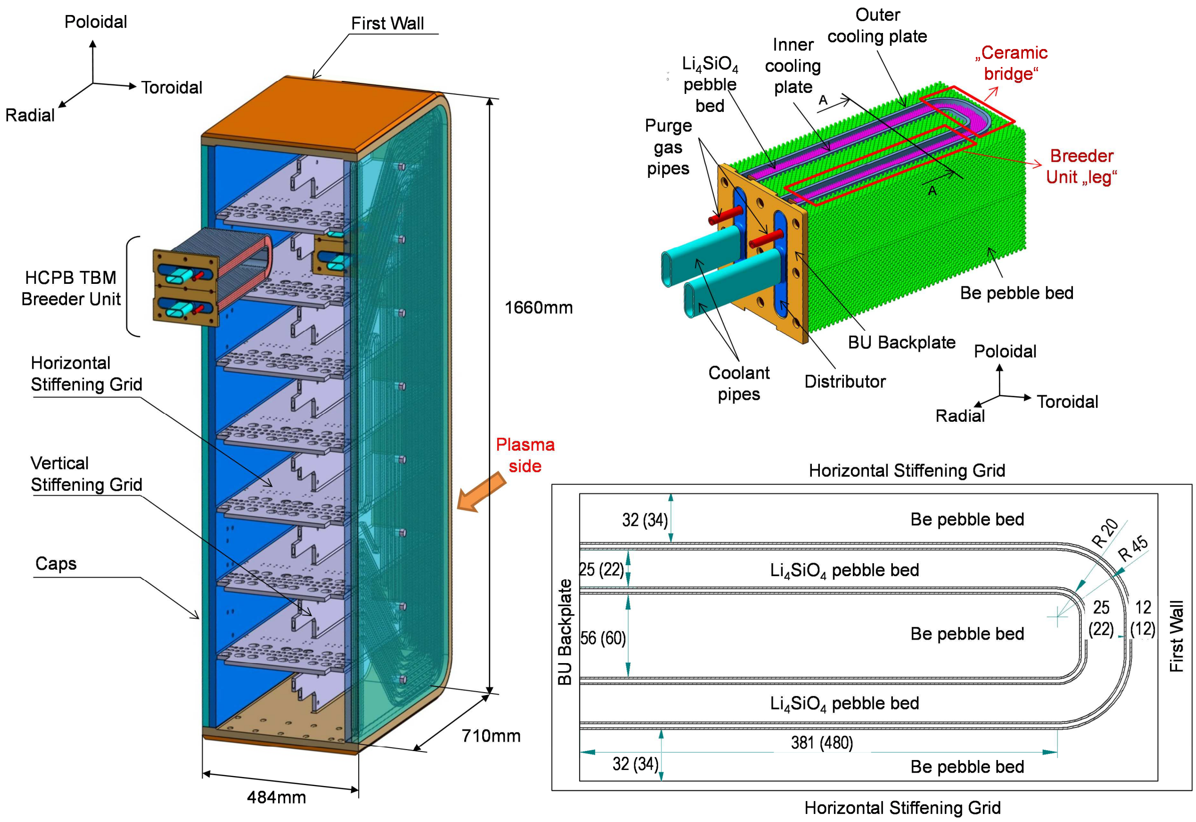

Figure 2.6: Left: the HCPB TBM in vertical arrangement for ITER (Cismondi et al., 2009), derived from the DEMO model B HCPB breeding blanket concept. Right-top: the DEMO relevant HCPB Breeder Unit conceptual design and its dimensions at the right-bottom picture, with information of the dimension used for the corresponding DEMO Breeder Unit (in parenthesis).

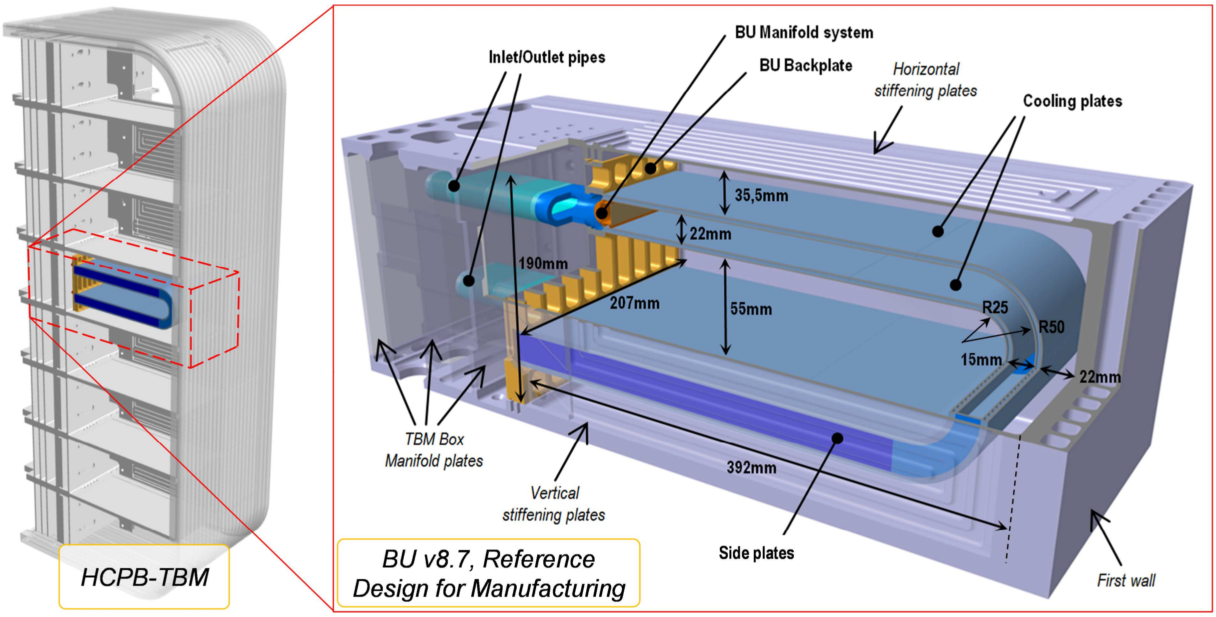

Figure 2.7: The HCPB Breeder Zone. Left: HCPB TBM Box structure with an installed Breeder Unit (the caps have been removed from the view to allow viewing the inner structures and a Breeder Unit). Right: Detail of the reference design of the HCPB Breeder Unit for manufacturing.

The knowledge of the parameters of the He coolant in the HCPB Breeder Unit and its surrounding components is fundamental for the design of an out-of-pile testing with a HCPB Breeder Unit mock-up, which necessitates a relevant heat extraction not only in the Breeder Unit cooling plates, but also in the surrounding structures (stiffening plates and caps).

During a design and development program launched during the years 2009-2011, detailed thermo-hydraulic and thermo-mechanical analyses have been performed by Hernández et al. (2011b; 2012) and Kiss (2009; 2010), achieving a reference design for manufacturing of a functional mock-up for testing and conforming the state-of-the-art of this component (Figure 2.7-right). Details of the design cycle of this component are described by Hernandez et al (2011a). The maximum temperature levels for the lithium breeder ceramic, the Be bed and the structural steel are about 800 $°C$, 650 $°C$ and 520 $°C$ respectively

Assuming this design as the reference for manufacturing, a quasi-full-scale fabrication mock-up has been constructed and it is detailed in Appendix A. This mock-up serves as a fabrication validation route, fulfilling the requirements of the selected codes and standards.

2.2.2 Nuclear performance of the HCPB TBM

The nuclear performance of the conceptual design of the vertical HCPB TBM has been studied by Pereslavtsev et al. (2010), who analysed a 40° toroid sector of ITER with the neutron transport code MCNP (Figure 2.8 left and middle) during an ITER power pulse (Section 1.1.3). The estimation of the total nuclear power in the HCPB TBM is 0.6 MW, while the average neutron wall loading on the First Wall amounts 0.72 MW/m^2 and the corresponding 14 MeV neutron current flux density is 3.18×10^{13} n/cm^2. The radial volumetric power distribution in the breeder zone, i.e the HCPB Breeder Unit structural steel and the Li_4SiO_4 and Be pebble beds, due to the different nuclear reaction is as shown in Figure 2.8 right, leading to a tritium production rate of 76.9 $mg/power\ day$.

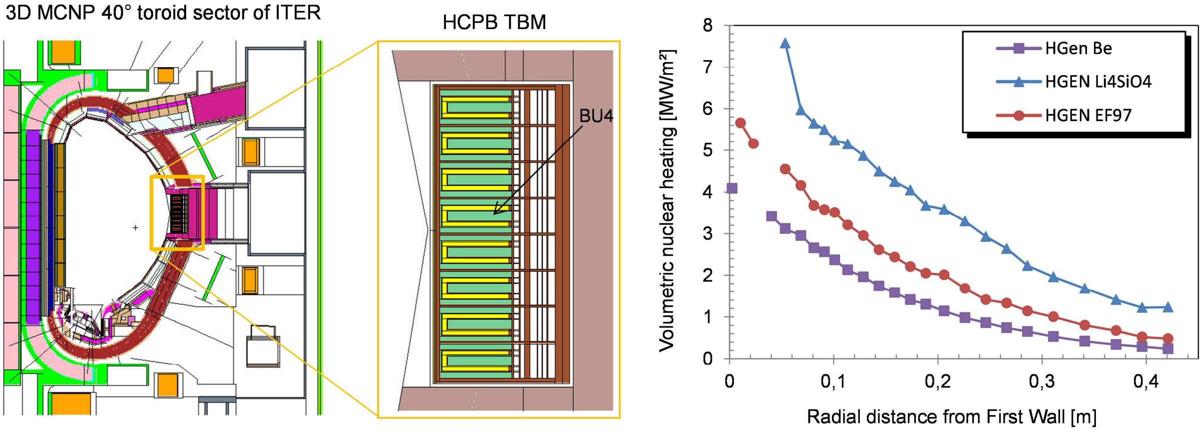

Figure 2.8: Left: "A-lite" model (40° toroid sector of ITER) built in MCNP5 for neutronic analyses. Middle: detail of the MCNP model of the HCPB TBM, with an indication ("BU4") of the Breeder Unit experiencing the highest nuclear heat generation. Right: Radial distribution of the volumetric heating produced in the different materials of the Breeder Unit 4 (Pereslavtsev et al., 2010).

The spatial distribution of the volumetric heating in the breeder zone is a cornerstone for the development of the HCPB TBM and the HCPB Breeder Units, as well as for the studies performed during the present research for the development of testing tools aimed at reproducing the nuclear volumetric heating in an out-of-pile testing of a HCPB Breeder Unit mock-up.

2.3 Validation of the thermo-mechanical performance of a HCPB TBM Breeder Unit mock-up

2.3.1 Validation through experimentation

Important efforts have been performed in the past for the design and construction of relevant in-pile and out-of-pile tests addressing different specific performance figures of the HCPB Breeder Unit for DEMO and the TBM.

Validation in nuclear environment ("in-pile" testing)

The most representative in-pile test is the so-called Pebble Bed Assemblies or PBA (van der Laan et al., 2000; 2002; van Til et al., 2012), which has been run in the High Flux Reactor (HFR) in Petten. Each assembly contained a disc (∅45 *mm* and 11 *mm* height) of Li_4SiO_4 or Li_2TiO_3 pebbles, sandwiched between 2 cylindrical layers of beryllium pebbles, both pre-compacted at 3 *MPa*. Both pebble beds were separated by floating plates of EUROFER97 and the whole assembly was inserted in capsules of ∅64 *mm*. In the set-up, 4 mock-ups with the aforementioned pebble bed assembly (2 with Li_4SiO_4 and 2 with Li_2TiO_3) were stacked in a long capsule and inserted in the HFR for 294 full power days, reaching a level of 2-3 dpa in the EUROFER97 (relevant for ITER but not for DEMO).

Under a real nuclear environment, the motivation for such test was to test a relevant DEMO pebble bed assembly of the HCPB Breeding blanket with a representative power density (like in Figure 2.8-right) that could reproduce the temperature profile in cylinder capsules. Despite this sophisticated integral set-up approach and in contrast to the HCPB TBM in ITER, the reduced space available in the HFR reactor core forced the PBA capsules' diameter (lateral extension) to be too small compared to the pebble bed disc thicknesses, thus reducing the relevancy of the test in terms of thermo-mechanical functionality of the pebble beds.

Validation in non-nuclear environment ("out-of-pile" testing)

Three set-ups, the so-called *HEBLO* (Norajitra et al., 2001), *HELICA* (Dell'Orco et al., 2006; 2007) and *HEXCALIBER* (Di Maio et al., 2008), are the most significant out-of-pile tests of relevant mock-ups, partially representing a HCPB breeding blanket.

On the one side, HEBLO reproduced a small section of the DEMO HCPB breeder zone designed by Dalle Donne et al. (1991; 1994) consisting of a portion of a Be pebble bed (45 *mm* thick) and Li_4SiO_4 (11 *mm* thick) enclosed in a representative MANET[8] steel structure featuring

---

[8] DIN 1.4914

an actively cooled First Wall and cooling plates. This experiment tried mimicking the nuclear volumetric heating in the pebble bed by means of plate heaters with homogeneous power heating in steady state experimental runs.

A similar concept but with cyclic thermal loads is used in the HELICA mock-up, where two KANTHAL plate heaters are introduced in an actively cooled cassette containing a Li_4SiO_4 pebble bed, dividing the bed into 3 parts of 4.6 *mm* thick. The HEXCALIBER experimental campaign is an extension of the HELICA, where an alternate stack of two Li_4SiO_4 (16 *mm* thick) and two Be (56 *mm* thick) pebble beds are heated by 2 electric plate heaters each. The pebble beds are contained in a T91 steel structure reproducing the First Wall, cooling plates and stiffening grids of a HCPB Breeding blanket. This last experiment demonstrated that the insertion of plate heaters tends to create artificially high local hydrostatic pressure in the pebble bed, to the point of endanger the mechanical integrity of the pebbles and the heaters themselves, losing the thermo-mechanical relevance of the experiment. To this effect, an additional non-relevant aspect is introduced by heating the pebble bed homogeneously with plate heaters, not being able to reproduce the exponential radial power density profile predicted by Pereslavtsev et al. (2010) and depicted in Figure 2.8-right.

2.3.2 Code validation and uncertainty quantification

Thermo-mechanical modeling of pebble beds

The correct setting of the temperature window of the breeder zone during normal operation leads to an optimum function of the breeding blanket, i.e. correct tritium release and extraction due to a good understanding and prediction of the temperature fields in the breeder zone. Therefore, the ability to model the thermo-mechanics of the pebble beds in a HCPB breeding blanket is fundamental for the design and development of the HCPB breeder units and future breeding blankets for DEMO.

The common approach for modeling the thermo-mechanics of granular materials like the pebble beds for a HCPB breeding blanket is to consider them as a continuum, as the pebbles are at least an order of magnitude smaller than the minimum characteristic length of the pebble bed. In this regard, the most popular models are the classic Drucker-Prager model (Drucker & Prager, 1952), which describes the onset of yield due to shear failure, and its more recent version, the Drucker-Prager-Cap (Sandler et al., 1976; Sandler & Rubin, 1979; Pelessone, 1989), which in addition takes into account the yield and hardening of the granular material when it is subjected to a hydrostatic (compressive) dominated stress state. Once the granular material reaches the onset of yield, specific flow rules must be defined for the correct description of the evolution of the inelastic strain increments as function of the stress state. The strong nonlinear elastic behavior of the pebble beds can be modeled by means of the relationship established by Coube (1998), where the effective Young modulus of the pebble bed is expressed as function of the hydrostatic and von Mises stresses.

Available commercial codes such as ANSYS (2013) or ABAQUS (2011) implement finite element formulations able to describe the yield surface of a granular material with the Drucker-

Prager or Drucker-Prager-Cap models, with associated or non-associated plastic flow rules and appropriate hardening laws. However, while ABAQUS allows the implementation of nonlinear elasticity in the same type of element where a Drucker-Prager-Cap yield surface has been defined, ANSYS allows only by default the specification of linear elasticity in these elements.

Due to the versatility of the ABAQUS code, practically all the related literature about modeling of pebble beds for fusion blankets has been performed in greater or lesser extent by means of this code, e.g. Bühler (2002), Reimann et al. (2002b), Hofer and Kamlah (2005), Gan et al. (2007c), Gan and Kamlah (2007a). The state of the art is found in the work of Gan (2008), who has developed a nonlinear elastic, Drucker-Prager-Cap-plastic model with an isotropic hardening law and creep effect in ABAQUS by means of a user defined material subroutine (so-called *UMAT*). The model takes into account the interfacial heat transfer between the pebble bed and the surrounding structure due to conduction (pebble-wall), convection (interstitial gas-wall) and radiation (pebble bed-wall). Furthermore, in the case a gap is formed between the pebble bed and the surrounding walls, the conduction between the pebbles and the wall vanishes and a new heat transfer term as function of the gap thickness is included in the simulation. The differentiating feature of this model from the rest is that its parameters have been identified and calibrated with certain available experimental results, instead of the traditional heuristic approach (trial and error).

There have been other studies that have analyzed the problem with alternative models other than or additional to the Drucker-Prager approach. Vella et al. (2001) combined the Drucker-Prager-Cap plasticity with a porous elasticity option in ABAQUS (Bühler, 1998), while Dell'Orco et al. (2007) and Di Maio et al. (2010) have utilized the so-called *Gurson model* (Gurson, 1977) instead of the Drucker-Prager in their proposal. In this approach, the pebble beds are idealized as porous continua with a stochastic distribution of voids that can be plastically compacted, reproducing in this way the thermo-mechanical behavior of the pebble beds in a fusion blanket. The main advantage of this model, contrasting with the model of Gan (2008), is its simplicity, to a point of allowing 3-dimensional simulations, although it does not take into account creep phenomena. However, its main disadvantage is the heuristic approach needed for the identification of its model parameters. These parameters are tuned to fit some experimental result, a method that poses uncertainty about its performance when extrapolated to other operating conditions.

On the other side, ANSYS is the preferred code in the ITER community for their activities in the design and engineering of diverse systems for a wide range of physical phenomena (Jong, 2006). In fact, the development of practically all breeding blanket concepts during the last years for ITER and DEMO presented in Section 2.1 and Section 2.2 have been performed predominantly in ANSYS. However, and due to the aforementioned limitations of this code to handle nonlinear elastic-Drucker-Prager-Cap plastic models in its default settings, it has not been favored in the area of pebble bed thermo-mechanical modeling and this is reflected in the almost non-existent literature about this topic in ANSYS. Only a recent work by Tucker et al (2013) is found starting to investigate the thermo-mechanical modeling of pebble beds in this code. The use of two codes limits the flexibility of the design teams, as both codes and specialized staff operating them are therefore needed for the development of breeding blankets. Due to the broad use of ANSYS in the ITER community, it would be advantageous to address a research to integrate the development of thermo-mechanical modeling for pebble beds into one code and, as Gan (2008) points out, in a more cost-effective manner, simplifying non-essential characteristics that would make the computation less demanding, less stiff and more stable, and by using the default and already optimized subroutines of the code.

Probabilistic modeling of breeding blanket components

The common approach for the design and development of breeding blankets for fusion reactors is the systematic use of deterministic FEM and/or Finite Volume Method (FVM) codes for the evaluation of the different blanket performance figures, mainly the thermo-hydraulics of the coolant and the temperature and stress fields in the structural and functional materials. Due to their deterministic nature, the input parameters in these models are treated as nominal values. However, each parameter of the blanket, either a physical or geometrical value, is in a greater or a lesser extent stochastic and can be described with a certain joint probability distribution. In the case that some of these parameters suffer from large scattering, this may affect the reliability of the performance figures from the simulation results. This information is in any case not available in the common deterministic approaches.

Although sensitivity analyses are usually performed to these deterministic FEM/FVM simulations, these calculations lack of a probabilistic approach, i.e. stochastic sampling of the input values according to their probability distribution functions and their propagation in the FEM/FVM model. This sensitivity studies may be performed by means of engineering judgment of “best” and “worst” cases but they lack of a quantification of the probability in which they can occur, resulting in conservative assumptions, which are often even unphysical, with the risk to develop uneconomical solutions.

A second approach is the use of the so-called *best-estimate* (BE) models, where realistic model parameters are used instead of conservative ones in order to obtain a best-estimate of the model’s output and, in a second step, the uncertainty in the model’s prediction is quantified. This is a common approach for many engineering fields, including the fission reactor physics modeling (e.g. D'Auria & Galassi, 1998; D'Auria & Mazzantini, 2011; OECD:NEA, 1998; OECD:NEA, 2005). In this particular case, the quantification of the model’s uncertainty is becoming the standard for safety analysis calculations during the licensing of a nuclear power plant in front of the Regulatory Body (IAEA, 2008). Despite not being a novel concept (Red-Horse et al., 2000), to the knowledge of the author there is no previous literature related to this approach, i.e. quantification of the uncertainty in the computational simulations of the thermo-hydraulic and/or thermo-mechanical performance of the breeding blankets for ITER or DEMO by means of a probabilistic approach. The traditional deterministic methods for the virtual product development of blanket components make not possible the quantification of the uncertainty of the outputs, which is central for a complete understanding of the performance and the reliability of the components under study and for a formal validation of the models with experimental results (Roy & Oberkampf, 2011) and it is therefore a field to be investigated. Moreover, this uncertainty quantification can be used to build metrics to statistically quantify the model’s agreement against available experimental data.

Chapter 3

Design, development and construction of a pre-test mock-up experiment "PREMUX" for the qualification of testing tools and as validation benchmark

In the previous Chapter, the nuclear power density generated in the pebble beds of a HCPB breeding blanket due to the nuclear reactions taking place in the Li_4SiO_4 and Be has been identified as the driver of the thermo-mechanical performance of the blanket and, hence, of the whole fusion reactor. It has also been acknowledged that previous out-of-pile thermo-mechanical validation experiments lack of an appropriate heater system that is able to reproduce the volumetric nuclear heating profile along the radial direction of the breeder zone. Traditional plate heaters are highly invasive and introduce non-relevant topologies and physical effects in the pebble beds. Therefore, a new heating system that has high flexibility to reproduce the radial profile of the power density and that has a low intrusion in the pebble beds is desired. The direct implementation of such a heating system in a full-scale HCPB TBM Breeder Unit mock-up test is nevertheless technically complex. Therefore, the construction of a dedicated relevant pre-test mock-up experiment (PREMUX) for a proof-of-concept of this new heating system is required. This Chapter begins with the definition of the testing goals of PREMUX and with the selection of the test area of the HCPB TBM Breeder Unit to be tested. The details concerning the design, development and construction of the new heater system and the PREMUX test itself are detailed thereafter, while the data acquisition systems and the test control tool software developed for PREMUX are described at the end of the Chapter.

3.1 Conceptual design of an out-of-pile test of a HCPB TBM Breeder Unit mock-up

The following main testing goals shall be considered for an out-of-pile test aimed to qualify the thermo-mechanical performance of a HCPB TBM Breeder Unit mock-up:

- obtaining key thermo-mechanical figures of merit of the pebble bed and the surrounding structural steel: strain/displacement fields and temperature maps by a precise simulation of the nuclear volumetric heating generated in the breeding zone,
- obtaining key thermo-hydraulic figures of merit of the helium coolant: outlet temperature, pressure drop and, if technically possible, the mass flow distribution in the cooling channels of the cooling plates of the Breeder Unit,
- acquirement of appropriate data so as to be used for the development and validation of models aimed to simulate the thermo-mechanical phenomena in the breeding zone,
- cyclic testing of the component to assess the fatigue life.

In a first campaign and in order to simplify the experimental set-up due to safety issues, Be could be substituted by a material with similar thermal properties and mechanical properties of the same order of magnitude. Candidates are copper alloys with zinc (e.g. CuZn33), whose thermal conductivities are comparable to that of Be. Research in this area is needed to investigate these potential candidates in order to assess their thermo-mechanical relevance with respect to a Be pebble bed.

3.1.1 Reproducing nuclear power heating in a HCPB TBM Breeder Unit in an out-of-pile experiment: Heater system requirements

As it has been introduced in Section 2.2.2, the nuclear volumetric heating in the pebble beds is the key thermal load in the Breeder Units. This volumetric heating has an exponential decay profile in the radial direction from the FW side towards the backplate (Pereslavtsev et al., 2010), which has to be mimicked by a relevant heating system in an out-of-pile test (Figure 3.1).

On the one side, the testing goals enumerated in Section 3.1 are to be executed under representative ITER operational conditions, with the exception of the fatigue life testing, in which the thermal cyclic loading can be accelerated, corresponding to the ITER power pulses. Therefore, the heater system shall be able to deploy a full power density profile in the 30 s ramp-up of the ITER pulse, which means that the system should have a low heat capacity in order to be able to handle relatively fast transients.

Secondly, the heater system should, ideally, not have any mechanical interaction with the pebble bed in order to keep full relevancy to the reactor conditions, i.e. the heater system should minimize any intrusion in the functional materials. A hypothetic way to heat up the pebble beds without altering their thermo-mechanics would be the use of microwave heating (e.g. Agrawal, 1998; Mondal et al., 2009; Yoshikawa, 2010). However, due to the fact that the pebble beds are contained inside steel structures, it is presumably challenging to transfer electromagnetic energy to the pebble beds without modification of the steel container topology or its material, loosing relevancy with respect of the real component. Therefore, this potential solution has not been taken into account as a primary option.

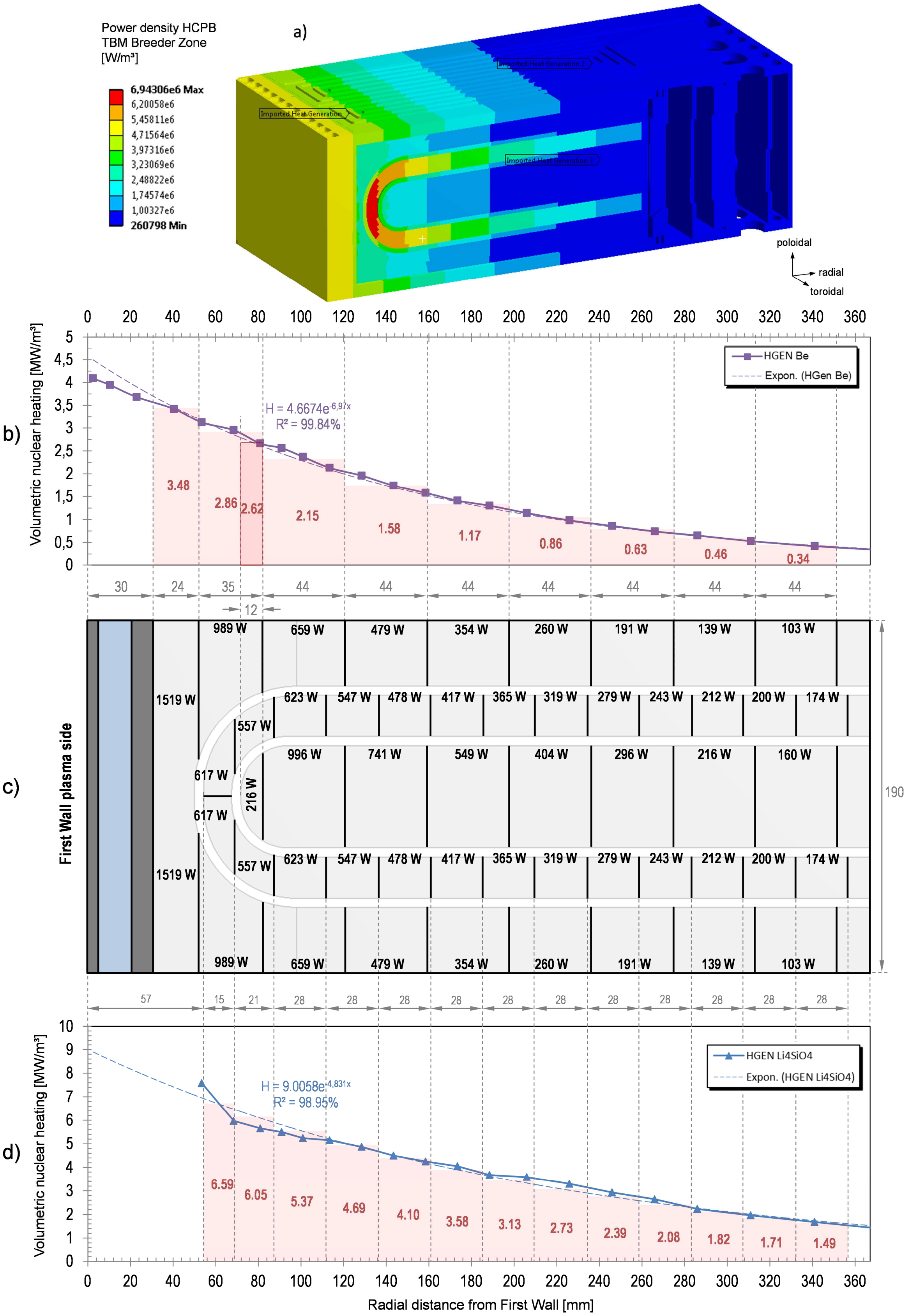

Figure 3.1: Power distribution in the HCPB TBM Breeder Unit after Pereslavtsev et al. (2010): a) 3D distribution, b) and d) radial distributions of the power density in the Be and Li4SiO4 pebble beds and c) subdivision of the pebble beds in sectors and (integrated) power production in each.

Therefore, traditional heater elements based on ohmic heating are taken as primary options for the heater system selection, although they have a certain and unavoidable level of intrusion in the pebble bed.

Finally, the heater system shall be chemically compatible with the functional materials and electrically isolated. It shall also withstand the temperature level expected in the reference design for the HCPB TBM Breeder Unit, which are about $800\ °C \div 900\ °C$ for the Li_4SiO_4 and $\sim 650\ °C$ for the Be pebble beds (Hernández et al., 2012; Moscardini et al., 2013).

3.1.2 Conceptual studies of an out-of-pile test with a HCPB TBM Breeder Unit mock-up: heater system comparison and selection

In order to select the most appropriate heater system for an out-of-pile test with a HCPB TBM Breeder Unit a conceptual study is performed in this Section. Here, the HCPB TBM Breeder Unit reference design presented in Section 2.2.1 (Figure 2.7) is assumed as basis for the conceptual analysis. As proposed in Figure 3.1, the Breeder Unit is subdivided in different sectors and a mean power production is obtained (Figure 3.1, picture c)) by integrating the power distribution curves of the Be (Figure 3.1, picture b)) and Li_4SiO_4 (Figure 3.1, picture d)) in the volume defined by each sector. This power production distribution is to be generated by an ohmic heater system.

Neuberger and Zeile (2009) performed a preliminary scoping analysis studying different conventional ohmic heaters, namely cartridge, ceramic plates, metallic strips, wire and foil elements. In that study the authors state the suitability of the plate heaters in front of the other alternatives due to their high temperature stability and large surface power limit. Later, Németh et al. (2012) have simulated the nuclear power density of the first reference HCPB TBM Breeder Unit mock-up (Section 2.2.1, Figure 2.6) with cartridge and plate heaters, showing that also cartridge heaters might be an option to be taken into account for an out-of-pile test.

Motivated by the aforementioned scoping analyses, a conceptual study of an out-of-pile test of a HCPB TBM Breeder Unit mock-up has been performed by FEM analysis in ANSYS. A third new concept based on a matrix of thin ($1\ mm$) linear wire heaters (picture c.1) of Figure 3.2) has been proposed (Hernández et al., 2013), as an alternative to the $6\ mm$ diameter cartridge (picture b.1) of Figure 3.2) and the $5\ mm$ thick ceramic plate heater (picture a.1) of Figure 3.2). The matrix of wire heaters is built upon a hexagonal arrangement, where the heater wires are passing by each vertex of the hexagon and its center, perpendicularly to the hexagon plane. In the case of the Li_4SiO_4 pebble bed, the hexagonal matrix has been proposed to have a side length of $7\ mm$, which is about an order of magnitude larger than the largest Li_4SiO_4 pebble diameter ($\sim 0.63\ mm$). A larger length of the hexagon sides would imply here a thicker bulk volume for the Li_4SiO_4 between heater wires, but also to have less heater wires available per sector, thus reaching the surface power limit of these kind of heaters, which is about $10\ W/cm^2$. Due to the poor thermal conductivity of the Li_4SiO_4 pebble bed and its uncertainties it is preferred not to reach this limit. For the Be pebble bed, the hexagon side length is of $11\ mm$, as here the pebble bed conductivity is better and the pebble size is the same as the heater wire diameter.

The Breeder Unit mock-up analyzed here is the reference design for manufacturing shown in Figure 2.7. For the simulation of the component the whole breeder zone is represented, with the exception of the surrounding cooling structures, i.e. the horizontal and vertical stiffening grids, the cap plate and the BU backplate: in the boundary interface between the steel and the pebble beds a known temperature distribution is applied, which originates from the latest thermal analysis of the component (Moscardini et al., 2013). By doing so, it is thus assumed that the out-of-pile test set-up is able to provide a relevant cooling leading to the temperature distribution in these interfaces of that of the in-pile simulation conditions. The He coolant conditions in the cooling plates of the Breeder Unit are the ones defined in Section 2.2.1 (a total He mass flow of 0.049 kg/s) and the power production subdivision of picture c) in Figure 3.1 is assumed. The material properties for the EUROFER structural steel and the pebble beds are the ones presented in Sections 2.1.2 and 2.1.3.

Figure 3.2 presents the results of the conceptual study. In the pictures a.2, b.2 and c.2 the computed resulting temperature distribution in the Breeder Unit are shown. Comparing the plate heaters to the cartridge ones it can be observed that the temperature distribution obtained with the former (picture a.2) of Figure 3.2) is more relevant to that in the in-pile conditions (picture d) of Figure 3.2). In fact, cartridge heaters generate an unrealistic pattern of temperature peaks which are higher than the temperature limits of the functional materials. This can be alleviated by increasing the number of cartridges in order to reduce the local power density. However, this will penalize the pebble bed thermo-mechanical relevancy, as the diameter of the cartridge heaters is large in comparison with the largest pebble diameter (1 order of magnitude smaller in the case of the Li_4SiO_4) and the already small offset separation between them (28 mm for the Li_4SiO_4). Also, despite the fair temperature relevancy obtained by the plate heater system (picture a.2) in Figure 3.2), this solution assumes the manufacturability of a curved heater to adapt it to the ceramic bridge shape of the Breeder Unit, which is presently to be yet demonstrated. Moreover, such plate heaters split the pebble beds in 2 unconnected parts, thus losing the thermo-mechanical relevancy of such an experimental set-up.

On the other side, it can be appreciated that the temperature distribution of the wire heater matrix (picture c.2) in Figure 3.2) is very close to the reference in-pile temperature distribution and gradients. This heater system has the additional key advantage of minimizing the intrusion in the pebble bed, as the wire diameter is in the same order of magnitude as the smallest pebble diameter in the case of the Li_4SiO_4 bed and exactly the same for the case of the Be pebble bed. In case that the pebble bed will suffer some small deformation (e.g. due to thermal expansion), the wire matrix is flexible enough to follow this deformation. Moreover, and in contrast to the other heating solutions, the small size of the heating elements makes them ideal to reproduce fast heating up and down transients, as their thermal capacity is low. In fact, a heater wire of 1 mm of outer diameter can be seen as a “linear pebble”, which is the closest topology to a single pebble in a radial-poloidal section, like the ones in Figure 3.2.

Due to all the advantages of the matrix of wire heaters, it has been chosen as the most promising heating system to accurately reproduce the neutronic power density of a HCPB TBM Breeder Unit in an out-of-pile test.

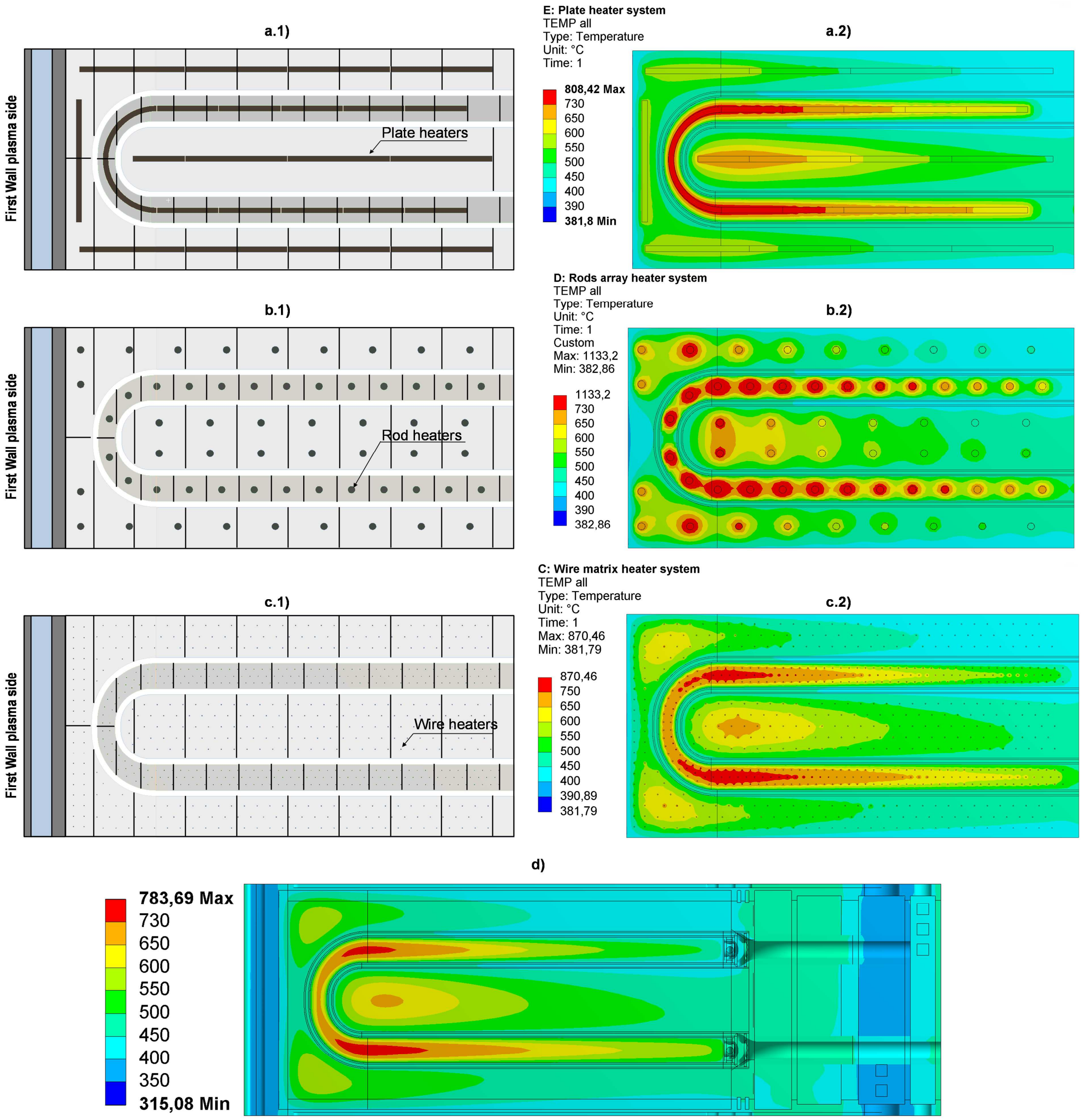

Figure 3.2: Conceptual studies of an out-of-pile test with a HCPB TBM Breeder Unit mock-up reproducing the nuclear power density with different ohmic heating systems. a.1) Conceptual experimental set-up with staged plate heaters; b.1) conceptual experimental set-up with rod heaters; c.1) conceptual experimental set-up with a matrix of wire heaters; a.2), b.2) and c.2) resulting temperature distribution for each of the latter experimental set-ups, respectivelly and d) tempearture distribution of the HCPB TBM Breeder Unit (with nuclear power density).

3.2 The PRE-test Mock-Up eXperiment (PREMUX)

3.2.1 Motivation and goals

In the last Section 3.1.2 it has been deduced that the most relevant heater system for an out-of-pile thermo-mechanical performance validation of a HCPB TBM Breeder Unit is a matrix of wire heaters in a hexagonal arrangement. Despite the identified advantages of this heater system concept, its technical feasibility and functionality has to be first proved before its implementation in a full-scale HCPB TBM Breeder Unit mock-up. Therefore, a *PRE-test Mock-Up eXperiment* (PREMUX) is proposed here for that purpose. PREMUX shall represent a part of a HCPB TBM Breeder Unit mock-up in order to proof the new heater concept under relevant operating conditions. Additionally, as PREMUX shall keep relevancy to a part of a HCPB TBM Breeder Unit mock-up, it can be utilized as a validation benchmark for predictive numerical methods. Consequently, PREMUX aims at 2 basic goals:

1. to serve as a proof-of-concept test for a new heater system to be later integrated in an out-of-pile testing of a functional mock-up of a HCPB TBM Breeder Unit,
2. to serve as a benchmark test for the validation of thermal and thermo-mechanical models.

The second goal requires PREMUX to explore a range of characteristic operating conditions so as to be able to benchmark the models built to validate the thermo-mechanical performance of a Breeder Unit numerically. For instance, in steady state conditions, different power densities in similar increasing steps up to the nominal value determined by Pereslavtsev (2010) (Section 2.2.2) can be explored.

PREMUX shall be able to reproduce ITER power pulses as shown in Section 1.1.3, representing the central proof-of-concept test for the heater system. This transient test runs define a key requirement for the new developed heater system, which is to keep its mechanical integrity while providing a full power density deployment in a time window of 30 s, as defined for ITER.

Additional tests in order to check other important pebble bed properties are desired. This is the case of the influence of the purge gas on the temperature of the pebble bed and the cross-checking of the thermal conductivity of the pebble bed at room temperature, in order to indirectly evaluate the degree of intrusion of the heater system in the bed.

3.2.2 Selection of the Breeder Unit region to test in PREMUX

In order to choose the part of the HCPB TBM Breeder Unit to test, the following selection criteria has been followed:

1. The region to test shall correspond to the material with the lowest thermal conductivity, in order to test the integrity of the heater system in media with low heat transfer capability and under risk of temperature peaks on the heater surface.
2. The region under study should correspond to a volume of pebble bed with the highest power density and where the highest temperature is to be expected.
3. The area to test shall reflect a region of difficult access and where the addition of instrumentation (e.g. thermo-couples or strain-gages) is technically the most challenging.

The region meeting the selection criteria listed above and considering the subdivision proposed in Figure 3.2 corresponds to the 2 volumes of the Li_4SiO_4 pebble bed just after the ceramic bridge, as delimited in the bottom picture of Figure 3.3 and as highlighted in the top picture of Figure 3.3. The dimensions of the resulting volume of pebble bed to be tested in PREMUX are given as well in Figure 3.3 bottom. For each of these 2 volumes, a heater block with the aforementioned hexagonal arrangement is to be designed and manufactured.

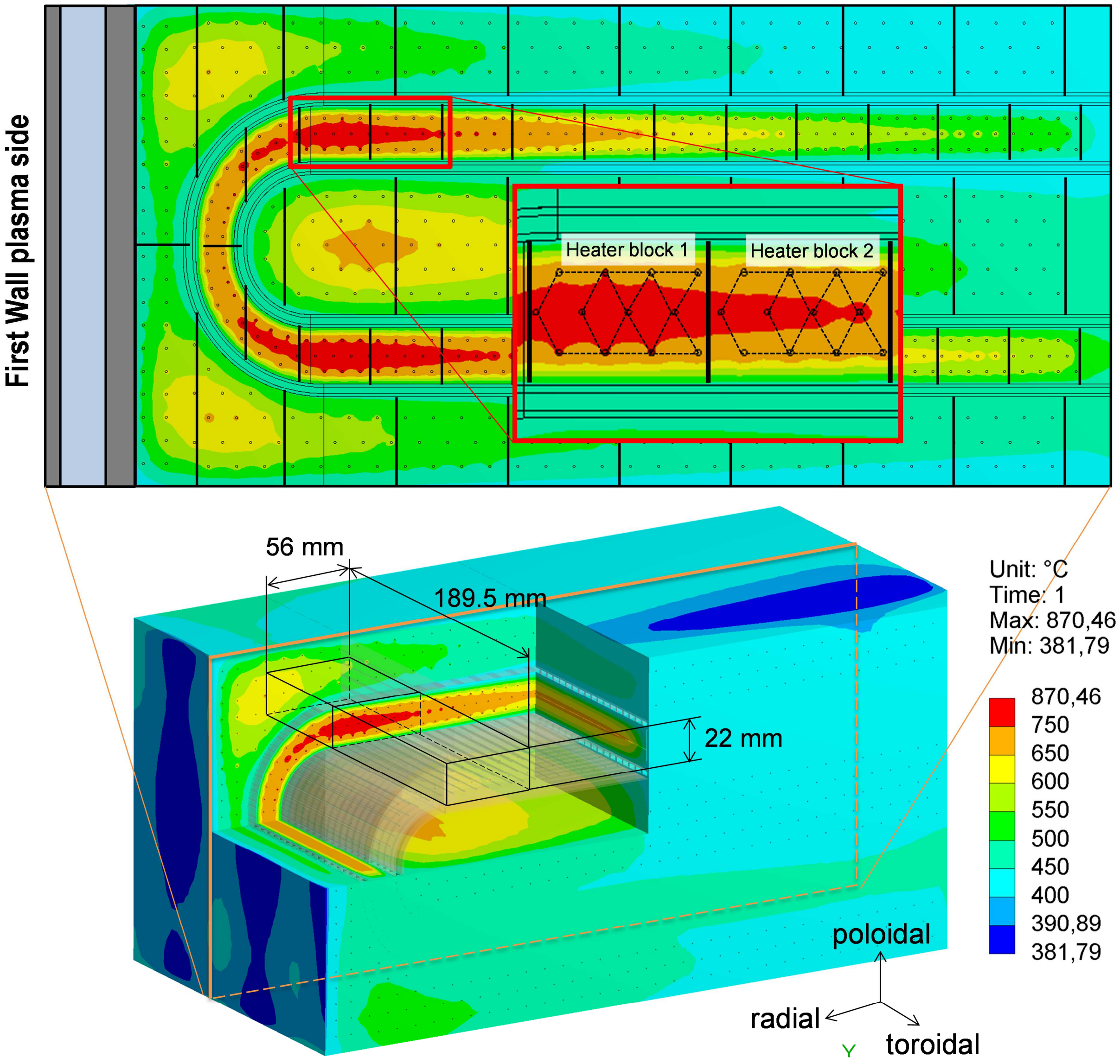

Figure 3.3: Selection of the region of the HCPB TBM Breeder Unit mock-up to test in PREMUX. Top: detail of the 2 heater blocks to be reproduced in PREMUX. Bottom: general isometric view of the mock-up with a 3D cutoff showing the prismatic volume to be reproduced in PREMUX.

3.3 Design and development of the PREMUX test section

3.3.1 Design, development and construction of the system of hexagonal matrix of wire heaters for PREMUX

The development and construction of the heater system for PREMUX has been performed in collaboration with the company THERMOCOAX®[9]. The basis for the heater system is a heating element formed by a single or double resistance heating wire at the core (namely *single core*, Figure 3.4 left or *twin core*, Figure 3.4 right, respectively) embedded in a magnesium oxide (MgO) compacted bed, which is utilized as electrical insulation. The heating wire with the compacted MgO is encosed in a cylindrical sheath of AISI 304L steel or Inconel Alloy 600.

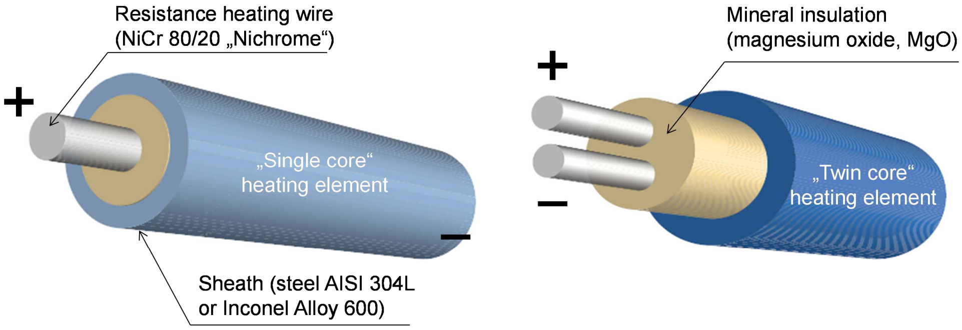

Figure 3.4: Basic heating element in PREMUX. Left: single core heating element. Right: twin core heating element. Pictures courtesy of THERMOCOAX®.

Therefore, in order to construct the heater system there is the possibility to use both the single and twin core configurations, both having advantages and disadvantages. The most notorious disadvantage of the single core cable is the need for bends in order to obtain the 12 straight and parallel heating cables needed for each heater block in PREMUX (see Figure 3.3). The number of bends and the size of the system complicate its production. In contrast, only 1 single core heating element would suffice to perform a whole heater block, simplifying the electrical connection to a power supply, being this the main advantage. On the other side, the twin core eliminates the need of bending the heating elements, ensuring straight heating wires without further corrections in the geometry. However, with this configuration a heater block would be composed by 12 twin core heating elements, which would necessitate the construction of a connection box. The implementation of such connection box is relatively complicated due to the large number and the small size of the connections to be performed, requiring its own electric insulation prior to be connected to a power supply. This development risk has been considered greater than performing the bends and therefore the single core configuration has been selected for the development and fabrication of the heater system in PREMUX.

Inconel Alloy 600 has been chosen for the heating element sheath, as the expected temperatures for the heater blocks 1 and 2 are higher than the limit specified by the manufacturer for the AISI 304L sheath, which is about 600 *°C*, while Inconel Alloy 600 allows

---

[9] http://www.thermocoax-nuclear.com/

temperatures up to 1000 $°C$ (THERMOCOAX, 1998). A third heating block has been included between the heater blocks 1 and 2, based on a twin core heating element. The purpose of this single cable heater block is to perform in-situ thermal conductivity tests with the Hot Wire Method at room temperature, as a confirmation test that the effective thermal conductivity of the pebble bed is in agreement with the one in the literature with this heater arrangement. For both versions, a maximum surface power density of 10 W/cm^2 is given by the manufacturer.

The heater cables are to be installed aligned with the toroidal direction as shown in Figure 3.3, practically covering all the toroidal length of the pebble bed (189.5 mm). However, the temperature measurements are to be acquired in a single radial-poloidal plane (from now on, the PREMUX *measurement plane*), transverse to the heater wires' axis, and situated at a distance of 82 mm from a side (Figure 3.6 top-left). The rationale for this value is described in the next Section 3.3.2.

Figure 3.5 depicts the conceptual cross-section in the measurement plane of PREMUX. The heater system has 3 different thermocouple positions: (1) thermocouples on the heater, (2) thermocouples in the pebble bed bulk and (3) thermocouples on the top and bottom faces of the PREMUX test box. Each group of these three types ideally forms an array of measurements that is ideally aligned with the resultant heat flux vector in the pebble bed. The thermocouples of the heater system are K-type, where the ones on the heater elements have an outer diameter of 0.5 mm and the rest, 1 mm.

Ideally, one of the straight parts of the heater cable should pass by the center of each hexagon forming the heater matrix layout. However, the heaters at this position have an offset of 1.6 mm (Figure 3.5, 3D CAD details in Figure 3.6 bottom), in order to increase the distance between thermocouple and the surrounding heater wires.

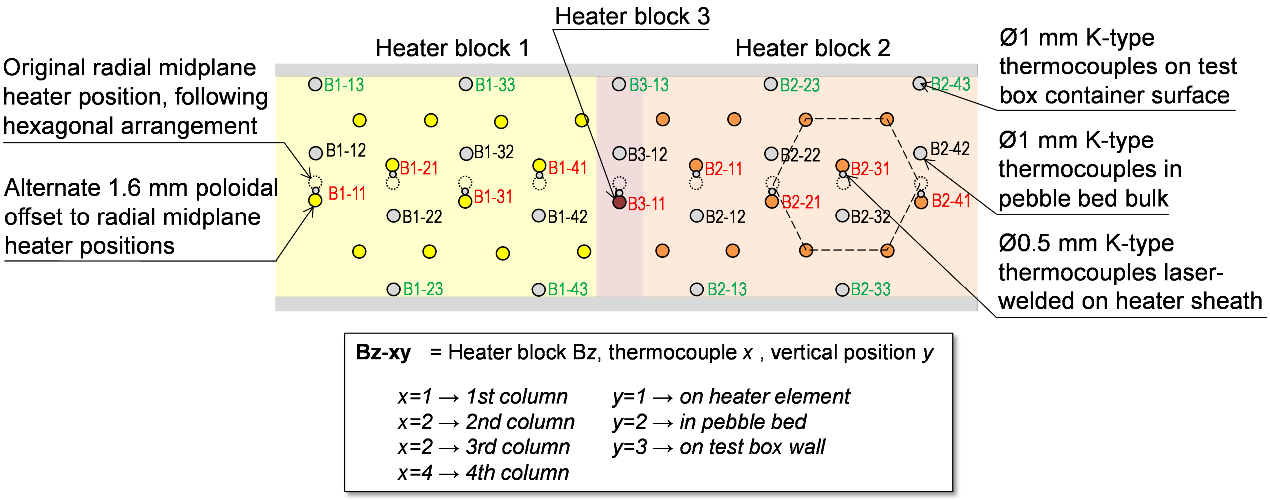

Figure 3.5: Cross-sectional view of the PREMUX measurment plane. Layout of heater wires and thermocouples positions and nomenclature used throughout this thesis.

Due to the large flexibility of the heater elements and the thermocouples, spacer plates are added to each heater block (Figure 3.6, close view in top-right view), which provides stiffness and overall geometrical stability to the system.

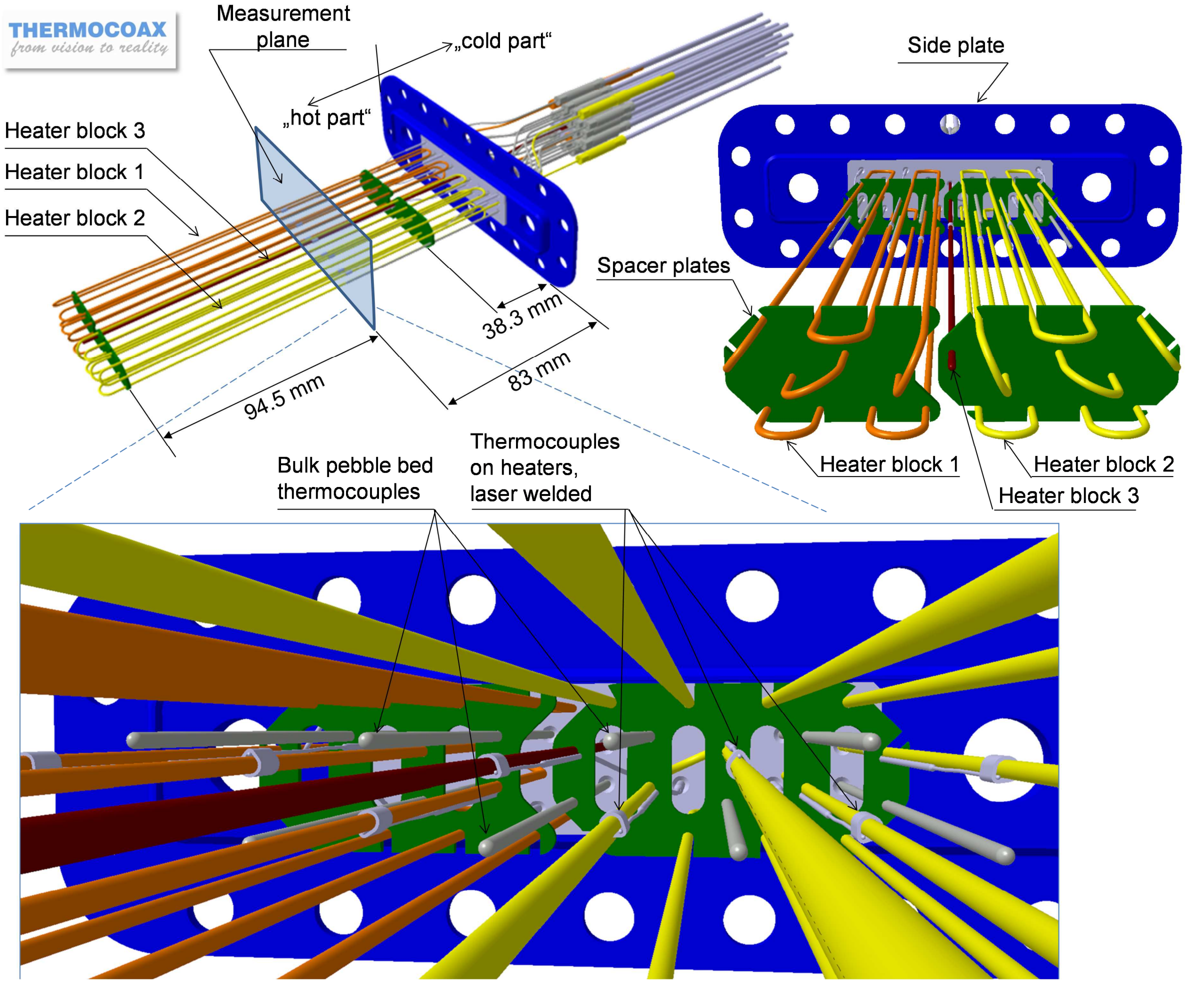

Figure 3.6: 3D CAD model of the PREMUX heater system developed by KIT and THERMOCOAX®. Top: isometric views with identification of the components. Bottom: close view to the system at the measurement plane. In this view, the pebble bed bulk thermocouples and the thermocouples on the heating elements can be observed.

Packing factor tests have been performed prior to the manufacturing of the heater system, so as to verify its low intrusion in the pebble bed. For this, a replica of the PREMUX test box container volume for the pebble bed has been built (Figure 3.7).

A first “dummy” heater block with twin core heaters and a second with austenitic steel wires, both of Ø1 *mm* and in a hexagonal matrix arrangement have been brazed to a side plate and inserted to the container replica. The resulting volume has been filled with reference Li_4SiO_4 pebbles placed on a vibratory sieve shaker in a vertical position (i.e. with the toroidal length of the box aligned with the gravity force vector), up to about 2/3 of the container volume. The vibratory sieve shaker has been switched on after this filling level, with a vibration frequency of 5 *Hz*. A very significant compaction of the pebble bed could be observed by simple visual inspection immediately after applying the mechanical vibration to the container replica.

The weight of the flask containing the pebbles has been measured with a precision scale (±0.5 *g*) before and after the filling, in order to determine the weight of pebbles inserted in the container volume, which has resulted in 638.5 *g*. The container volume has been obtained with the CAD model of the replica. By means of a Li_4SiO_4 pebble density ($2.389\ g/cm^3$, Reimann et al. (2005)) and the measured weight of the filled pebbles, a packing factor of $(64.3 \pm 0.778)\%$ has been reached, which is in line with the values found in the literature, as pointed out in Section 2.1.3.

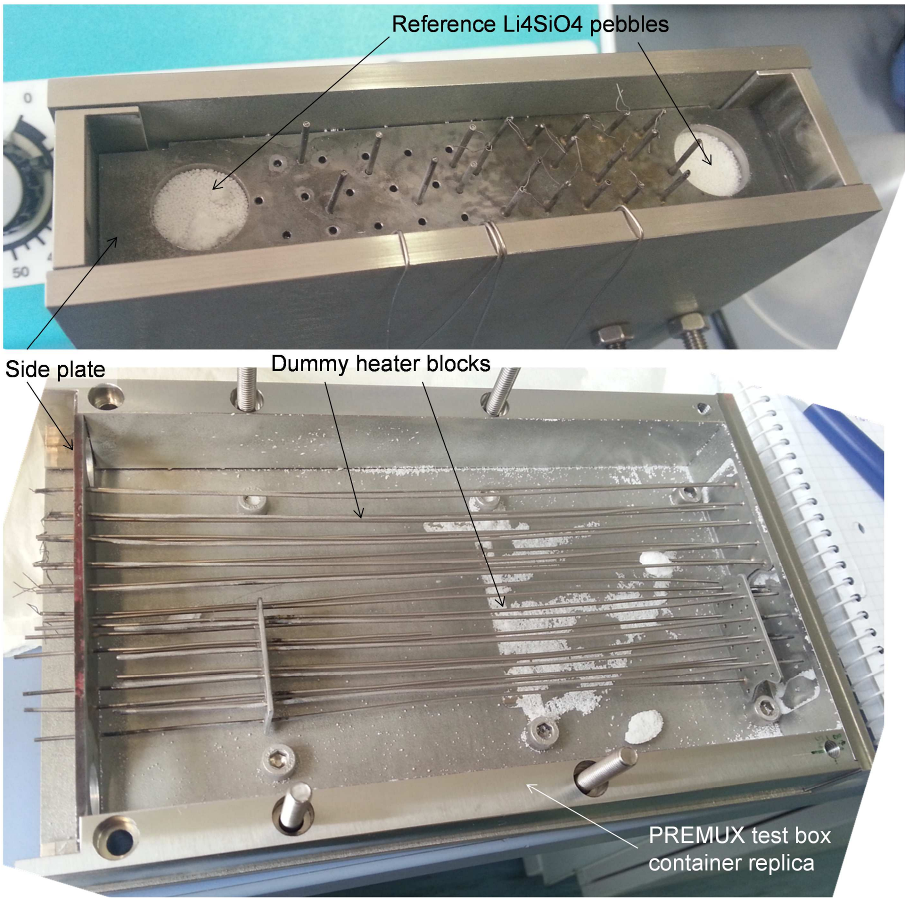

Figure 3.7: Pebble bed packing factor test prior to the fabrication of the PREMUX heater system. Top: replica of the test box container volume filled with reference Li_4SiO_4 pebbles. Bottom: disassembled top lid of the container replica showing the inner volume with the heater blocks after the filling test. Formation of pebble clusters can be observed between the heater wires.

As shown by Reimann et al. (2006) and later by Gan et al. (2010), the local packing factor of the pebble bed in the vicinity of a boundary surface is reduced and it is a function of the surface curvature. Therefore, the insertion of additional surfaces into the pebble bed reduces, in general, the packing factor. However, due to the small curvature radius of the heater wires, the high packing factor obtained suggests that the local reduction of the packing factor is negligible and that the heater system has therefore a low influence in the pebble bed packing factor, as it is required.

Figure 3.8-right shows a photo of the heater system after their manufacturing by THERMOCOAX® and Figure 3.8-bottom, an infrared imagery of the go/no-go tests performed to each heater block before the assembly of the heater system in PREMUX, where (a), (b) and (c) corresponds respectively to the heater blocks 1, 2 and 3.

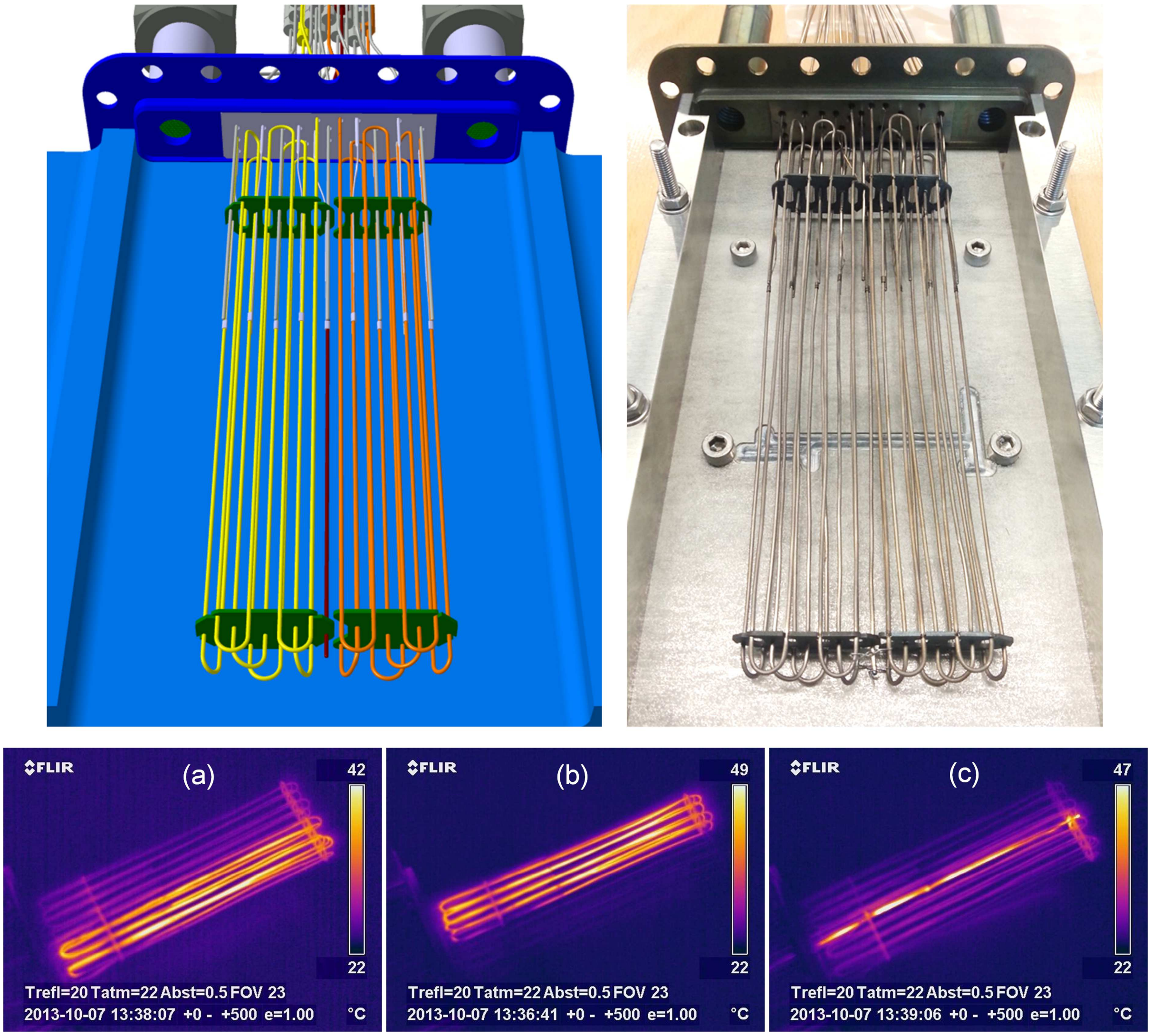

Figure 3.8: Hexagonal matix of wire heaters for PREMUX. Top-left: 3D CAD model. Top-right: realization of the heater system by THERMOCOAX® and insertion of the assembly in a container replica. Bottom: infrared imaging of the go/no-go test performed to each of the heater blocks before their assembly in PREMUX. The tests where performed for a few seconds with 110 V and 0.1 A, where (a) is the heater block 1, (b) is the heater block 2 and (c) is the heater block 3.

Each heating element is connected to a so-called cold part, which is a part with low line resistance that connects the heating part (the "hot part") with the power supply. The cold part line resistances of the heater blocks 1 and 2 at room temperature are $\mathrm{r}_{\mathrm{cold},0}^{\mathrm{H}_1} = \mathrm{r}_{\mathrm{cold},0}^{\mathrm{H}_2} = 0.6\ \Omega/\mathrm{m}$ and for the heater block 3, $\mathrm{r}_{\mathrm{cold},0}^{\mathrm{H}_3} = 5.22\ \Omega/\mathrm{m}$, with accuracies of 8% and 10% respectively. The length of the "hot parts" of the heater blocks 1 and 2 are $\mathrm{L}_{\mathrm{cold}}^{\mathrm{H}_1} = \mathrm{L}_{\mathrm{hot}}^{\mathrm{H}_2} = 2.15$ m and $\mathrm{L}_{\mathrm{hot}}^{\mathrm{H}_3} = 0.175$ m for the heater block 3, with an accuracy of 5% in all cases. In order to reduce the uncertainty in the heating system, the total heater blocks' resistances have been measured and are summarized in Table 3.1.

Once the heater system has been commissioned, the actual positions of the heaters and thermocouples have been determined by 3D digitalization with an accuracy of at least 0.02 mm by means of an ATOS III Triple Scan laser-scanning camera (Figure 3.9 left). This is needed in order to minimize the error in the temperature measurements due to the thermocouple position uncertainty. The point cloud dataset has been imported into CATIA V5 (Figure 3.9 top-right) and the deviations with respect the reference values (Figure 3.9 bottom-right) have been identified and taken into account in the numerical models described in Chapters 5 and 6.

Table 3.1: Table of total line resistances for each heater block in the PREMUX heater system.

Total heater resistance [Ω]		Standard uncertainty [Ω]		Expanded uncertainty ($2\boldsymbol{\sigma}$) [Ω]	
$\boldsymbol{R^{H_1}_{tot,0}}$	24.1	$u_{R^{H_1}_{tot,0}}$	0.075	$U_{R^{H_1}_{tot,0}}$	0.149
$\boldsymbol{R^{H_2}_{tot,0}}$	25.9	$u_{R^{H_2}_{tot,0}}$	0.086	$U_{R^{H_2}_{tot,0}}$	0.171
$\boldsymbol{R^{H_3}_{tot,0}}$	18.2	$u_{R^{H_3}_{tot,0}}$	0.104	$U_{R^{H_3}_{tot,0}}$	0.207

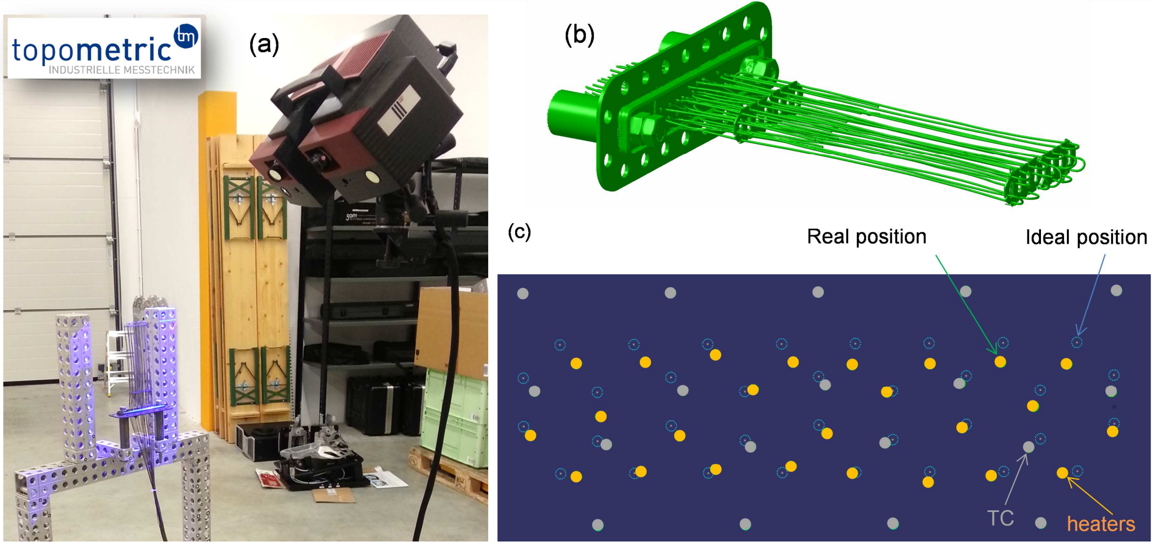

Figure 3.9: 3D digitalisation of the heater system for PREMUX. Left: 3D laser-scan performed by the company Topometric. Top-right: 3D digitalized CAD model of the heater system. Bottom-right: quantification of the position deviations with respect the reference values.

The heater blocks 1 and 2 are each connected to an Elektro-Automatik model EA PS8360-15 2U power supply and the heater block 3 to a model EA PS8160-15 2U. The communication between these components and a computer is performed by Ethernet and controlled through a desktop computer by means of the software LabView.

3.3.2 Design, development and construction of the PREMUX test box

Container volume and materials

The conceptual sketch of the PREMUX test box is depicted in the left picture of Figure 3.10 The poloidal and toroidal dimensions of the Li_4SiO_4 pebble bed are relevant to a HCPB TBM Breeder Unit mock-up, i.e. 22 *mm* (poloidal) × 189.5 *mm* (toroidal). A length of 56 *mm*, which corresponds to 4 times a distance of 7 *mm* between heater wires for both heater blocks, would be in principle necessary for the radial dimension. However, this dimension has been enlarged up to

118 mm (see also Figure 3.3) in order to have enough bulk material and avoid eventual boundary effects affecting the results in the pebble bed bulk.

The pebble bed is contained in a prismatic container of 9Cr-0.5Mo-1.75W-V-Nb steel, namely P92 (EN designation: 1.4901) for availability and economy reasons. Despite this material difference with the original EUROFER97 steel foreseen for the HCPB TBM Breeder Unit, both steels are 9% Cr-based alloys and are chemically similar, thus making the P92 a relevant and economic substitute material for EUROFER97, especially from the point of view of the thermal conductivity. Several fabrication experiments performed by Neuberger et al. (2011) confirm as well the suitability of P92 as substitute material for EUROFER97 after welding tests of EUROFER97 with P92.

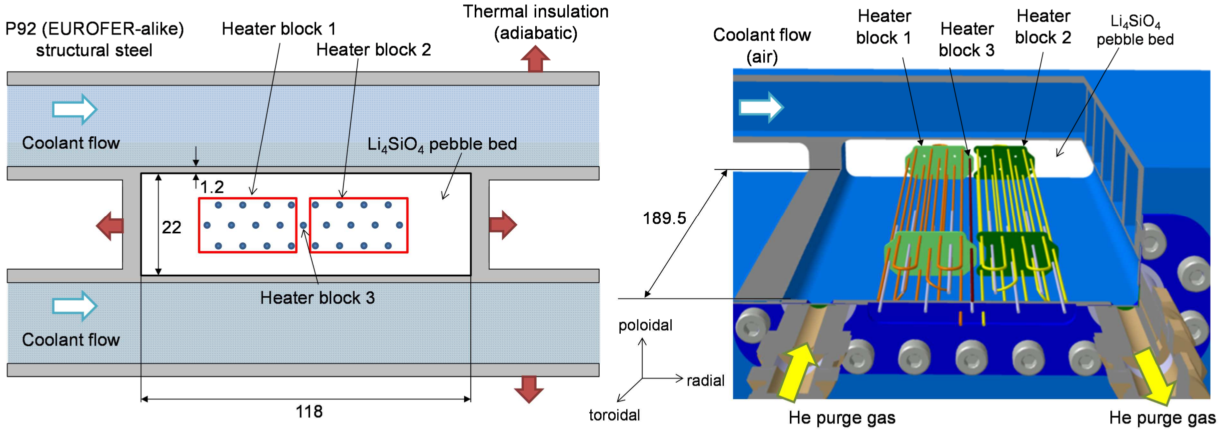

Figure 3.10: PREMUX test section. Left: conceptual picture with the Li_4SiO_4 pebble bed radial and poloidal dimensions. Right: 3D section CAD cut-off of the PREMUX test box, with focus on the heater blocks and detail of the toroidal pebble bed dimension.

The top and bottom sides of the prismatic container have cooling channels, which extracts the heat produced in the volumetrically heated pebble bed. The wall thickness of the test box between the pebble bed and the cooling channels is 1.2 mm thick as in a Breeder Unit mock-up. The cross-section of the cooling channels should be 4.5 $mm \times 2.6$ mm to be relevant with the Breeder Unit dimensions, as stated in Section 2.2.1. However, an air cooling loop facility (L-STAR/LL, Section 3.4) has been available to run PREMUX during the duration of this thesis. Therefore a suitable rescaling of the test box to fit the operating conditions of this loop has been proposed and it is deduced in the following lines.

Design of a relevant thermo-hydraulic cooling scheme and main test box dimensions

In order to achieve a physically similar cooling to a HCPB Breeder Unit, the cooling channels of PREMUX has been dimensioned by means of the Buckingham's Π-Theorem (Buckingham, 1914; Siekmann & Thamsen, 2009).

Let Q_j, $\forall j = 1 \dots r$ and q_k, $\forall k = 1 \dots m$ be physical quantities different from the trivial solution so that the dimensions of $(Q_1, \dots, Q_j, \dots, Q_r)$ form a fundamental system of units and the dimensions of $(q_1, \dots, q_i, \dots, q_m)$ are contained in the latter fundamental system of units $(r + m = n)$. Let as well

$$\phi(Q_1, \dots, Q_j, \dots, Q_r, q_1, \dots, q_i, \dots, q_m) = 0 \ , \tag{3.1}$$

be a physical relation. Then, the Π-Theorem states that it exists a group of dimensionless quantities Π_i in the form

$$\Pi_i = \frac{q_i}{\prod_{j=1}^{r} Q_j^{x_{ji}}} \ , \tag{3.2}$$

for an adequate choice of exponents x_{ji} so that any physical relation as in Eqn. (3.1) can be rescaled and expressed in terms of the Π_i dimensionless quantities (or parameters)

$$\Psi(\Pi_1, \dots, \Pi_{n-r}) = 0 \ . \tag{3.3}$$

In the particular case of the heat transfer capability of the coolant in the cooling channels of PREMUX, the primary physical quantities involved are the coolant's density ρ_c, dynamic viscosity μ_c and thermal conductivity k_c, as well as the mass flow in a channel $\dot{m}_c$ and its cross-sectional area A_c. For this set of $n = 5$ quantities, a fundamental set of $r = 4$ units $\{[M], [L], [T], [\theta]\}$ can be identified, denoting $[M]$ for the mass, $[L]$ for the length, $[T]$ for the time and $[\theta]$ for the temperature. Therefore, the problem of the heat transfer in the coolant can be written with $m = n - r = 1$ dimensionless parameter Π_1 after the Π-Theorem.

As $[\rho_c] \equiv [ML^{-3}]$, $[\mu_c] \equiv [ML^{-1}T^{-1}]$, $[k_c] \equiv [MLT^{-3}\theta^{-1}]$, $[\dot{m}_c] \equiv [MT^{-1}]$ and $[A_c] \equiv [L^2]$ and choosing $q_1 = \dot{m}_c$ and $Q_1 = A_c$, $Q_2 = \rho_c$, $Q_3 = \mu_c$ and $Q_4 = k_c$ then

$$\Pi_1 = \frac{q_1}{\prod_{j=1}^{4} Q_j^{x_{j1}}} = \frac{\dot{m}_c}{A_c^{x_{11}} \rho_c^{x_{21}} \mu_c^{x_{31}} k_c^{x_{41}}} = \dot{m}_c A_c^{\bar{x}_{11}} \rho_c^{\bar{x}_{21}} \mu_c^{\bar{x}_{31}} k_c^{\bar{x}_{41}} \ , \tag{3.4}$$

$$[\Pi_1] \equiv [MT^{-1}][L^2]^{\bar{x}_{11}}[ML^{-3}]^{\bar{x}_{21}}[ML^{-1}T^{-1}]^{\bar{x}_{31}}[MLT^{-3}\theta^{-1}]^{\bar{x}_{41}} = 1^0, \tag{3.5}$$

denoting $-x_{j,i} = \bar{x}_{1,1}$ for clarity. The following linear system can be therefore written to solve the exponents $(\bar{x}_{11}, \dots, \bar{x}_{41})$ by constructing an equation for each of the units:

$$\Pi_1: \begin{cases} [M][M]^{\bar{x}_{21}}[M]^{\bar{x}_{31}}[M]^{\bar{x}_{41}} = [1]^0 \Leftrightarrow 1 + \bar{x}_{21} + \bar{x}_{31} + \bar{x}_{41} = 0 \\ [L^2]^{\bar{x}_{11}}[L^{-3}]^{\bar{x}_{21}}[L^{-1}]^{\bar{x}_{31}}[L]^{\bar{x}_{41}} = [1]^0 \Leftrightarrow 2\bar{x}_{11} - 3\bar{x}_{21} - \bar{x}_{31} + \bar{x}_{41} = 0 \\ [T^{-1}][T^{-1}]^{\bar{x}_{31}}[T^{-3}]^{\bar{x}_{41}} = [1]^0 \Leftrightarrow -1 - \bar{x}_{31} - 3\bar{x}_{41} = 0 \\ [\theta^{-1}]^{\bar{x}_{41}} = [1]^0 \Leftrightarrow -\bar{x}_{41} = 0 \end{cases} , \tag{3.6}$$

The solution of the system in Eqn. (3.6) is $\bar{x}_{11} = -\frac{1}{2}$, $\bar{x}_{21} = \bar{x}_{41} = 0$ and $\bar{x}_{31} = -1$, leading to

$$\Pi_1 = \frac{\dot{m}_c}{\mu_c \sqrt{A_c}} \ . \tag{3.7}$$

Then, in order to have thermo-hydraulic similarity in PREMUX (the model) with respect to a HCPB Breeder Unit (the prototype), Π_1 for both the model $(\Pi_{1,mod})$ and the prototype $(\Pi_{1,prot})$ must be the same:

$$\Pi_{1,mod} = \Pi_{1,prot} \Leftrightarrow \frac{\dot{m}_{c,mod}}{\mu_{c,mod}\sqrt{A_{c,mod}}} = \frac{\dot{m}_{c,prot}}{\mu_{c,prot}\sqrt{A_{c,prot}}} \ . \tag{3.8}$$

Eqn. (3.8) allows using gases other than He at high pressure and high temperature. Air at a nominal pressure of 0.2 *MPa* has been chosen as cooling medium for PREMUX in order to fit the requirements of the L-STAR/LL air loop. In order to simplify the construction of the experiment, the air inlet has been assumed to be at room temperature (~20 $°C$) and the outlet at ~60 $°C$ (i.e. a temperature increase of ~40 $°C$ from inlet to outlet). This temperatures allow the use of Nusselt correlations (e.g. Gnielinski, 1976) for the determination of the heat transfer coefficient between the cooling channels walls and the air coolant. Moreover, they also allow the use of flexible, nonmetallic hoses as connecting parts between the PREMUX test box and the ancillary systems to the L-STAR/LL air loop, simplifying the experiment construction. The left picture in Figure 3.11 plots the relationship in Eqn. (3.8) assuming air properties at a mean temperature of $20\ °C + \frac{40}{2}\ °C = 40\ °C$ and 0.2 MPa of pressure and considering a coolant mean mass flow in the prototype of $\dot{m}_{c,prot} = \frac{0.049\ kg/s}{60} = 8.167 \cdot 10^{-4}\ kg/s$, flowing through rectangular cross-section of 4.5 mm × 2.6 mm, with a mean temperature of $\frac{400+500}{2} = 450\ °C$ and pressure of 8 MPa, as described in Section 2.2.1.

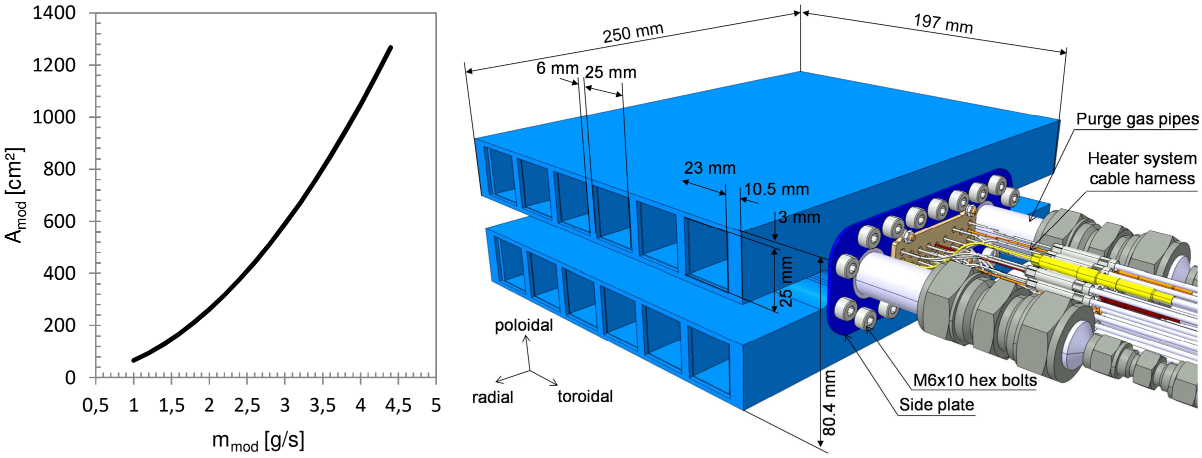

Figure 3.11: Relationship between the mass flow in the cooling channel of the model (PREMUX) and its cross-sectional area to have thermo-hydraulic similarity between PREMUX and a HCPB TBM Breeder Unit (left) and 3D CAD picture of the PREMUX test box cooling channels.

Considering the (toroidal) depth of the pebble bed (189.5 mm), 6 squared cooling channels of 25 mm with 6 mm thick ribs between them can be realized (Figure 3.11 right). With these channels' dimensions, an air mass flow of ~0.003 kg/s is required after Eqn. (3.8) to have thermo-hydraulic similarity in PREMUX with respect to an out-of-pile test with a HCPB TBM Breeder Unit mock-up. The outer ribs are thicker (10.5 mm) in order to be able to accommodate the threads of standard M6 × 10 hex socket bolts, which fasten the side plates of the PREMUX test box, closing the volume for the Li_4SiO_4 pebble bed and serving as fixation for the heater system and the instrumentation (mainly thermocouples).

The test box (Figure 3.11 right) is manufactured out of two quasi-symmetrical[10] halves, being the poloidal midplane of the test box the quasi-symmetry plane of these 2 halves. In order to achieve a low distortion while joining the components of the test box, electron beam technique is used for welding. Each half of the test box already features the pebble bed volume and the

---

[10] The halves are not completely symmetric due to a blind pocket at the top and bottom surfaces of the pebble bed container volume, as a guide to center a metal strip with the wall thermocouples.

cooling channels, which are performed by means of wire-cut electrical discharge machining. The radial length of the cooling channels, and therefore of the test box, is 250 *mm*. This length is set by a limitation in the spark erosion machine, which is about 300 *mm* for standard industrial devices like the one available for the manufacturing of the PREMUX test box.

Test box side plates

The pebble bed is swept with low pressure reference purge gas ($\mathrm{He} + 0.1\mathrm{w.t}\%\mathrm{H}_2$). The H_2 content has been neglected in PREMUX, as it is assumed that it does not to contribute significantly to the effective thermal conductivity of the pebble bed, therefore pure He has been utilized as purge gas. Also, the He purge gas in PREMUX is stagnant (there is not a continuous flow of purge gas in the bed), which as first approximation is assumed to be a realistic condition, as the velocity of the purge gas flow is of only a few mm/s (Section 2.2.1).

The side plate containing the heater system (Figure 3.11 right) features as well 2 *purge gas pipes* in order to allow the purge gas to enter the pebble bed. The inner diameter of the pipes is manufactured with a thread to fasten a set screw. This set screw has been customized by drilling a central hole through the whole length of the set screw and welding a filter plate at one of the sides (Figure 3.12 right). The filter plate of the set screw permits the flow of He purge gas inside the pebble bed while keeping the pebbles in the test box. Swagelok® fittings connect the purge gas pipes with the He tubing. Between the Swagelok® fitting and the tubing a gauge pressure transmitter (ABB 261AS) and a ball valve have been installed. The tubing is connected to a He gas bottle on one side and to a vacuum pump (Alcatel Adixen 2005SD Pascal) on the other.

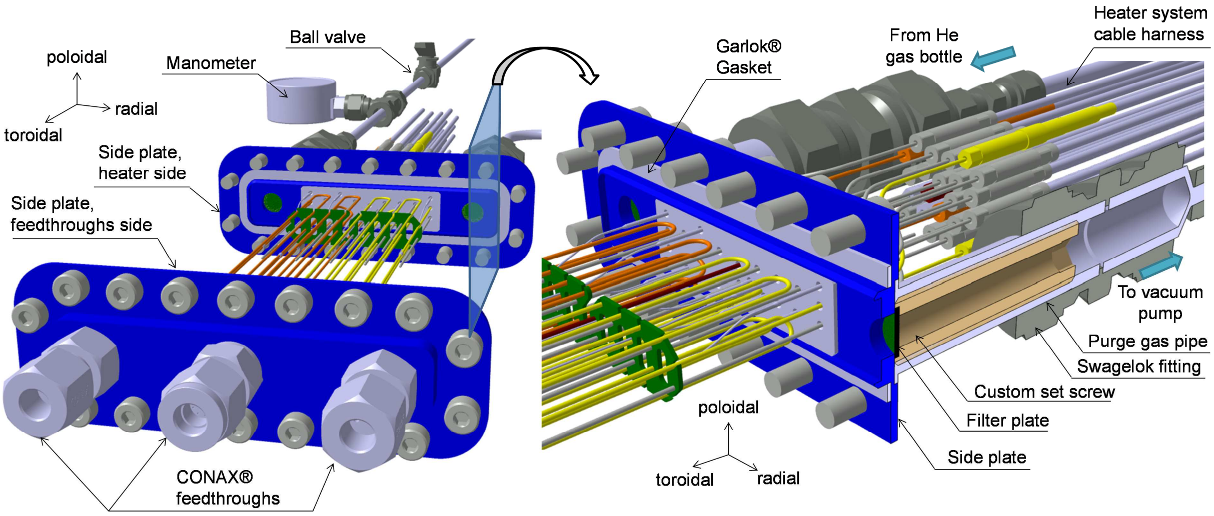

Figure 3.12: Side plates of PREMUX. Left: general isometric view of the side plates, with section cut plane highlighted in semi-transparent blue colour. Right: 3D cutoff view of the side plate with attached heater system and purge gas piping structure.

For the purge gas sweeping of the pebble bed, the ball valve at the side of the He gas bottle (Figure 3.12 right) is first closed and the ball valve at the side of the vacuum pump is opened, being the vacuum pump switched on during several hours creating a medium vacuum (0.1 Pa to 1 Pa). Then, He gas at ∼15 $°C$ is allowed to flow through the pebble bed by opening the ball valve at the side of the He gas bottle. The pressure of the He purge gas at the outlet of the gas bottle is regulated by a pressure regulator and it is set by means of the ideal gas state equation, in order that the He purge gas pressure reaches the reference conditions described in Section 2.2.1 at the steady state at the different predefined power levels in PREMUX. The ball valve at the side of the vacuum pump is then closed, the vacuum pump is switched off and after ~1 minute the ball valve at the side of the He gas bottle is as well closed. After each experiment, the ball valve at the side of the vacuum pump is opened and the vacuum pump is activated to perform again medium vacuum. This procedure allows observing the purge gas propagation through the bed, as there is the target pressure on the purge gas pipe of the He gas bottle and medium vacuum at the other purge gas pipe. It has been observed that the resistance of the purge gas to flow through the pebble bed is very low, as the pressure build up on the vacuum side occurs practically instantaneously. This observation is important when thinking about an eventual in-box loss of coolant accident (LOCA): the coolant leak from a cooling plate to the pebble bed will not build up pressure locally at the region of the leakage due to the hydraulic resistance of the pebble bed, but the coolant should fill the voids of the beds relatively fast.

The side plates are fastened with an arrangement of M6 × 10 hex socket bolts, as shown in (Figure 3.12-right), as it has been preferred to have the possibility to mount and dismount the side plates to have access to the heater system and replace it if damaged. Reasonable He tightness at high temperatures is then ensured at the side plates with Garlok® Style 9900TI gaskets (Figure 3.12-right). The gasket dimensions and the bolt arrangement have been determined following the VDI 2230 norm (VDI-Richtlinie 2230 T1, 2003).

Test box interface pipes to the PREMUX ancillary system

The connection of the PREMUX test box to the ancillary air loop components is effectuated through inlet and outlet interface pipes of 22 *mm* and 18 *mm* of outer and inner diameter respectively, made out of P92 steel and welded by electron beam to the test box (Figure 3.13).

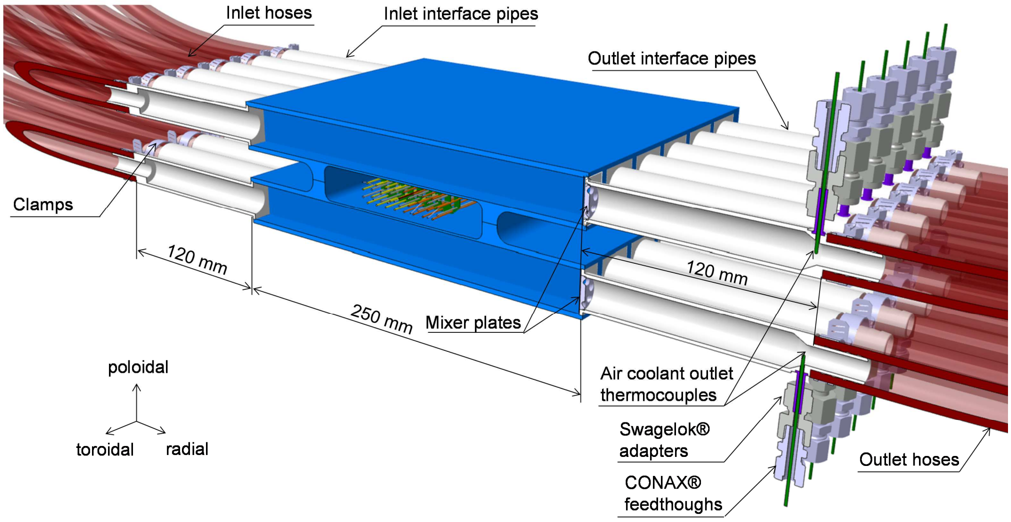

Figure 3.13: 3D cutoff view of the PREMUX test box with the interface pipes and connection hoses.

The length of the interface pipes is 120 *mm*, which are close to the recommended value of 10 times the pipe inner diameter (i.e. 180 *mm* entry length) to have a hydrodynamically fully developed flow region (Çengel & Cimbala, 2006). Though, it has not been possible to manufacture longer interface pipes due to a limitation in the electron beam welding. The electron beam has to travel parallel to the length of these pipes and, due to the ferromagnetic nature of P92, the longer the pipes, the more is the susceptibility of the electron beam to be influenced by the induced magnetic field in the ferromagnetic steel, despite the efforts to demagnetize it.

The outlet interface pipes features ∅1.5 *mm* K-type thermocouples as shown in Figure 3.13, which measure the air coolant outlet temperature. Due to the relatively short length of the interface pipes, mixer plates are placed at the end of the test box rectangular cooling channels in order to increase the temperature homogeneity at the flow cross-section where the temperature measurements are performed. This is achieved by increasing the vorticity of the outlet flow, which is promoted by the shape of these mixer plates, as shown by Hernández et al. (2014).

Pebble filling

Once the interface pipes are welded, the heater system is inserted on the test box and the side plates are tightened. The PREMUX test box is then placed vertically as shown in Figure 3.7 and fixed to an aluminum frame mounted on a vibratory sieve shaker. The procedure to fill the PREMUX test box is equivalent to the one shown in Section 3.3.1.

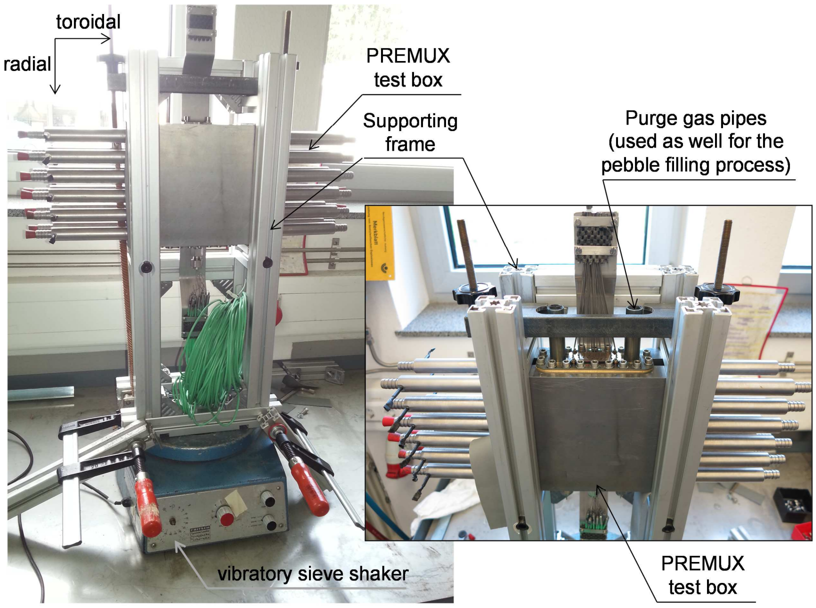

Figure 3.14: Pebbles filling procedure set-up. The PREMUX test box is placed vertically (i.e. radial direction alligned with the gravity vector) on a vibratory sieve shaker fixed to an aluminium frame.

Test box thermal insulation

Once the test box has been filled with the Li4SiO4 pebbles it has been thermally insulated with a surrounding layer of mineral fiber blanket of about 70 *mm* and a thermal conductivity of 0.075 W/mK (ASTM Standard C553-13, 2013). The estimation of the heat losses in the system due to the not perfectly insulated system is detailed in Section 4.3.1.

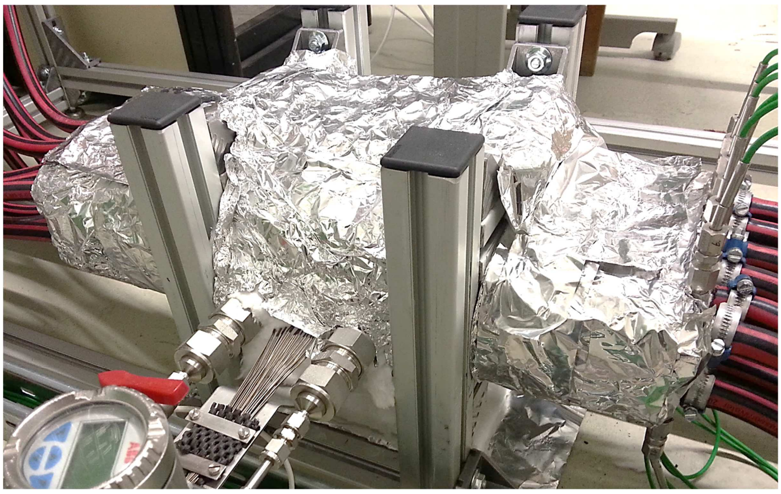

Figure 3.15: Thermal insulation of the PREMUX test box with mineral fiber blanket

3.4 Integration of PREMUX in the air loop L-STAR/LL

3.4.1 The L-STAR/LL air loop

Several air and He loops are available at KIT-INR for fluid-dynamics and component testing (KIT-INR, 2015). Among them, the so-called *Luft–STab, Abstandshalter, und Rauigkeiten*[11] Large Loop, L-STAR/LL (KIT-INR, 2010; KIT-INR, 2015) is a pressurized air loop that originally served as benchmark test rigs for the qualification of CFD codes, which aimed at studying flows over rough surfaces and their heat transfer performance and flow structure, especially designed for nuclear fission reactors. The L-STAR/LL loop (Figure 3.16) is composed by 2 parallel branches with 3 side channel blowers Becker SV 6.690 each (components denoted as LL-CP-*nn* in the bottom-left picture of Figure 3.16, where *nn* refers to the compressor number in that branch). The power of each side channel blower is 18 kW and the system can pump air at a maximum mass flow of 660 g/s at 0.3 MPa of absolute pressure, with air temperatures ranging from < 280 °C and < 390 °C at the inlet and outlet of the attached test section, respectively. The air is supplied by an own pressurized air system at KIT-INR, at a pressure of ~6 bar (gauge). The air of this system contains no oils, has a maximum dew point of –15 °C and a filter Ultrair® FF 0288 SUPERPLUS filters out particles down to a size of 0.01 μm. These 3 characteristics corresponds to an air quality of 141 after the DIN EN ISO 8573-1:2010 (2010).

As the total air mass flow rate required in PREMUX is $2 \times 6 \times 0.003 = 0.036\ kg/s \equiv 36\ g/s$, the available mass flow rate of the loop has been downsized by disabling the branch A (greyed out branch in bottom-left picture in Figure 3.16). After each compression stage in the side channel blowers, the increased air temperature is cooled down with water cooled heat exchangers. The details of the instrumentation and the flow schema of the water cooling loop is given by KIT-INR (2010). The temperature at the inlet and outlet of each compression stage is monitored with K-type thermocouples (denoted by LL-TT-*nn* in the schema of Figure 3.18, where *nn* is the number of the thermocouple in a branch), as well as the absolute pressure of the

---

[11] in English “air-rod, spacer grid and roughness”.

air at the inlet of each compression stage, which is measured gauge pressure transmitters (denoted as LL-PA-*nn* in the schema of Figure 3.18, being *nn* the number of the gauge pressure transmitters in the loop). A differential pressure transmitter measures the pressure drop in the side channel blowers of a branch (LL-PD-1B). The side channel blowers are powered by programmable frequency drives Danfoss VLT 5000. For PREMUX, these devices have been configured to be controlled analogically by a current input signal (4 mA to 20 mA).

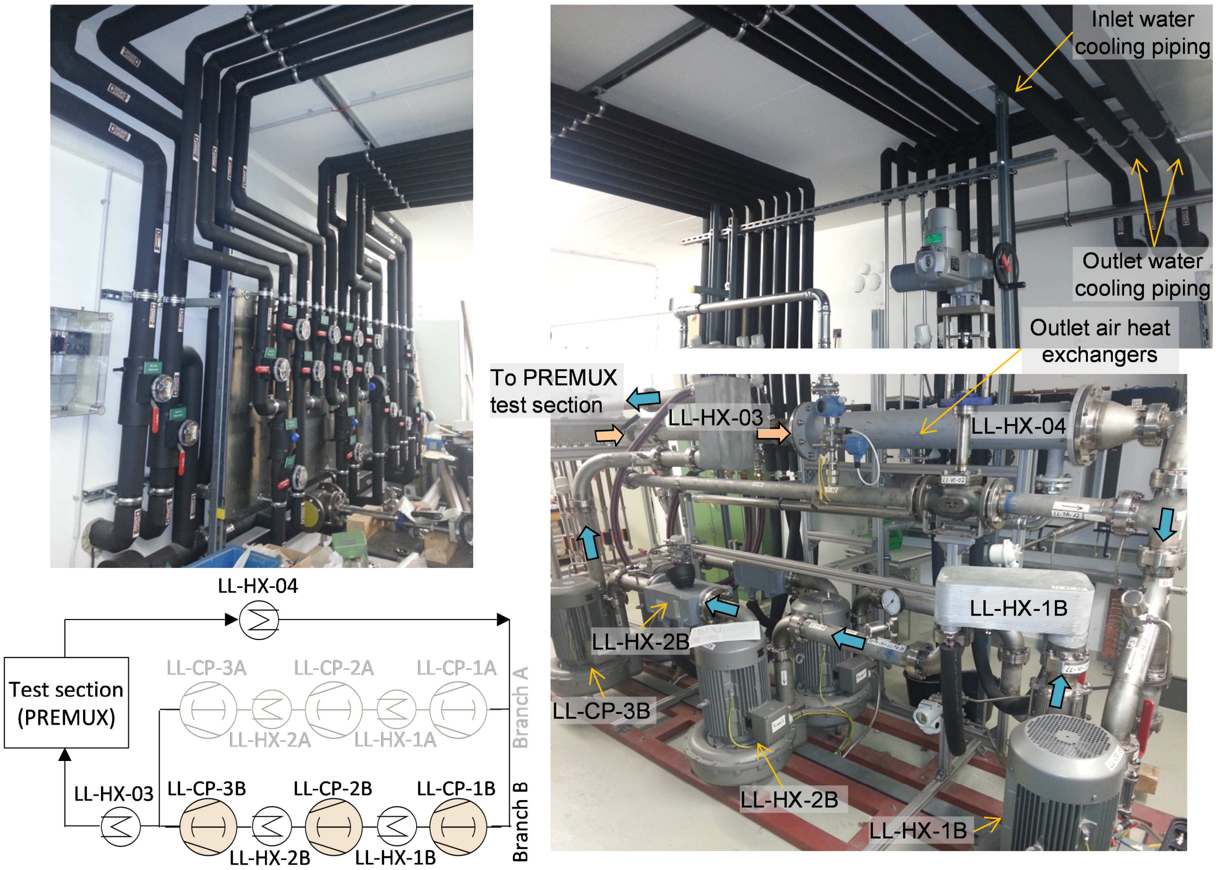

Figure 3.16: L-STAR/LL air loop at KIT-INR. Top-left: water-cooled piping and control valves. Right: L-STAR/LL air loop systems (blue arrows: fresh air, orange arrows: hot air from PREMUX). Bottom-left: simplified schema of the PREMUX test section in the L-STAR/LL loop.

3.4.2 PREMUX ancillary system

All the components that serve as an interface between the test box and the L-STAR/LL loop are included in the *PREMUX ancillary system* a, shown in Figure 3.17. Rubber hoses of ¼” connect the interface pipes of the test box with the ¼” intermediate piping, where outlet and inlet buffer tanks are attached to. These buffer tanks have been developed and manufactured with two purposes: first, as dampening components for eventual pressure peaks that might arise in the air supply system in KIT-INR, and secondly, as air mass flow distributor (at the inlet) or collector (at the outlet) for the cooling channels in the test box. For this second goal and due to the reduced available space in the test room of the L-STAR/LL, the size of the buffer tanks has been designed as a tradeoff between compactness and mass flow distribution steadiness and homogeneity (Hernández et al., 2014).

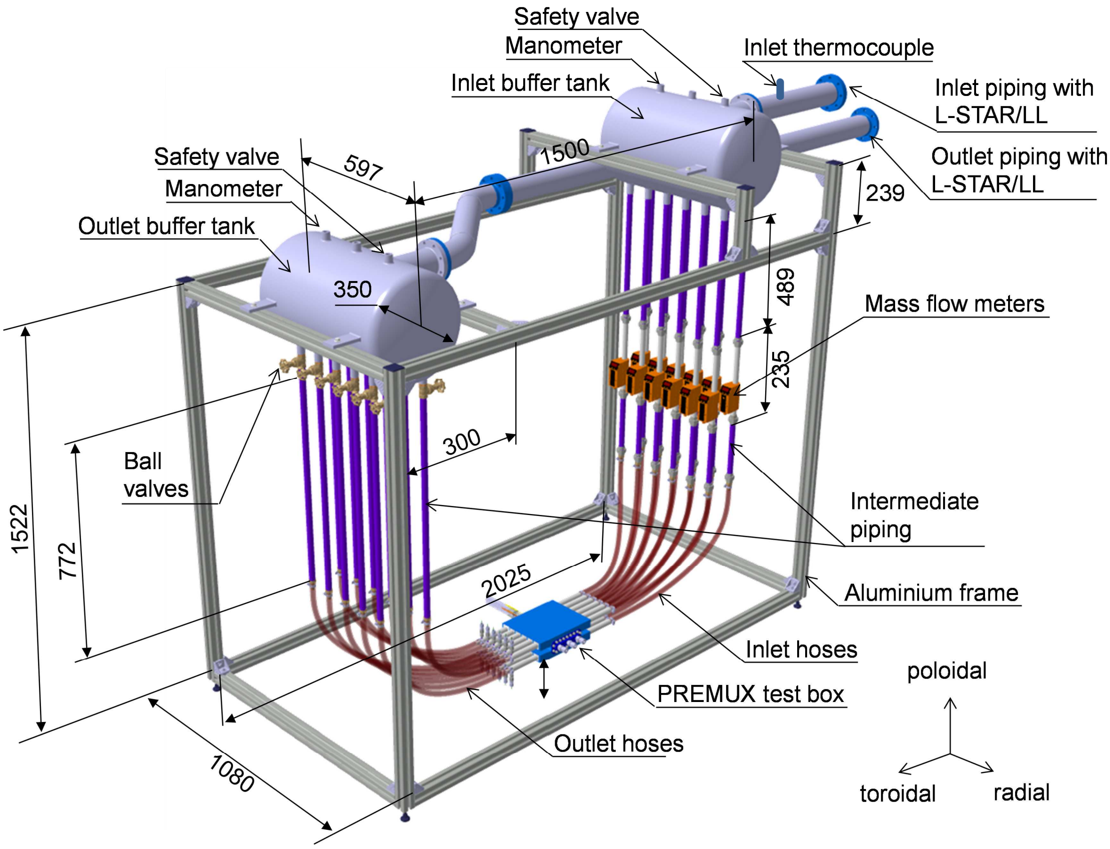

Figure 3.17: PREMUX ancillary components and integated test box

Ball valves connect the outlet buffer tank and each intermediate pipe, serving as a manual mass flow regulation for each cooling channel of the test section. The installation of these valves downstream the PREMUX test box instead of upstream is performed in order to avoid disturbances induced by these components in the air flow. After the inlet buffer tanks, calorimetric flow meters IFM Efector 300 SD6000 are installed. The length of the intermediate piping upstream the flow meters is about 30 times the inner diameter of these pipes, so as to maximize the flow development at the entrance of these flow meters. A safety valve in the L-STAR/LL loop, as well as in the outlet buffer tank have been installed, which are activated in case the air pressure surpasses 0.3 MPa.

A thermocouple has been installed at the inlet of the ancillary system (designated as LL-TT-02), which represents the inlet temperature of the air coolant in the PREMUX test box. A gauge pressure transmitter is placed on the inlet buffer tank (designation TS-PA-01), as well as manometers and a differential pressure transmitted between the inlet and outlet buffer tanks (designation TS-PD-01). The whole system is supported on a Bosch 45 × 45H aluminum structure, as shown in Figure 3.17.

3.4.3 PREMUX integration in L-STAR/LL

The complete schema summarizing the integrated PREMUX and L-STAR/LL experimental set-up is provided in Figure 3.18.

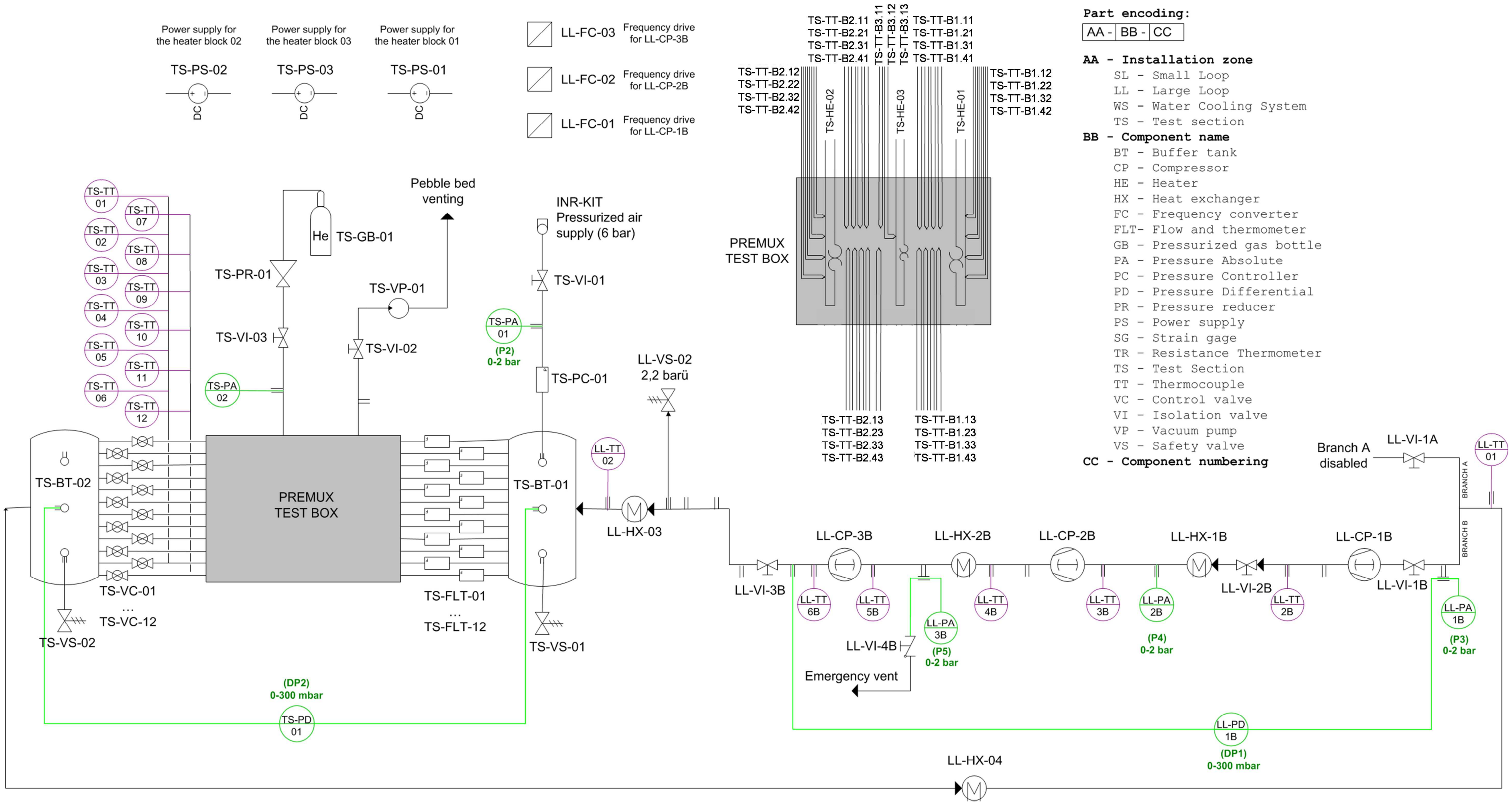

Figure 3.18: Schema of the integrated PREMUX−L-STAR/LL experimental set-up, with a detail of the test box measurement instrumentation.

The complete experimental facility during an experimental run is shown in Figure 3.19.

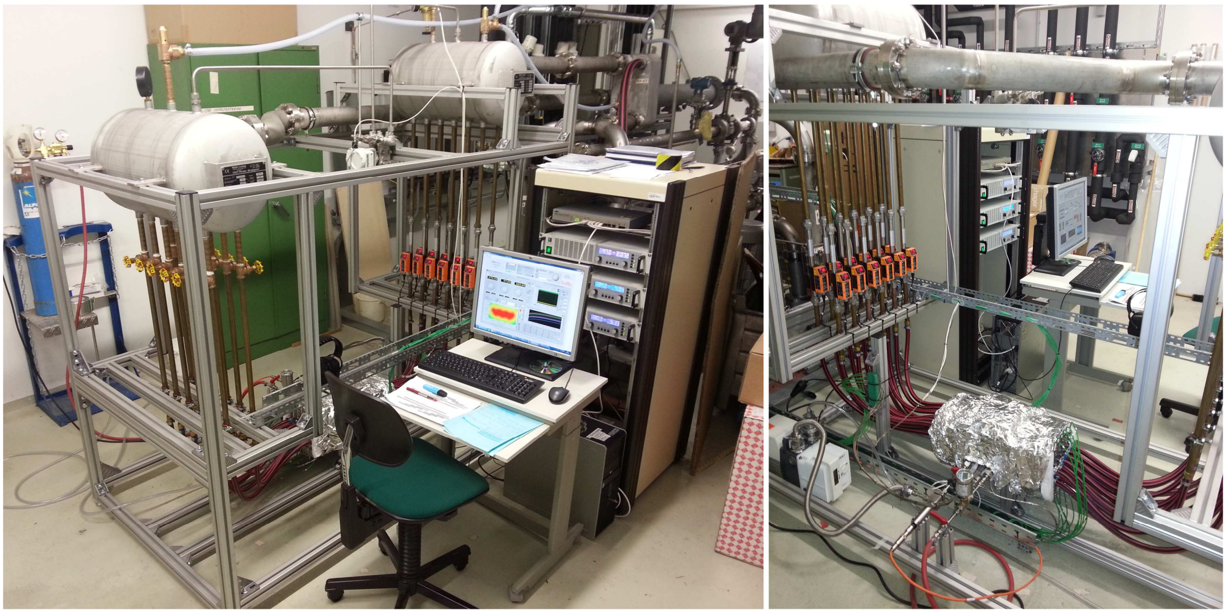

Figure 3.19: Pictures of the integrated PREMUX−L-STAR/LL experimental set-up. Left: general view of the set-up during an experimental run. Right: especific view of the PREMUX test box and ancillary system during an experimental run.

3.5 Data acquisition system and development of a Control Toolbox for the PREMUX testing campaign

3.5.1 Data acquisition system

3.5.2 Development of a Control Toolbox software for PREMUX

For the control, monitoring and data logging of the measurements acquired in PREMUX, a dedicated program, namely *PREMUX Control Toolbox*, has been developed with Labview 2012 (Hernández et al., 2014). This program has been coded modularly, so that it can be expanded to control more than 3 heater blocks, for instance in the case of a full-scale HCPB Breeder Unit mock-up experimental campaign.

The Control Toolbox consists of 3 main panels. In the first one (Figure 3.20-top left), the heater control and data acquisition of the Li_4SiO_4 pebble bed temperatures is performed. With these temperatures, a real time reconstruction of the temperature distribution in the pebble bed is executed in the Control Toolbox.

Four algorithms are available in Labview 2012 for the interpolation of scattered data as the one in the measuring plane of PREMUX, namely the nearest neighbour (Okabe et al., 2000), linear (Watson and Philip, 1984), cubic (Watson, 1992) and biharmonic spline interpolation (Sandwell, 1987).

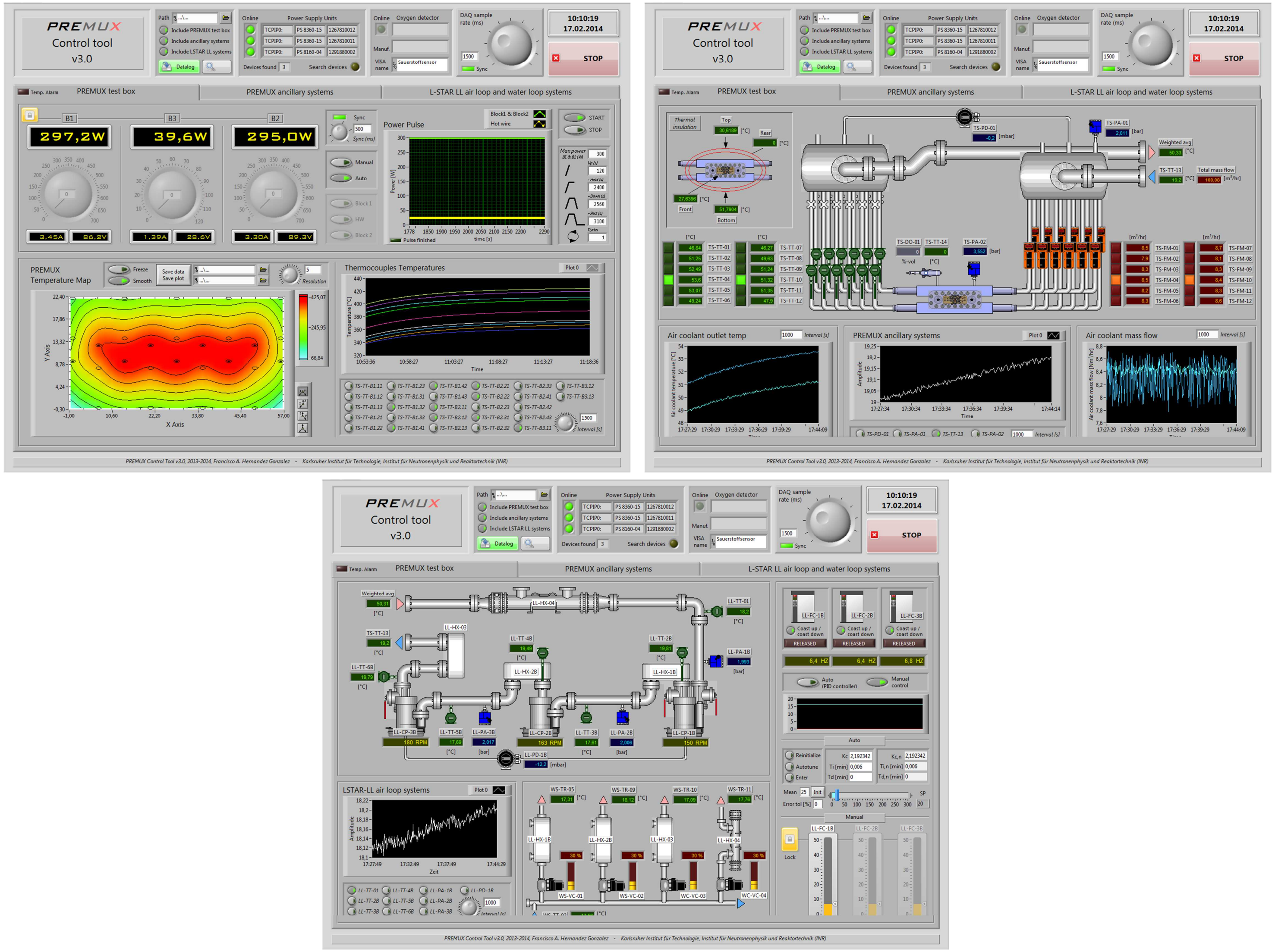

Figure 3.20: PREMUX Control Toolbox software created with Labview. Top left: panel for the heater control and data acquisition of the pebble bed tempeartures. Top right: panel for the ancillary system. Bottom: L-STAR/LL monitoring and side channel blowers control with the frequency drives.

The first three are based on triangulation schemes, while the biharmonic spline is based on the use of a radial basis function. From the triangulation schemes, the best performing is the cubic one (Foster and Evans, 2008). The biharmonic spline interpolation performs similarly to the cubic scheme, but it requires: (1) the data originates from a smooth function and (2) that the data points to interpolate are not too close to each other. As the pebble bed thermal conductivity is a linear function of the temperature and, in lesser degree, of the volumetric plastic strain (Reiman and Hermsmeyer, 2002a), the solution to the heat equation in the pebble bed can be expressed with smooth functions, meeting the condition (1). On the other side, the 27 data points corresponding to the 27 thermocouples in the pebble bed are relatively sparse and homogeneously distributed through the measuring plane, meeting the condition (2).

Therefore, as the biharmonic spline interpolation is computationally more efficient than the cubic scheme (Foster and Evans, 2008), it is more suitable for a real time application like the one in the PREMUX Control Toolbox with a fair number of interpolation locations. As an example, the biharmonic interpolation has run smoothly interpolating a grid of 55×35 points at a sample rate of 500 ms. The details on the biharmonic spline interpolation, which are used along this Thesis for the visualization of the temperature distribution reconstruction in the pebble bed is covered in the Apendix D.

The heater system control can be executed either in manual or automatic mode. In the manual mode, each heater block current is controlled via direct user input. In the automatic mode, the program executes ITER-like power pulses. Here, the user specifies first the characteristics of the pulse, i.e. the ramp-up, flat-top, ramp-down and dwell-times, together with the maximum power level at the flat-top time and the number of pulses to execute.

The second panel of the Control Toolbox (Figure 3.20-top right) is dedicated to the monitoring of the ancillary system, which comprises the air coolant temperature inlet and outlet from each interface pipe at the PREMUX test box, the mass flow distribution at each cooling channel, air absolute pressure and the inlet and outlet and absolute pressure of the stagnant He purge gas in the pebble bed.

The third panel (Figure 3.20-bottom) is dedicated to the monitoring of the L-STAR/LL systems. This consist on the data acquisition of the air coolant temperatures and (absolute) pressures and the water cooling temperatures as indicated in the chart in Figure 3.18. The control of the side channel blowers is executed by a current controlled input at the frequency drives. An option for the automatic control of the side channel blowers has been implemented in the Control Toolbox. This automatic control aims at maintaining a constant pressure drop in the ancillary system for a better regulation of the mass flow in each cooling channel of the test section via a PID controller. However, this option has not been needed in PREMUX and the cooling channels mass flow could be regulated by setting manually the corresponding current to the frequency drives so as to obtain the desired total mass flow in the test section.

Chapter 4

Testing campaign and experimental results with PREMUX

In order to proof the functionality of the new developed heater system, two types of experiments have been performed. The first aims at evaluating the capability of the heater system to reproduce and measure the temperature profile of the pebble bed at several steady state relevant ITER power load conditions. The experimental results obtained with this first type of experiments are presented here and will be used as well as benchmark data for the validation of the thermo-mechanical models developed in the next Chapter. The second type of experiments aims at qualifying the heaters by reproducing relevant neutronic volumetric heating from the ITER transient pulses. Additional tests have been performed as well, on the one side, for the determination of the Li_4SiO_4 pebble bed thermal conductivity at room temperature with the hot wire method and, on the other side, for benchmarking the influence of the purge gas pressure on the pebble bed temperature. The Chapter ends with a discussion on the experimental results of each of the tests performed with PREMUX.

4.1 Design of the experimental matrix

4.1.1 Steady state power runs

For the chosen area of interest of the HCPB Breeder Unit (Figure 3.3), a total heating power of $623\ W + 547\ W = 1170\ W$ (Figure 3.1, picture c)) is required. Therefore, one (single core) heater block must be able to produce then at least 623 W. In terms of surface heating, that represents 9.2 W/cm^2, taking into account the heater data given in Section 3.3, which is still below the manufacturer limit of 10 W/cm^2. However, a power closer to this limit, 9.7 W/cm^2, has been applied for the proof-of-concept tests for reliability reasons, reaching a total heating power of ~1360 W, distributed in the 2 single core and the 1 twin core heating blocks. This power level will be tagged as “very high” (VHI) within this work.

From this VHI power level, other 4 levels, labeled as “high” (HI), “medium” (MED), “low” (LO) and “very low” (VLO) have been defined for the steady state, decreasing in power by about 200 W to 300 W: ~1130 W (HI), ~920 W (MED), ~595 W (LO) and ~290 W (VLO).

As defined in Section 3.3.2, in all experimental runs the air coolant mass flow of all cooling channels of the PREMUX test box has been maintained to 0,003 kg/s. The inlet air coolant temperature has been ~20 $°C$ and the purge gas pressure (at the steady state) has been ~4 bar.

The experimental matrix of the steady state runs are based on the finding of Dalle Donne et al. (2000). These authors established the following linear relationship for the effective thermal conductivity of the reference Li_4SiO_4 pebble beds, $k_{eff}^{Li_4SiO_4}$, as function of the pebble bed local temperature T:

$$k_{eff}^{Li_4SiO_4}(T) = 0.768 + 4.96 \times 10^{-4} \cdot T \ , \tag{4.1}$$

where $k_{eff}^{Li_4SiO_4}$ and T are expressed in $W/(mK)$ and $°C$ respectively. The expression above has been generalized by Reimann and Hermsmeyer (2002a) including the effect of the volumetric inelastic strain of the bed ε_{vol}^{in} (expressed in %):

$$k_{eff}^{Li_4SiO_4}(T, \varepsilon_{vol}^{in}) = 0.768 + 4.96 \cdot 10^{-4} T + 0.045 \varepsilon_{vol}^{in} \ . \tag{4.2}$$

It can be noticed that the effect of the ε_{vol}^{in} in the thermal conductivity for this pebble bed is very small, thus allowing the treatment of the Li_4SiO_4 pebble bed independent from the stress-state of this pebble bed. Given this result, 6 experimental runs for each power level have been performed randomly. The ramp-up time has been 120 s and the quasi-steady states have been reached at about 4100 s (VHI), 3700 s (HI), 3600 s (MED), 2600 s (LO) and 2300 s (VLO). The quasi-steady state condition has been considered when the increment in the highest temperature measurement has been slower than 0.1 °C/min. In order to determine the steady state temperatures, a statistical procedure has been used and incorporated to the so-called *uncertainty budget* (Taylor and Kuyat, 1994) of the measurements, as described in Section 4.2.

4.1.2 Transient power runs

While the steady state experimental runs build a database for the validation of numerical predictive tools, they are not enough to complete the proof of the concept, as the heating cycles are not relevant to those in ITER. In order to verify the performance of the heaters also by reproducing the relatively fast transient ramp-ups of ITER, 3 consecutive heating cycles have been completed in PREMUX at the VHI power condition. Beginning from an initial pebble bed temperature of 50°C, 3 ITER-like power transients have been performed, which consist of a 30 s heating ramp-up to a VHI power level, 430 s of flat top corresponding to the plasma burn-up phase at VHI condition, 60 s of burn-termination-like ramp-down to the initial power conditions (0 W) and 510 s “dwell time” until the next pulse begins.

4.1.3 Additional tests

Runs for the determination of the thermal conductivity at room temperature of the Li_4SiO_4 pebble bed

In order to determine the effective thermal conductivity of the Li_4SiO_4 pebble bed at room temperature, Hot-Wire Method tests (Enoeda et al., 1998) have been conducted. This experimental campaign aims at verifying indirectly that other factors like purge gas composition in the pebble bed and that the packing factor of the bed are in the expected range by comparing the measured effective thermal conductivity of the Li_4SiO_4 pebble bed in PREMUX with the values of the literature (Reimann et al., 2006b). For this experimental campaign, 5 runs have been performed at a pebble bed temperature of ~30 *°C* with a very low power input (heating power ~9 *W*) for 120 *s*.

Runs for the determination of the influence of the purge gas pressure in the temperature of the Li_4SiO_4 pebble bed

Reimann and Hermsmeyer (2002a) stated that the influence of the purge gas pressure in the pebble bed thermal conductivity is negligible. The assessment of this influence has been evaluated in a dedicated additional experimental campaign. The steady state run performed at HI power level and 4 *bar* has been performed again here at 2 *bar* with 3 repetitions. The resulting temperature distributions of the Li_4SiO_4 pebble bed are then compared to each other, in order give an additional support to the observation of Reimann and Hermsmeyer with a relevant part of a HCPB Breeder Unit mock-up.

4.2 Evaluation of the experimental uncertainty

For each measured magnitude of interest in PREMUX, different error sources have been identified and their associated standard uncertainty classified in 2 categories: type A and type B.

The type A standard uncertainties are defined as those *"based on any valid statistical method for treating data"* (Taylor and Kuyat, 1994). In the case of the temperature measurements in the pebble bed, preliminary steady state experimental runs have demonstrated that steady state conditions cannot be reached during reasonably long test run durations (< 5000 s). Due to the relatively large amount of experimental runs to be performed, a quasi-steady state condition has been defined instead, as described in Section 5.1.1. The estimation of the steady state temperatures are then determined by evaluating the temperature at $t \to \infty$ from a nonlinear fitting of those quasi-steady state temperature measurements. This approach assumes that the involved physics are continuous, differentiable for all the independent parameters, meaning that there are not sudden bifurcations, such as laminar-turbulent transitions, buoyant to mixed convection, time-dependent oscillatory system behavour, etc.

The estimation of the uncertainties with a coverage factor of 2 (2σ) are as well determined by evaluating the 95% prediction interval of these nonlinear regression fittings at $t \to \infty$: these 95% prediction intervals conform the type A standard uncertainty for the PREMUX steady state temperatures. This procedure has been utilized as well to determine the type A standard uncertainty of the outlet air coolant temperatures.

Contrarily, the coolant inlet and the flow rate are constant in average during the experimental runs and their type A standard uncertainties are determined by simpler statistical analysis, i.e. by a summation in quadrature of the standard deviations, assuming that every experimental run has the same population's variance.

The type B standard uncertainties are those that are determined by other methods than statistical analysis (Taylor and Kuyat, 1994). In the present work, the accuracy of the measurement instruments, the data acquisition system, instruments calibration reports and measurement resolution errors are considered in this group.

Both type A and B standard uncertainties are thereafter integrated into the uncertainty budget and a combined expanded uncertainty is then calculated following the ISO guide to the expression of uncertainty in measurement (ISO/IEC Guide 98-3:2008, 2008), taking into account a coverage factor to account for a confidence of 95%.

4.2.1 Type A standard uncertainty

Measurements with time-evolving expected value

The estimation of the steady state temperatures from the quasi-steady state temperature measurements have been determined by nonlinear regression for the pebble bed and the coolant outlet temperatures. For each thermocouple (TC) measurement at a power level P, $T_{TC,P}$, all 6 experimental runs have been plotted against the time and the curve

$$T_{TC,P}(t;\boldsymbol{\theta}^{TC,P}) = \theta_1^{TC,P}\left[1 - \frac{t}{\theta_2^{TC,P}} e^{-\left(\frac{t}{\theta_3^{TC,P}}\right)^{\theta_4^{TC,P}}}\right] + \varepsilon_0 \ , \tag{4.3}$$

has been fitted, being $\varepsilon_0 \sim N(0,\sigma^2)$ the random errors and $\theta_1^{TC,P}$, $\theta_2^{TC,P}$, $\theta_3^{TC,P}$ and $\theta_4^{TC,P}$ the set of curve fitting parameters for each measurement and power level. The adjusted R^2 is better than 98% with the exception only for the VLO power level, where the fitting is slightly lower (min 90%). From Eqn. (4.3), it can be observed that at $t \to \infty$, the steady state temperature $T_{TC}(\infty;\boldsymbol{\theta}^{TC,P}) = \theta_1^{TC,P}$.

As it has been introduced in the previous section, the prediction interval of the steady state temperature at $t \to \infty$ constitutes the type A error of $T_{TC}(\infty;\boldsymbol{\theta}^{TC,P})$, which is to be included in the uncertainty budget of the temperature measurement. Naming $\hat{T}_{TC,P}$ and $\hat{\boldsymbol{\theta}}^{TC,P}$ as the estimation of $T_{TC,P}$ and $\boldsymbol{\theta}^{TC,P}$ respectively, the Taylor series expansion of $T_{TC,P}(t;\boldsymbol{\theta}^{TC,P})$ ($\mathcal{T}[T_{TC,P}]$) around a point $t = t_0$ reads:

$$\mathcal{T}[T_{TC,P}] = \hat{T}_{TC,P} \approx T_{TC,P} + \left.\frac{\partial T_{TC,P}}{\partial \boldsymbol{\theta}^{TC,P}}\right|_{t=t_0} \left(\hat{\boldsymbol{\theta}}^{TC,P} - \boldsymbol{\theta}^{TC,P}\right), \tag{4.4}$$

where

$$\left.\frac{\partial T_{TC,P}}{\partial \boldsymbol{\theta}^{TC,P}}\right|_{t=t_0} = \left.\begin{pmatrix} \dfrac{\partial T_{TC,P}}{\partial \theta_1^{TC,P}} \\ \cdots \\ \dfrac{\partial T_{TC,P}}{\partial \theta_p^{TC,P}} \end{pmatrix}\right|_{t=t_0} . \tag{4.5}$$

It has to be noted that $\hat{T}_{TC,P} - T_{TC,P} \approx 0$ when the number m of samples is large, as it is in PREMUX (~10^4 when all 6 measurements for a $T_{TC,P}$ are combined). Therefore,

$$\begin{aligned} T_{TC,P} - \hat{T}_{TC,P} &\approx T_{TC,P} - \left(T_{TC,P} + \left.\frac{\partial T_{TC,P}}{\partial \boldsymbol{\theta}^{TC,P}}\right|_{t=t_0} \left(\hat{\boldsymbol{\theta}}^{Bz.xy,P} - \boldsymbol{\theta}^{TC,P}\right)\right) \\ &= \varepsilon_0 - \left.\frac{\partial T_{TC,P}}{\partial \boldsymbol{\theta}^{TC,P}}\right|_{t=t_0} \left(\hat{\boldsymbol{\theta}}^{TC,P} - \boldsymbol{\theta}^{TC,P}\right) . \end{aligned} \tag{4.6}$$

The estimated value of $T_{TC,P} - \hat{T}_{TC,P}$ reads

$$E\big(T_{TC,P} - \hat{T}_{TC,P}\big) \approx E(\varepsilon_0) - \left.\frac{\partial T_{TC,P}}{\partial \boldsymbol{\theta}^{TC,P}}\right|_{t=t_0} E\Big(\hat{\boldsymbol{\theta}}^{TC,P} - \boldsymbol{\theta}^{TC,P}\Big) = 0 \ , \tag{4.7}$$

and its variance is

$$\begin{aligned} V\big(T_{TC,P} - \hat{T}_{TC,P}\big) &\approx V(\varepsilon_0) - V\left(\left.\frac{\partial T_{TC,P}}{\partial \boldsymbol{\theta}^{TC,P}}\right|_{t=t_0} \left(\hat{\boldsymbol{\theta}}^{TC,P} - \boldsymbol{\theta}^{TC,P}\right)\right) \\ &= \sigma^2 + \sigma^2 \left(\left.\frac{\partial T_{TC,P}}{\partial \boldsymbol{\theta}^{TC,P}}\right|_{t=t_0}\right)^T [F(\boldsymbol{\theta}^{TC,P})^T F(\boldsymbol{\theta}^{TC,P})]^{-1} \left.\frac{\partial T_{TC,P}}{\partial \boldsymbol{\theta}^{TC,P}}\right|_{t=t_0} \\ &= \sigma^2 \left[1 + \left(\left.\frac{\partial T_{TC,P}}{\partial \boldsymbol{\theta}^{TC,P}}\right|_{t=t_0}\right)^T [F(\boldsymbol{\theta}^{TC,P})^T F(\boldsymbol{\theta}^{TC,P})]^{-1} \left.\frac{\partial T_{TC,P}}{\partial \boldsymbol{\theta}^{TC,P}}\right|_{t=t_0} \right], \end{aligned} \tag{4.8}$$

with

$$F(\boldsymbol{\theta}^{TC,P}) = \begin{bmatrix} \left.\dfrac{\partial T_{TC,P}}{\partial \theta_1^{TC,P}}\right|_{t=t_1} & \cdots & \left.\dfrac{\partial T_{TC,P}}{\partial \theta_p^{TC,P}}\right|_{t=t_1} \\ \vdots & \ddots & \vdots \\ \left.\dfrac{\partial T_{TC,P}}{\partial \theta_1^{TC,P}}\right|_{t=t_m} & \cdots & \left.\dfrac{\partial T_{TC,P}}{\partial \theta_p^{TC,P}}\right|_{t=t_m} \end{bmatrix} . \tag{4.9}$$

Naming $A(\boldsymbol{\theta}^{TC,P}) = F(\boldsymbol{\theta}^{TC,P})^T F(\boldsymbol{\theta}^{TC,P}) = A$ and considering Eqs (4.7) and (4.8), the distribution of $T_{TC,P} - \hat{T}_{TC,P}$ reads:

$$T_{TC,P} - \hat{T}_{TC,P} \sim N_A \left(0, \sigma^2 \left[1 + \left(\left.\frac{\partial T_{TC,P}}{\partial \boldsymbol{\theta}^{TC,P}}\right|_{t=t_0}\right)^T A^{-1} \left.\frac{\partial T_{TC,P}}{\partial \boldsymbol{\theta}^{TC,P}}\right|_{t=t_0} \right]\right), \tag{4.10}$$

where N_A denotes that $T_{TC,P} - \hat{T}_{TC,P}$ is asymptotically normal.

As the root mean square error s of the nonlinear regression is an unbiased estimator of σ and it is asymptotically independent of $\hat{\boldsymbol{\theta}}^{TC,P}$, then Eqn (4.10) can be rewritten as:

$$\frac{T_{TC,P} - \hat{T}_{TC,P}}{s \sqrt{1 + \left(\left.\dfrac{\partial T_{TC,P}}{\partial \hat{\boldsymbol{\theta}}^{TC,P}}\right|_{t=t_0}\right)^T A\big(\hat{\boldsymbol{\theta}}^{TC,P}\big)^{-1} \left.\dfrac{\partial T_{TC,P}}{\partial \hat{\boldsymbol{\theta}}^{TC,P}}\right|_{t=t_0}}} \sim \text{asymp. } t_{1-\alpha,m-p} \ , \tag{4.11}$$

where p the number of parameters of the nonlinear regression model, (here, $p = 4$) and $t_{1-\alpha,m-p}$ is the t-Student distribution with $m - p$ degrees of freedom at a statistical significance of α.

Hence, the asymptotic 95% prediction interval for $\hat{T}_{TC,P}\left(t_0; \hat{\boldsymbol{\theta}}^{TC,P}\right)$ reads:

$$t_{95\%,m-4}\, s \sqrt{1 + \left(\left.\frac{\partial T_{TC,P}}{\partial \hat{\boldsymbol{\theta}}^{TC,P}}\right|_{t=t_0}\right)^T A(\boldsymbol{\theta}^{TC,P})^{-1} \left.\frac{\partial T_{TC,P}}{\partial \hat{\boldsymbol{\theta}}^{TC,P}}\right|_{t=t_0}} \,. \tag{4.12}$$

Only the temperatures and uncertainty estimations in the steady state are of interest here. Taking into account the expression of $T_{TC,P}$ in Eqn. (4.3), the derivatives of $T_{TC,P}\left(t_0; \hat{\boldsymbol{\theta}}^{TC,P}\right)$ evaluated at $t = t_0 \to \infty$ in Eqn (4.5) are:

$$\left.\frac{\partial T_{TC,P}}{\partial \hat{\boldsymbol{\theta}}^{TC,P}}\right|_{t=\infty} = \left.\begin{pmatrix} 1 - \dfrac{t}{\theta_2^{TC,P}} e^{-\left(\frac{t}{\theta_3^{TC,P}}\right)^{\theta_4^{TC,P}}} \\ \dfrac{\theta_1^{TC,P}}{\left(\theta_2^{TC,P}\right)^2} t\, e^{-\left(\frac{t}{\theta_3^{TC,P}}\right)^{\theta_4^{TC,P}}} \\ \left(\dfrac{t}{\theta_3^{TC,P}}\right)^{\theta_4^{TC,P}} \dfrac{\theta_1^{TC,P}}{\theta_2^{TC,P}} t \ln\left(\dfrac{t}{\theta_3^{TC,P}}\right) e^{-\left(\frac{t}{\theta_3^{TC,P}}\right)^{\theta_4^{TC,P}}} \\ -\left(\dfrac{t}{\theta_3^{TC,P}}\right)^{\theta_4^{TC,P}} e^{-\left(\frac{t}{\theta_3^{TC,P}}\right)^{\theta_4^{TC,P}}} t\, \dfrac{\theta_1^{TC,P}\theta_4^{TC,P}}{\theta_3^{TC,P}\theta_2^{TC,P}} \end{pmatrix}\right|_{t=\infty} = \begin{pmatrix} 1 \\ 0 \\ 0 \\ 0 \end{pmatrix}, \tag{4.13}$$

and the matrix $A(\boldsymbol{\theta}^{TC,P}) = a_{ij}(\boldsymbol{\theta}^{TC,P}) = F(\boldsymbol{\theta}^{TC,P})^T F(\boldsymbol{\theta}^{TC,P})$ reads

$$\begin{aligned} & A(\boldsymbol{\theta}^{TC,P}) = F(\boldsymbol{\theta}^{TC,P})^T F(\boldsymbol{\theta}^{TC,P}) = \\ & = \begin{bmatrix} \left.\dfrac{\partial T_{TC,P}}{\partial \theta_1^{TC,P}}\right|_{t=t_1} & \cdots & \left.\dfrac{\partial T_{TC,P}}{\partial \theta_1^{TC,P}}\right|_{t=t_m} \\ \vdots & \ddots & \vdots \\ \left.\dfrac{\partial T_{TC,P}}{\partial \theta_p^{TC,P}}\right|_{t=t_1} & \cdots & \left.\dfrac{\partial T_{TC,P}}{\partial \theta_p^{TC,P}}\right|_{t=t_m} \end{bmatrix} \begin{bmatrix} \left.\dfrac{\partial T_{TC,P}}{\partial \theta_1^{TC,P}}\right|_{t=t_1} & \cdots & \left.\dfrac{\partial T_{TC,P}}{\partial \theta_p^{TC,P}}\right|_{t=t_1} \\ \vdots & \ddots & \vdots \\ \left.\dfrac{\partial T_{TC,P}}{\partial \theta_1^{TC,P}}\right|_{t=t_m} & \cdots & \left.\dfrac{\partial T_{TC,P}}{\partial \theta_p^{TC,P}}\right|_{t=t_m} \end{bmatrix} \\ & = \begin{bmatrix} \displaystyle\sum_{i=1}^m \left(\left.\frac{\partial T_{TC,P}}{\partial \theta_1^{TC,P}}\right|_{t=t_i}\right)^2 & \cdots & \displaystyle\sum_{i=1}^m \left(\left.\frac{\partial T_{TC,P}}{\partial \theta_1^{TC,P}} \frac{\partial T_{TC,P}}{\partial \theta_p^{TC,P}}\right|_{t=t_i}\right) \\ \vdots & \ddots & \vdots \\ \displaystyle\sum_{i=1}^m \left(\left.\frac{\partial T_{TC,P}}{\partial \theta_p^{TC,P}} \frac{\partial T_{TC,P}}{\partial \theta_1^{TC,P}}\right|_{t=t_i}\right) & \cdots & \displaystyle\sum_{i=1}^m \left(\left.\frac{\partial T_{TC,P}}{\partial \theta_p^{TC,P}}\right|_{t=t_i}\right)^2 \end{bmatrix}. \end{aligned} \tag{4.14}$$

Considering Eqn. (4.13) and (4.14), the prediction interval for $\hat{T}_{TC,P}\left(\infty; \hat{\boldsymbol{\theta}}^{TC,P}\right)$ of Eqn. (4.12) reads:

$$t_{95\%,m-4}s\sqrt{1+\begin{pmatrix}1\\0\\0\\0\end{pmatrix}^T a_{ij}(\boldsymbol{\theta}^{TC,P})^{-1}\begin{pmatrix}1\\0\\0\\0\end{pmatrix}} = t_{95\%,m-4}s\sqrt{1+\frac{1}{a_{11}(\boldsymbol{\theta}^{TC,P})}} \ . \qquad (4.15)$$

Given that the number of samples m is large, then $\frac{1}{a_{11}(\boldsymbol{\theta}^{TC,P})} \cong 0$ and $t_{95\%,m-4} \cong 1.96$. Therefore, the temperature measurement estimation of the steady state with an expanded uncertainty of 95% confidence reads:

$$\hat{T}_{TC,P}\left(\infty;\hat{\boldsymbol{\theta}}^{TC,P}\right) = \hat{\theta}_1^{TC,P} \pm 1.96s \ , \qquad (4.16)$$

being the root mean square error s of the nonlinear regression the standard uncertainty of the steady state temperature measurements, i.e. $u\left(\hat{T}_{TC,P}\left(\infty;\hat{\boldsymbol{\theta}}^{TC,P}\right)\right) = s$.

Measurements with constant expected value in time

In this group, for each experimental run at a power level P, a measurement with an instrument I, $M_{I,P}$, is constant in time. Let $E(M_{I,P}) = \overline{M}_{I,P}$ be the mean of $M_{I,P}$ obtained after n_O number of observations, with $O = 1, \dots, r$ test runs. Then, the pooled average $\overline{M}_{I,pool}$ for all the experimental runs is calculated as:

$$\overline{M}_{I,pool} = \frac{\sum_{P=1}^{r} n_O \overline{M}_{I,P}}{\sum_{P=1}^{r} n_O} \ . \qquad (4.17)$$

On the other side, let $V(M_{I,P}) = \sigma_{M_{I,P}}^2$ be the variance of $M_{I,P}$. The unbiased estimator of $\sigma_{M_{I,P}}^2$ is its standard deviation $s_{M_{I,P}}^2$. Then, the pooled standard deviation of all the test runs is estimated as (Coleman & Steele, 2009):

$$s_{M_{I,pool}}^2 = \frac{\sum_{P=1}^{r} (n_P - 1) s_{M_{I,P}}^2}{\sum_{P=1}^{r} n_P - r} \ , \qquad (4.18)$$

considering equal population's variances for each experimental run. Therefore, the standard uncertainty of a measurement M_I is estimated by $s_{M_{I,pool}}$, i.e. $u(M_I) = s_{M_{I,pool}}$.

4.2.2 Type B standard uncertainty

Type B standard uncertainty encompasses all uncertainties that cannot be classified as type A. In the case of PREMUX, the following type B sources of uncertainty for the temperature measurements are considered:

- Data acquisition measurement error of the NI9214 module;
- Accuracy of the K-type thermocouples;
- Resolution of the measurement.

The uncertainty source in the measurement because of positioning errors of the thermocouples is assumed to be negligible due to the knowledge of the thermocouple location with an accuracy of at least 0.02 *mm*, as indicated in Section 3.3.1.

For the measurements of the air coolant mass flow with the calorimetric flow meters, the following type B uncertainty sources are considered:

- Instrument calibration
- Accuracy of the flow meters
- Resolution of the measurement
- Data acquisition measurement error of the NI9203 module;

According to the ISO/IEC Guide 98-3:2008 (2008), the associated uncertainty for the aforementioned uncertainty sources is computed by means of their accuracy. Let $a_{E_i}^{-}$ and $a_{E_i}^{+}$ be the lower and upper limits of the accuracy for a source of experimental error E_i. Then, for the uncertainties originated by sources with unknown parent distribution and equal likelihood for any value of the distribution, it is assumed that their parent distribution is a uniform distribution of limits $\left[a_{E_i}^{-}, a_{E_i}^{+}\right]$ as a conservative approach and the standard uncertainty is calculated as $u(E_i) = \left|a_{E_i}^{-}\right|/\sqrt{3}$ (e.g. accuracy and NI module's measurement error). For error sources with unknown parent distribution but with known most likely value, a triangular distribution is assumed and the standard uncertainty is in this case computed as $u(E_i) = \left|a_{E_i}^{-}\right|/6$ (e.g. resolution error sources).

4.2.3 Combined standard and expanded uncertainties

For a generic measurement M, once all N_A associated type A standard uncertainties u_{M,A_i} and all N_B associated B standard uncertainties u_{M,B_i} are determined, they are all to be integrated in a combined standard uncertainty as:

$$u_M = \sqrt{\sum_{A_i=1}^{N_A} u_{M,A_i}^2 + \sum_{B_i=1}^{N_B} u_{M,B_i}^2} \; . \tag{4.19}$$

In case a measured quantity M is to be obtained by means of a data reduction equation $r(\boldsymbol{x}) = r(x_1, \dots, x_i, \dots, x_m)$, (e.g. the mass flow rate by measuring a normalized –volumetric– flow rate), with $\boldsymbol{x}$ a vector of internal variables to be directly measured, u_X has been then determined by means of the Taylor Series Method (TSM) for propagation of uncertainties (Coleman & Steele, 2009) as:

$$u_M = \sqrt{\sum_{A_i=1}^{N_A} \left(\frac{\partial r}{\partial x_i}\right)^2 u_{x_i,A_i}^2 + \sum_{B_i=1}^{N_B} \left(\frac{\partial r}{\partial x_i}\right)^2 u_{x_i,B_i}^2} \; . \tag{4.20}$$

With a standard uncertainty, the measurement M can be expressed as $M \pm u_M$. However, in order to take into account a certain confidence level, an expanded uncertainty U_M is provided in all the experimental results in this work, calculated as:

$$U_M = k_{\%} u_M \; . \tag{4.21}$$

where $k_{\%}$ is a coverage factor, which is a function of the confidence wanted for the uncertainty, in practice approximated by a t-Student distribution (Coleman & Steele, 2009). In this context, a confidence of 95% has been assumed for the expression of the uncertainties, which corresponds to $k_{\%} \approx 2$.

4.3 Experimental results for the steady state power runs

4.3.1 Global heat balance of PREMUX

Due to the operation of the PREMUX test box without a vacuum vessel, non-negligible heat losses are expected through the thermal insulation and salient objects of the test box acting as fins, such as the heater and thermocouple wires, the purge gas pipes and instrumentation feedthoughts.

For the assessment of these heat losses, the control volume depicted in Figure 4.2-top has been used. This control volume includes the PREMUX test box and the thermal insulation. In this picture, $\dot{Q}_{heat}$ is the heat provided by the heater system; $\dot{Q}_{loss}$ represents the heat losses in the control volume; $\dot{m}_{in,i}$ and $\dot{m}_{out,i}$ are the mass flows at the inlet and outlet of each cooling channel *I*; $h_{in,i}$ and $h_{out,i}$ are the enthalpies of the air coolant for each cooling channel i at the inlet and outlet; $c_{in,i}$ and $c_{out,i}$ is the coolant mean velocities for each cooling channel at the inlet and outlet and $z_{in,CM}$ and $z_{out,CM}$ are the heights of the center of mass of the air coolant at the inlet and outlet of each cooling channel.

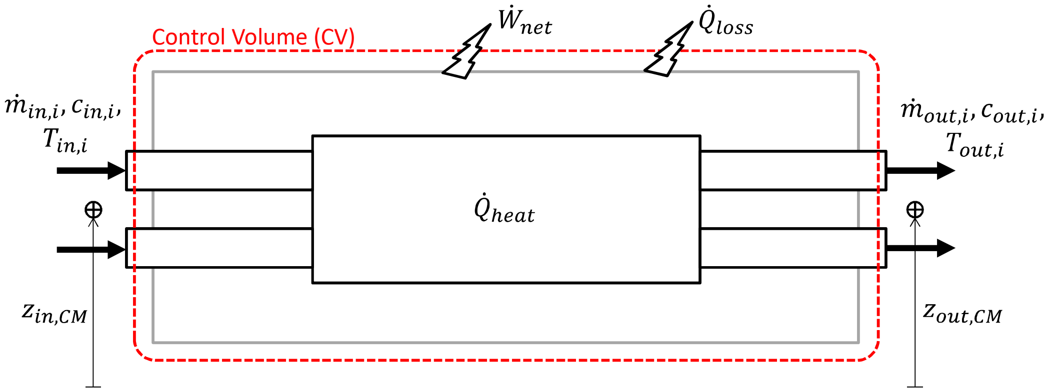

Figure 4.1: Control volume selected for the heat balance assessment in PREMUX.

The application of the principle of conservation of energy to this control volume leads to:

$$\begin{aligned}\dot{Q}_{heat} - \dot{Q}_{loss} + \sum_{i=1}^{12} \dot{m}_{in,i} \left(h_{in,i} + \frac{{c_{in,i}}^2}{2} + g z_{in,CM} \right) \\ = \dot{W}_{net} + \sum_{i=1}^{12} \dot{m}_{out,i} \left(h_{out,i} + \frac{{c_{out,i}}^2}{2} + g z_{out,CM} \right),\end{aligned} \tag{4.22}$$

where g is the gravity acceleration. The coolant gas does not effectuate a work. Moreover, neither there is a change in the heights nor mass flows ($\dot{m}_{in,i} = \dot{m}_{out,i} = \dot{m}_i$) along the cooling channels and the velocity change of the air is negligible, Eqn. (4.22) reduces to:

$$\dot{Q}_{loss} = \dot{Q}_{heat} - \sum_{i=1}^{12} \dot{m}_i (h_{out,i} - h_{in,i}) \ , \tag{4.23}$$

and as

$$h_{out,i} - h_{in,i} = \int_{T_{in,i}}^{T_{out,i}} c_{p,air} dT \approx c_{p,air} (T_{out,i} - T_{in,i}) \ , \tag{4.24}$$

being $c_{p,air}$ the specific heat of the air, the heat loss reads

$$\dot{Q}_{loss} = \dot{Q}_{heat} - \sum_{i=1}^{12} \dot{m}_i c_{p,air} (T_{out,i} - T_{in,i}) \ , \tag{4.25}$$

The results of the evaluation of the heat loss as function of the heater power are summarized in Figure 4.2. It can be seen that $\dot{Q}_{loss}$ increases linearly with $\dot{Q}_{heat}$ (Figure 4.2-left) and an average of 13.6% of the heat produced by the heater system is lost (Figure 4.2-right) by natural convection through the thermal insulation surfaces, as well as through the different salient features of the test box. In particular, relative losses of 13.2%, 14.8%, 11.5%, 10.7% and 17.9% have been obtained for the VHI, HI, MED, LO and VLO power levels, respectively.

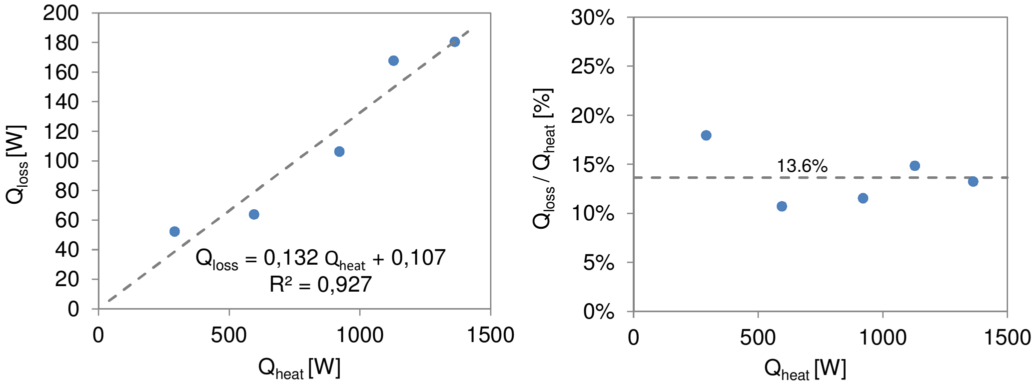

Figure 4.2: Assessment of PREMUX global heat balance. Left: plot of the heating power vs. the heat loss. Right: plot of the ratio of the heat loss to the heating power.

4.3.2 Dimensional analysis

In order to verify the coherency of the temperature measurements in the pebble bed, a dimensional analysis of the experimental data is proposed. For this, this data is first reduced to adequate dimensionless parameters determined by means of the Π-Theorem and then compared to each other for its coherency.

For the physics involved in the temperature distribution in the Li_4SiO_4 pebble bed at the steady state regime and for a given power density and a constant and equal rate of cooling for each regime, the following descriptive variables are proposed: the total heating power applied in the pebble bed, G; the effective thermal conductivity of the Li_4SiO_4 pebble bed k_{eff} (Eqn. (4.1)); the local temperature of the pebble bed, T; and 3 characteristic lengths, namely the thickness of the pebble bed, L_{pb}, and the x_{TC} and y_{TC} coordinates of a thermocouple position at the

PREMUX measurement plane. Therefore, it is assumed that it exist a function $\Phi(\,G,k_{eff},T,L_{pb},x_{TC},y_{TC})=0$ describing this physics.

For these variables, the following dimensions are identified: $G\equiv[P]$, where $[P]$ denotes the dimension of power, $k_{eff}\equiv[PL^{-1}\theta^{-1}]$, $T\equiv[\theta]$ and $L_{pb}\equiv x_{TC}\equiv y_{TC}\equiv[L]$, i.e. $\{[P],[L],[\theta]\}$ as fundamental dimensions, with $dim(\{[P],[L],[\theta]\})=r=3$. As the number of descriptive variables is $n=6$, the number of dimensionless Π_i groups is $n-m=3$. Hence, after the Π-Theorem it can be demonstrated that it exists a functional relationship Ψ so that:

$$\Phi(\,G,k_{eff},T_l,L_{pb},x_{TC},y_{TC})=0\Longleftrightarrow\Psi(\Pi_1,\Pi_2,\Pi_3)=0\ , \tag{4.26}$$

with

$$\Pi_1=\frac{k_{eff}}{G^{x_{11}}T^{x_{21}}{L_{pb}}^{x_{31}}}=k_{eff}G^{\bar{x}_{11}}T^{\bar{x}_{21}}{L_{pb}}^{\bar{x}_{31}}\ , \tag{4.27}$$

$$\Pi_2=\frac{x_{TC}}{G^{x_{12}}T^{x_{22}}{L_{pb}}^{x_{32}}}=x_{TC}G^{\bar{x}_{12}}T^{\bar{x}_{22}}{L_{pb}}^{\bar{x}_{32}}\ , \tag{4.28}$$

$$\Pi_3=\frac{y_{TC}}{G^{x_{13}}T^{x_{23}}{L_{pb}}^{x_{33}}}=y_{TC}G^{\bar{x}_{13}}T^{\bar{x}_{23}}{L_{pb}}^{\bar{x}_{33}}\ , \tag{4.29}$$

and

$$\Pi_1\equiv[PL^{-1}\theta^{-1}][P]^{\bar{x}_{11}}[\theta]^{\bar{x}_{21}}[L]^{\bar{x}_{31}}=1^0, \tag{4.30}$$

$$\Pi_2\equiv[L][P]^{\bar{x}_{12}}[\theta]^{\bar{x}_{22}}[L]^{\bar{x}_{32}}=1^0, \tag{4.31}$$

$$\Pi_3\equiv[L][P]^{\bar{x}_{13}}[\theta]^{\bar{x}_{23}}[L]^{\bar{x}_{33}}=1^0, \tag{4.32}$$

leading to the following linear systems of equations

$$\Pi_1\colon\begin{cases}1+\bar{x}_{11}=0\\-1+\bar{x}_{21}=0\\-1+\bar{x}_{31}=0\end{cases},\ \Pi_2\colon\begin{cases}\bar{x}_{12}=0\\\bar{x}_{22}=0\\\bar{x}_{32}+1=0\end{cases}\ \text{and}\ \Pi_3\colon\begin{cases}\bar{x}_{13}=0\\\bar{x}_{23}=0\\\bar{x}_{33}+1=0\end{cases}, \tag{4.33}$$

After solving, the dimensionless parameters read:

$$\Pi_1=\frac{k_{eff}TL_{pb}}{G}=\frac{T}{\dfrac{G}{k_{eff}L_{pb}}}\ ,\Pi_2=\frac{x_{TC}}{L_{pb}}\ \text{and}\ \Pi_3=\frac{y_{TC}}{L_{pb}}\ , \tag{4.34}$$

Π_1 can be understood as a dimensionless local pebble bed temperature θ_{L}, which is a ratio between the actual local temperature of the bed with respect to a reference temperature calculated as $\frac{\mathrm{G}}{\mathrm{k_{eff}L_{pb}}}$ that can be ideally interpreted as the temperature difference that an infinitely long pebble bed of thickness $\mathrm{L_{pb}}$ would have when the power G is to flow through it when the thermal conductivity is $\mathrm{k_{eff}}$ at the temperature T.

This θ_L is then function of the dimensionless coordinates $(\xi_1,\xi_2)=\left(\frac{x_{TC}}{L_{pb}},\frac{y_{TC}}{L_{pb}}\right)$. Considering Eqn. (4.26), the following dimensionless expression can be then written:

$$\Psi(\Pi_1,\Pi_2,\Pi_3)\equiv\Psi(\theta_L,\xi_1,\xi_2)=0\Leftrightarrow\theta_L=\Psi'(\xi_1,\xi_2). \tag{4.35}$$

Ψ' can be reconstructed by means of biharmonic spline interpolation with all the experimental data available for each of the power levels VHI, HI, MED, LO and VLO. Figure 4.3 depicts the positions of the temperature measurements in PREMUX at the measurement plane and Figure 4.4 plots the resulting surface after the interpolation, together with the experimental data points.

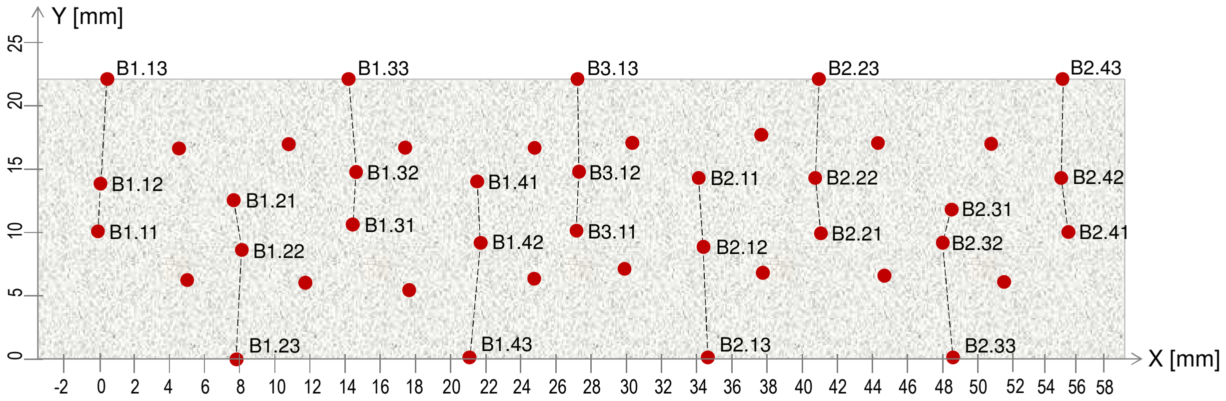

Figure 4.3: Temperature measurement positions in PREMUX.

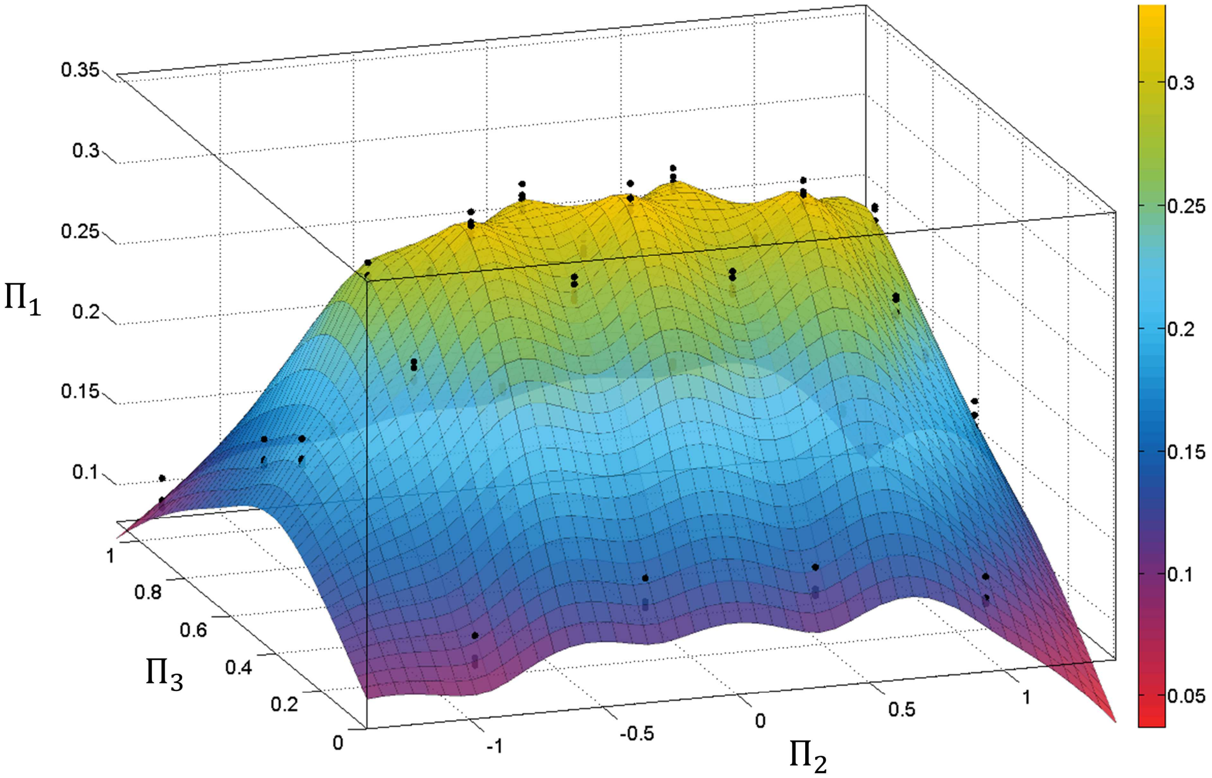

Figure 4.4: Dimensionless temperature distribution $\Pi_1 \equiv \theta_L$ in the pebble bed as function of the dimensionless thermocouple coordinates $\Pi_2 \equiv \xi_1$ and $\Pi_3 \equiv \xi_2$.

Figure 4.5 depicts the different plots of θ_L vs. $\xi_2 = \frac{y_{TC}}{L_{pb}}$ for each $\xi_1 = \frac{x_{TC}}{L_{pb}}$ for a better comparison of all experimental data points and the resulting dimensionless heat fluxes $\partial\theta_L / \partial\left(\frac{y_{TC}}{L_{pb}}\right)$. The uncertainty bars are plotted with a 95% confidence interval.

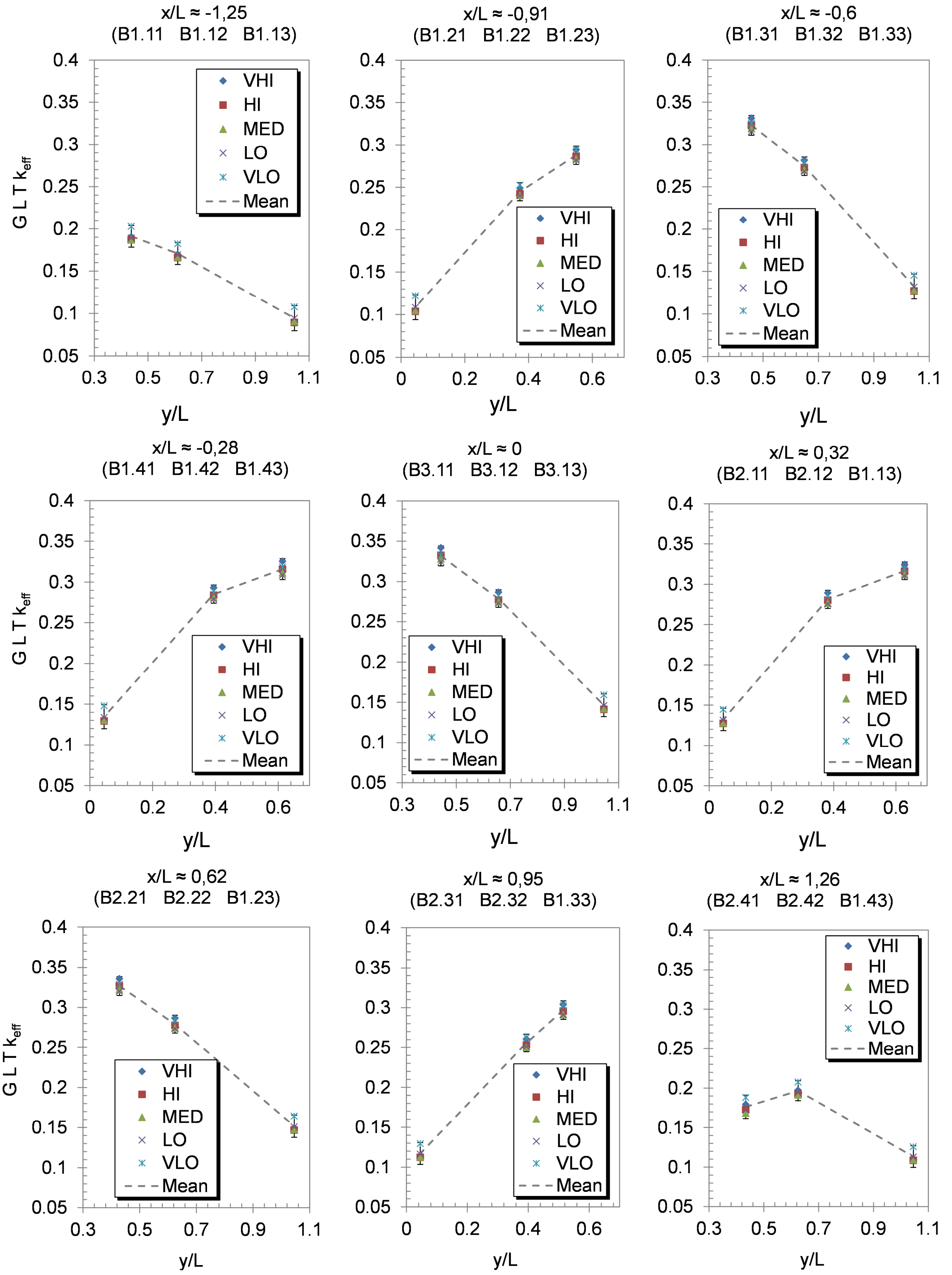

Figure 4.5: Assessment of PREMUX global heat balance. Left: plot of the heating power vs. the heat loss. Right: plot of the ratio of the heat loss to the heating power.

This analysis evidences that the solutions are self-similar: any temperature field has the same $\Psi'(\xi_1, \xi_2)$ field for a given G, i.e. that the temperature fields are reduced at the steady state to a single dimensionless temperature field, as shown in Figure 4.4 for any given power.

Likewise, all heat fluxes follow a similar pattern independently of the power level set, showing the coherency of the obtained experimental data. The knowledge of the function $\Psi'(\xi_1, \xi_2)$ reduces the independent variables of the problem to 2, which are just the coordinates of the temperature θ_L.

An anomalous behavior of the dimensionless temperature at the thermocouple B2.41 can be anticipated, as it suggests a 0 heat flux about the thermocouple B2.42, meaning that a heat source is located there, which is not the case. A more detailed analysis of this thermocouple is done in the next section with possible explanations to this effect and countermeasures to avoid this phenomenon for future assemblies of the heater system as the one presented here.

4.3.3 Temperature maps in the Li_4SiO_4 pebble bed

The experimental results for each power level are depicted in the following figures (Figure 4.6 to Figure 4.8). At the top of each figure, the temperature reconstruction in the pebble bed is provided and performed by means of biharmonic spline interpolation. At the bottom, each thermocouple has been plotted against its y position in the pebble bed, together with the uncertainty bars representing a confidence of 95%, as detailed in Section 4.3.2.

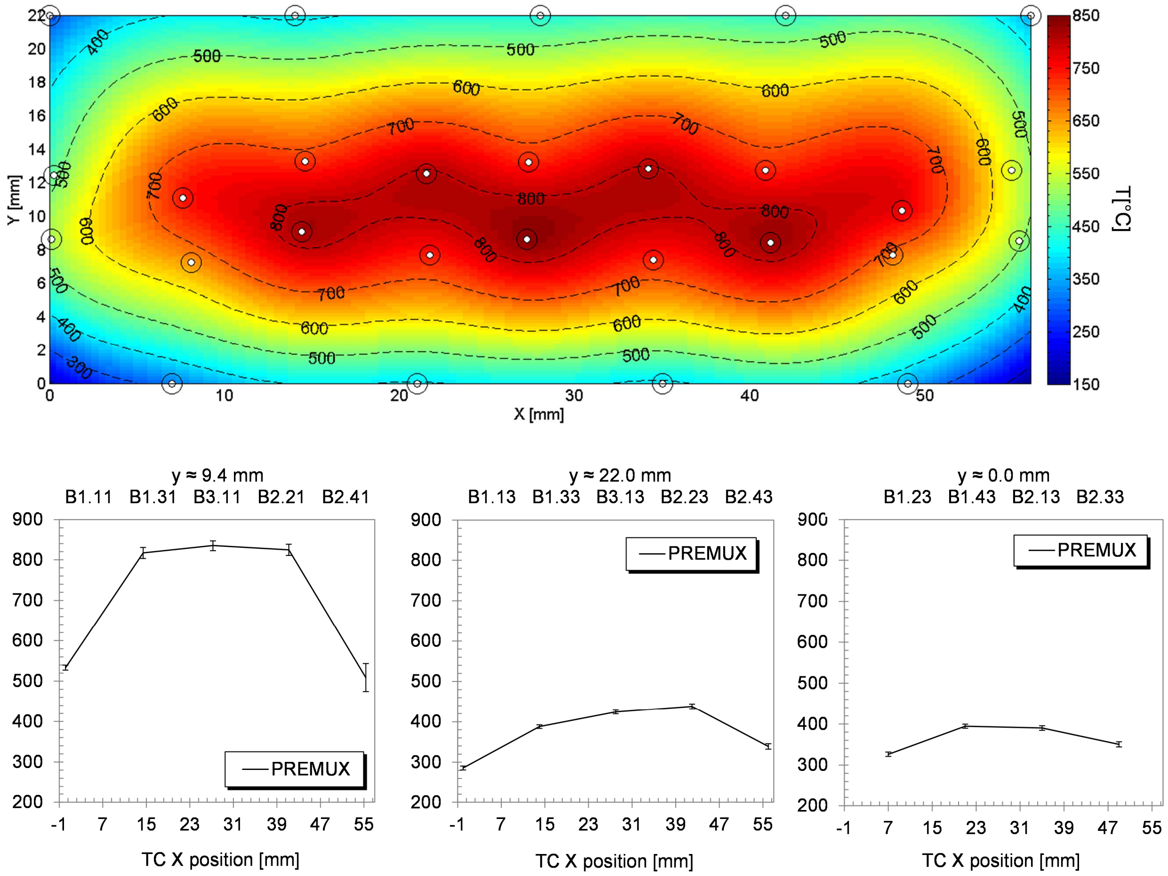

Figure 4.6: Steady state temperatures in PREMUX for the VHI power level at different coordinates. Top: temperature map (biharmonic spline interpolation of measured data). Bottom: Li_4SiO_4 pebble bed temperatures along longitudinal (x) direction (uncertainty with a coverage fator 2).

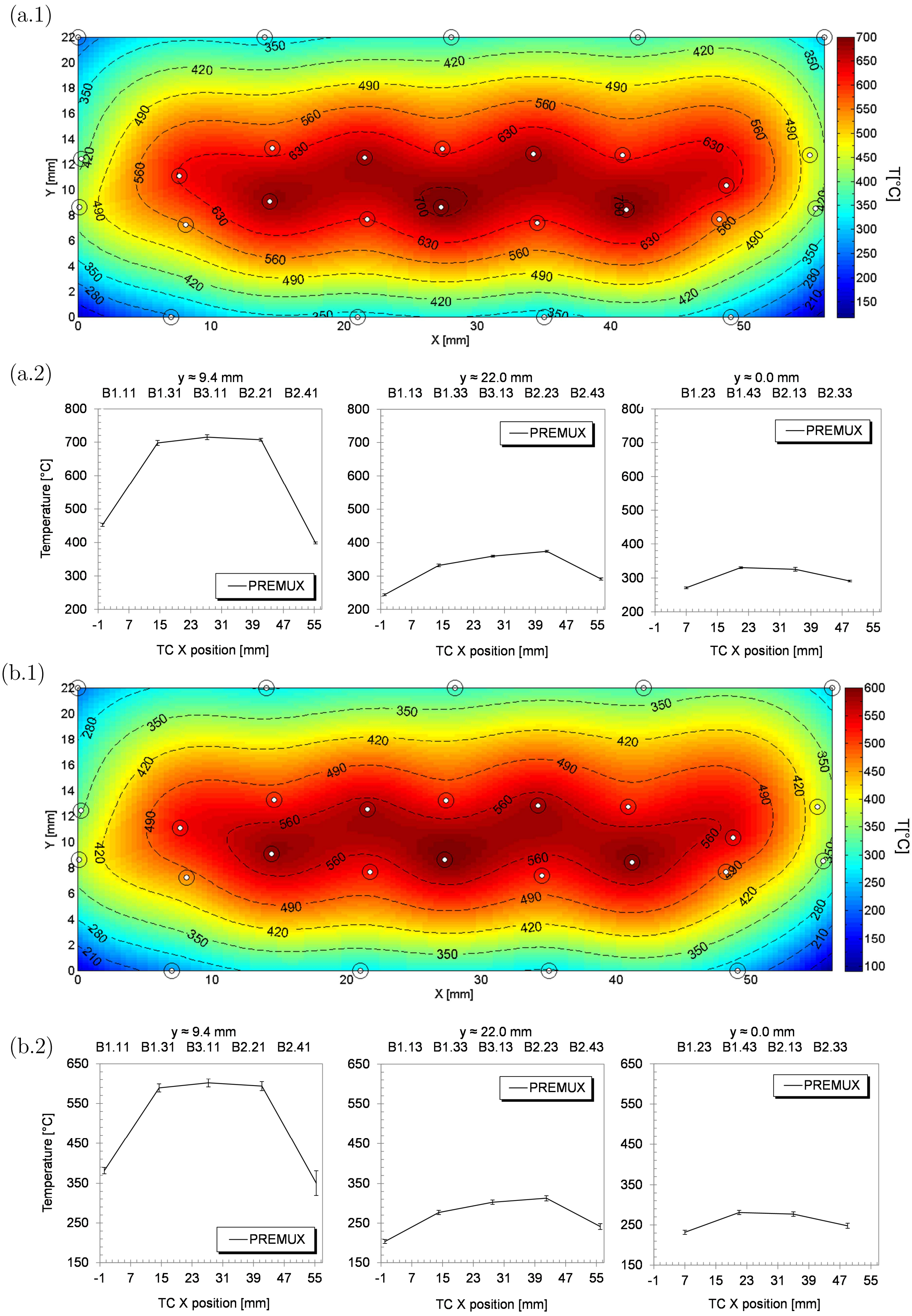

Figure 4.7: Steady state temperatures for the HI (a) and MED (b) power level. (a.1) and (b.1): temperature map (biharmonic spline interpolation of measured data); (a.2) and (b.2): Li_4SiO_4 pebble bed temperatures along longitudinal (x) direction (uncertainty with coverage fator 2).

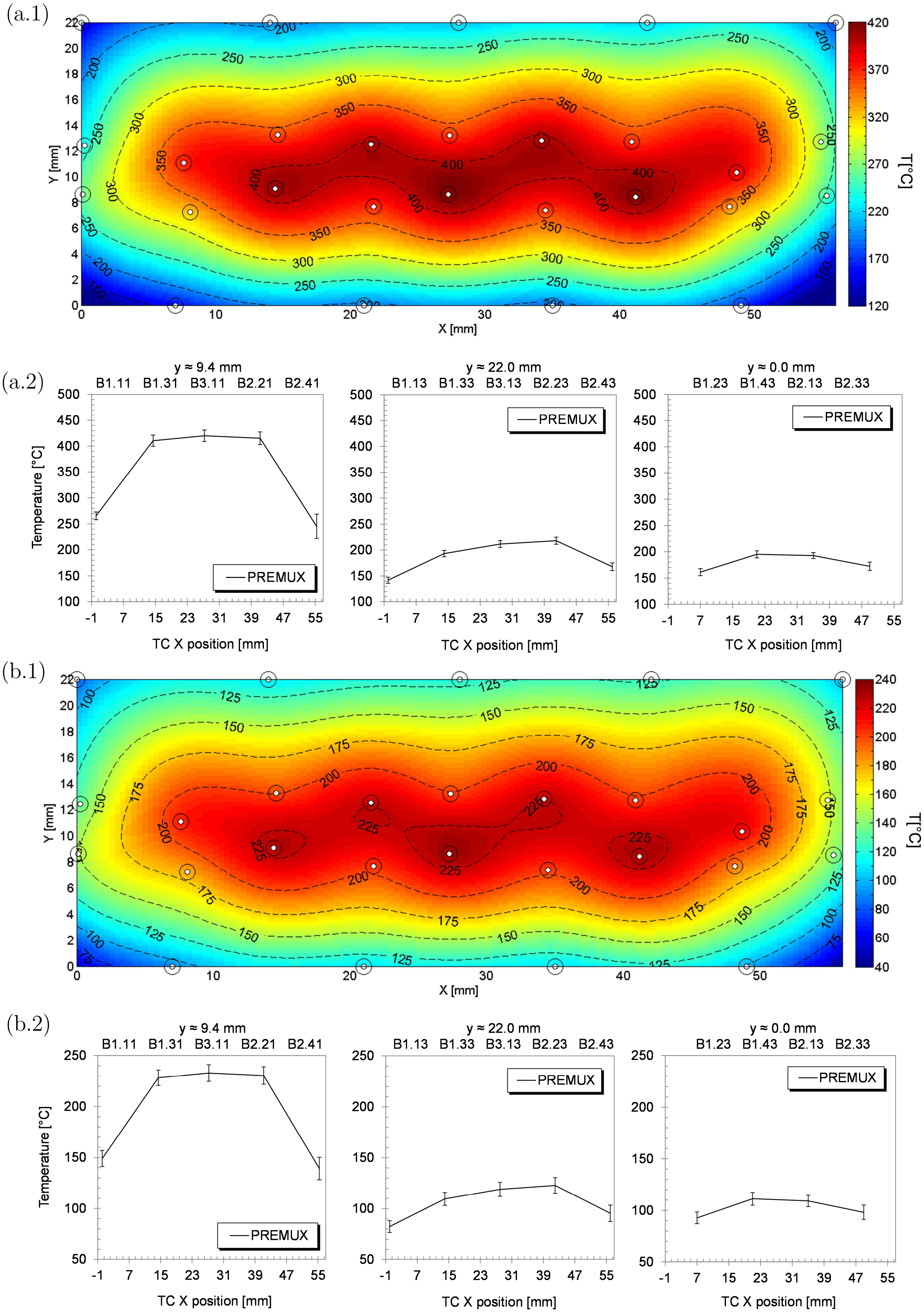

Figure 4.8: Steady state temperatures for the LO (a) and VLO (b) power level. (a.1) and (b.1): temperature map (biharmonic spline interpolation of measured data); (a.2) and (b.2): Li_4SiO_4 pebble bed temperatures along longitudinal (x) direction (uncertainty with coverage fator 2).

Maximum temperatures of 835.3 °C, 711.1 °C, 601.8 °C, 384.1 °C and 232.9 °C have been reached in the Li_4SiO_4 pebble bed for the VHI, HI, MED, LO and VLO power levels, respectively. For all power levels it is observed that the expanded uncertainty of the temperature measurements is between 1% and 2%, with the exception of the thermocouple B2.41, where the expanded uncertainty is about 6%. After several cycles, this thermocouple has systematically measured a significantly lower temperature than it has been expected in the thermal and thermo-mechanical models that will be described in the following Chapters 5 and 6.

In the case of a complete gap formation between the pebble bed and the top surface of the test box due to successive inelastic deformations, some asymmetry would be expected due to the reduction of the contact conductance between the test box and the pebble bed, with higher temperatures at the upper top side. However, it can be also observed that the temperatures at the top and bottom surface of the test box after multiple runs do not have significant differences and that the temperature distribution is approximately symmetric with respect to the horizontal midplane of the pebble bed for any of the power levels. This may indicate that, a complete gap formation between the pebble bed and the surrounding steel that can happen after successive thermal expansions and inelastic deformation does not occur or that the influence of this gap does not significantly affect the thermal contact conductance. The latter is likely to be case, as in the case of the lithium ceramics the contact conductance is dominated by the purge gas thermal conductivity, as it will be seen in Section 5.7.4 (Figure 5.23), and that could explain the low influence of the gap formation in the temperature distribution of the pebble bed.

In Figure 4.9 to Figure 4.13 the transversal (y axis) heat flux is depicted. When comparing the heat fluxes, the one from B2.41 to B2.42 appears strongly different from the pattern observed for its quasi-equivalent counterpart from B1.11 to B1.12, as already anticipated by the dimensional analysis of the previous section.

This temperature uncertainty and the anomalous heart flux observed at the B2.41 suggests that the pebble bed has experienced a slight motion during the operation and has moved this thermocouple outwards towards a colder region. Even if the motion has been small, due to the strong gradients present in the pebble bed it can lead to the observed deviations.

This motion could be explained by the fact that the pebble bed may not be perfectly homogenous after the filling process and there might be regions where the packing factor is lower: after several cycles, this local inhomogeneity might tend to be compensated by allowing some pebble bed motion. An alternative or additional effect may be as well produced due to the excessive flexibility of the heater wires. During the insertion of the heater system and the filling of the pebble bed volume, it may be possible that this thermocouple position could be already altered from the measured location with the 3D laser scan.

In order to avoid an excessive movement of a thermocouple due to an eventual pebble bed motion caused by the presence of regions with lower packing factor or due to an excessive flexibility, additional spacer plates can be installed in the heater system, so as to reduce the free length of the heater cables between spacer plates. The spacer plate separation in the heater blocks 1 and 2 is 137 mm. After the outcome of the experimental results presented here, this plate separation has been found to offer too much flexibility and it is recommended to reduce this distance to about 1/3 (i.e. about 45 mm), as a trade-off between minimization of disturbing objects into the pebble bed (number of spacer plates) and increase of geometrical stability of the heater system (rigidity).

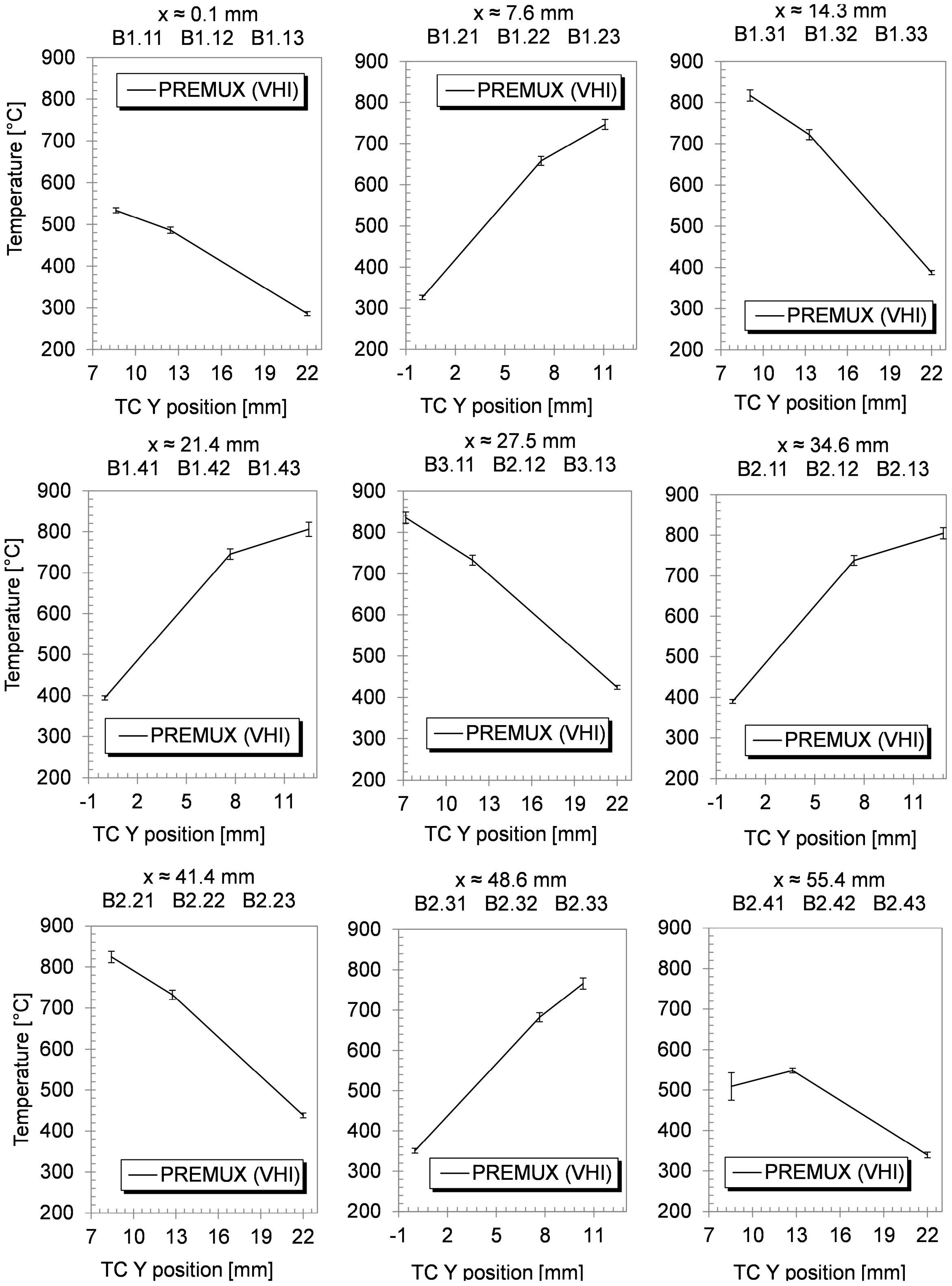

Figure 4.9: Steady state temperatures of the Li_4SiO_4 pebble bed in PREMUX for the VHI power level temperatures along transversal (y) direction (uncertainty expressed with a coverage fator 2).

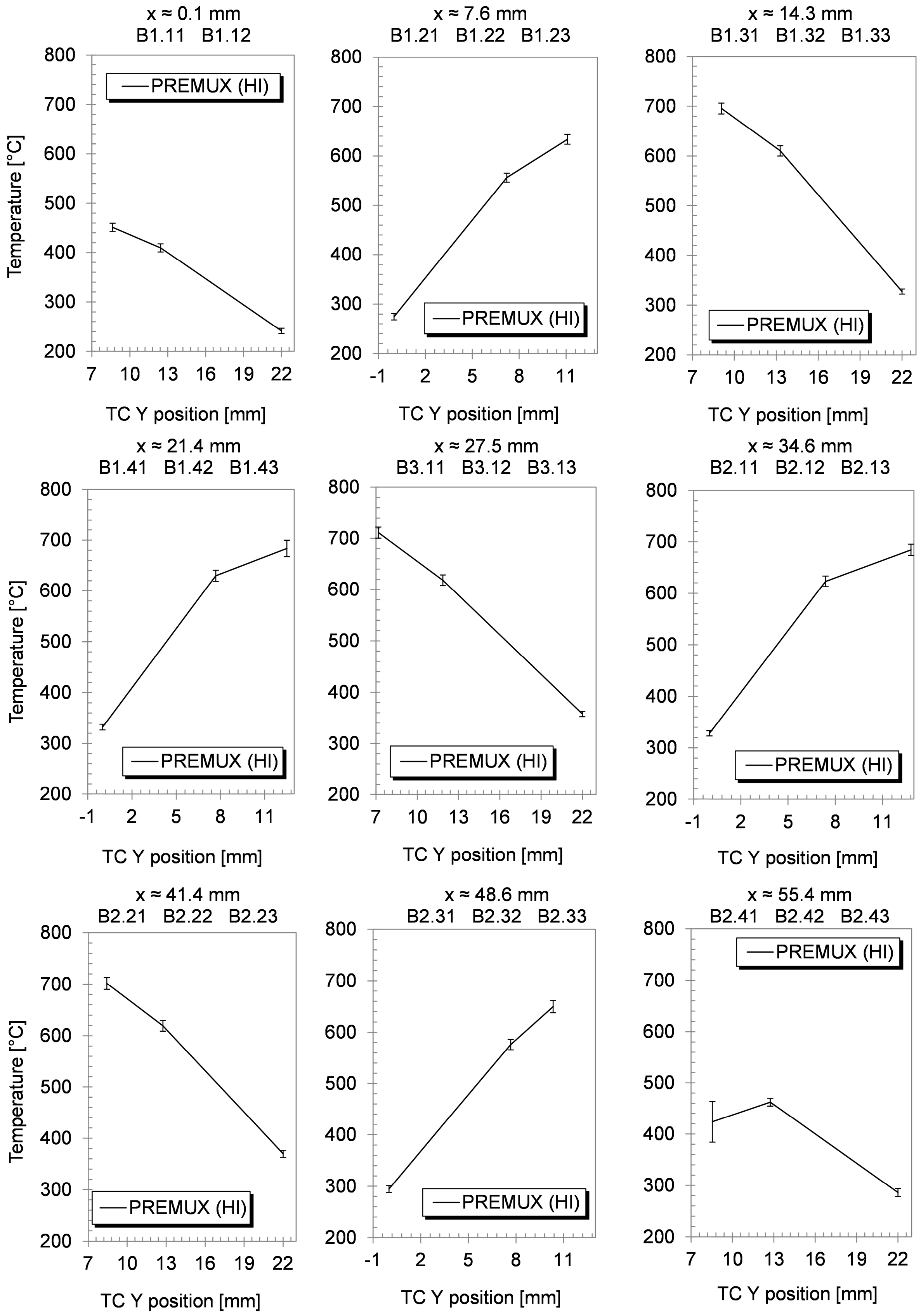

Figure 4.10: Steady state temperatures of the Li_4SiO_4 pebble bed in PREMUX for the HI power level temperatures along transversal (y) direction (uncertainty expressed with a coverage fator 2).

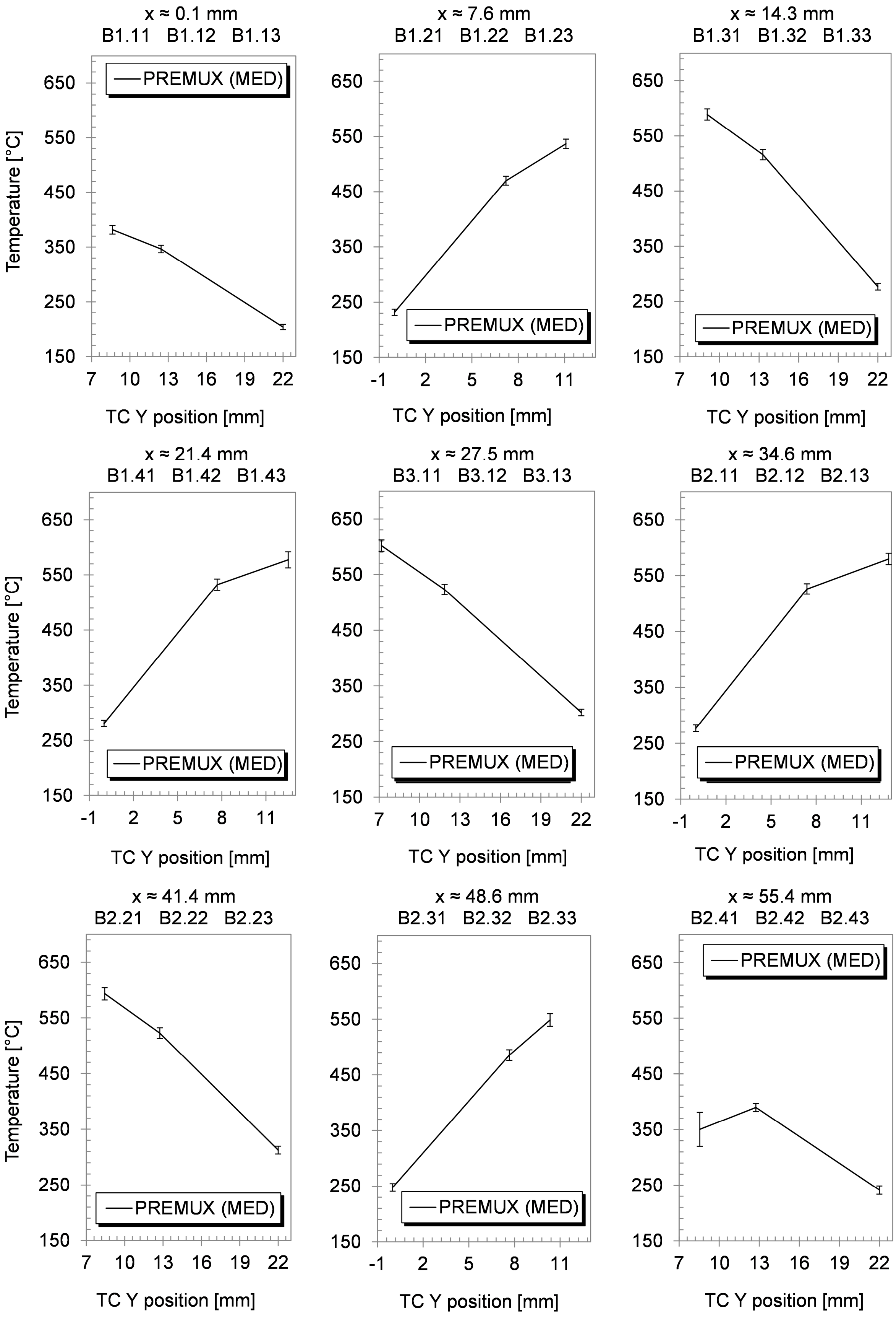

Figure 4.11: Steady state temperatures of the Li_4SiO_4 pebble bed in PREMUX for the MED power level temperatures along transversal (y) direction (uncertainty expressed with a coverage fator 2).

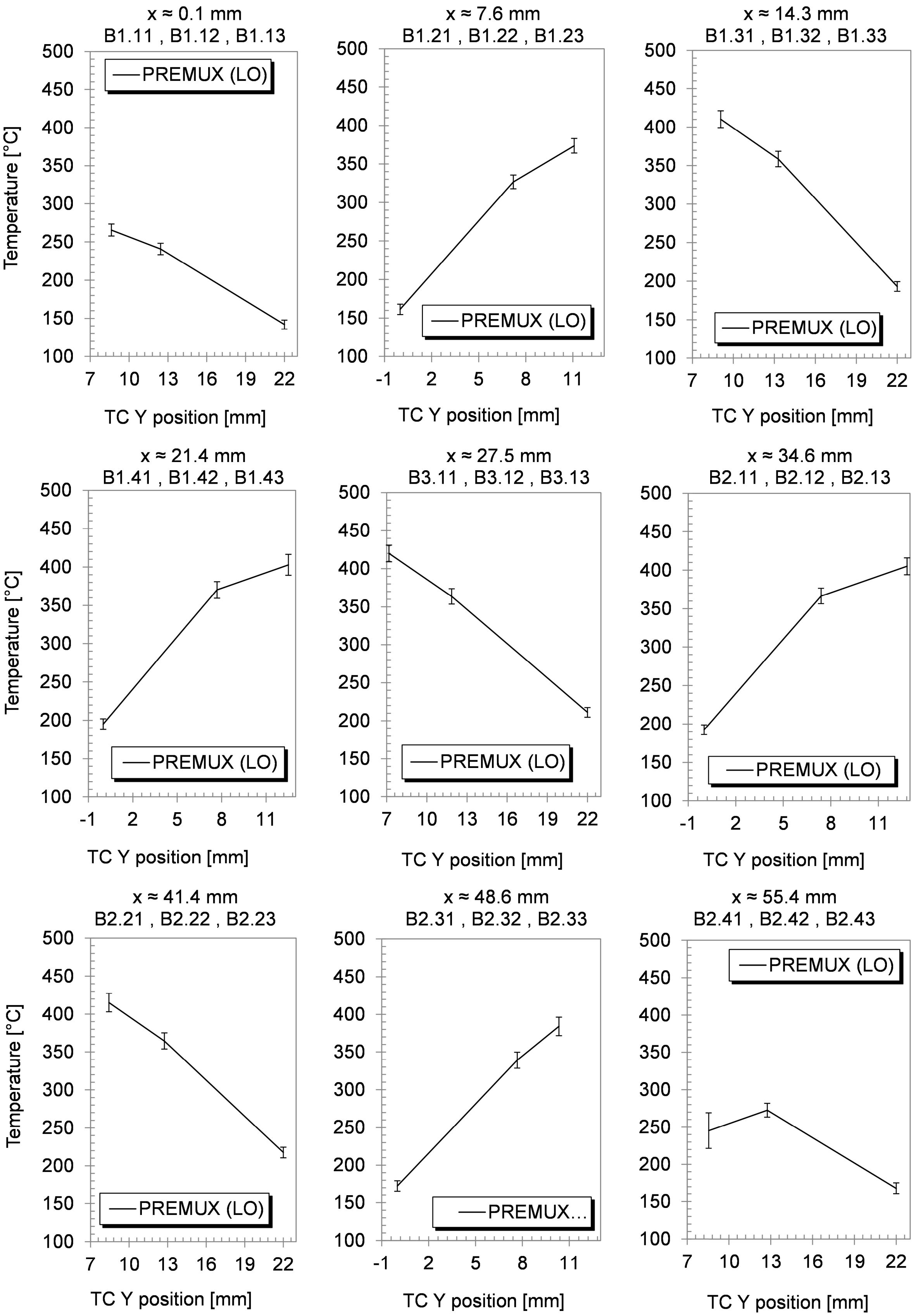

Figure 4.12: Steady state temperatures of the Li_4SiO_4 pebble bed in PREMUX for the LO power level temperatures along transversal (y) direction (uncertainty expressed with a coverage fator 2).

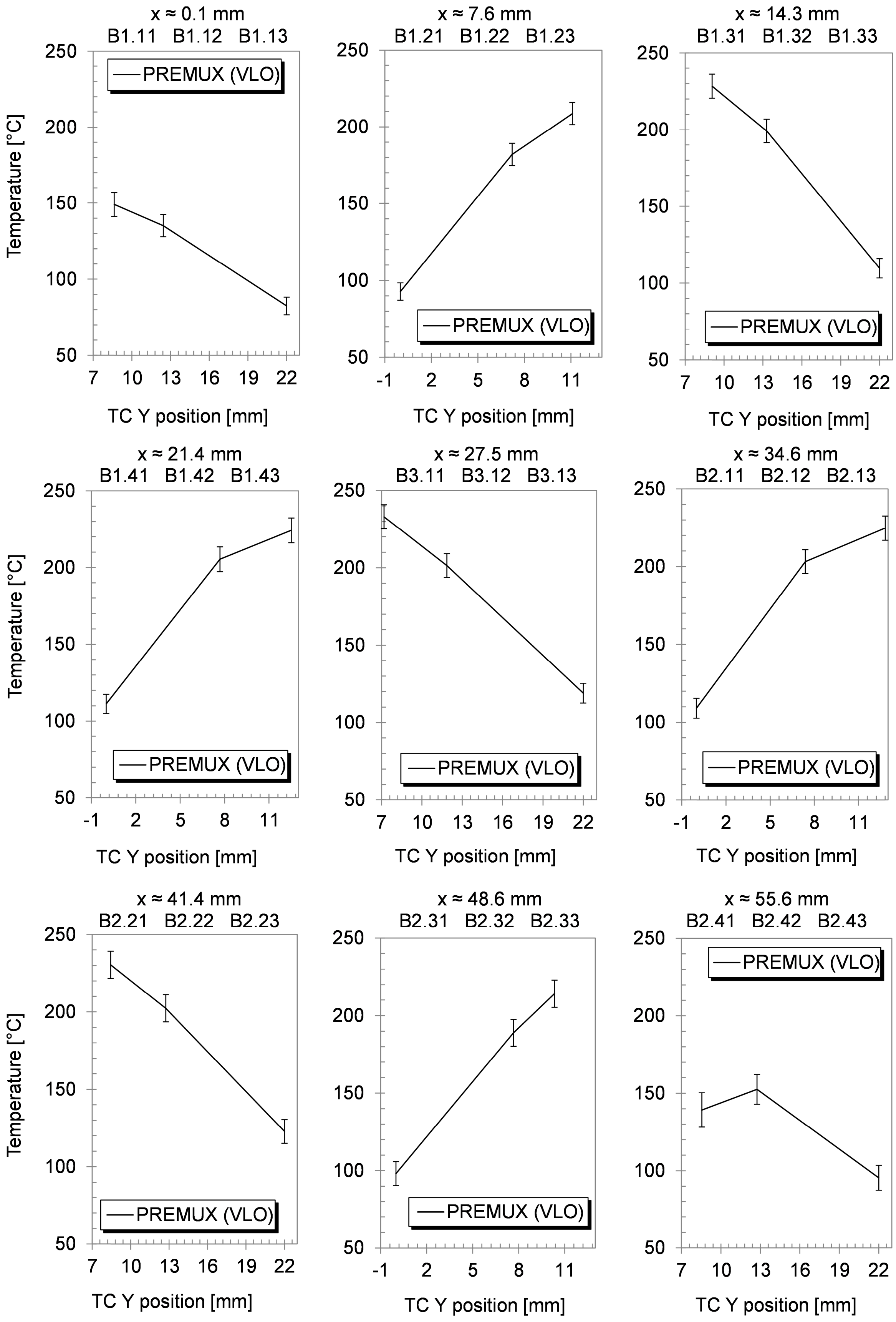

Figure 4.13: Steady state temperatures of the Li_4SiO_4 pebble bed in PREMUX for the VLO power level temperatures along transversal (y) direction (uncertainty expressed with a coverage fator 2).

4.4 Experimental results for the transient power runs

The crucial requirement of a heater system for the HCPB Breeder Unit, together with a low intrusion in the pebble bed and flexibility to adapt it to the U shape of this component, is the reproduction of the ITER power pulses. As a proof-of-concept, 3 operation cycles have been reproduced with the heater system prototype in PREMUX at the highest power level VHI. The experimental results for these 3 cycles are plotted in Figure 4.14, showing the time series of the temperature measurement in the 3 central thermocouples (B3.11, B3.12, B3.13, see Figure 4.9-middle). In this figure the power deployed by the 3 heaters is represented as well.

Each cycle has a duration of 1000 s and consists of a current ramp-up from 0 A to 5.16 A (heater block 1), to 4.94 A (heater block 2) and to 2.07 A (heater block 3) in 30 s, a flat top at these current levels of a duration of 430 s, followed by a ramp-down in 60 s to 0 A in all the heaters and a final flat bottom of 480 s.

Despite the tested proof-of-concept conditions constitutes a local upper limit in the operational temperatures of the HCPB Breeder Unit Li_4SiO_4 pebble bed, it has been reproduced successfully.

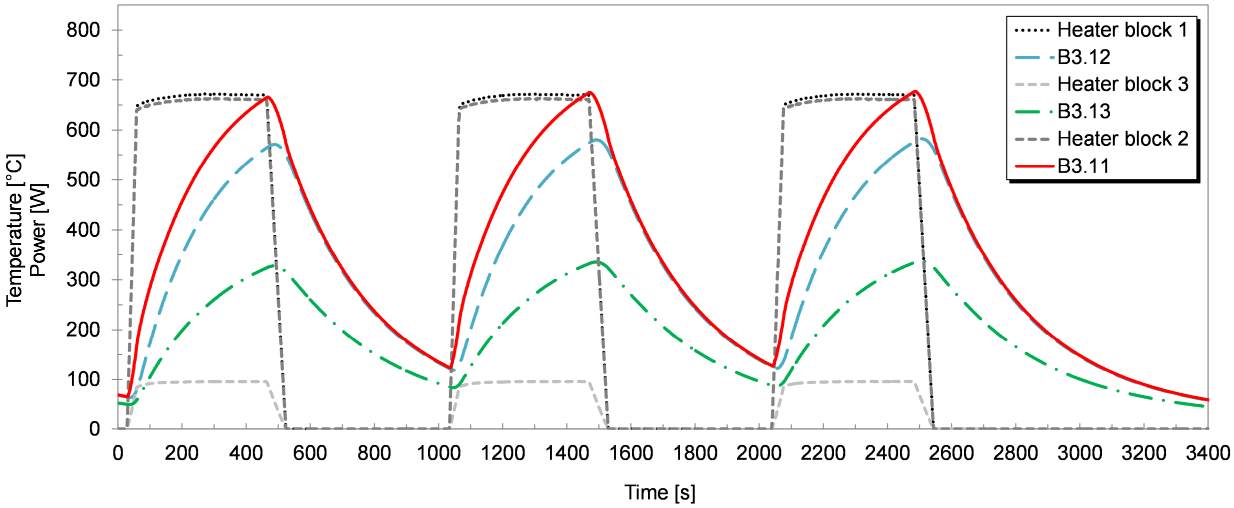

Figure 4.14: Cyclic testing of the PREMUX heater system. Time series plot of the total heating power released by the heaters at VHI power levels and temperature evolution at B3.11, B3.12 and B3.13. The heater system reproduces successfully ITER-like power pulses (ramp-up to full power in 30 s, flat top of 430 s and ramp-down in 60 s).

4.5 Experimental results for the additional tests

4.5.1 Experimental results for the thermal conductivity of the Li_4SiO_4 pebble bed at room temperature

A first set of additional experiments has aimed at empirically determining the effective thermal conductivity of the Li_4SiO_4 pebble bed close to room temperature (T ≈ 30 $°C$) in

PREMUX, which serve to indirectly verify the influence of the heater system on the thermo-mechanics of the pebble bed.

These experiments have been conducted following the so-called *Hot-Wire Method* (HWM), first used by Enoeda et al. (1998) according to the Japanese standard JIS R 2616:2001 (2001) and equivalent to the DIN EN ISO 8894-1:2010 (2010), and later by Reimann et al. (2002a) and Lo Frano and Aquaro (2014).

The HWM is a standard procedure aimed at determining the (effective) thermal conductivity k_{eff} of poor conducting materials, like the Li_4SiO_4 pebble bed in the HCPB Breeder Unit and in PREMUX. It is based on the axisymmetric transient heat conduction of a line heat source embedded in an infinite homogeneous medium, which is governed by the following partial differential equation:

$$\frac{\partial^2 T}{\partial r^2}+\frac{1}{r}\frac{\partial T}{\partial r}=\frac{1}{\alpha}\frac{\partial T}{\partial t}\ , \tag{4.36}$$

where T is the temperature of the medium, r is the radial coordinate and α is the thermal diffusivity of the medium. The method assumes that the linear heat source starts to provide a constant power per unit length q at $t_{ini}=0$ and that the medium has a uniform initial temperature $T(t_{ini})=T_{ini}$. The solution to Eqn. (4.36) is given by the expression after Carslaw and Jaeger (1959):

$$T-T_{ini}=-\frac{q}{4\pi k_{eff}}(\gamma+\ln\frac{r^2}{4\alpha t}+\sum_{n=1}^{\infty}\frac{\left(-\frac{r^2}{4\alpha t}\right)^n}{n\times n!})\ , \tag{4.37}$$

where γ is the Euler-Mascheroni constant ($\gamma=0.5772$). Eqn. (4.37) can be approximated with an error of less than 1% eliminating the infinite summation term (Nix et al., 1967), leading to:

$$T-T_{ini}=\frac{q}{4\pi k_{eff}}\left(\ln\frac{4\alpha t}{r^2}-\gamma\right), \tag{4.38}$$

Differentiating (4.38) with respect to the $\ln \mathrm{t}$ yields:

$$dT=\frac{q}{4\pi k_{eff}}d(\ln t)\ . \tag{4.39}$$

After an initial transient $t_1$and until a time t_2, it is observed that $\frac{dT}{d(\ln t)}$ is nearly constant and, therefore, the time evolution of T is linear with respect to $\ln t$, with a slope $\frac{q}{4\pi k_{eff}}$. This result leads to the expression used by Enoeda et al. (1998):

$$k_{eff}=\frac{q}{4\pi}\frac{\ln\frac{t_2}{t_1}}{T_2-T_1}\ . \tag{4.40}$$

where $T_1=T(r,t_1)$ and $T_2=T(r,t_2)$. After t_2, edge and end effects becomes relevant and $\frac{dT}{d(\ln t)}$ is no longer constant, invalidating Eqn. (4.40).

In PREMUX, the pebble bed volume is finite, thus differing from the assumptions of the HWM. Andersson and Bäckström (1976) estimated that when

$$r_0 > 4\sqrt{\alpha t} \ , \tag{4.41}$$

the effect of the finiteness of the medium in the temperature distribution is less than 0.1%.

Moreover, the heater 3 in PREMUX, which is acting as the idealized line heat source, is finite as well: it consists of a single cable of length 175 mm and ∅1 mm, which has a ∅0.5 mm thermocouple (B3.11) welded on it by laser, which is the one used for measuring $T(t_i)$. In order to assess the impact of the finiteness of the heater length l in the HWM assumption of perfect radial heat flow of the heat source, Blackwell (1954) proposed that when

$$l > \sqrt{\frac{4\alpha t}{0.0632}} \ , \tag{4.42}$$

the axial heat flow can be neglected. When the conditions of Eqn. (4.41) and (4.42) are met, Eqn. (4.40) can be considered as the asymptotic solution of a HWM test.

In PREMUX, 5 experimental runs with the HWM have been conducted with a current pulse of 0.696 A, which corresponds to a heating power of 12.7 W. The time series of the temperature for the 5 tests are plotted in Figure 4.15. The run #1 has been the first test, beginning after a long period of rest of the PREMUX test section. Runs #2 to #5 have been executed afterwards. Therefore an offset of about -2 $°C$ of run #1 with respect to the rest is observed, as the initial temperature condition of run #1 could not be reached for the rest of the runs in a reasonable time due to time constraints. However, the data of run #1 is relevant, as the parameter of importance is $T_2 - T_1$ and the starting temperatures are still considered nearly the same.

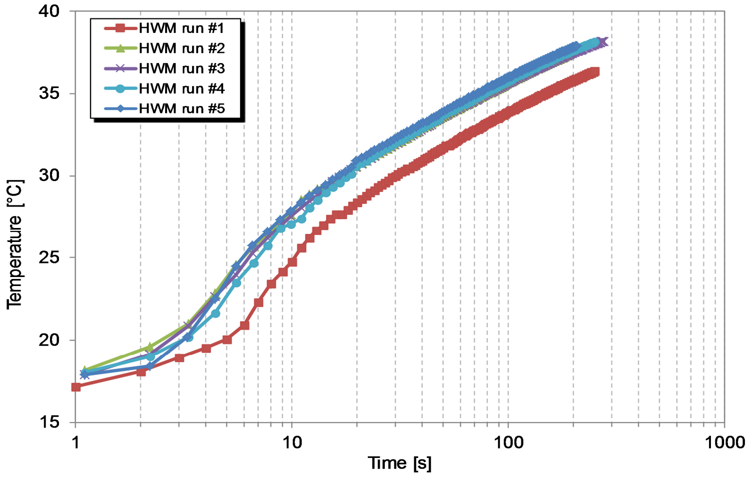

Figure 4.15: Hot-wire method (HWM) for the determination of the thermal conductivity of the Li_4SiO_4 pebble bed at ~35 $°C$. In the graph, the 5 experimental runs performed in PREMUX are shown. The time instants $t \approx 30s$ to $t \approx 150s$ have been considered for the determination of the slope of the curves in the logarithmic plot.

It is observed that the temperature increases almost linearly after $t_1 = 30\ s$ during at least 120 s (and therefore, $t_2 = 150\ s$). The temperature of the pebble bed is ~35 $°C$ and, at this temperature, the effective density of the pebble bed is $\rho_{Li_4SiO_4} = 1526\ \frac{kg}{m^3}$ (Reimann et al., 2005) and its heat capacity, $c_{p_{Li_4SiO_4}} = 1400 \frac{J}{Kg°C}$ (Reimann et al., 2005), hence $\alpha = k_{eff}^{Li_4SiO_4} \Big/ \left(\rho_{Li_4SiO_4} \cdot c_{p_{Li_4SiO_4}}\right) = 3.678 \cdot 10^{-7}\ \frac{m^2}{s}$. Taking into account these material properties and that $t = 120\ s$, Eqn. (4.41) yields $r_0 > 0.027\ m$ and Eqn. (4.42) yields $l > 0.053\ m$. The pebble bed is not an axisymmetric body, it has a height of $0.022\ m$ and a length of $0.118\ m$: while the length meets the condition of $r_0 > 0.027\ m$, the height does not. However, the height is relatively close and the combination could be considered as marginally acceptable. On the other side, as the heater 3 has a length of $0.175\ m$, Eqn. (4.42) is fulfilled.

The effective thermal conductivity of the Li_4SiO_4 pebble bed measured in PREMUX at an average temperature of ~35 °C has been $k_{eff}^{Li_4SiO_4} = (0.788\ \pm 0.295)\ \mathrm{W/mK}$, where the uncertainty is expressed with a coverage factor 2. The expected value is in good agreement[12] when compared with the value of Reimann and Hermsmeyer (2002a) in Eqn. (4.2)) at the same temperature, $k_{eff}^{Li_4SiO_4} = 0.786\ \mathrm{W/mK}$. This, together with the high packing factor obtained during the filling process of PREMUX (Section 3.3.2) supports the hypothesis of a low pebble bed disturbance due to the presence of the heater system. The outcomes of the uncertainty analyses of the thermal conductivity experiments are summarized in Figure 4.16.

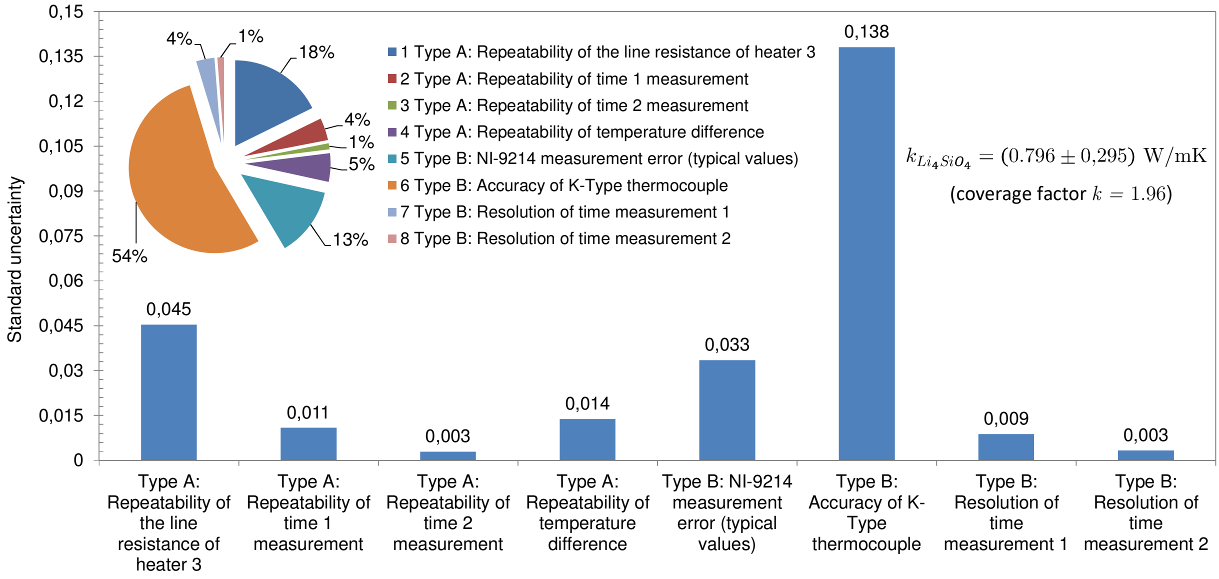

Figure 4.16: Uncertainty analysis of the Li_4SiO_4 thermal conductivity at room temperature. Plot of the absolute partial standard uncertainties for each type of error source (coverage factor $k = 1.96$) and detail of the uncertainty contributions relative to the total uncertainty of the thermal conductivity. The highest uncertainties are the ones associated to the accuracy of the K-type thermocouple, which represents a 54% of the total uncertainty, followed by the accuracy of the heater line resistance (18%) and the typical measurement error of the data acquisition system (NI-9214), with 13%. It can be identified that 87% of the total uncertainty in the thermal conductivity measurement has its origin in Type B sources.

---

[12] Only a qualitative evaluation is possible, as information about the uncertainty of the expression of $k_{eff}^{Li_4SiO_4}$ after Reimann and Hermsmeyer (2002a) is not given by these authors.

As it can be seen, the main uncertainty contributor is the accuracy of the K-type thermocouple. This uncertainty could be reduced by 60% in case of using an instrument with higher accuracy as, for instance, a grade A resistance temperature detector.

4.5.2 Experimental results for the determination of the influence of the purge gas pressure in the temperature of the Li_4SiO_4 pebble bed

A second class of additional tests performed in PREMUX aims at determining the influence of the purge gas pressure in the temperature distribution in the Li_4SiO_4 pebble bed. Previous studies from Reimann and Hermsmeyer (2002a) concluded that the change of conductivity with the purge gas pressure is negligible: these results are reproduced in PREMUX here.

Taking as reference the results obtained at the HI power level and for a purge gas pressure of 4 *bar* obtained in Section 5.3, these have been repeated reducing the purge gas pressure to 2 *bar*. The results for both experiments are shown in Figure 4.17 (measurement uncertainties expressed with coverage factor 2). Here it can be observed, that there are no significant temperature differences between both tests, confirming the results of Reimann and Hermsmeyer (2002a).

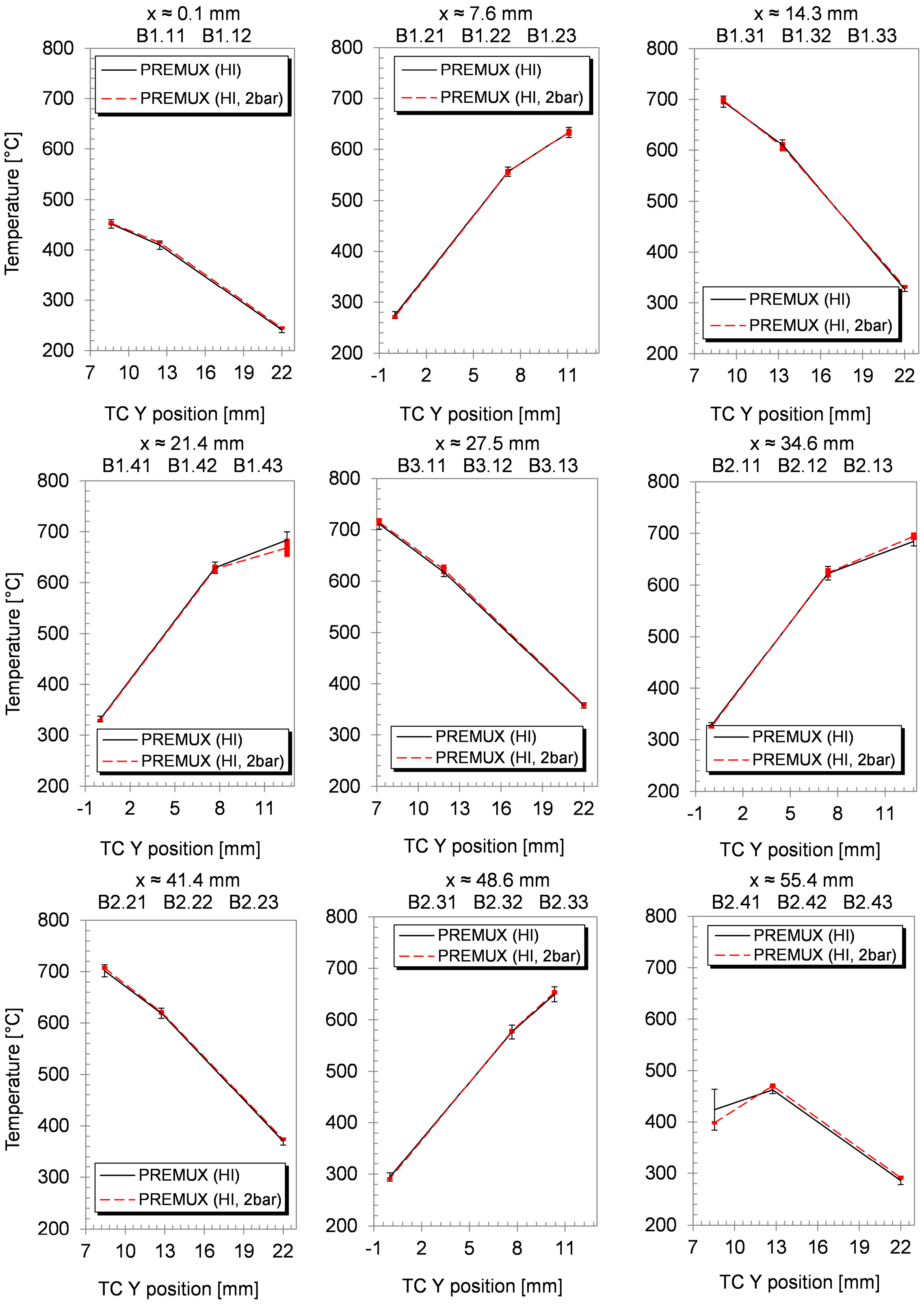

Figure 4.17: Comparison between the pebble bed temperatures with a purge gas pressure of 2 bar and 4 bar at the steady state for the "HI" power level (1100W total heating power). The uncertanity bars represents a confidence interval of 95% (coverage factor 2). It can be noticed that the purge gas pressure has not signifficant influence to the pebble bed temperatures in the range from 2 *bar* to 4 *bar*.

Chapter 5

Development of a simplified thermo-mechanical model for pebble beds and application to PREMUX

Due to the reduced size of the pebbles, usually of an order of magnitude between 10^{-4} m to 10^{-3} m (Reimann et al., 2005), the pebble bed in a HCPB Breeder Unit can be idealized as a continuum with nonlinear elasticity and pressure-dependent onset on yielding, together with creep and swelling thermo-mechanical properties. In order to predict this behavior, finite element codes offer phenomenological modeling techniques to implement the required physics of the pebble beds. However, the resulting codes tend to be numerically stiff and/or instable and computationally too costly to build complete models of the HCPB Breeder Units or to run numerous iterations.

The work presented in this Chapter continues the research performed by Gan (2008) with focus on cost-effective simulations by modeling with verified and optimized routines existing in the ANSYS code. In Gan's model (2008), the elasto-plastic material properties are expressed in terms of von Mises vs. hydrostatic pressure coordinates with a yield function constructed out of a piecewise function, which contrasts with the formulation developed in the present Chapter, based on the stress invariants coordinates with a single, smooth yield function. Appropriate transformations have been found and applied to map the parameters from Gan's customized subroutine into the ANSYS default elastic-plastic routines. Despite some important limitations of these default routines, they can be circumvented by accepting a multilinear approximation of the stress-strain of the pebble beds. The simplified model developed here reproduces the nonlinear elastic nature of the pebble beds, the pressure-dependent plasticity in conjunction with an isotropic hardening law and implements a thermal conductivity formulation as a function of the volumetric plastic strains and the temperature of the bed. A detailed description of the two models, the required transformations and its application to PREMUX are given in this Chapter.

5.1 Introduction

The effective thermal conductivity of Li_4SiO_4 pebble beds as the one studied in PREMUX is given by the expression after Reimnann and Hermsmeyer in Eqn. (4.2). For low temperatures,

ε_{vol}^{in} is usually small (e.g. see Chapter 8 of Gan (2008)) and Eqn. (4.2) is dominated by the temperature term. On the other side, for high temperatures ε_{vol}^{in} is larger, but the term associated to the temperature is still dominating in Eqn. (4.2), making the thermal conductivity of the Li_4SiO_4 pebble bed to be still mainly driven by the temperature. This is due to the fact that the Li_4SiO_4 pebble bed conductivity has a similar conductivity as the surrounding helium purge gas (Reimann et al., 2002b). This is a main motivation in the next Chapter to further simplify the thermo-mechanical assessment of PREMUX, which only contains a Li_4SiO_4 pebble bed. However, this is not the case for the Be beds, as the ε_{vol}^{in} has a large impact in the evaluation of the effective thermal conductivity, $k_{eff}^{Be}(T, \varepsilon_{vol}^{in})$. Reimann et al. (2006b) established the following empirical relationship for the $k_{eff}^{Be}(T, \varepsilon_{vol}^{in})$:

$$\begin{aligned} k_{eff}^{Be}(T, \varepsilon_{vol}^{in}) = {} & 1.81 + 0.0012 \cdot T - 5 \times 10^{-7} \cdot T^2 \\ & + (9.03 - 1.386 \times 10^{-3} \cdot T - 7.6 \times 10^{-6} \cdot T^2 + 2.1 \times 10^{-9} \cdot T^3) \cdot \varepsilon_{vol}^{in} \end{aligned} \tag{5.1}$$

As the volumetric strain increases due to the heating up of the pebble beds, so does also the thermal conductivity as a consequence of the increased contact area between the pebbles. This improvement of the thermal conductivity influences the temperature field in the pebble bed, which in turn directly influences the thermal expansion.

This temperature and strain dependence of the thermal conductivity expressions requires a fully coupled treatment of the thermo-mechanical behaviour of the pebble bed. Therefore, the development of coupled thermo-mechanical models is still essential for a predictive assessment of the thermo-mechanical functionality of the pebble beds in a HCPB breeder zone. However, these models are known to be numerically stiff and/or instable and time-consuming, facts that make the assessment of blanket assembly as a whole difficult, even assuming 2-dimensional idealizations of the components. With a correct definition of the boundary conditions, simplified blanket regions can be studied first with these models. Information of the mean strain states of the pebble beds in different areas of the blanket can be transferred to a more accurate thermal model (such as the one developed in the next Chapter) to treat the problem in a decoupled way, as a trade-off approach between physics reliability and a cost-efficient engineering design.

5.2 Code limitations and a workaround solution

5.2.1 Limitation on modeling nonlinear elasticity

The pebble beds in fusion blankets experience stress-dependent nonlinear elasticity, pressure-dependent yielding, rate-dependent plasticity (volumetric creep), irradiation-induced swelling and strain-dependent thermal conductivity during the reactor's operation. A model for the pebble bed thermo-mechanics for fusion blankets should integrate, ideally, all these phenomena.

While ANSYS offers a large range of material combinations for plasticity models, it lacks an appropriate element type in its library that can account with nonlinear elasticity in combination with pressure dependent plasticity models able to represent the compaction of the pebble bed, like the Drucker-Prager-Cap model (Sandler et al., 1976; Pelessone, 1989; Schwer & Murray, 1994). For nonlinear elasticity, ANSYS counts on two approaches: hyperelasticity (oriented to elastomers, foams or biological type materials) and multilinear elasticity. On the one side, the combination of hyperelasticity with a plastic model is incompatible, as the hyperelastic model does not account for energy dissipation due to plastic phenomena. On the other side, the multilinear elastic model supports energy dissipation, but it supports only the classic version of the Drucker-Prager yield criteria (Drucker & Prager, 1952), which is not suitable to represent the physics involved in the pebble considered here, as it will be discussed in Section 5.4.2. Furthermore, the Young modulus and thermal conductivity can be only temperature-dependent.

As an alternative, ANSYS offers the capability to write user-defined material subroutines (the so-called *UserMat* subroutines). However, and as stated in Section 2.4, the motivation of the model developed here is to keep as much as possible the default and already verified material definitions of ANSYS while keeping the essential characteristics of the pebble bed thermo-mechanics (nonlinear elasticity, Drucker-Prager-Cap plasticity). Altogether should lead to a simplified thermo-mechanical model to be easily used in the initial blanket design phases.

In order to overcome this first limitation of ANSYS, a multilinear elastic-plastic algorithm (from now on, referred to as "MEPLAS") has been developed. The working principle of this algorithm is depicted in Figure 5.1.

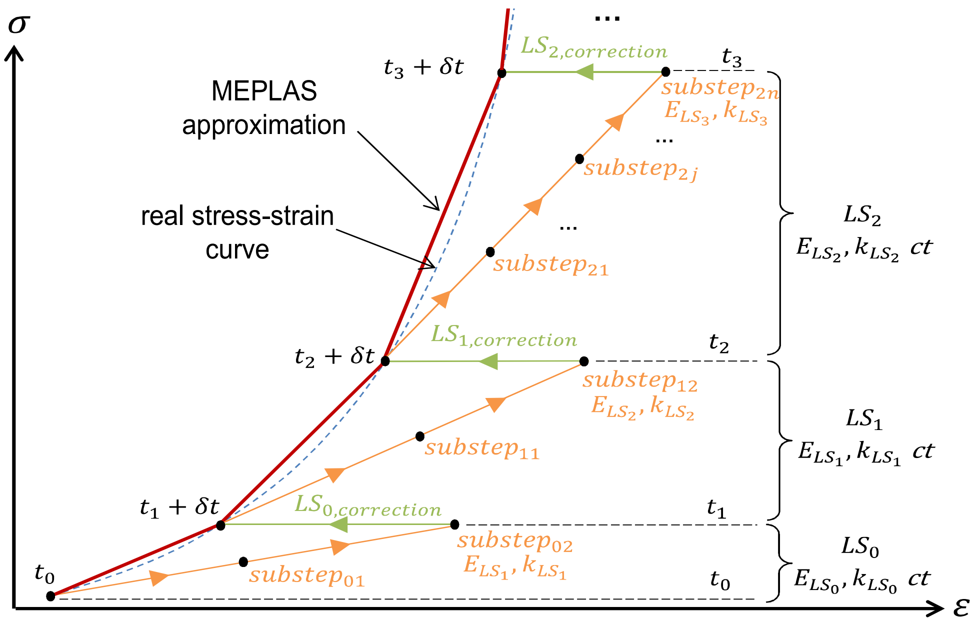

Figure 5.1: Conceptual graph of the MEPLAS algorithm. LS_0 represents the first load step, where some appropiate initial (constant) Young modulus E_{LS_0} and thermal conductivity k_{LS_0} for the pebble bed are defined. At a load step LS_i, several substeps ($substep_{ij}$) are performed during a fixed simulation time interval to reach the next LS_{i+1}: once the last substep ($substep_{in}$) has been reached, E_{LS_i} and k_{LS_i} are updated with the current information of the stress-state of the pebble bed and a final corrective substep of duration $\Delta t \to 0$ is performed for a to finally reach LS_{i+1}.

In the first load step (LS_0), an appropriate initial and constant Young modulus E_{LS_0} and thermal conductivity k_{LS_0} for the pebble bed are defined and a standard elastic-plastic iterative solution starts with the linear properties. A fixed time step is defined at the beginning of the iterative process, which sets the duration between any two adjacent load steps LS_i and LS_{i+1}

$(t_{i+1} - t_i = t_{j+1} - t_j, \forall i, j)$. Each LS_i is computed as a static system and each time step sets only progressive increments of thermal load from room temperature to the nominal operation condition, where in each of them equilibrium, compatibility and the fulfillment of the stress-strain laws are ensured by the code internal default solution subroutine and are reached before proceeding to the next LS_{i+1}. While being in a load step LS_i, the number of n substeps $(substep_{i1}, substep_{i2} \dots substep_{in})$ performed to reach the next LS_{i+1} is controlled by ANSYS and it is large enough to ensure the convergence and equilibrium of the current load step LS_i.

During a load step LS_i, the Young modulus E_{LS_i} and thermal conductivity k_{LS_i} remain constant. Once the equilibrium of LS_i is reached at a certain simulation time t in the $substep_{in}$, the (local) Young modulus and thermal conductivity of the pebble bed are updated with the current information of the stress-strain and temperature fields, leading to a new $E_{LS_{i+1}}$ and $k_{LS_{i+1}}$. These two new material properties will be used as in input for the next load step LS_{i+1}. At this point ($substep_{in}$, time t), a final iteration with the new $E_{LS_{i+1}}$ and k_{i+1} is performed at a time $t + \Delta t$, which corresponds to the starting point of the new LS_{i+1}. The increments of the external loads in this substep can be considered negligible by choosing an arbitrary small time increment Δt, which produces an iteration that has virtually the same thermal loads and strain as the one at time t, but with corrected material properties for the current stress state.

The algorithm is implemented as a User Command in ANSYS Workbench and although only steady state cases have been analysed in the present work, the algorithm could be used also for transient analyses with a minor modification in the algorithm.

5.2.2 Limitation on modelling stress-dependent material properties

By default, ANSYS restricts the linear material properties like Young modulus or thermal conductivity to be a function exclusively of the temperature. Dependencies on other variables like the stress state are not allowed by default: once the linear material properties of a material are defined in the pre-processor, they cannot be changed and they remain constant with respect to other variables, except for the temperature.

This second important limitation can be circumvented by defining *meta-elements* in which the Young modulus E_{LS_i} and the thermal conductivity k_{LS_i} properties are updated at the end of each converged load step LS_i. Figure 5.2 shows an example of a *meta-discretization* of a 2-dimensional finite element domain. During the pre-processing stage, the bounding box dimensions $(L \times H)$ for the whole finite element domain and for each meta-element $\mathcal{E}_i$ $(\Delta x \times \Delta y,$ where $\Delta x = x_{i+1} - x_i$ and $\Delta y = y_{i+1} - y_i)$ are defined. Then, appropriate linear material properties are given to all those finite elements e_l belonging to $\mathcal{E}_i$. The condition for $e_l \in \mathcal{E}_i$ is that the centroid of e_l is contained in the rectangular domain $\mathcal{R}$ of each $\mathcal{E}_i$ defined by $(x, y) \in \mathbb{R}^2 | (x_i \leq x \leq x_{i+1}) \bigwedge (y_i \leq y \leq y_{i+1})$.

During the execution of the MEPLAS algorithm, E_{LS_i} and k_{LS_i} of each $\mathcal{E}_i$ remain constant during a load step LS_i. At the end of LS_i, information of the stress and strain fields are read from the solution file and E_{LS_i} and k_{LS_i} are then updated giving $E_{LS_{i+1}}$ and $k_{LS_{i+1}}$.

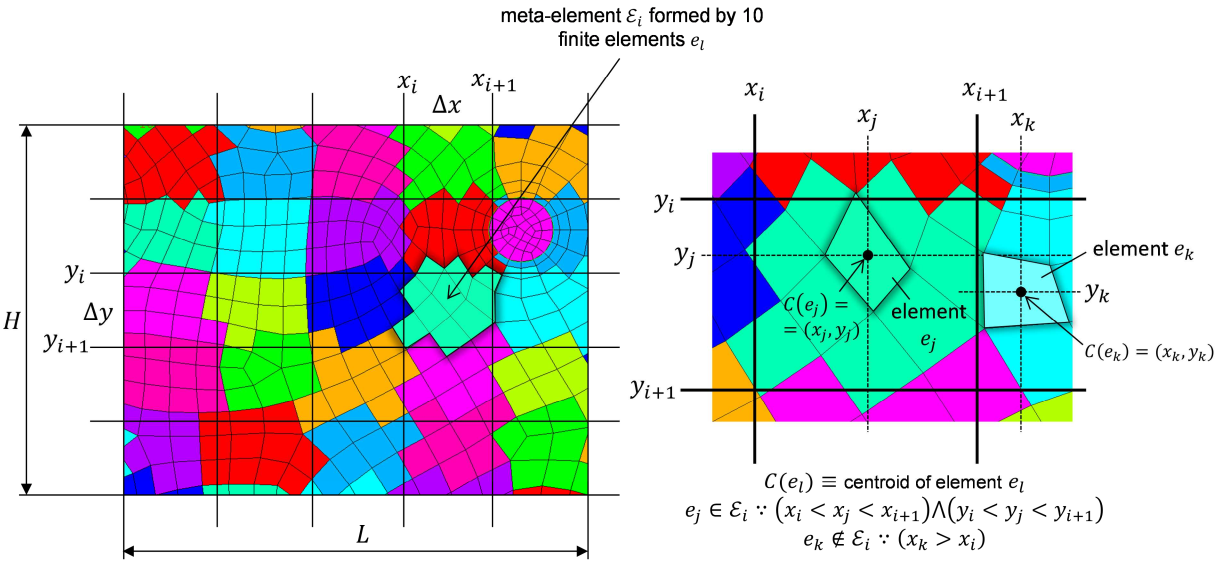

Figure 5.2: Example of meta-discretization of the finite element domain into meta-elements (2-dimensional case). Each meta-element $\mathcal{E}_i$ is bounded by a rectangular area $\mathcal{R} = \{(x, y) \in \mathbb{R}^2 \ |(x_i \leq x \leq x_{i+1}) \bigwedge (y_i \leq y \leq y_{i+1})\}$ and it is formed by a group of m finite elements e_l so that $\mathcal{E}_i = \bigcup_{l=1}^{m} e_l$ and $e_l \in \mathcal{E}_i \iff (x_i < x_l < x_{i+1}) \bigwedge (y_i < y_l < y_{i+1})$, where (x_l, y_l) are the centroid coordinates of e_l, $C(e_l)$.

This meta-discretization can be generalized for the case of 3-dimensional analyses. The meta-elements are represented in ANSYS as *element types* with a particular material number identifier. The only restriction identified with this method is the number of meta-elements (i.e. material identifiers) that ANSYS can handle, which is of $O(10^5)$ as of its version 14.5. However, this limit is currently not likely to be reached, as on the one side each meta-element can group several finite elements without a sensible loss of accuracy in the solution[13] and, on the other side, calculations with pebble beds involve normally an order of magnitude of $O(10^4)$ elements to keep reasonable calculation times. The definition of the size of the meta-element is flexible and can be as small as a finite element (i.e. $e_l \equiv \mathcal{E}_i$), or as big as the solution is still grid independent.

5.3 Implementation of the thermal conductivity and nonlinear elasticity

5.3.1 Strain-dependent thermal conductivity

For the calculation of the thermal conductivities of the Li_4SiO_4 and beryllium pebble beds, Eqs. (4.2) and (5.1) are implemented in the MEPLAS algorithm. Once a load step is finished, the algorithm scans through all the $\frac{H}{\Delta x} \cdot \frac{L}{\Delta y}$ meta-elements of the model, updating $k_{eff}^{Li_4SiO_4}$ and k_{eff}^{Be} with the last information of T and ε_{vol}^{in}.

---

[13] The solution accuracy with the meta-discretization method has been measured by performing sensitivity analysis on the size of the domain $\mathcal{R}$ of the meta-elements while applying this thermo-mechanical model to the case of the PREMUX mock-up.

5.3.2 Stress-dependent nonlinear elasticity

Experimental observations performed with uniaxial compression tests (e.g. Reimann & Müller, 1998; 2000; 2002b; Hofer & Kamlah, 2005) demonstrate the strong nonlinear plastic behaviour of the pebble beds. Reimann, et al. (2000) proposed a power law in order to express the Young modulus of the pebble bed as a function of its stress state:

$$E = A_e \sigma_e^n \ . \tag{5.2}$$

In the expression above, σ_e is an equivalent stress and n is an exponent determined experimentally. For the calculation of A_e a modified version of the one proposed by Gan and Kamlah (2007a) is used:

$$A_e = 2C_1^U \left(C_2^U + C_3^U T^{C_4^U}\right) f(\nu)^{1-\frac{n}{2}} \ , \tag{5.3}$$

with $n = C_5^U$, and

$$f(\nu) = \frac{(1+\nu)(1-2\nu)}{2(1-\nu)} \ . \tag{5.4}$$

The Poisson's ratio ν of the Li_4SiO_4 and beryllium pebble beds is $\nu = 0.25$ (Bühler, 1998).

Gan's expression for A_e includes an extra term $g(\varepsilon_{vol}^{in})$ used to adjust E in ABAQUS to the experimental loading/unloading paths in the uniaxial compression tests of Reimann, et al. (2006a). In the present work, this term has not been included, as the prediction without the first order functional $g(\varepsilon_{vol}^{in})$ has fitted well with the experimental results (Section 5.5).

The coefficients C_1^U, C_2^U, C_3^U, C_4^U and C_5^U of Eqn. (5.4) are derived from the so called "Reimann's fits" (Reimann et al., 2006a) for the unloading path of his uniaxial compression tests. The following table summarizes the "Reimann's fits" for both loading and unloading branches observed in the oedometric tests, as the loading path will be recalled later.

Table 5.1: Coefficients of the "Reimann fits" (Reimann et al., 2006a) for the loading and unloading paths of the uniaxial compression tests.

Fitting Curve: $\boldsymbol{\sigma^L = \left[C_1^L (C_2^L + C_3^L T^{C_4^L}) \varepsilon^{e+p}\right]^{\frac{1}{1-C_5^L}}}$			Fitting Curve: $\boldsymbol{\sigma^U = \left[C_1^U (C_2^U + C_3^U T^{C_4^U}) \varepsilon^{e}\right]^{\frac{1}{1-C_5^U}}}$		
Loading path			Unloading path		
Coefficient	Li_4SiO_4	Beryllium	Coefficient	Li_4SiO_4	Beryllium
$\boldsymbol{C_1^L}$	125.0	313.0	$\boldsymbol{C_1^U}$	176.0	1074.0
$\boldsymbol{C_2^L}$	1.0	1.0	$\boldsymbol{C_2^U}$	1.0	1.0
$\boldsymbol{C_3^L}$	$-9.6 \cdot 10^{-10}$	0.0	$\boldsymbol{C_3^U}$	0.0	0.0
$\boldsymbol{C_4^L}$	3.0	0.0	$\boldsymbol{C_4^U}$	3.0	0.0
$\boldsymbol{C_5^L}$	0.50	0.33	$\boldsymbol{C_5^U}$	0.66	0.6

Taking into account Eqs. (5.3), (5.4) and Table 5.1, the following values for A_e are found:

$$\begin{aligned} A_e|_{Li_4SiO_4} &= 195.8 \ , \\ A_e|_{Be} &= 895.0 \ . \end{aligned} \tag{5.5}$$

As already identified by Gan (2008), the research of Coube (1998) on powder die compaction has strong similarities with the power law of Reimann, et al. in Eqn. (5.2). Coube proposed the following functional form for the Young modulus for his pebble beds:

$$E = E_0 + A_e \left[\frac{3}{2}(1-2\nu)p^2 + \frac{1+\nu}{3}q^2\right]^{\frac{n}{2}} \ , \tag{5.6}$$

where p is the hydrostatic pressure, q the von Mises stresses and

$$E_0 \to 0 \ , \tag{5.7}$$

taking into account Eqn. (5.2).

With Eqn. (5.2) and (5.6) the equivalent stress σ_e can be written as:

$$\sigma_e = \sqrt{\left[\frac{3}{2}(1-2\nu)p^2 + \frac{1+\nu}{3}q^2\right]} \ . \tag{5.8}$$

In a similar way as for the thermal conductivity, all these expressions with the indicated values for the corresponding parameters have been implemented in the MEPLAS algorithm in ANSYS. The stress-state of the pebble bed is retrieved after the completion of a load step for the update of σ_e and then the Young modulus E is recalculated according to Eqn. (5.2).

5.4 The Drucker-Prager Cap yield criterion, plastic flow potential, isotropic hardening law and formulation differences

Some fundamental expressions and stress relationships from the Theory of Continuum Mechanics and Plasticity (Wu, 2005) are recalled here and used afterwards to introduce the formulation differences in the plasticity models implemented in the most used Finite Element (FE) codes in the area of nuclear fusion, namely ANSYS and ABAQUS.

5.4.1 The Stress Tensor: Principal components and stress invariants

Following Cauchy's law, the stress tensor $\overline{\overline{\boldsymbol{\sigma}}} \in \mathbb{R}^{3\times 3}$ defines a linear mapping on an orthonormal vector base of vectors $\boldsymbol{e}_x$, $\boldsymbol{e}_y$, $\boldsymbol{e}_z$ between a unit normal vector $\boldsymbol{n} = n_x\boldsymbol{e}_x + n_y\boldsymbol{e}_y + n_z\boldsymbol{e}_z$ on a solid's surface and the vector of forces per unit surface $\boldsymbol{t} = t_x\boldsymbol{e}_x + t_y\boldsymbol{e}_y + t_z\boldsymbol{e}_z$ (traction vector):

$$\boldsymbol{t} = \overline{\overline{\boldsymbol{\sigma}}} \cdot \boldsymbol{n} \Longleftrightarrow \begin{bmatrix} t_x \\ t_y \\ t_z \end{bmatrix} = \begin{bmatrix} \sigma_{xx} & \sigma_{xy} & \sigma_{xz} \\ \sigma_{yx} & \sigma_{yy} & \sigma_{yz} \\ \sigma_{zx} & \sigma_{zy} & \sigma_{zz} \end{bmatrix} \begin{bmatrix} n_x \\ n_y \\ n_z \end{bmatrix} \ . \tag{5.9}$$

Applying Cauchy's second law of motion it can be proved that the stress tensor is symmetric, meaning that $\sigma_{ij} = \sigma_{ji}$. This symmetry property ensures that it will always exist an orthonormal base of eigenvectors ($\boldsymbol{\sigma}_1$, $\boldsymbol{\sigma}_2$, $\boldsymbol{\sigma}_3$) where the stress tensor is diagonal. These eigenvectors constitute the principal stress directions and their associated eigenvalues σ_1, σ_2, σ_3 (or $\sigma_I = \max\{\sigma_1, \sigma_2, \sigma_3\}$, $\sigma_{III} = \min\{\sigma_1, \sigma_2, \sigma_3\}$ and $\sigma_{II} = \{\sigma_1, \sigma_2, \sigma_3\} - \{\sigma_I, \sigma_{III}\}$) are the principal stresses.

The stress tensor can be decomposed into a hydrostatic $\bar{\bar{\boldsymbol{P}}}$ and a deviatoric $\bar{\bar{\boldsymbol{S}}}$ part, so that $\bar{\bar{\boldsymbol{\sigma}}} = \bar{\bar{\boldsymbol{P}}} + \bar{\bar{\boldsymbol{S}}}$:

$$\begin{bmatrix} \sigma_{xx} & \sigma_{xy} & \sigma_{xz} \\ \sigma_{yx} & \sigma_{yy} & \sigma_{yz} \\ \sigma_{zx} & \sigma_{zy} & \sigma_{zz} \end{bmatrix} = \begin{bmatrix} p & 0 & 0 \\ 0 & p & 0 \\ 0 & 0 & p \end{bmatrix} + \begin{bmatrix} \sigma_{xx} - p & \sigma_{xy} & \sigma_{xz} \\ \sigma_{yx} & \sigma_{yy} - p & \sigma_{yz} \\ \sigma_{zx} & \sigma_{zy} & \sigma_{zz} - p \end{bmatrix} , \tag{5.10}$$

where

$$\bar{\bar{\boldsymbol{P}}} = \begin{bmatrix} p & 0 & 0 \\ 0 & p & 0 \\ 0 & 0 & p \end{bmatrix} , \tag{5.11}$$

$$\bar{\bar{\boldsymbol{S}}} = \begin{bmatrix} s_{xx} & s_{xy} & s_{xz} \\ s_{yx} & s_{yy} & s_{yz} \\ s_{zx} & s_{zy} & s_{zz} \end{bmatrix} = \begin{bmatrix} \sigma_{xx} - p & \sigma_{xy} & \sigma_{xz} \\ \sigma_{yx} & \sigma_{yy} - p & \sigma_{yz} \\ \sigma_{zx} & \sigma_{zy} & \sigma_{zz} - p \end{bmatrix} . \tag{5.12}$$

The term p is the mean stress or *hydrostatic pressure*. Despite its name, care has to be taken to differentiate a *compressive hydrostatic pressure* $-p$ from p. Therefore and to avoid confusion, the nomenclature $\bar{x} = -x$ is taken to represent negative magnitudes.

The deviatoric tensor is, as $\bar{\bar{\boldsymbol{\sigma}}}$, symmetric and thus, diagonalizable. $\bar{\bar{\boldsymbol{S}}}$ is of especial interest in the analysis of plasticity, as it is often considered the sole initiator of the yield mechanism in some of the most used yield criteria in materials (e.g. von Mises and Tresca-Guest criteria).

If the above expressions in Eqs. (5.11) and (5.12) are considered in the case of a base of eigenvectors, then the following relations are found:

$$s_1 = \sigma_1 - \frac{1}{3}(\sigma_1 + \sigma_2 + \sigma_3) , \tag{5.13}$$

$$s_2 = \sigma_2 - \frac{1}{3}(\sigma_1 + \sigma_2 + \sigma_3) , \tag{5.14}$$

$$s_3 = \sigma_3 - \frac{1}{3}(\sigma_1 + \sigma_2 + \sigma_3) . \tag{5.15}$$

The calculation of the principal deviatoric stresses (s_1, s_2, s_3) results from solving the characteristic equation of $\bar{\bar{\boldsymbol{S}}}$. This is obtained by imposing $\det\left(\bar{\bar{\boldsymbol{S}}} - \sigma\bar{\bar{\boldsymbol{I}}}\right) = 0$, where $\bar{\bar{\boldsymbol{I}}}$ is the identity matrix:

$$s^3 - J_1 s^2 + J_2 s - J_3 = 0 . \tag{5.16}$$

The 3 roots of Eqn. (5.16) are the principal deviatoric stresses (s_1, s_2, s_3) and the coefficients J_1, J_2, J_3 are the stress invariants of $\bar{\bar{\boldsymbol{S}}}$. If the diagonal form of $\bar{\bar{\boldsymbol{S}}}$ is taken, then the stress invariants of $\bar{\bar{\boldsymbol{S}}}$ can be calculated using the components of s_i:

$$J_1 = s_1 + s_2 + s_3 = 0 , \tag{5.17}$$

$$J_2 = \frac{1}{2}(s_1^2 + s_2^2 + s_3^2) \ , \tag{5.18}$$

$$J_3 = s_1 s_2 s_3 \ . \tag{5.19}$$

The same procedure can be applied to obtain the stress invariants of $\bar{\bar{\boldsymbol{\sigma}}}$:

$$I_1 = \sigma_1 + \sigma_2 + \sigma_3 \ , \tag{5.20}$$

$$I_2 = \sigma_1\sigma_2 + \sigma_2\sigma_3 + \sigma_3\sigma_1 \ , \tag{5.21}$$

$$I_3 = \sigma_1\sigma_2\sigma_3 \ . \tag{5.22}$$

It can be noticed that $J_1 = \mathrm{tr}\bar{\bar{\boldsymbol{S}}} = 0$, $J_2 > 0$ always and J_2 corresponds to the (squared) equivalent shear stress τ^2 (being $sign(\tau) = sign(J_3)$) and $I_1 = \mathrm{tr}\bar{\bar{\boldsymbol{\sigma}}}$, while I_3 and J_3 corresponds to the $\det\bar{\bar{\boldsymbol{S}}}$ and $\det\bar{\bar{\boldsymbol{\sigma}}}$ respectively.

Due to the linearity of this operator the trace operator reads to:

$$\mathrm{tr}\bar{\bar{\boldsymbol{\sigma}}} = \mathrm{tr}\left(\bar{\bar{\boldsymbol{P}}} + \bar{\bar{\boldsymbol{S}}}\right) = \mathrm{tr}\left(\bar{\bar{\boldsymbol{P}}}\right) + \mathrm{tr}\left(\bar{\bar{\boldsymbol{S}}}\right) \ . \tag{5.23}$$

Alternatively, and knowing that $\mathrm{tr}\bar{\bar{\boldsymbol{S}}} = 0$, then Eqn. (5.23) reads:

$$\sigma_1 + \sigma_2 + \sigma_3 = 3p \ , \tag{5.24}$$

and as $\sigma_1 + \sigma_2 + \sigma_3 = I_1$ (Eqn. (5.20)), the following relationship applies:

$$p = \frac{1}{3} I_1 \ . \tag{5.25}$$

The stress invariants of $\bar{\bar{\boldsymbol{\sigma}}}$ and $\bar{\bar{\boldsymbol{S}}}$ are not all independent from each other. The following relationships can be found by means of the relations in Eqs. (5.13), (5.14) and (5.15):

$$J_2 = \frac{1}{6}[(\sigma_1 - \sigma_2)^2 + (\sigma_2 - \sigma_3)^2 + (\sigma_3 - \sigma_1)^2] = \frac{1}{3} I_1^2 - I_2 \ , \tag{5.26}$$

$$J_3 = \frac{2}{27} I_1^3 - \frac{1}{3} I_1 I_2 + I_3 \ . \tag{5.27}$$

A coordinate system can be defined considering the stress invariants (Figure 5.3, left), where the I_1 axis is defined by $\sigma_1 = \sigma_2 = \sigma_3$ (thus parallel to the hydrostatic pressure p) and the J_2 and J_3 are contained in the so-called π-*plane*. The π-plane is perpendicular to I_1 and here the material only experiences deviatoric stresses.

In an uniaxial compression test the pebble bed is usually compressed in a cylindrical container and two of the principal stresses are equal to the lateral stress σ_{Lat} on the cylindrical container, while the third principal stress equals to the axial stress σ_{Axi}. Under these conditions the stress invariants reads:

$$I_1 = \sigma_1 + \sigma_2 + \sigma_3 = \sigma_{Axi} + 2\sigma_{Lat} \ , \tag{5.28}$$

$$J_2 = \frac{1}{3} I_1^2 - I_2 = \frac{1}{3}(\sigma_{Axi} - \sigma_{Lat})^2 \ , \tag{5.29}$$

$$J_3 = \frac{2}{27}(\sigma_{Axi} - \sigma_{Lat})^3 \ . \tag{5.30}$$

Then, the pebble bed is said to be in *triaxial extension* when the lateral stress is higher than the axial stress ($\sigma_{Axi} < \sigma_{Lat}$, therefore $\tau < 0$), while in a *triaxial compression* the axial compressive stress is higher than the lateral stress ($\sigma_{Axi} > \sigma_{Lat}$, therefore $\tau > 0$). More generally, given an initial $\bar{I}_1 > 0$, a granular material experiences triaxial extension when loaded in a positive principal stress direction and is under triaxial compression when loaded in a negative principal stress direction. Normally, the pebble beds and the granular materials in general present different yield levels depending if they are under a triaxial extension or compression stresses (Foster et al., 2005). To help modelling this different yield behavior, a Haigh-Westergaard coordinate system (Figure 5.3, right) can be defined in this π-plane. In this coordinate system, ρ is the radial and β_L the polar coordinate, also known as *Lode angle*, which is normally defined from -30° for the case of triaxial extension, going through 0° at pure a shear stress state and finishing at 30° at the triaxial compression state

The second deviatoric invariant J_2 is used by von Mises (1913) to build his yield criterion and J_3 is used in the Drucker-Prager Cap yield surface to take into account the difference in yield strength of a material in a stress plane perpendicular to the I_1 axis. Therefore, I_1, J_2 and J_3 are most often chosen to represent the three independent stress invariants of the stress tensor due to their utility for the analysis of plasticity.

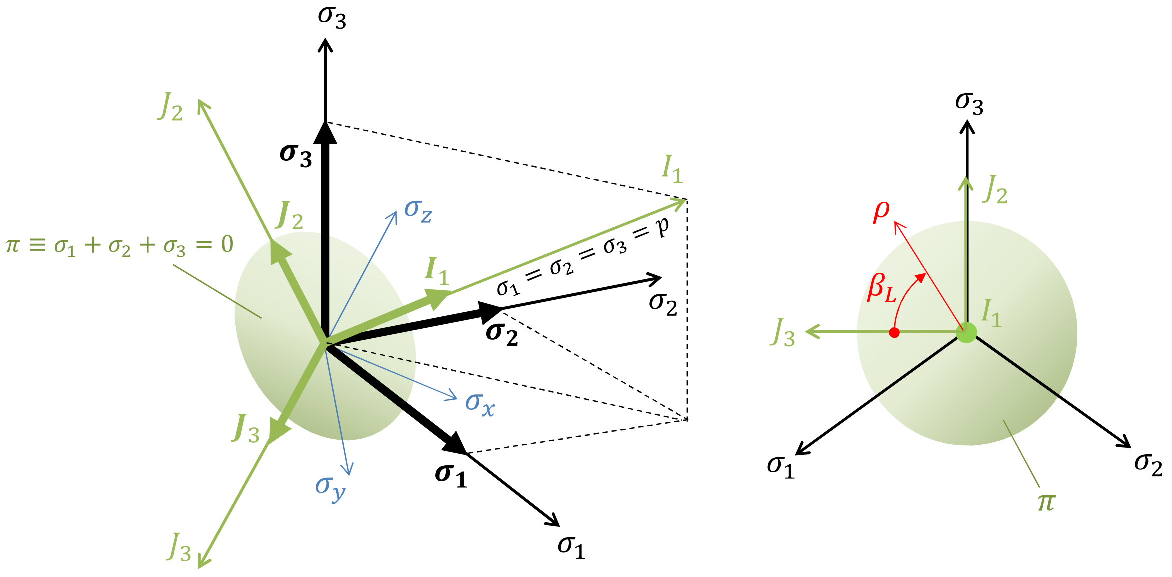

Figure 5.3: Left: an orthonormal axis system (blue), principal stress directions (black) and invariant stress directions (green). Right: view on the π-plane, detail of the Haight-Westergaard coordinates (in red) that are used for the representation of the differences in yield behavior of a granular material under triaxial compression or tension stresses in this plane.

5.4.2 Yield criteria and the Drucker-Prager Cap yield surface

The onset of yield in a material is considered to happen when its stress state is located on a yield surface Y, which takes the form of a functional relationship between the stress components of the stress tensor.

In the case of the von Mises criterion (1913), Y_{vM} is defined as:

$$Y_{vM}(\sigma_1, \sigma_2, \sigma_3) \equiv \sqrt{\frac{1}{2}[(\sigma_1 - \sigma_2)^2 + (\sigma_2 - \sigma_3)^2 + (\sigma_3 - \sigma_1)^2]} = \sigma_Y \ , \tag{5.31}$$

where σ_Y is the material's yield stress found from tensile tests and the left term corresponds to the von-Mises stress q.

Considering Eqn. (5.26), the von Mises yield surface can be expressed as a function of J_2:

$$Y_{vM}(J_2) \equiv \sqrt{3J_2} = \sigma_Y \ , \tag{5.32}$$

and then, in terms of stress invariants, the von Mises stress reads:

$$q = \sqrt{3J_2} = \sqrt{3}\tau \ . \tag{5.33}$$

Geometrically, Y_{vM} corresponds to a cylinder with axis coincident with $\bar{I}_1$ and radius equal to σ_Y (Figure 5.4 (a)). For the case of ductile materials, once the stress state will reach σ_Y the material will harden, increasing the value of σ_Y and thus enlarging the radius of the cylinder. It can be noticed that Y_{vM} does not make distinctions between compressive or tensile stresses and it is therefore not suitable for the study of plasticity of granular materials, as this kind of materials normally have a very limited or zero cohesion (I_1 axis) and their yield strength increases with increasing $\bar{p}$.

A closer representation of the yield phenomena for geomaterials is given by the classical Mohr-Coulomb theory (Coulomb, C. A., 1773). In this theory, the shear failure stress increase proportionally to $\bar{I}_1$ with a slope $\tan\beta_{MC}$, where β_{MC} is the so-called *Mohr-Coulomb friction angle*. The Mohr-Coulomb in invariant coordinates reads:

$$Y_{MC}(I_1, J_2, \beta_L) \equiv \sqrt{J_2} = \frac{C_0 \cos\beta_{MC} - \frac{I_1}{3}\sin\beta_{MC}}{\cos\beta_L - \frac{I_1}{\sqrt{3}}\sin\beta_L \sin\beta_{MC}} \ , \tag{5.34}$$

where C_0 is a material parameter indicating a residual cohesive internal stress at zero applied load. The resulting yield surface corresponds to a pyramid with an irregular hexagonal base (Figure 5.4 (b)). Y_{MC} can characterize the dependency of the shear failure on the hydrostatic pressure, which is a basic characteristic of the granular materials and also the different yield behaviour between triaxial compression and extension loads, which is a common feature for granual materials. Indeed, for triaxial compression ($\beta_L = 30°$):

$$Y_{MC}(I_1, J_2)|_{\beta_L=30°} \equiv \sqrt{J_2} = \frac{2\sqrt{3}}{3 - \sin\beta_{MC}}\left(C_0 \cos\beta_{MC} - \frac{I_1}{3}\sin\beta_{MC}\right) \ , \tag{5.35}$$

and for triaxial extension ($\beta_L = -30°$):

$$Y_{MC}(I_1, J_2)|_{\beta_L=-30°} \equiv \sqrt{J_2} = \frac{2\sqrt{3}}{3 + \sin\beta_{MC}}\left(C_0 \cos\beta_{MC} - \frac{I_1}{3}\sin\beta_{MC}\right) \ . \tag{5.36}$$

A ratio between triaxial extension to triaxial compression ψ can be then defined and for the Mohr-Coulomb yield surface reads:

$$\psi = \frac{3 - \sin\beta_{MC}}{3 + \sin\beta_{MC}} \,. \tag{5.37}$$

Fossum and Bannon (2004) observed that the slope of the shear failure surface at a triaxial compression state is related to ψ as:

$$\psi = \frac{1}{1 + \sqrt{3}\left(\dfrac{\partial\sqrt{J_2}}{\partial \bar{I}_1}\right)\Bigg|_{\beta_L = 30°}} \,. \tag{5.38}$$

Despite the improved representation given by the Mohr-Coulomb yield surface, the presence of sharp edges in Y_{MC} makes its numerical treatment difficult at the pyramid's edges. A smooth alternative is the one given by Drucker and Prager (1952), who modified the von Mises criterion introducing also the dependence of the yield surface on the hydrostatic pressure p (i.e. on I_1) as in the Mohr-Coulomb surface, leading to the classic Drucker-Prager yield criterion:

$$Y_{DP}(I_1, J_2) \equiv \alpha I_1 + \sqrt{J_2} - \sigma_0 = 0 \,. \tag{5.39}$$

Y_{DP} is a cone with axis aligned with I_1. α is the slope of the generatrix with the I_1 axis and has a direct relationship to the so-called *Drucker-Prager friction angle* β, which will be shown in Section 5.4.3, while σ_0 defines the position of the apex (Figure 5.4 (c)).

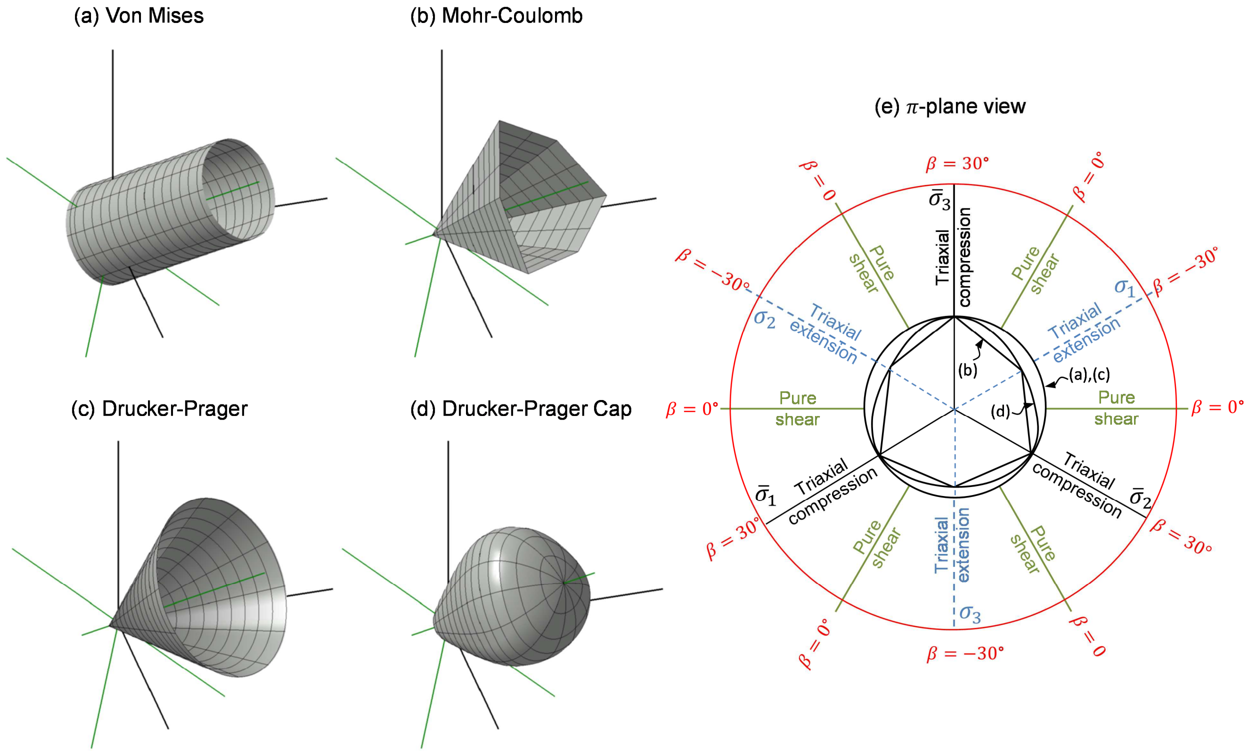

Figure 5.4: From (a) to (d): Topology comparison between von Mises, Mohr-Coulomb, Drucker-Prager and (smooth) Drucker-Prager Cap yield surfaces, with a representation of the principal and invariant axes (compressive region). Figure (e): representation of the π-*plane* with detail of the main stress states and comparison between the yield surfaces. It can be observed that the smooth Drucker-Prager Cap surface can be seen as the smooth approximation of the Mohr-Coulomb one, with the addition of the compaction cap.

Y_{DP} assumes a directly proportional increase (proportionality factor given by the parameter α) in the shear failure after an increase of I_1. Also, and as it happens in the Mohr-Coulomb criteria, elastic behavior of the material is expected in this model for any stress state confined inside the infinite long cone defined by Y_{DP}, otherwise the material experience shear failure when the load reaches the yield surface.

As it happens for Y_{vM} and Y_{MC}, the Drucker-Prager yield surface does not bound the elastic deformation of the for stress states inside Y_{DP}. However, it is observed that granular materials yield practically from the beginning of the load application, which differs from the model proposed by Drucker and Prager. This results in a need for an additional part in the yield surface, the so-called *hardening* or *compaction cap,* which bounds the stress in the vicinity of I_1: once the stress state reaches the cap surface, the granular material yields and hardens itself, without failure, i.e. while hardening under increasing loading, the cap also expands, defining new loci for the yield strength.

The addition of the caps to the original Drucker-Prager yield surface was first proposed by Drucker, Gibson and Henkel (1955) and led to the so-called Drucker-Prager Cap yield surface. This yield function Y_{DPC}^{Piece} was defined then as *piecewise* expression consisting of the Drucker-Prager shear failure cone and the compaction caps, which were assumed as spherical surfaces (Figure 5.5 (a), (b) and (c)).

Sandler and DiMaggio (1976) generalized the proposal of Drucker, Gibson and Henkel (1955) by assuming an exponential shear failure surface and an elliptical compaction cap, also in a *piecewise* functional form. The exponential part for the shear failure was introduced in order to accommodate better fittings with the available experimental data on different granular materials. This has been found to be a more accurate representation of the shear failure, as the linear dependence defined by the Mohr-Coulomb or the Drucker-Prager criteria tends to exaggerate the yield strength of the geomaterial at high pressures (Foster et al., 2005). On the other side, elliptical caps have been observed to fit better the experimental data than the circular ones (Coube, 1998; Pavier, E., 1998; Riera, M. D., 1999).

As it happens for the Mohr-Coulomb yield surface, an important drawback of the Y_{DPC}^{Piece} as defined by Sandler and DiMaggio (1976) is the presence of a non-smooth geometry, in this case in form of a singular corner at the connection between the exponential shear failure surface and the elliptical cap surface. The numerical implementation of these yield surfaces is not robust and arises integration and convergence problems at the singularities, where the derivatives are not unique.

However, Pelessone (1989)[14] proposed a smooth, single equation Drucker-Prager Cap yield surface (Y_{DPC}^{Smooth}). This Y_{DPC}^{Smooth} is composed by 3 surfaces (Figure 5.4 (d) and Figure 5.6,

---

[14] While Pelessone (1989) introduced the concept of a single, smooth yield surface, many others made key contributions, especially in the area of continuous and smooth cap models, see e.g. Lade and Kim (1988b), Schwer and Murray (1994), Swan and Seo (1999), Fossum and Fredrich (2000), Foster et al. (2005) and Xia and Masud (2006).

right), namely the shear failure envelope $Y_s(I_1)$, the compaction cap $Y_c(I_1, K_0)$ and the *expansion cap* $Y_t(I_1)$, all 3 smoothly joined and modulated by the Lode function $\Gamma^2(\beta_L)$:

$$Y_{DPC}^{Smooth}(I_1, J_2, J_3, K_0) \equiv \Gamma^2(\beta_L) J_2 - Y_s^2(I_1) Y_c(I_1, K_0) Y_t(I_1) = 0 \ . \tag{5.40}$$

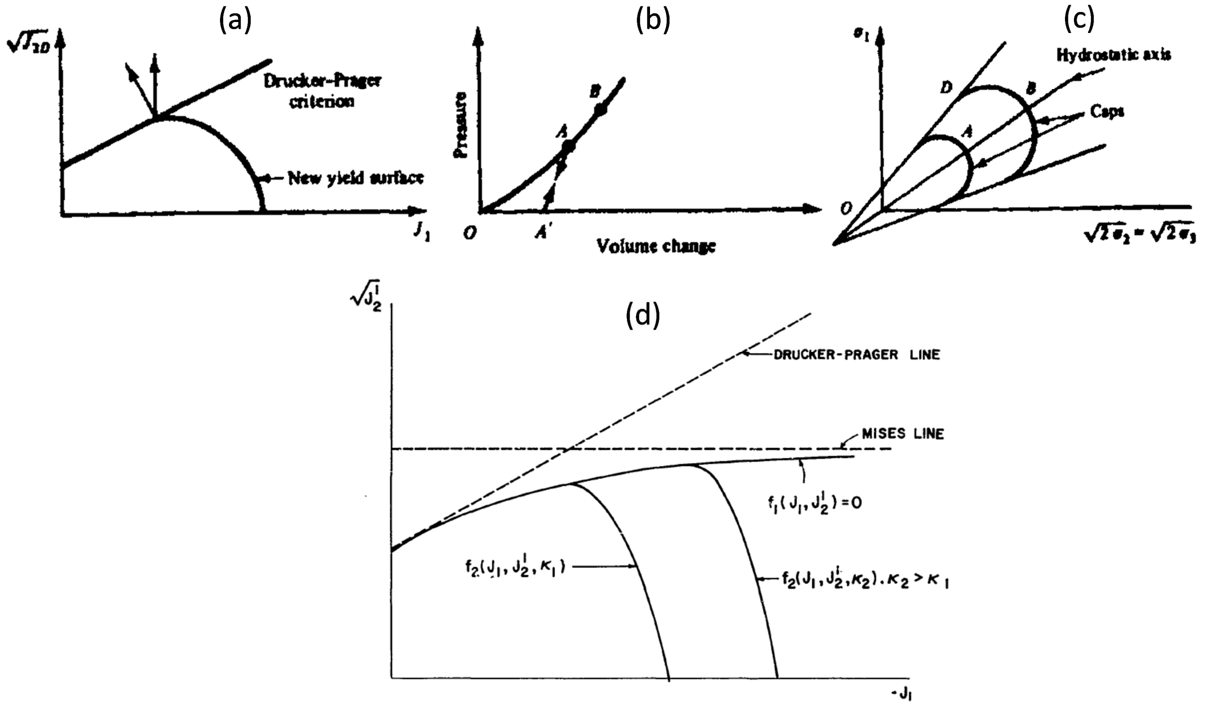

Figure 5.5: Top: Drucker-Prager Cap piecewise yield surface by Drucker, Gibson and Henkel (1955). (a) shows the Drucker-Prager shear failure line and the addition of the "new yield surface" (circular cap). (b) indicates the volume change under a load path A'-A-B. (c) depicts the effect of the cap displacement from A to B under compaction stresses. Bottom: Generalized (piecewise) Drucker-Prager Cap yield surface by Sandler, DiMaggio and Baladi (1976), with detail of the shear failure surface f_1 and the eliptical hardening cap f_2 in 2 compaction situations.

The Lode function Γ^2 (β_L) is expressed as:

$$\Gamma(\beta_L) = \frac{1}{2}\left(1 + \sin 3\beta_L + \frac{1}{\psi}(1 - \sin 3\beta_L)\right) \ , \tag{5.41}$$

and it takes into account the different yield behavior in the π-plane (Figure 5.6, left). ψ is the ratio of triaxial extension to triaxial compression strengths, and

$$\beta_L(J_2, J_3) = -\frac{1}{2}\sin^{-1}\left(\frac{3\sqrt{3}J_3}{2J_2^{\frac{3}{2}}}\right) \ , \tag{5.42}$$

is the Lode angle (defined from $-30° \leq \beta_L \leq 30°$). A requirement of the Lode function is that it must be convex to ensure also the convexity of Y_{DPC}^{Smooth}, which is fulfilled when $\frac{7}{9} \leq \psi \leq \frac{9}{7}$ (Fossum & Brannon, 2004).

The shear envelope Y_s (I_1) has the following expression:

$$Y_s(I_1) = \sigma_0 - Ae^{(\beta^Y I_1)} - \alpha^Y I_1 \ , \tag{5.43}$$

where σ_0, A, β^Y and α^Y are material parameters: σ_0 is related the cohesion of the pebble bed[15]; The exponential term $Ae^{(\beta^Y I_1)}$ allows a better, more flexible approximation of the shear envelope shape; And α^Y is the slope of the shear envelope with respect the I_1 axis as already seen in Eqn. (5.39).

The compaction cap $\boldsymbol{Y_c(I_1, K_0)}$ is expressed as:

$$Y_c(I_1, K_0) = 1 - H(K_0 - I_1)\left(\frac{I_1 - K_0}{R_c^Y Y_s(K_0)}\right)^2 . \tag{5.44}$$

Here, H is the Heaviside function and K_0 is the point on the $\bar{I}_1$ axis where Y_c starts to be combined with the shear envelope through the effect of H (Figure 5.6, right). When the hardening of the cap occurs, K_0 moves towards $\bar{I}_1$. R_c^Y is a material parameter expressing the ratio of a to b (Figure 5.6, right) of the compaction cap.

It is important to note an additional marker point X_0 in Figure 5.6 (right). This point indicates the intersection of the cap with $\bar{I}_1$ and it is involved in the hardening function that will be explained later in this Section. The relationship between K_0 and X_0 is given by:

$$X_o = K_o - R_c^Y Y_s(K_0) \ . \tag{5.45}$$

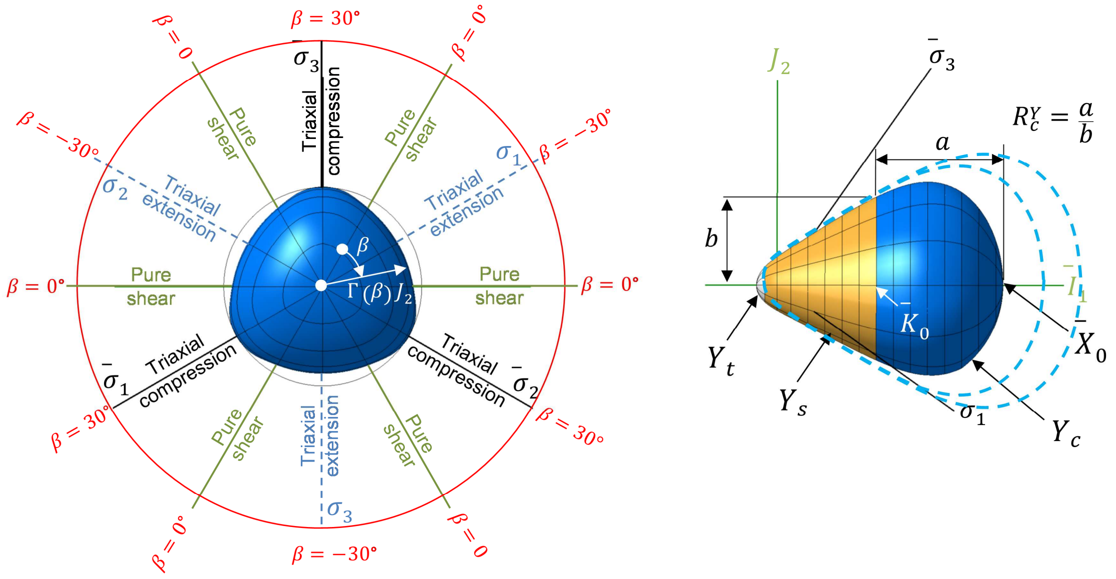

Figure 5.6: Drucker-Prager Cap yield surface. Left: view from the π-plane, detail of the Lode angle and representation of the triaxial compression, extension and pure shear directions. Right: parallel view to the $I_1 \times J_2$ plane and detail of the 3 yield functions forming the Y_{DPC}^{Smooth} surface. K_0 marks the point where the Heaviside function in Y_c starts to affect the product $Y_c Y_s^2$, combining both the shear envelope and the compaction cap. X_0 marks the intersection of the cap with $\bar{I}_1$.

---

[15] In granular materials, cohesion refers to the amount of (positive) hydrostatic pressure that it is able to bear, which is normally very low or negligible.

The expansion cap $\boldsymbol{Y_t(I_1, \sigma_0)}$ takes the form of:

$$Y_t(I_1, \sigma_0) = 1 - H(I_1) \left(\frac{I_1}{R_t^Y Y_s(0)} \right)^2 . \tag{5.46}$$

In this case, R_t^Y is a material parameter analog to R_c^Y in Eqn. (5.44) that represents a ratio of I_1 to J_2 of the expansion cap.

5.4.3 Formulations of the Drucker-Prager Cap yield surface in FE codes

Practically all the existing literature about pebble bed modeling in solid breeding blankets for fusion reactors is based on the use of the commercial code ABAQUS. The yield surface implemented in this code (from now on Y_{DPC}^{ABQ}) is similar to the formulation of Sandler and DiMaggio (1976), with the particularity of having a linear shear failure surface instead of the exponential one. The Y_{DPC}^{ABQ} is expressed in terms of hydrostatic (compressive) pressure $\bar{p}$ and von Mises stresses q and it is constructed piecewise by a shear envelope Y_s^{ABQ} and an elliptical compaction cap Y_c^{ABQ}. In order to alleviate the issues at the singularity corner joining Y_s^{ABQ} and Y_c^{ABQ}, a transition surface Y_t^{ABQ} is added to the piecewise definition of Y_{DPC}^{ABQ}:

$$Y_{DPC}^{ABQ} = \begin{cases} Y_s^{ABQ} \equiv t - \bar{p} \tan\beta + d = 0 \ , \\ Y_c^{ABQ} \equiv \sqrt{(\bar{p} - \bar{p}_a)^2 + \left[\dfrac{Rt}{1 + \alpha - \dfrac{\alpha}{\cos\beta}} \right]^2} - R(d + \bar{p}_a \tan\beta) = 0 \ , \\ Y_t^{ABQ} \equiv \sqrt{(\bar{p} - \bar{p}_a)^2 + \left[t - \left(1 - \dfrac{\alpha}{\cos\beta}\right)(d + \bar{p}_a \tan\beta) \right]^2} - \alpha(d + \bar{p}_a \tan\beta) = 0. \end{cases} \tag{5.47}$$

In Eqn. (5.47) (ABAQUS®, 2011), β is the Drucker-Prager friction angle and refers to the angle of the shear envelope slope with the $\bar{p}$ axis and d is related to the pebble bed cohesion in an equivalent way to σ_0 in Eqn. (5.43). α is a small value activating the transition surface Y_t^{ABQ}, so as to make Y_{DPC}^{ABQ} a C^1 function (but not C^∞, i.e. smooth). $\bar{p}_a$ is the point on the $\bar{I}_1$ axis marking the separation between the shear envelope and the compaction cap regions, in the same way as K_0 in the Y_{DPC}^{Smooth} and R is the ratio between the major axis (parallel to the t coordinate) and the minor axis (parallel to the $\bar{p}$ coordinate) of the ellipse resulting from intersecting the cap surface Y_c^{ABQ} with a plane $t \times \bar{p}$ (Figure 5.7, right).

In the expression of $Y_{DPC}^{ABQ}(\bar{p}, t)$, the coordinate t is used instead of q. Here, t is the deviatoric stress measure, which is calculated as:

$$t = \frac{q}{2} \left[1 + \frac{1}{K} - \left(1 - \frac{1}{K}\right) \left(\frac{r}{q}\right)^3 \right] . \tag{5.48}$$

The expression above is analog to $\Gamma^2(\beta, \psi) J_2$ in Eqn. (5.40). The von Mises stress q is modified according to the expression in Eqn. (5.48), which is a function of the third invariant ($r = \sqrt{3J_2}$), in order to account for differences of yield strength in the π-plane, leading to a deviatoric stress measure t (Figure 5.7, middle).

It can be noticed as well that $Y_{DPC}^{ABQ}(\bar{p}, t)$ does not have an extension cap portion (Figure 5.7, right). This lets the existence of a singularity located at $p = d\cot\beta$, which can lead to numerical integration issues, as here the plastic flow vector is not unique.

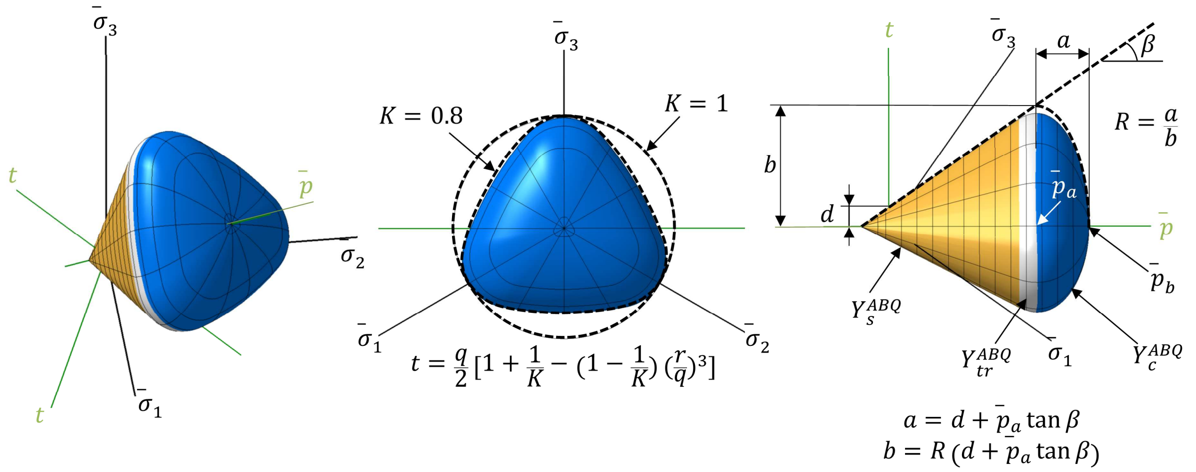

Figure 5.7: Isometric view of the Y_{DPC}^{ABQ} (left), parallel view to the π-plane (middle) and parallel view to a plane $t \times \bar{p}$ (right).

The Y_{DPC}^{Smooth} as defined by Pelessone is available by default in ANSYS (from now on Y_{DPC}^{ANS}) under the name of "Extended Drucker-Prager Cap" model (ANSYS®, 2013). By combining Eqs. (5.43) to (5.46), Y_{DPC}^{ANS} reads:

$$\begin{aligned} Y_{DPC}^{ANS} \equiv \Gamma^2(\beta_L) J_2 - \left(\sigma_0 - A e^{(\beta^Y I_1)} - \alpha^Y I_1\right)^2 \times \\ \times \left[1 - H(K_0 - I_1)\left(\frac{I_1 - K_0}{R_c^Y Y_s(K_0)}\right)^2\right] \times \left[1 - H(I_1)\left(\frac{I_1}{R_t^Y Y_s(0)}\right)^2\right] = 0\,. \end{aligned} \tag{5.49}$$

For modelling Y_{DPC}^{ANS}, 7 parameters must be then identified: ψ, σ_0, A, β^Y, α^Y, R_c^Y, R_t^Y, while Y_{DPC}^{ABQ} has 4: β, d, R, K.

5.4.4 Plastic flow potential for the Drucker-Prager Cap criterion and its different implementations in FE codes

The flow rule refers to the plastic stress-strain law once the yield occurs. Taking the Lévy-Mises equation as starting point, the law is generalized as (Wu, 2005):

$$d\varepsilon_{ij}^p = d\lambda \frac{\partial F(\sigma_{ij})}{\partial \sigma_{ij}}\,. \tag{5.50}$$

where $d\varepsilon_{ij}^p$ are the inelastic strain increments, λ is a proportionality constant regulated by the hardening law of the material and F is a function of the stresses known as the *plastic flow potential*. The derivatives of F gives the direction of $d\varepsilon_{ij}^{pl}$. By using $F(\sigma_{ij}) = Y(\sigma_{ij})$, the inelastic strain increments would be normal to the yield function, leading to a so-called *associative flow rule*. While this condition is often true for many materials (e.g. metals), it has been suggested after experimental observations that it is not valid for granular materials (Lade, 1988a)[16]. Hence, an adequate $F(\sigma_{ij})$ for a non-associative flow rule must be defined for the pebble beds.

In ANSYS, the non-associated flow potential $F^{ANS}(I_1, J_2, J_3, K_0)$ is constructed by using the expressions in Eqs. (5.40) to (5.46) and substituting the parameters β^Y, α^Y, R_c^Y, R_t^Y by β^F, α^F, R_c^F, R_t^F, respectively. This construction allows a fine tuning of the flow potential in case the corresponding experimental data is available, but requires a new set of 4 parameters that must be identified.

In ABAQUS, $F^{ABQ}(\bar{p}, t)$ is constructed again as a piecewise function:

$$F^{ABQ}(\bar{p}, t) = \begin{cases} F_s^{ABQ} = \sqrt{[(\bar{p} - \bar{p}_a)^2 \tan\beta] + \left[\dfrac{Rt}{1 + \alpha - \dfrac{\alpha}{\cos\beta}}\right]^2} \ , \\ F_c^{ABQ} \equiv \sqrt{(\bar{p} - \bar{p}_a)^2 + \left[\dfrac{Rt}{1 + \alpha - \dfrac{\alpha}{\cos\beta}}\right]^2} \ . \end{cases} \tag{5.51}$$

Note that associativity is considered in the compaction cap, while the shear envelope flow potential is non-associated. F_s^{ABQ} and F_c^{ABQ} are the equations of ellipses and once the material parameters for the yield function Y_{DPC}^{ABQ} are identified, the flow potential is automatically established, not permitting a calibration of the $F^{ABQ}(\bar{p}, t)$ as it happens in ANSYS with $F^{ANS}(I_1, J_2, J_3, K_0)$.

5.4.5 Isotropic hardening law and its different formulations in FE codes

The pebble beds in fusion blankets are not subjected to fast rates of change in shear strains and are considered to be quasi-static (Gan, 2008). Therefore, the hardening of the shear envelope is not considered. In ANSYS, the following expression of Fossum and Fredrich (2000) relating ε_{vol}^{in} and the cap hardening marker X_0 is available:

$$\varepsilon_{vol}^{in}(X_0) = W_1 \{ e^{[D_1(X_0 - X_{0,i}) - D_2(X_0 - X_{0,i})^2]} - 1 \} \ , \tag{5.52}$$

where W_1, D_1 and D_2 are material parameters to be identified. $X_{0,i}$ refers to the position of the X_0 marker at the beginning of the calculation. The relationship between K_0 in Eqn. (5.44) and X_0 reads:

$$K_0 \ = X_0 + R_c^Y Y_s(K_0) \ . \tag{5.53}$$

In ABAQUS the evolution of the point $\bar{p}_a$ in Eqn. (5.51) is driven then by the cap hardening law defined in $\bar{p}_b$:

---

[16] Despite the use of non-associated flow potentials is broadly accepted due to their agreement with experimental results, this approach is still disputed and the underlying physics are yet not well understood, as pointed by Fossum and Brannon (2004). On the one side, non-associative flow rules clashes with the Drucker's postulate for the stability of a material (Drucker, 1957), which leads to a normality rule (associative flow rule). On the other side, Sandler and Pucik (1993) mathematically proved that these models lack robustness and are unstable.

$$\bar{p}_a = \frac{\bar{p}_b - Rd}{(1 + R\tan\beta)} \ , \tag{5.54}$$

and $\bar{p}_b$ is expressed as a user defined function of ε_{vol}^{in}:

$$\bar{p}_b = \bar{p}_b(\varepsilon_{vol}^{in}) \ . \tag{5.55}$$

Gan and Kamlah (2007a) established the following relationships based on the uniaxial compression tests of Reimann, et al. (2006a):

$$\begin{aligned} \bar{p}_b &= -\frac{3\sec^2\beta(\cos\beta + R\sin\beta)(-3\cos\beta + \sqrt{4+9R^2}\sin\beta)}{-9 + (4+9R^2)\tan\beta}\sigma_y \ , \\ \varepsilon_{vol}^{in} &= \frac{(\sigma_y)^{1-C_5^L}}{C_1^L(C_2^L + C_3^L T^{C_4^L})} - \frac{(\sigma_y)^{1-C_5^L}}{C_1^U(C_2^U + C_3^U T^{C_4^U})} \ . \end{aligned} \tag{5.56}$$

where R and β are the material parameters of Y_{DPC}^{ABQ}, σ_y the axial stress in the experiments of Reimann and C_i^L and C_i^U are the so-called *Reimann fits* of the loading and unloading paths shown in the next Section. By combining both expressions in Eqn. (5.56), the hardening law $\bar{p}_b(\varepsilon_{vol}^{in})$ is obtained.

5.5 Conversion and identification of material parameters between piecewise and smooth Drucker-Prager Cap yield surfaces

The conversion of the material parameters from the piecewise ($Y_{DPC}^{ABQ}(\bar{p}, t, \bar{p}_b)$) to the smooth ($Y_{DPC}^{ANS}(I_1, J_2, J_3, K_0)$) formulations in this Section is done by converting the expressions Y_s^{ABQ} and Y_c^{ABQ} to an invariant formulation and comparing the resulting expressions against Y_s^{ANS} and Y_c^{ANS}, respectively, when this has been possible. Despite the apparent parallelisms between Y_{DPC}^{ANS} and Y_{DPC}^{ABQ}, it has to be noted that an identical correspondence between both yield surfaces is not possible due to the different way the surfaces are composed (in ANSYS by combining effects of the cap expansion, shear envelope and cap compression and in ABAQUS by piecewise functions definitions).

Initial considerations

Gan (2008) does not consider in his model the differences between triaxial extension and compression, therefore Eqn. (5.48) reduces to $t = q$.

For the sake of simplification, the small transition surface of Y_{DPC}^{ABQ} is not considered for the conversion. Therefore, Y_{DPC}^{ABQ} in Eqn. (5.47) now reads:

$$Y_{DPC}^{ABQ} = \begin{cases} Y_s^{ABQ} \equiv q - \bar{p}\tan\beta + d = 0 \ , \\ Y_c^{ABQ} \equiv \sqrt{(\bar{p} - \bar{p}_a)^2 + (Rq)^2} - R(d + \bar{p}_a\tan\beta) = 0 \ . \end{cases} \tag{5.57}$$

Conversion and identification of the shear envelope parameters $\boldsymbol{A}, \boldsymbol{\beta^Y}, \boldsymbol{\sigma_0}, \boldsymbol{\alpha^Y}$

Considering $\bar{p} = -\frac{1}{3}I_1$ (derived from Eqn. (5.25)) and $q = \sqrt{3J_2}$ (Eqn. (5.33)), Y_s^{ABQ} reads:

$$Y_s^{ABQ} \equiv \sqrt{3J_2} + \frac{1}{3} I_1 \tan\beta + d = 0 \ . \tag{5.58}$$

Comparing Y_s^{ABQ} with Y_s^{ANS} in Eqn. (5.49) for $\bar{I}_1 < \bar{K}_0$ (only shear yielding) and considering $\Gamma(\beta_L) = 1$ as in Y_{DPC}^{ABQ}, $A = 0, \forall \beta^Y$ and the parameters σ_0 and α^Y are:

$$\begin{aligned} \sigma_0 &= 3\sqrt{3}d \, , \\ \alpha^Y &= \frac{\sqrt{3}\tan\beta}{9} \, . \end{aligned} \tag{5.59}$$

Taking into account that $\beta = 60°$ and d~0 (Gan and Kamlah, 2007a), the following values are considered:

$$\begin{aligned} A &= 0, \forall \beta^Y \ , \\ \sigma_0 &\sim 0 \ , \\ \alpha^Y &= \frac{1}{3} \ . \end{aligned} \tag{5.60}$$

Conversion and identification of the compaction cap parameter $\boldsymbol{R_c^Y}$

It will be considered that the activation of the compaction cap in Y_c^{ABQ} and Y_c^{ANS} occurs at the same point, i.e. $\bar{K}_0 \equiv \bar{p}_a$. Y_c^{ABQ} in Eqn. (5.57) can be rewritten as the equation of an ellipse of center $(\bar{p}, q) = (\bar{p}_a, 0)$ and semi-axis $2R(d + \bar{p}_a \tan\beta)$ and $2(d + \bar{p}_a \tan\beta)$:

$$Y_c^{ABQ} \equiv \frac{q^2}{(d + \bar{p}_a \tan\beta)^2} + \frac{(\bar{p} - \bar{p}_a)^2}{[R(d + \bar{p}_a \tan\beta)]^2} = 1 \ . \tag{5.61}$$

Rewriting the expression above to isolate q:

$$q^2 = (d + \bar{p}_a \tan\beta)^2 - \frac{(\bar{p} - \bar{p}_a)^2}{R^2} \ . \tag{5.62}$$

Applying the same variable transformation as for the shear envelope and operating:

$$\begin{aligned} 3J_2 &= \left(d - \frac{1}{3} K_0 \tan\beta\right)^2 - \frac{(I_1 - K_0)^2}{(3R)^2} \ , \\ \frac{3J_2}{\left(d - \frac{1}{3} K_0 \tan\beta\right)^2} &= 1 - \left(\frac{I_1 - K_0}{3R\left(d - \frac{1}{3} K_0 \tan\beta\right)}\right)^2 \ . \end{aligned} \tag{5.63}$$

Now, substituting the parameters $\tan\beta$ and d according to (5.59) and operating:

$$\frac{3J_2}{\left(\frac{3}{\sqrt{3}}(\sigma_0 - K_0\alpha)\right)^2} = 1 - \left(\frac{I_1 - K_0}{3R\frac{3}{\sqrt{3}}(\sigma_0 - K_0\alpha)}\right)^2 \ . \tag{5.64}$$

In Eqn. (5.64) it can be identified that $\sigma_0 - K_0\alpha = Y_s^{ABQ}(K_0)$. Therefore, Eqn. (5.64) now reads:

$$\frac{3J_2}{3\left(Y_s^{ABQ}(K_0)\right)^2} = 1 - \left(\frac{I_1 - K_0}{3\sqrt{3}R\ \left[Y_s^{ABQ}(K_0)\right]}\right)^2 . \tag{5.65}$$

And solving for $\sqrt{J_2}$:

$$\sqrt{J_2} = Y_s^{ABQ}(K_0)\sqrt{1 - \left(\frac{I_1 - K_0}{3\sqrt{3}R\ Y_s^{ABQ}(K_0)}\right)^2} . \tag{5.66}$$

Comparing the expression above with Eqn. (5.49) the parameter R_c^Y is identified:

$$R_c^Y = 3\sqrt{3}R . \tag{5.67}$$

and considering $R = \frac{9}{10}$ (Gan and Kamlah, , 2007a):

$$R_c^Y = \frac{27\sqrt{3}}{10} \approx 4.677 . \tag{5.68}$$

Identification of the expansion cap parameter R_t^Y

The parameter R_t^Y cannot be identified by conversion and comparison with Y^{ABQ}, as Y^{ABQ} lacks of an expansion cap. This parameter is, nevertheless, not important, as it is not influencing the region of the stress-state where the pebble beds are, which is in the area of the compaction cap.

As the pebble beds in fusion blankets are considered to be cohesionless (Bühler, 2002), the parameter d (or σ_0, respectively) tends to 0. However, a positive value must be kept for these values in order to avoid numerical issues. While in Y^{ABQ} this lets the existence of a cohesion of value $p = d\cot\beta$, in Y^{ANS} this effect can be reduced by setting a reasonably low value.

Identification of the Lode function parameter ψ

As Gan's (2008) model does not consider the possible difference between the triaxial compression and expansion strengths, ψ should be therefore set to 1. In the present work is proposed that ψ follows the same relationship as in the Mohr-Coulomb theory given by Eqn. (5.38), as suggested by Fossum and Brannon (2004):

$$\psi = \frac{1}{1 + \sqrt{3}\left(\dfrac{\partial\sqrt{J_2}}{\partial \bar{I}_1}\right)\Bigg|_{\beta_L = 30°}} = \frac{1}{1 + \sqrt{3}(\alpha^Y + A\beta^Y e^{-\beta^Y \bar{I}_1})} . \tag{5.69}$$

As $A = 0$ (Eqn. (5.59)), ψ in Eqn. (5.69) reduces to:

$$\psi = \frac{1}{1 + \sqrt{3}\alpha^Y} = \frac{3}{3 + \tan\beta} , \tag{5.70}$$

where $\frac{7}{9} \leq \psi \leq \frac{9}{7}$ in order to fulfill the convexity requirement of the yield surface.

Taking into consideration the identified $\beta = 60°$, then ψ should be 0.634. However, this would violate the convexity requirement, hence ψ is set to its lower bound, which is:

$$\psi = \frac{7}{9} \,, \tag{5.71}$$

Identification of the flow potential parameters $\boldsymbol{\beta^F}, \boldsymbol{\alpha^F}, \boldsymbol{R_c^F}, \boldsymbol{R_t^F}$

F_s^{ABQ} in Eqn. (5.51) corresponds to an ellipse of center $(\bar{p}, q) = (\bar{p}_a, 0)$ and semi-axis $2(d + \bar{p}_a)$ and $2(d + \bar{p}_a \tan\beta)$. However, applying the findings of Eqn. (5.59), F_s^{ANS} reduces to the equation of a line:

$$F_s^{ANS} \equiv \sqrt{J_2} - \sigma_0 + \alpha^F I_1 = 0 \ . \tag{5.72}$$

It can be noticed that a correspondence between the flow potential parameters of F_s^{ABQ} and F_s^{ANS} is not possible and β^F, α^F, R_c^F and R_t^F must be then deduced from the underlying physical phenomena that they represent.

The parameter $\boldsymbol{\beta^F}$ is not influencing the flow potential, as the exponential term of F^{ANS} is cancelled by setting $A = 0$.

The parameter $\boldsymbol{\alpha^F}$ can be expressed by means of Eqn. (5.59) as:

$$\alpha^F = \frac{\sqrt{3}\tan\varphi}{9} \ . \tag{5.73}$$

In this case, φ is the so-called *angle of dilatancy* or *dilation angle*. For a material following a non-associative flow rule, this angle is defined as the ratio of volumetric plastic strains to the plastic shear strain (Bolton, 1986), meaning that the material increases its volume with increasing shear strain when $\varphi > 0$.

After applying the Lévy-Mises equation (Eqn. (5.50)) to F_s^{ANS}, the relationship between the plastic Poisson's ratio, ν^p, and $\tan\varphi$ is found (Dean & Crocker, 2001):

$$\tan\varphi = \frac{3(1 - 2\nu^p)}{2(1 + \nu^p)} \ . \tag{5.74}$$

On the other side, the Drucker Prager friction angle β can be expressed as a function of the Poisson's ratio ν^* (ν^* meaning plastic ν^p or elastic ν^e depending on the stress state of the bed) and the pebble bed static friction coefficient μ_s (Gan, 2008):

$$\tan\beta = 3\frac{\sqrt{(1 - 2\nu^*)^2 + 3\mu_s^2(1 - \nu^*)^2}}{1 + \nu^*} \ . \tag{5.75}$$

Solving Eqn. (5.75) for ν^* and introducing the resulting expression in Eqn. (5.74) leads to:

$$\tan\varphi = \frac{3}{2} \cdot \frac{\cos^2\beta\,(9\mu_s^2 - 1) + 1 - 2\cos\beta\,\sqrt{3[4\mu_s^2 + 3 - \cos^2\beta\,(13\mu_s^2 + 3)]}}{\cos\beta\,\sqrt{3[4\mu_s^2 + 3 - \cos^2\beta\,(13\mu_s^2 + 3)]} - 18\cos^2\beta\,(\mu_s^2 + 1)} \ . \tag{5.76}$$

The evolution of $\tan\varphi$ as a function of μ_s and parametrized by β is shown in Figure 5.8. It can be noticed that in the range $0 \leq \mu_s \leq 0.2$, the dilatancy angle varies only about ±3.5%, thus showing a low sensitivity.

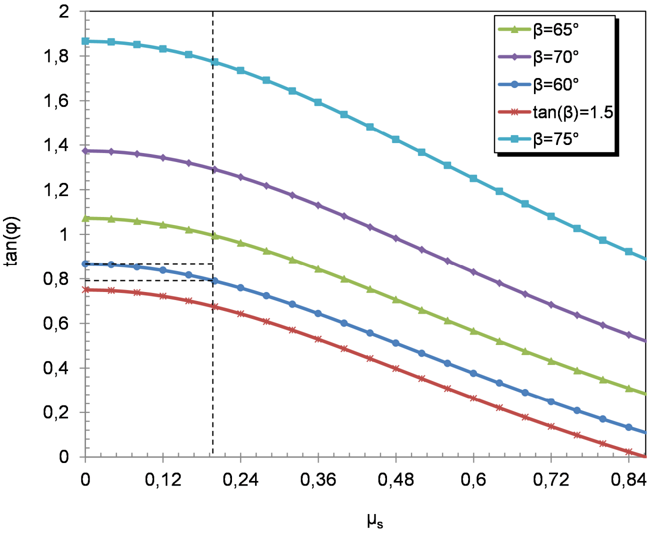

Figure 5.8: Parametric plot of $\tan\varphi$ as a function of the static friction coefficient μ_s of the pebble bed ($0 \leq \mu_s \leq \sqrt{3}/2$), with parameter the Drucker Prager friction angle β. The curve corresponding to $\tan\beta = 1.5$ represents a lower limit, as lower values of β leads to unphysical softening behaviour (Gan and Kamlah, , 2007a). The dashed lines highlight $\mu_s = 0.2$ and the range of the angle of dilatancy from $0 \leq \mu_s \leq 0.2$, showing a low sensitivity (angle variations <3.5%).

In the present work, $\mu_s = 0.2$ has been considered as a characteristic value for this kind of pebble beds (Gan et al., 2014). With this value and given that $\beta = 60°$, a value of 38.3° for the dilatancy angle φ is found. Therefore, applying Eqn. (5.73):

$$\alpha^F = 0.152 \; . \tag{5.77}$$

The parameter R_t^F controls the shape of the expansion cap region of the flow potential and, as it happens for R_t^Y, it does not have any correspondence with F^{ABQ}. Therefore, its value is chosen following the same argumentation as for R_t^Y.

The parameter $\boldsymbol{R_c^F}$ regulates the shape compaction cap region of the flow potential. Its value is deduced by imposing that the point X_0 of Y^{ANS} defined in Eqn. (5.53) must coincide with the respective point X_0 of F^{ANS}, in the same way as it is defined in F^{ABQ}:

$$X_0 = K_0 - R_c^Y Y_s(K_0) = K_0 - R_c^F F_s(K_0) \; . \tag{5.78}$$

The above condition leads to:

$$R_c^F = \frac{\alpha^Y R_c^Y}{\alpha^F} \; , \tag{5.79}$$

and considering the values of each of these parameters given in Eqs (5.60), (5.68) and (5.73), the following value for R_c^F is found:

$$R_c^F = 10.24 \; , \tag{5.80}$$

Conversion and identification of the isotropic hardening law parameters $\boldsymbol{W_1, D_1, D_2}$

The expression of the isotropic hardening law in ANSYS as presented in Eqn. (5.52) strongly differs from the one obtained by Gan and Kamlah (2007a) in Eqn. (5.56): a conversion of the parameters by simple inspection is not possible. The identification of the parameters W_1, D_1 and D_2 is then achieved numerically by fitting $\bar{p}_b(\varepsilon_{vol}^{in})$ to $\varepsilon_{vol}^{in}(X_0)$.

First, the values of the “Reimann’s fits” (Table 5.1) are applied to the coefficients of $\bar{p}_b(\varepsilon_{vol}^{in})$ in Eqn. (5.56). $\varepsilon_{vol}^{in}(X_0)$ is then converted to $\varepsilon_{vol}^{in}(\bar{p}_b)$ by setting $X_0 = -3\bar{p}_b$ and $X_{0,i} = -3\bar{p}_a$ in Eqn. (5.52), where $X_{0,i}$ is the initial value of X_0 and equals to $\sigma_0 R_c^Y$ (Eqn. (5.53)).

Once these conversions are introduced, the curve fitting is performed by a nonlinear Generalized Reduced Gradient solver. Note in Table 5.1 that the temperature affects the hardening law of the Li_4SiO_4. In order to take into account this in the code, the curve fitting has been performed at 4 different temperatures T_i ($T_1 = 50°C$, $T_2 = 550°C$, $T_3 = 750°C$ and $T_4 = 850°C$), thus obtaining a group of parameters W_{1,T_i}, D_{1,T_i} and D_{2,T_i} for each temperature level T_i. During a simulation, given a $T_i < T_j < T_{i+1}$ and $\bar{p}_b$, the code will interpolate the value of ε_{vol}^{in} so that $\varepsilon_{vol}^{in}(\bar{p}_b)|_{T_j} \in \left[\varepsilon_{vol}^{in}(\bar{p}_b)|_{T_i}, \varepsilon_{vol}^{in}(\bar{p}_b)|_{T_{i+1}}\right]$. These temperatures have been favored over others in order to set the parameters W_{1,T_i}, D_{1,T_i} and D_{2,T_i} at the same temperatures where uniaxial compression tests of Reimann, et al. (2006a) were performed: these experimental results are used in the next Section 5.6 as a benchmark for a preliminary validation of the present thermo-mechanical model of the pebble beds. The results of the curve fitting for the Li_4SiO_4 and beryllium pebble bed hardening laws are shown in Figure 5.9. and the values of the W_{1,T_i}, D_{1,T_i} and D_{2,T_i} are summarized from Table 5.2 to Table 5.5.

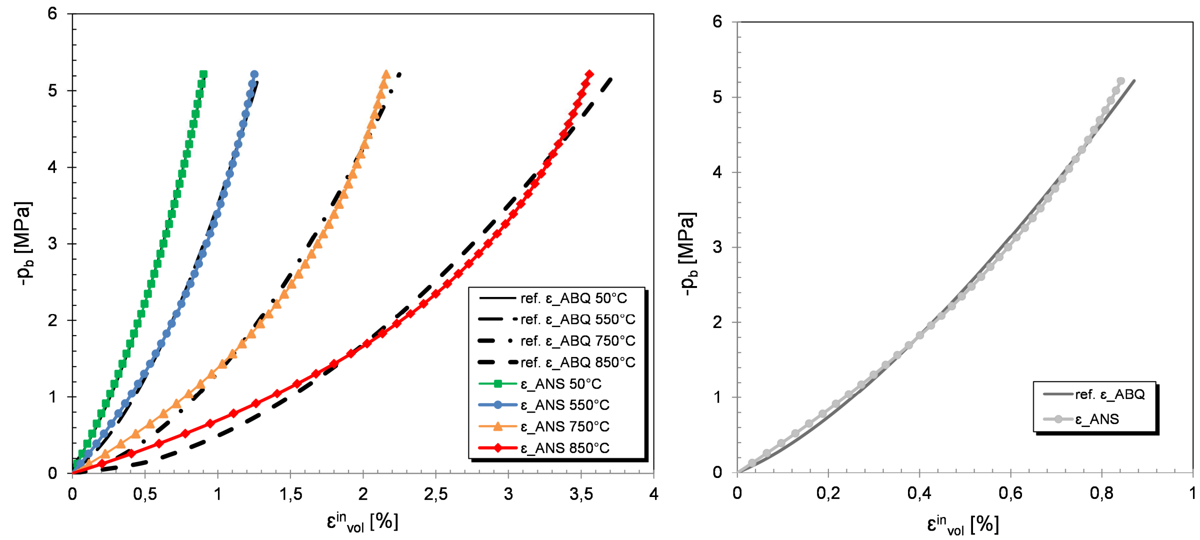

Figure 5.9: Curve fitting of the reference hardening laws for Li_4SiO_4 (left) and beryllium (right) pebble beds obtained by Gan and Kamlah (2007a) for ABAQUS. As temperature effects are considered for the hardening law of the Li_4SiO_4, the curve fitting for this material is done at 4 different temperatures T_i and for each temperature a set of parameters W_{1,T_i}, D_{1,T_i} and D_{2,T_i} is obtained. Despite the different formulations of the hardening law between ANSYS and ABAQUS, the goodness of fit for is in all the cases not less than 98%.

As a concluding summary, the next tables compile the values of the parameter evaluation required for the ANSYS thermo-mechanical model:

Table 5.2: Summary of the parameter values for the implementation of nonlinear elasticity in ANSYS.

Nonlinear elasticity		
Parameter	Li_4SiO_4 pebble bed	Beryllium pebble bed
$\boldsymbol{E_0}$	~0 (set to 50MPa)	~0
$\boldsymbol{\nu}$	0.25	0.25
$\boldsymbol{n}$	0.66	0.6
$\boldsymbol{A_e}$	195.8	895.0

Table 5.3: Summary of parameter values for the implementation of the Drucker-Prager Cap yield criteria in ANSYS.

Drucker-Prager Cap yield surface		
Parameter	Li_4SiO_4 pebble bed	Beryllium pebble bed
$\boldsymbol{A}$	0	
$\boldsymbol{\beta^Y}$	no influence (set to 0)	
$\boldsymbol{\sigma_0}$	~ 0	
$\boldsymbol{\alpha^Y}$	1/3	
$\boldsymbol{R_c^Y}$	4.677	
$\boldsymbol{R_t^Y}$	1	
$\boldsymbol{\psi}$	7/9	

Table 5.4: Summary of parameter values for the implementation of the plastic flow potential function in ANSYS.

Flow potential function		
Parameter	Li_4SiO_4 pebble bed	Beryllium pebble bed
$\boldsymbol{\alpha^F}$	0.152	
$\boldsymbol{\beta^Y}$	no influence (set to 0)	
$\boldsymbol{R_c^F}$	10.24	
$\boldsymbol{R_t^F}$	1	

Table 5.5: Summary of parameter values for the implementation of the isotropic hardening law in ANSYS.

Isotropic hardening law					
Parameter	Li_4SiO_4 pebble bed				Beryllium pebble bed
	50°C	550°C	750°C	850°C	
$\boldsymbol{W_1}$	$1.403 \cdot 10^{-2}$	$1.646 \cdot 10^{-2}$	$2.540 \cdot 10^{-2}$	$4.018 \cdot 10^{-2}$	$1.088 \cdot 10^{-2}$
$\boldsymbol{D_1}$	$6.581 \cdot 10^{-8}$	$9.154 \cdot 10^{-8}$	$1.213 \cdot 10^{-8}$	$1.386 \cdot 10^{-8}$	$1.083 \cdot 10^{-9}$
$\boldsymbol{D_2}$	0	0	0	0	$7.799 \cdot 10^{-14}$

5.6 Preliminary validation of the thermo-mechanical model

For a quick assessment of the performance of the thermo-mechanical model developed in ANSYS, a preliminary validation using the experimental stress-strain data from the uniaxial tests of Reimann, et al. (2006a) is performed here.

The uniaxial compression tests of Reimann were executed in a cylindrical containment with Li_4SiO_4 and Be pebble beds. While for the case of Be the tests were run for just one temperature, the stress-strain relationships for the case of the Li_4SiO_4 pebble bed were obtained at 4 temperature levels (50°C, 550°C, 750°C and 850°C). For both beds, the tests were performed by axially compressing the beds from 0 *MPa* to a maximum of 6 *MPa*.

For the validation, a 2D axisymmetric model of the cylindrical containment has been prepared in ANSYS. Taking into account the findings obtained in Section 5.5, a thermo-mechanical model of these 2 pebble beds has been implemented and executed running the MEPLAS algorithm.

The results of the benchmark exercise are plotted in Figure 5.10. For both pebble beds, and all temperature levels for the case of Li_4SiO_4, the pebble bed models show a good agreement with the empirical curves of Reimann at all temperatures, both in shape and residual values. The root mean square deviations, scaled to the range of 6 *MPa*, are of 9.41% (Li_4SiO_4, 50 *°C*), 4.66% (Li_4SiO_4, 550 *°C*), 1.9% (Li_4SiO_4, 750 *°C*), 5.52% (Li_4SiO_4, 850 *°C*) and 6.79% (Be). These results give a preliminary validation of the phenomenological modeling developed in this chapter.

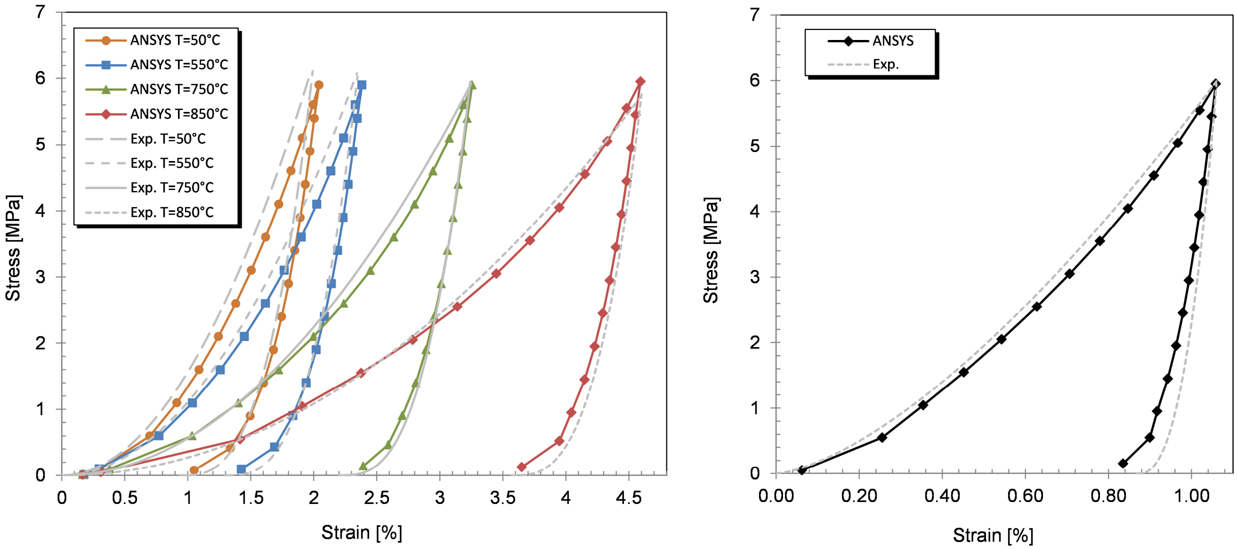

Figure 5.10: Comparison between the developed MEPLAS algorithm in ANSYS and the experimental results of the uniaxial compression tests. Left: Li_4SiO_4 pebble bed tested at 4 temperature levels; Right: beryllium pebble bed. The benchmark study shows a good agreement between thermo-mechanical model and the experimental results of Reimann for both pebble beds.

As an applied example, a steady state 2D thermo-mechanical model of PREMUX is built in the next Section 5.7.

5.7 Application to PREMUX

In this Section, the steady state run performed in PREMUX at the highest power level (VHI) is modeled in 2D (Figure 5.11 bottom). This 2D geometry represents the measurement plane as defined in 3.3.1, which corresponds to the longitudinal midplane of a 3D slice of the PREMUX test box (top-right) passing by the cooling channels No.4 and No.10, as shown in Figure 5.11 top-left.

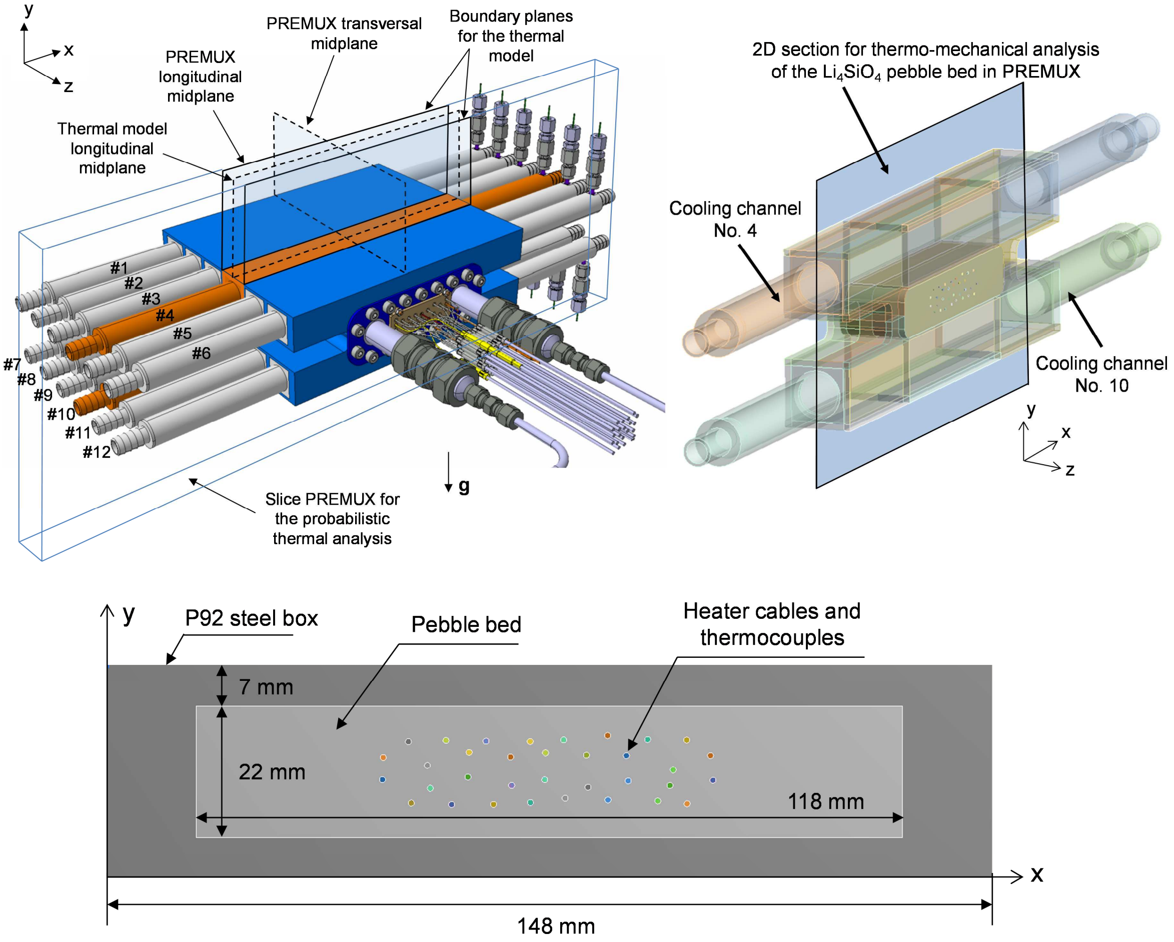

Figure 5.11: CAD model of the PREMUX test box (top left); the orange highlighted region corresponds to the slice bounded by the blue prism. The 2D model is then extracted as an intersection of this slice with the longitudinal midplane (top right). Bottom: 2D section to be analyzed with the MEPLAS-Drucker-Prager Cap model. The 5 mm corner radii in the pebble bed volume have been removed and the box have been shortened to simplify the model.

Due to the 2D nature of the model, an equivalent heat transfer coefficient is used for the calculation of the convective heat transfer between the steel walls and the air coolant. In order to model that heat transfer, the use of the Gnielinski correlation (1976) for the calculation of the Nusselt number ($\overline{Nu}_{D_h}^{Gn}$) would be appropriated if the cooling channels were long enough. However, the welding between these pipes and the test box creates a step that induces flow separation in the coolant gas short after it, producing a so-called *backward-facing step flow* and invalidating the Gnielinski correlation for this problem.

In the next subsection, an analytical expression is developed to correct the $\overline{Nu}_{D_h}^{Gn}$ obtained by the Gnielinski correlation for flows over backward-facing steps as the one present in PREMUX. Thereafter, and making use of this correction factor, an equivalent heat transfer coefficient is derived, after applying some necessary transformations to adapt the 3D heat transfer problem to the 2D geometry proposed here.

5.7.1 Correction factor for the Nusselt number obtained by the Gnielinski correlation for flows over a backward-facing step

As detailed in Section 3.3.2, an arrangement of inlet and outlet interface pipes are welded to the PREMUX test box, acting as interface elements between the L-STAR/LL air loop and the test box. However, the circular cross-sections of these pipes are smaller than the test box cooling channels, creating a sudden expansion of the flow at the entrance of the PREMUX test box. This sudden expansion (Figure 5.12) is expected to produce a local change of the Nu (from now on, Nu_x) along the longitudinal direction x of the channel and therefore of the convective heat transfer. This is due to the induced flow separation after the diameter discontinuity, which increases the dissipation rate due to the increased turbulence, making the Gnielinski correlation not valid under these conditions.

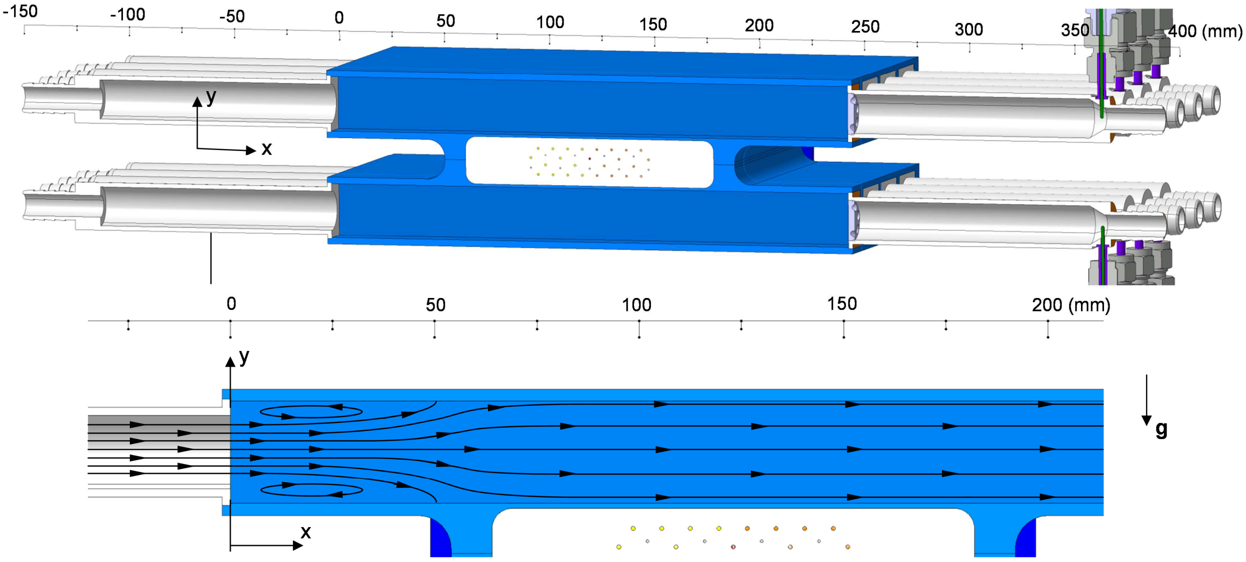

Figure 5.12: Sudden expansion of the cooling channel diameter in a cooling channel of the PREMUX test box. Top: isometric view with cross-section cut of the cooling channels #4 and #10. Bottom: Detailed cross-section view of the channel #4 with ilustrative streamlines. The sudden change of diameter from the inlet pipe to the cooling channel induces a flow separation, which produces a local increase of the convective heat transfer.

As there is no analytical solution to the problem of fluid over a backward-facing step and the validation of the turbulence models in CFD numerical approach with Reynolds Averaged Navier-Stokes (RANS) solutions is still under discussion (it normally leads to underprediction of the reattachment point (Lasher & Taulbee, 1992) and the Nu_x (Kim & Lee, 1994), a correlation based on experimental results is needed.

Abundant literature exists on experimental testing of flow past a backward-facing step with different fluids (normally water and air). A comprehensive review of most important references can be found in Kazi et al. (2012). From this review can be seen that many authors agree with the following observations: (1) the Nu_x reaches a peak after a distance proportional to the height of the backward-facing step, (2) the flow reattachment point depends on the ratio of the upstream diameter d to downstream diameter D_h and (3) the value of the Nu_x peak depends on the Reynolds number.

Despite the abundant literature, no explicit correlation or correction factor in the form of a single expression have been ever reported. Only Woche et al. (2005) give an expression of the $Nu_x/\overline{Nu}^{Gn}_{D_h}$ as function of the Reynolds number, the ratio of upstream to downstream diameters $\frac{d}{D_h}$ and the height H of the step. However, these expressions are given as stepwise functions and only for the region after the flow reattaches, which coincides with the maximum Nu_x. As a single expression is required for the model developed here, these stepwise expressions of Woche et al. (2005) are not appropriate to model the local heat transfer changes along the entire cooling channel in PREMUX. Therefore a correction factor in the form of one equation $\Phi\left(Re, \frac{x}{H}, \frac{d}{D_h}\right)$ for $\overline{Nu}_{D_h}$ is developed below.

The backward-facing step height H in a cooling channel in PREMUX is not constant along the perimeter of the cooling channel (Figure 5.13). As the correction factor $\Phi\left(Re, \frac{x}{H}, \frac{d}{D_h}\right)$ is to be used with the mentioned 1D correlation of Gnielinski, an averaged $\bar{H}$ must be assumed.

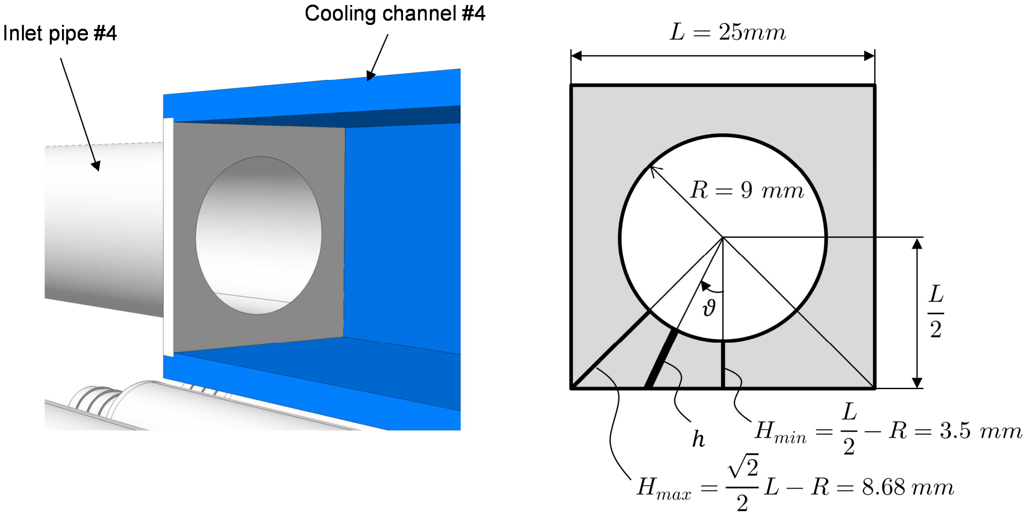

Figure 5.13: Left: isometric view of the backward-facing step in a cooling channel in the PREMUX test box. Right: dimensions of the step. For the calculation of the local Nu_x an averaged step height $\bar{H}$ has been considered.

The step height h_s can be expressed as a function of the angle ϑ and the geometrical dimensions shown in Figure 5.13:

$$h_s = \frac{L/2}{\cos\vartheta} - R\ . \tag{5.81}$$

Therefore, the average $\bar{H}$ is calculated by integrating the expression in Eqn. (5.81) between $-\frac{\pi}{4} \leq \vartheta \leq \frac{\pi}{4}$ and averaging by $\frac{\pi}{2}$:

$$\bar{H} = \frac{\displaystyle\int_{-\pi/4}^{\pi/4} \left(\frac{L/2}{\cos\vartheta} - R\right) d\vartheta}{\pi/2} = 5.03\ mm\ . \tag{5.82}$$

The experimental data from Lee et al. (2011) have been used to develop the correction factor for $\overline{Nu}_{D_h}^{Gn}$. These empirical results are selected due to their similarity with the conditions in PREMUX, as they used air as fluid for their experiments over a relatively broad range of Reynolds numbers $(4300 \leq Re \leq 44500)$ and for $\frac{d}{D_h} = 0.4$, which is of the same order of magnitude as in PREMUX $(\frac{d}{D_h} = 0.72)$. Moreover, the observations of these authors are representative of similar ones found in the literature (e.g. Baughn et al. (1984), Yap (1989), Woche et al. (2005)).

Figure 5.14 shows the profile of the local change of Nu_x normalized with $\overline{Nu}_{D_h}^{DB}$ after Lee et al. (2011) and Yap (1989). The normalization with $\overline{Nu}_{D_h}^{DB}$ is very common by other authors and it represents the Nusselt number obtained with the Dittus-Boelter correlation (Boelter et al., 1965):

$$Nu_{D_h}^{DB} = 0.0243 Pr^{0.4} Re_{D_h}^{0.8}\ . \tag{5.83}$$

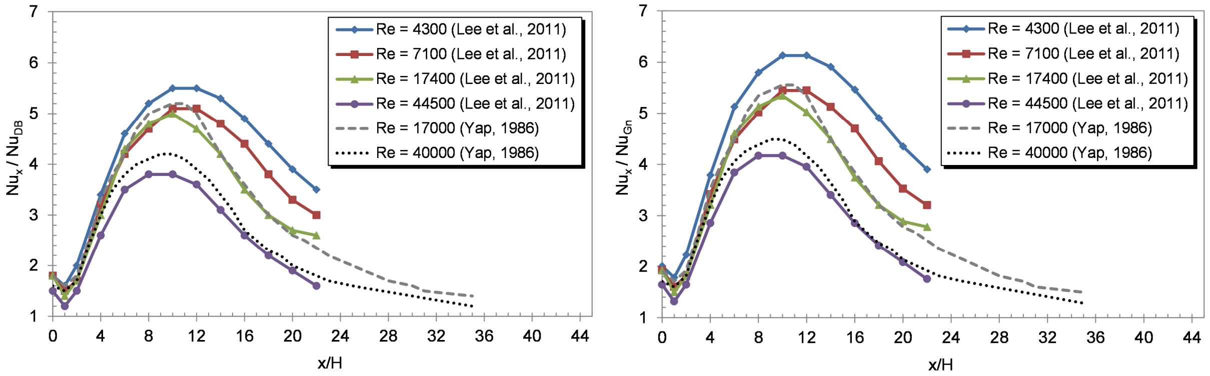

Figure 5.14: Experimental results of the local Nusselt change past a backward-facing step. Left: original dataset after Lee et al. (2011) and Yap (1989) of $Nu_x/\overline{Nu}_{D_h}^{DB}$ as function of the adimensional position x/H, $d/D_h = 0.4$ and air as fluid. Right: transformed dataset $Nu_x/\overline{Nu}_{D_h}^{Gn}$ as function of x/H. Note that $Nu_x/\overline{Nu}_{D_h}$ reaches here a maximum after ~10 times the height H of the step and the maximum is a function of the Reynolds number.

The correction factor $\Phi\left(Re, \frac{x}{H}, \frac{d}{D_h}\right)$ developed here has been obtained by fitting the experimental results of Lee et al. (2011) to a meta-model in the form of a single equation. Prior to the fitting, these experimental results have been transformed by multiplying $Nu_x/\overline{Nu}_{D_h}^{DB}$ by $\overline{Nu}_{D_h}^{DB}/\overline{Nu}_{D_h}^{Gn}$, resulting in $Nu_x/\overline{Nu}_{D_h}^{Gn}$. Then, an appropriate single equation meta-model has been fitted by means of Least Absolute Residuals (LAR) nonlinear regression. In order to illustrate the selection of the meta-model, the profile of $Nu_x/\overline{Nu}^{DB}_{D_h}$ obtained by Yap (1989) at $Re = 40000$ ($\frac{d}{D_h} = 0.4$) is used and depicted in Figure 5.15.

It can be seen that the evolution of $Nu_x/\overline{Nu}^{DB}_{D_h}$ as function of x/H has two different parts. A first one before the maximum, where the Nu_x increases apparently proportional to a polynomial function of the type $\frac{1}{\varphi_1}[(\frac{x}{H})^2 + 1]$ and a second one after the maximum occurs, where the evolution is potentially dominated by an exponential decay function like $e^{-\frac{1}{\varphi_3}(\frac{x}{H})} + 1$, which tends towards 1 when $\frac{x}{H} \to \infty$. When both parts are multiplied, they lead to a function that can reproduce well the evolution of $Nu_x/\overline{Nu}_{D_h}$. The exponential term can be modified as $e^{-\frac{1}{\varphi_3}(\frac{x}{H})Re^{\varphi_2}} + 1$ to take into account the effect of the Re in the value of the peak. Therefore, the meta-model proposed for the fitting is:

$$\Phi\left(Re, \frac{x}{H}\right) = \frac{1}{\varphi_1}\left[\left(\frac{x}{H}\right)^2 + 1\right] e^{-\frac{1}{\varphi_3}\left(\frac{x}{H}\right)Re^{\varphi_2}} + 1 \ . \tag{5.84}$$

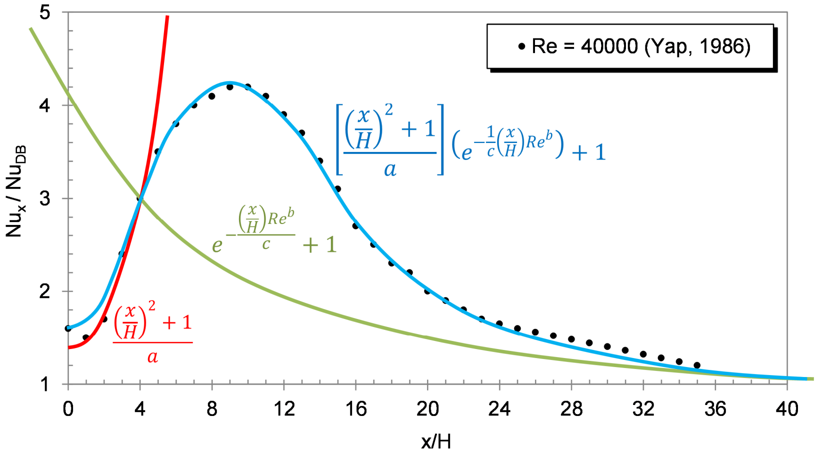

Figure 5.15: Construction of a one-equation correction factor for $\overline{Nu}^{DB}_{D_h}$ in a backward-facing step problem: it can be observed that the graph of $Nu_x/\overline{Nu}^{DB}_{D_h}$ can be approximated by multiplication of a polynomial part (red curve) and an exponential part (green curve), leading to the approximation of the experimental results when both parts are multiplied (blue curve).

The nonlinear LAR regression leads to the following values: $\varphi_1 = 3.23 \pm 2.17\%$, $\varphi_2 = 0.108 \pm 3.70\%$ and $\varphi_3 = 13.6 \pm 3.68\%$ (coefficients expressed with a confidence interval of 95%). The 3D plot of $\Phi(\frac{x}{H}, Re)$ for $\frac{d}{D_h} = 0.4$ is represented in Figure 5.16. The goodness of fit of this regression is 99.8%, with a Root Mean Square Error (RMSE) of 0.078. As the value of $Nu_x/\overline{Nu}^{Gn}_{D_h}$ tends asymptotically towards 1 as $\frac{x}{H} \to \infty$, $\forall Re$, the accuracy of the fitting of Φ can be expressed in relation to 1: in that case, RMSE(%) = 7.80%.

The correction factor in Eqn. (5.84) is therefore valid for $4300 \leq Re \leq 44500$ and only for $\frac{d}{D_h} = 0.4$. In order to extend the validity of this expression to other diameter ratios, the following expression of Woche et al. (2005) relating the Nu_x peak ($Nu_{x_{max}}$) as function of the $\frac{d}{D_h}$ and Re_{D_h} is available:

$$Nu_{x_{max}} = 0.0945\left(\frac{Re_{D_h}}{d/D_h}\right)^{0.72} \quad \text{and} \quad \frac{8}{29} \leq \frac{d}{D_h} \leq \frac{22}{29}\,. \tag{5.85}$$

The expression above can be rescaled in order to be introduced in Eqn. (5.84) as another term that takes into account the effect of d/D_h , so that the term gives 1 when $\frac{d}{D_h} = 0.4$. This rescaling is done by applying the scaling factor $\left[0.0945\left(\frac{Re_{D_h}}{0.4}\right)^{0.72}\right]^{-1}$ to Eqn. (5.85):

$$\frac{0.0945\left(\frac{Re_{D_h}}{d/D_h}\right)^{0.72}}{0.0945\left(\frac{Re_{D_h}}{0.4}\right)^{0.72}} = \frac{0.517}{(d/D_h)^{0.72}}\,. \tag{5.86}$$

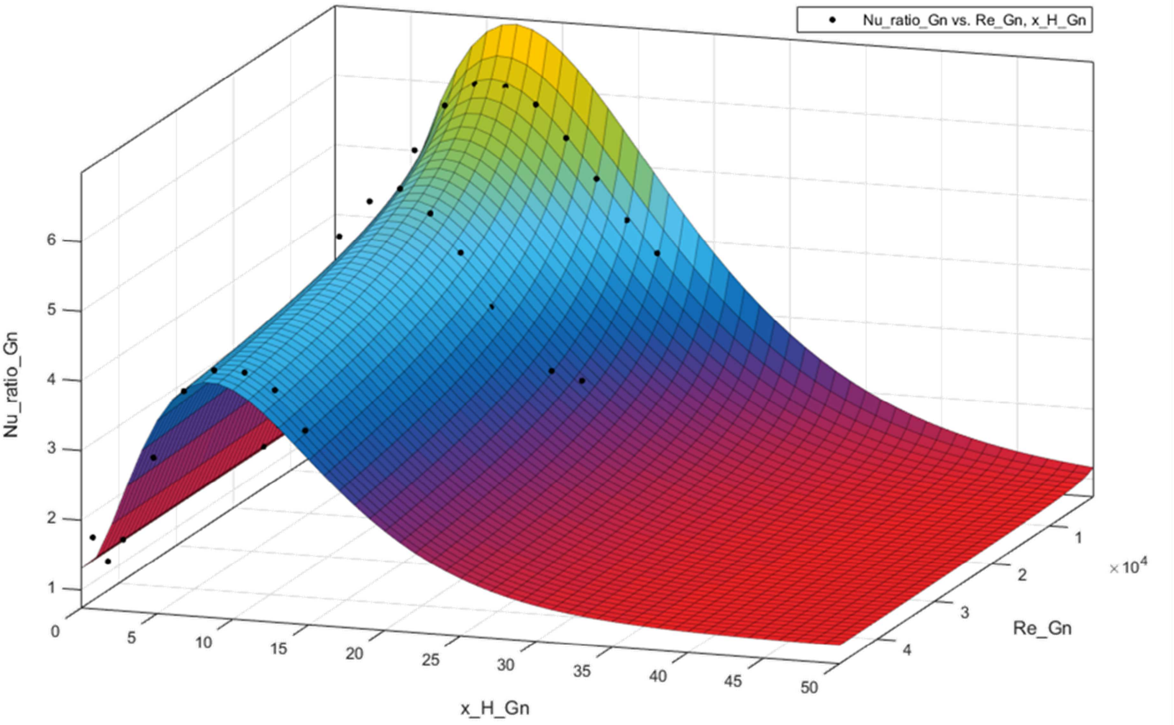

Figure 5.16: Graphical representation of the correction factor $\Phi(\frac{x}{H}, Re)$ for of $\overline{Nu}^{Gn}_{D_h}$ for the problem of the flow over a backward-facing step ($\frac{d}{D_h} = 0.4$): $\Phi(\frac{x}{H}, Re)$ fits very well the experimental data of Lee et al. (2011), with R^2-adj= 99.8% and RMSE=7.80%.

Hence, the correction factor Φ for $\overline{Nu}^{Gn}_{D_h}$ for a flow over a backward-facing step now reads:

$$\Phi\left(Re, \frac{x}{H}, \frac{d}{D_h}\right) = \frac{1}{\varphi_1}\left[\left(\frac{x}{H}\right)^2 + 1\right]\left[e^{-\frac{1}{\varphi_3}\left(\frac{x}{H}\right)Re^{\varphi_2}}\right]\left[\frac{0.517}{(d/D_h)^{0.72}}\right] + 1\,, \tag{5.87}$$

which is valid for $4300 \leq Re \leq 44500$ and $\frac{8}{29} \leq \frac{d}{D_h} \leq \frac{22}{29}$. Therefore, the evolution of Nu_x after the backward-facing step along the cooling channel reads:

$$Nu_x = \overline{Nu}^{Gn}_{D_h} \cdot \Phi = \overline{Nu}^{Gn}_{D_h} \cdot \left[\frac{1}{\varphi_1}\left[\left(\frac{x}{H}\right)^2 + 1\right]\left[e^{-\frac{1}{\varphi_3}\left(\frac{x}{H}\right)Re^{\varphi_2}}\right]\left[\frac{0.517}{(d/D_h)^{0.72}}\right] + 1\right]\,, \tag{5.88}$$

with $\varphi_1 = 3.23 \pm 2.17\%$, $\varphi_2 = 0.108 \pm 3.70\%$ and $\varphi_3 = 13.6 \pm 3.68\%$.

5.7.2 Equivalent heat transfer coefficient

The corrected $\overline{Nu}_{D_h}^{Gn} \cdot \Phi$ proposed in the last Section is valid along the perimeter of the cooling channel considering a uniform wall temperature along this perimeter. However, in the 2D section studied here, only 1 of the 4 walls of a squared cooling channel is represented in the geometry and, furthermore, the temperature distribution varies along the perimeter of the channel due to the inhomogeneous heat flux. Denoting $h_{ch}(x)$ as the local heat transfer coefficient, $\bar{T}_{wall_i}(x)$ the mean temperature of the wall i, $q_{wall_i}(x)$ the local heat flux through at the wall i and $q_{ch}(x)$ the local total heat flux, it follows that:

$$\begin{aligned} q_{wall_i}(x) &= h_{ch}(x)\big(\bar{T}_{wall_i}(x) - T_{\infty,air}\big) \ , \\ q_{ch}(x) &= h_{ch}(x) \sum_{i=1}^{4} \big(\bar{T}_{wall_i}(x) - T_{\infty,air}\big) \ . \end{aligned} \tag{5.89}$$

2D analyses with a relevant geometry reveals that the temperature difference between the wall and the air coolant $\big(T_{wall_i}(x) - T_{\infty,air}\big)$ for the non-heated cooling channel's walls (namely $wall_2$, $wall_3$ and $wall_4$) are about 20% cooler in the surfaces belonging to the ribs ($wall_2$ and $wall_3$) and about 30% cooler in surface opposite to the heated one ($wall_4$) with respect to the heated wall $wall_1$ (Figure 5.17).

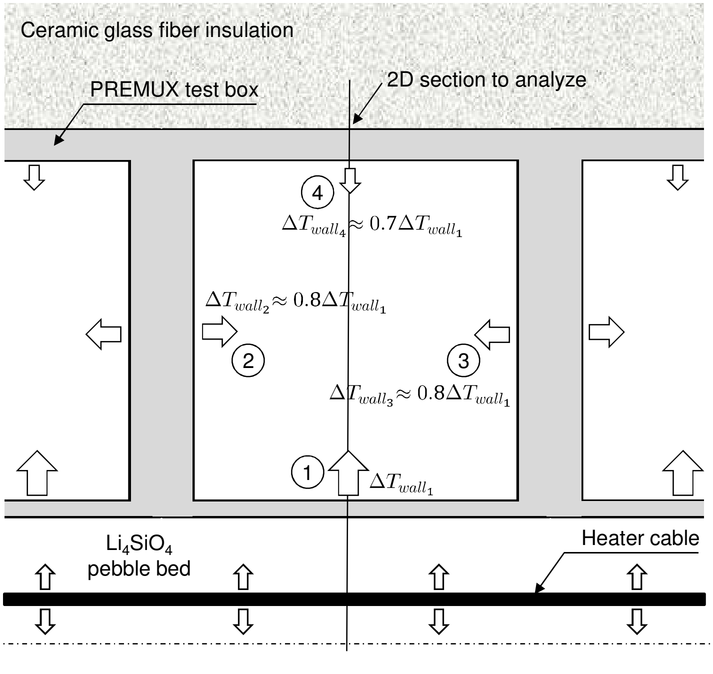

Figure 5.17: Averaged distribution of the temperature differences between wall and fluid

Therefore, the following relationships can be written:

$$\begin{aligned} q_{wall_1}(x) &= h_{ch}(x)(T_{wall_1}(x) - T_{\infty,air}) \\ q_{wall_2}(x) = q_{wall_3}(x) &= h_{ch}(x)(T_{wall_2}(x) - T_{\infty,air}) \\ &= h_{ch}(x)\big[0.8(T_{wall_1}(x) - T_{\infty,air})\big] \ , \\ q_{wall_4}(x) = h_{ch}(x)(T_{wall_4}(x) - T_{\infty,air}) &= h_{ch}(x)\big[0.7(T_{wall_1}(x) - T_{\infty,air})\big] \ , \end{aligned} \tag{5.90}$$

$$
\begin{aligned}
q_{ch}(x) = h_{ch}(x) \sum_{i=1}^{4} \big(T_{wall_i}(x) - T_{\infty,air}\big) \\
&= h_{ch}(x)\big[(1 + 2 \cdot 0.8 + 0.7)\big(T_{wall_1}(x) - T_{\infty,air}\big)\big] \\
&= \ 3.3 \ h_{ch}(x)\big(T_{wall_1}(x) - T_{\infty,air}\big) \ .
\end{aligned}
$$

Taking into account the relationships in Eqn. (5.90) and the correction factor in Eqn. (5.88), the following corrected heat transfer coefficient $h_{corr}(x)$ for the thermo-mechanical model is obtained:

$$
\begin{aligned}
h_{corr}(x) = 3.3 \ \overline{Nu}_{D_h}^{Gn} \Phi \frac{k_{air}}{D_h} = \\
= 3.3 \ \overline{Nu}_{D_h}^{Gn} \left[\left[\frac{(\frac{x}{5.03})^2 + 1}{3.23} \right] \left[e^{-\frac{1}{13.6}(\frac{x}{H}) Re^{0.108}} \right] \left[\frac{0.517}{\left(\frac{d}{D_h}\right)^{0.72}} \right] + 1 \right] \frac{k_{air}}{D_h} \qquad (5.91)
\end{aligned}
$$

5.7.3 Model set-up

The finite element model consists of 9496 elements (about 77% belonging to the pebble bed) of the so-called type *PLANE223*[17]. The mesh (Figure 5.18 top) has been refined in the interfaces between the pebble bed and the heaters/thermocouples, as these areas are subjected to the highest thermal and mechanical gradients. Figure 5.18 right shows the meta-discretization performed for its use with the MEPLAS algorithm. Every meta-element has a fixed bounding box dimension of length 5.9 mm and height of 2.2 mm, resulting in 200 meta-elements. For the meta-element sensitivity analysis, a second mesh with 1600 meta-elements has been generated.

The material properties of the Li_4SiO_4 and Be pebble beds and the identified parameters described in the least Sections are considered. Other properties (coefficient of thermal expansion, densities and heat capacity) are obtained from Reimann et al. (2005). For the interface between the pebble bed and the steel box, a frictional contact condition has been defined, with a friction factor of 0.2. A bonded contact condition between heaters and thermocouples with the pebble bed has been defined, as the inserted elements in the pebble bed can follow pebble bed displacements during the operation due to their flexibility.

The heaters and thermocouples are modeled as homogeneous NiCr wires: due to the parallel positioning of the thermocouples with respect to the heater wires, the heat flux vector field is quasi-perpendicular to the thermocouples, thus minimizing the temperature distortion due to the presence of these instrumentation, also not requiring to precisely model the geometry of the heaters and thermo-couples with their inner structures.

P92 steel material properties according to Richardot et al. (2000) are applied to the test box. On the other side, air is considered to be a prefect gas, whose properties are described by Dixon

---

[17] A PLANE223 finite element type is defined in the ANSYS code as a 2D coupled-field 8-node solid elements with a maximum of 4 degrees of freedom per node. This finite element definition is able to account for multi-field analyses, in which thermal-structural behavior is included (ANSYS®, 2013)

(2007). Translational displacements are disabled at the node at the (0,0) $[m]$ coordinate, while only y displacement is allowed for the node at (0.148,0) $[m]$.

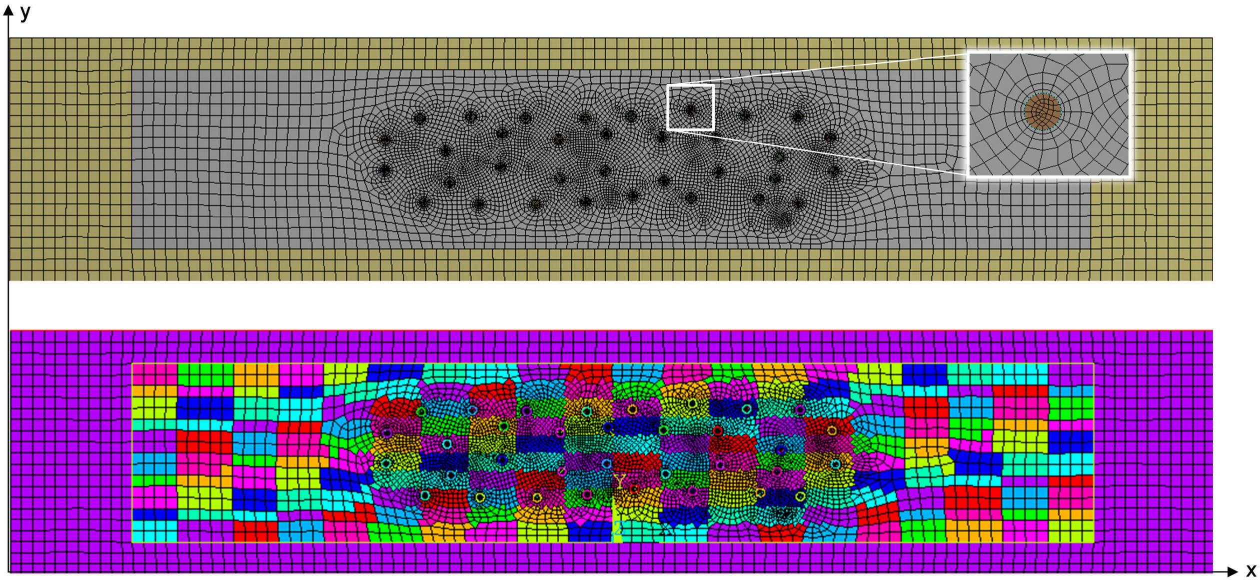

Figure 5.18: Top: finite element mesh for the thermo-mechanical model of PREMUX. The mesh refinement around the heater cables and thermocouples can be seen in the enlarged view at the right side of the figure. Bottom: meta-element discretization of the same finite element domain. Every colored element represents a different meta-element of bounding box dimensions 5.9 mm × 2.2 mm.

For modeling the heat transfer between the wall and the pebble bed, the use of the empirical correlation of Dalle Donne and Sordon (1990) has been applied.

An averaged nominal value for the heat generation has been set for all heaters, The nominal volumetric heating of a heater wire at room temperature for the power level VHI ($3.67 \cdot 10^{-8}$ W/m^3 for the heaters 1 and 2 and $3.64 \cdot 10^{-8}$ W/m^3 for the heater 3) has been corrected for the increased resistivity at high temperatures by multiplying them by the resistivity factor for Nichrome 80/20[18] (Table 6.2) and averaging the result for the number of heater wires. This has led to an averaged volumetric heating of $3.88 \cdot 10^{-8}$ W/m^3 for each heater wire in the steady state regime. As described in Section 4.3.1, about 13.6% of the heat produced in the PREMUX test section is lost due to the lack of a perfect insulation in average. Therefore, due to the impossibility to represent the thermal insulation (3D heat loses) in the proposed 2D section for the analysis, the power density defined in the thermo-mechanical model has been reduced to $3.88 \cdot 10^{-8} \frac{W}{m^3} \times 0.864 = 3.35 \cdot 10^{-8} \frac{W}{m^3}$ instead.

At the top and bottom surfaces of the steel box, a convective heat transfer defined by Eqn. (5.91) has been applied. The air coolant outlet temperature can be easily estimated by means of its heat capacity. As the total heat to be extracted in PREMUX during the VHI experimental run, discarding the heat losses, is $Q_{VHI,net} = 1360\ W \cdot 0.864 = 1175\ W$ and taking into account

---

[18] Data from *MatWeb:* `http://www.matweb.com`

a coolant inlet of $T_{in,air} = 19.5\ °C$ and a heat capacity of $C_{p,air} = 1006\ \frac{J}{kg}°C$, the air coolant $T_{out,air}$ outlet is calculated as:

$$T_{out,air} = T_{in,air} + \frac{Q_{VHI,net}}{12\dot{m}_c C_{p,air}} \approx 52\ °C\ . \tag{5.92}$$

Therefore, a linear law from 19.5 $°C$ to 52 $°C$ has been applied to specify the coolant bulk temperature to be accounted in the heat transfer between the test box cooling channel and the air coolant flow.

The model is solved in ~30 minutes on an Intel Core i7-2600K workstation with 16 Gb RAM and 4 physical CPUs of 3.4 GHz at a mean solver computational rate of ~9.5 $Gflops$.

5.7.4 Discussion

The temperature distribution obtained with the MEPLAS-Drucker-Prager-Cap (MEPLAS-DPC) model is shown in Figure 5.19. In order to assess the quality of these results, Figure 5.20 compares the temperatures obtained by the MEPLAS-DPC model with the experimental results. It can be observed that despite the simplifications applied to the model, the temperatures are in a good agreement to those registered in PREMUX.

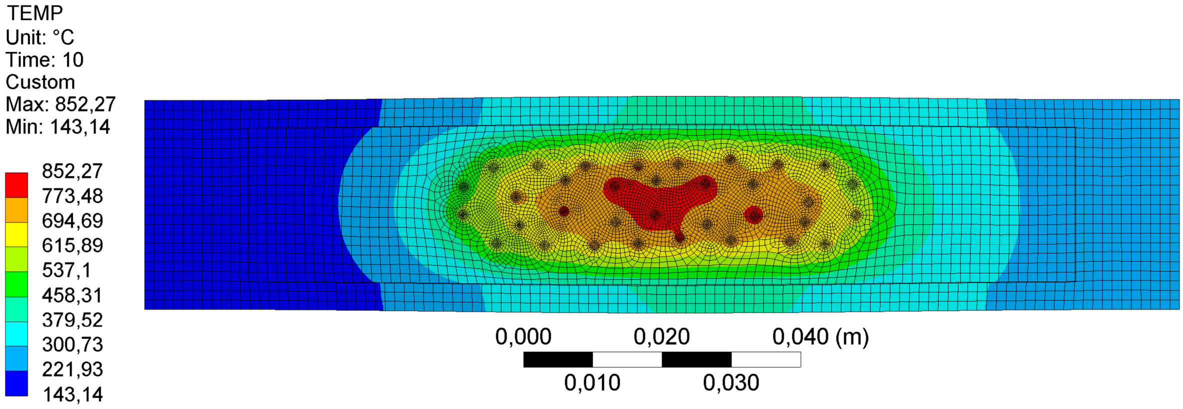

Figure 5.19: Tempearture distribution obtained with MEPLAS-Drucker-Prager-Cap model reproducing a VHI power level at the measurement plane in PREMUX.

The thermal conductivity distribution is shown in Figure 5.21. The maximum value for the thermal conductivity (1.23 W/mK) is located at the surroundings of the heater 3 and the minimum (0.85 W/mK) is located at the outmost left side of the pebble bed domain.

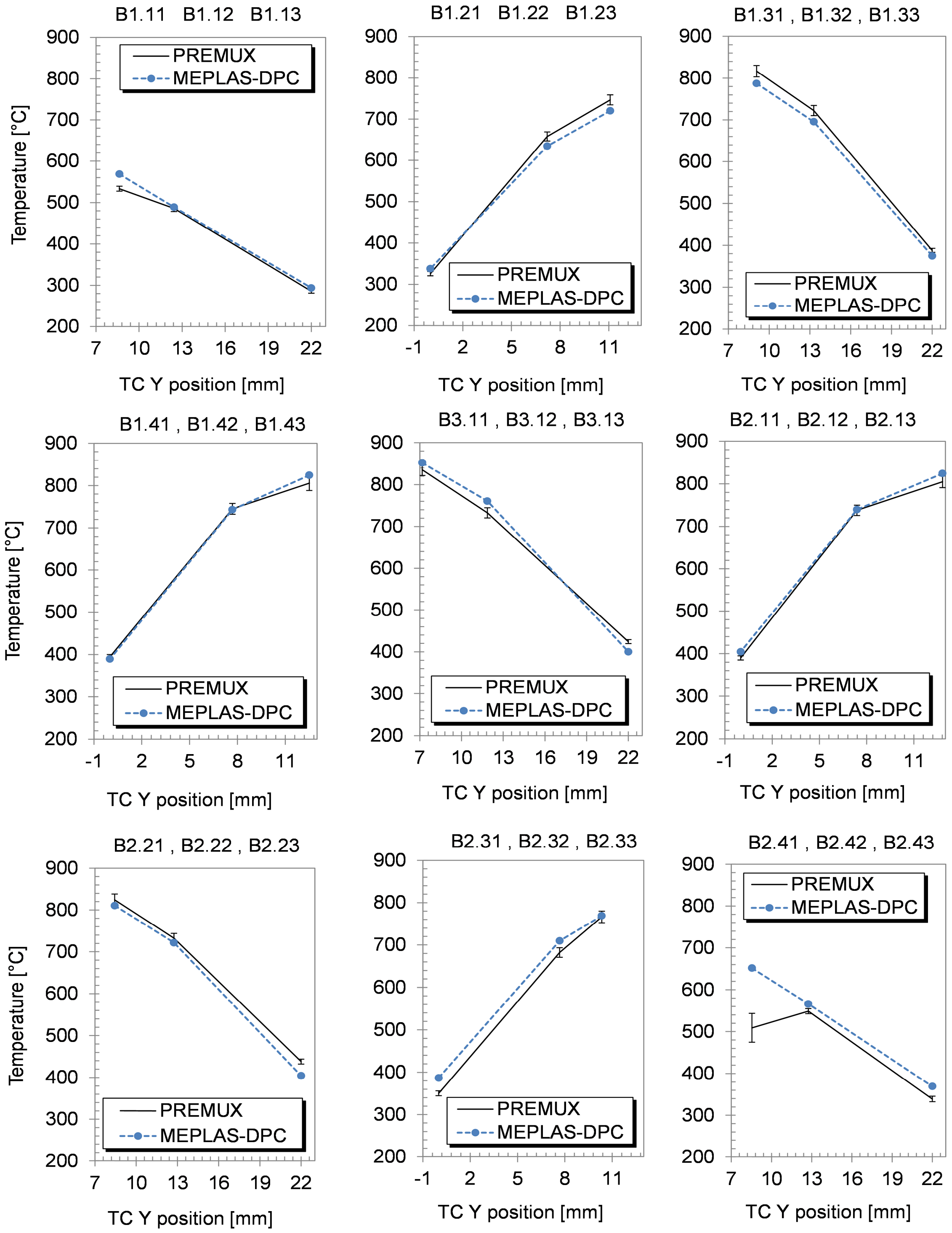

Figure 5.20: Comparison of simulated temperatures (MEPLAS-DPC) with measured in PREMUX in the VHI (highest heating power) experiment.

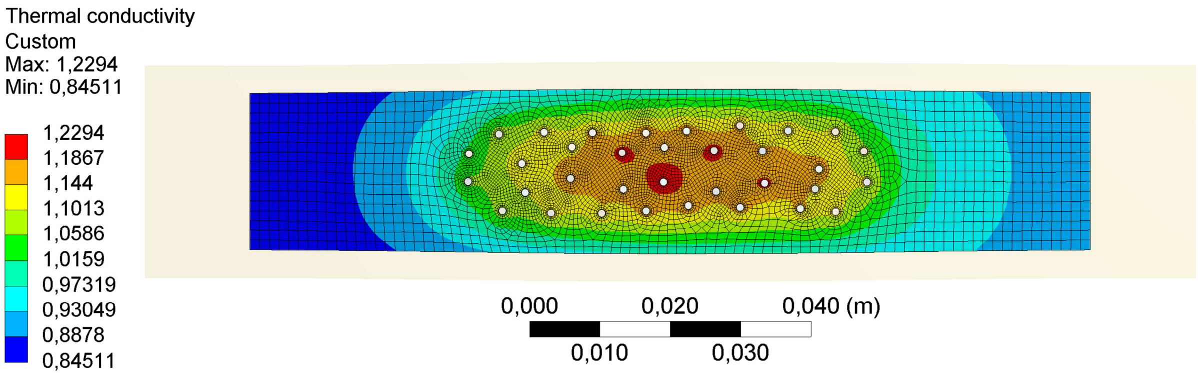

Figure 5.21: Thermal conductivity $[W/mK]$ of the Li_4SiO_4 pebble bed.

It can be observed that thermal conductivity and the temperature fields are positively correlated, where an increase of thermal conductivity mostly responds to a directly proportional increase of temperature. This contrasts with the behavior of the Li_4SiO_4 bulk material, in which its thermal conductivity decreases with increasing temperature (Figure 5.22).

The reason for the different conductivity behavior originates in the different heat transport mechanisms in both materials. While in bulk Li_4SiO_4 conduction is the heat transport mechanism, in a Li_4SiO_4 pebble bed there are 3 heat transport mechanisms, namely heat conduction between pebbles and between pebbles and interstitial gas (the helium purge gas), convection (though negligible in fusion blankets due to the low flow rate of the purge gas) and radiation. The relative importance of each of these 3 mechanisms in the total heat transport in a pebble bed is highly dependent on the average contact area between the pebbles and the number of these contacts, being the conduction the leading mechanism when the average number and contact areas increase due to the compaction of the bed after an external force is applied or, in the case of the breeding blankets, after the inelastic volumetric strain resulting from the confined thermal expansion of the bed in the steel containment of the blanket.

Therefore, the effective thermal conductivity of the pebble bed after a compaction is normally led by the thermal conductivity of the bulk material. This can be clearly observed in the case of the Be pebble bed (Figure 5.22-right). With no compaction, the increase of the effective thermal conductivity of the Be pebble bed is driven by the increasing conductivity of the interstitial helium purge gas, as the importance of the thermal conductivity of the bulk Be is diminished due to the poor average number and contact area between pebbles. However, the effective thermal conductivity is mostly influenced by the bulk Be after the compaction of the bed, especially due to its large thermal conductivity (of about an order of magnitude larger) in comparison with the effective thermal conductivity of the pebble bed.

On the other side (Figure 5.22-left), the effective thermal conductivity of the Li_4SiO_4 pebble bed increases with an increase of the temperature despite of its compaction, e.g. during the operation in PREMUX. In this case, the thermal conductivity of the bulk Li_4SiO_4 is relatively low, while the thermal conductivity of the interstitial helium gas is similar to the effective thermal conductivity. Hence, here the helium gas conduction leads the effective conductivity of the bed and compensates the counter-acting contribution of the bulk Li_4SiO_4.

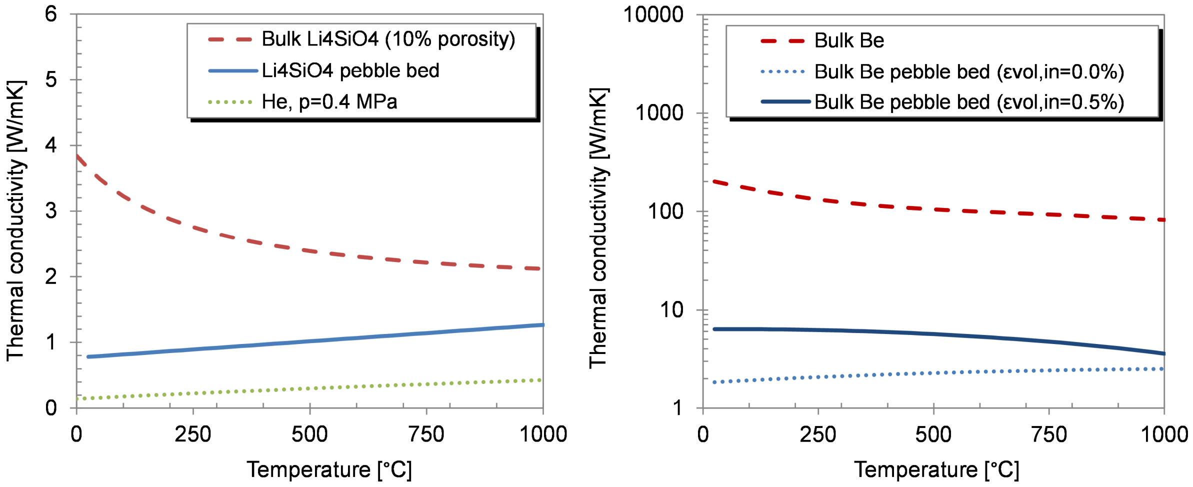

Figure 5.22: Left: Thermal conductivities of bulk Li_4SiO_4 (Akiyama, 1991), Li_4SiO_4 pebble bed (Reimann & Hermsmeyer, 2002a) and helium (Petersen, 1970). Right: bulk Be (Erfling & Grüneisen, 1942) and Be pebble beds (Reimann et al., 2006b) with inelastic volumetric strains (evol,in) of 0.0% and 0.5%.

Figure 5.23 depicts the inelastic volumetric strain field, which shows a maximum value of 0.87% also in the vicinity of the heater 3. As expected, the contribution of the inelastic volumetric strain to the thermal conductivity is low, even in the vicinity of the heater, which is between 2% to 3% according to Eqn. (4.2). This influence is mostly vanished when the experimental uncertainties in the thermal conductivity values are taken into account, thus making a pure thermal computation meaningful. As stated in Section 5.1, while this is true for the Li_4SiO_4 pebble bed, it is not for Be pebble beds, since if one would assume the same results for Be, the contribution of the volumetric inelastic strain would be as high as about 50%.

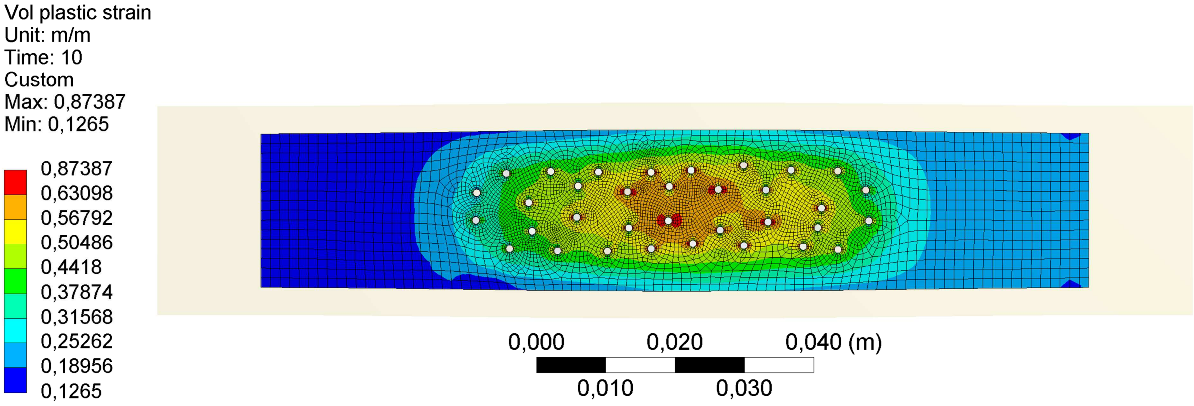

Figure 5.23: Volumetric inelastic strain [%] at the steady state for the VHI power level.

Figure 5.24 shows the steady state results for the von Mises stress (top), hydrostatic pressure (middle) and the inelastic volumetric strains (bottom) mechanical fields.

Peaks of von Mises stress can be seen around the heater wires located at the central part of the pebble bed, with values of ~1.8 *MPa*. In contrast, most of the actively heated part of the pebble bed has a lower von Mises stress, between 1 MPa to 1.4 MPa, which are values in line to the ones reported for similar mock-ups at relevant temperatures (Gan & Kamlah, 2007b; 2007c).

The maximum hydrostatic pressure in the pebble bed is ~2.1 MPa and it is located as well around the central heater and thermocouple wires. To be observed is that a compaction of the pebble bed is expected at each point of it. As it happens for the values of the von Mises stress, the bulk volume of the pebble bed experiences a maximum hydrostatic pressure which is lower than the aforementioned peaks, about 1 MPa to 1.4 MPa. Following the correlation between the maximum normal contact force and the hydrostatic pressure by Gan (2008), this force is between 2~3 N, which is lower than the average crush load of $(7 \div 8)\ N \pm 20\%$ for $\emptyset 0.5\ mm$ dried pebbles reported by Piazza (2001b) and Reimann (2005). Therefore, a reduced risk of pebble cracking is expected.

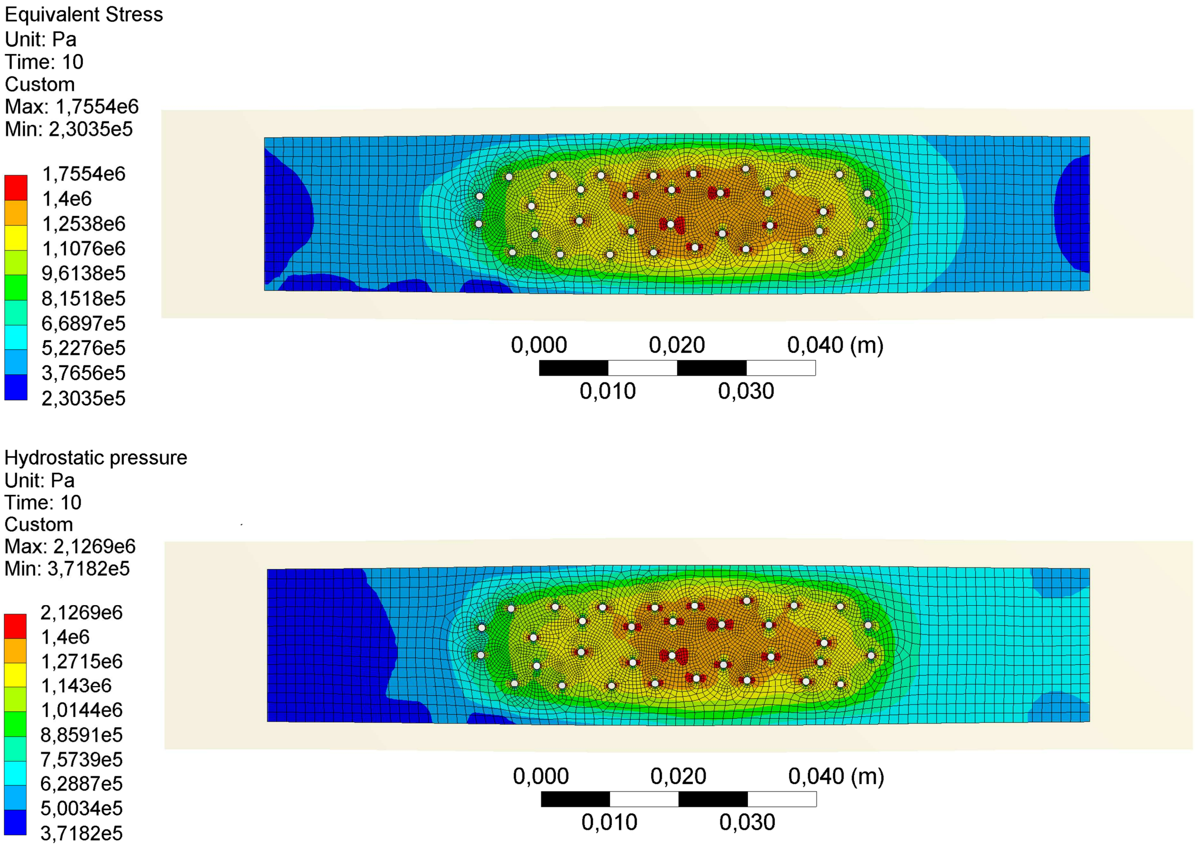

Figure 5.24: Mechanical fields in the Li_4SiO_4 pebble bed in PREMUX for the VHI power level at the steady state. Top: von-Mises stresses. Bottom: hydrostatic pressure.

After the experimental campaign with PREMUX and during the decommissioning of the pebbles, a direct visual inspection has indeed not evidenced significant amount of crushed pebbles. However, some amount dust has been observed while extracting the pebbles from the test box. Later post-mortem analyses on the decommissioned pebbles by sieving have revealed that (Kolb, 2016):

- 9.8 wt.% of the decommissioned pebbles are non-spherical,

- of all spherical decommissioned particles, 1.8 wt.% are smaller than 250 μm, which despite their sphericity they can be considered as fragments due to the minimum manufacturing requirement diameter of 250 μm of the pebbles,
- of all non-spherical decommissioned particles, 10.6 wt.% are smaller than 250 μm and larger than 125 μm,
- of all non-spherical decommissioned particles, 2.1 wt.% are smaller than 125 μm.

Defining dust in this case as particles of less than 125 μm, a non-negligible amount of dust has been lost during the decommissioning of the pebbles and therefore the precise determination of the dust formed in PREMUX is not conclusive, but it can be said that has been not less than 0.2 wt.%. On the other side, the total amount of what it can be considered as decommissioned crushed fragments has been ~2.7 wt.%, which is a rather low value, in line with the model prediction.

To be noted is that in any operational condition, for any pebble bed type, the inelastic volumetric strain originates exclusively from the different thermal expansion between the pebble bed and the steel containment where the bed is enclosed, not from an external force applied to the pebble bed. The pebble beds thermal expansion coefficient is larger than the structural steel, thus producing a self-compaction of the bed during the heating-up phase of the breeding blanket.

In Section 5.1 it has been presented that the thermal conductivity of the pebble beds has not only a temperature but also a strain dependency. In Section 5.3.2 it has been also shown that the nonlinear elasticity has as well dependency on the temperature and stress fields. This view of the phenomena, i.e. to express these two material parameters as a functional relationship between the thermal and stress-strain fields in the pebble beds, requires a fully coupled thermo-mechanical approach as described along this Chapter. However, these phenomena may be possible to be expressed solely from a thermal point of view in the particular case of pebble beds for fusion blankets, as the confined thermal expansion, which is the sole mechanism for inelastic volumetric strain, is only a function of the temperature.

Hence, for the sake of further model simplicity, it would be desirable to introduce alternative expressions for the thermal conductivity and the nonlinear elasticity as a function only of the differential thermal expansion between the pebble bed and the steel containment. This will have two positive effects: the possibility of decoupling the temperature and stress-strain fields from the analysis and the possibility of set-up thermo-mechanical pebble bed models with the default, verified and optimized default material routines of the usual commercial codes.

Although the aforementioned approach would decouple the thermal and mechanical fields and separate analyses could be performed, special care must be taken for the correct modeling of the pebble bed-steel wall interface. During the breeding blanket operation, a permanent inelastic deformation will remain in the bed as a result of the inelastic compaction of the pebble bed after a heating-up cycle. During the cooling-down phase of the pulse a gas gap may be produced as a consequence, affecting the heat transfer in the interface layer wall-pebble bed, thus affecting the temperature distribution. This is again a coupled thermo-mechanical effect. However, the gap formation may be also again predicted by means of the differential thermal expansions between the bed and its steel containment, being able to express it as a function of temperature, resulting again in decoupled, simplified analysis.

Chapter 6

Probabilistic finite element modeling, statistical validation and application using PREMUX

In order to formally validate the finite element models used to predict the thermo-mechanical functionality of the solid breeding blankets by means of statistical methods, a methodology for the conversion of these models into probabilistic finite element models is proposed and developed in this Chapter. This finite element methodology is complementary and based on deterministic finite element approaches like the one presented in the last Chapter. However, for the sake of simplicity the probabilistic methodology will be introduced here to a pure thermal model. This model captures the main characteristics of the system, with the exception of the coupled thermo-mechanical phenomena of the pebble bed, which has been neglected here thanks to the low influence of the strain field to the thermal conductivity in the Li_4SiO_4 pebble beds. The approach presented here then aims at predicting the thermal performance of PREMUX by means of a probabilistic finite element thermal simulation of and its validation by proposing an inference test between the stochastic outputs from the finite element model and the ones obtained from the PREMUX experimental campaign as a validation metric.

6.1 Background

In order to assess the thermo-mechanical performance of a breeder blanket (or e.g. the HCPB-TBM in ITER) a deterministic approach is traditionally applied (e.g. Cismondi et al., 2009; 2010; 2012; Hernández et al., 2011b; 2012). In this approach the input parameters of the model such as material properties, geometrical dimensions, boundary conditions and loads are known without any degree of uncertainty. While this approach is widely used for the design of blanket components, it does not take into account the inherent variability of these input parameters from their expected values, thus not allowing the study of the uncertainty propagation in the model or sensitivity analysis of relevant outputs against these stochastic input parameters.

However, these stochastic data are of key importance. On the one side, they help to quantify the reliability and operational domain of the component in the reactor with a given confidence level. On the other side, they help the detailed design of a mock-up, as they allow a better understanding of the behavior of the system, especially during the design phase of an experiment. These statistical figures permit the identification of the most sensitive parameters of the system and where the uncertainty of the input data can threaten the experimental campaign, as well as a correct validation of the predictive models using experimental data.

Several sets of input parameters can be randomly chosen (sampling) inside their operational range according to their probability density distributions in order to perform computer simulations, but this procedure is excessively time consuming, if not impractical for large and/or complex models such as the one presented in the last Chapter. Therefore, after a probabilistic model is defined a meta-model can be built with the so-called *response surface* method, which approximates the finite element model by a far simpler closed form mathematical expression by means of an appropriate selection of a characteristic set of *response points* (i.e. the determination of the outputs according to a selected set of input parameters). Once the response surface is determined, a stochastic sampling of the inputs is run using now the meta-model, in order to obtain the probability distributions of the outputs of the model. The use of a probabilistic model allows not only the aforementioned statistical analyses (sensitivity & uncertainty), but also "what-if" scenarios and further optimization procedures using robust design, design for Six Sigma or reliability design tools.

Thanks to the steady increase of the computational resources in the last decades, the use of probabilistic models is beginning to be extensively used in some industrial areas (e.g. Reh et al. (2006), Allen et al. (2003; 2000), Allen and Yu (2002)). In the following Sections, the probabilistic finite element approach is introduced in the design of breeding blanket components for fusion applications. For this, a probabilistic thermal model is developed to reproduce the underlying input and model uncertainties in PREMUX, as an example for a future application for the design of the HCPB BU mock-up for testing and, in general, for any other reactor's component development.

6.2 Probabilistic modelling: Design of Experiments, response surface meta-modelling and stochastic sampling

The probabilistic analysis of PREMUX has been performed in ANSYS Workbench with the DesignXplorer module. The procedure to build and execute the probabilistic model is depicted in the flow chart of Figure 6.1.

In a first step, a mechanistic thermal model $\Theta(\boldsymbol{x}^{det})$ is built and deterministic model inputs x_i^{det} (material parameters and boundary conditions) are defined, in which only their expected (average) values are considered.

The probabilistic model $\tilde{\Theta}$ is then built taking Θ as basis and choosing those model inputs which are to be converted into stochastic model inputs $\boldsymbol{x}^{sto}$**.** The stochastic inputs are characterized by their probability density functions pdf so that $x_i^{sto} \sim pdf(\mu_i, \sigma_i)$, where $\mu_i$and

σ_i^2 are respectively the population mean and the variance of x_i^{sto}. As these populations are unknown, the average and standard deviation of a known sample of x_i^{sto} are respectively taken as unbiased estimators of μ_i and σ_i. The knowledge of the uncertainty in the input parameters is a fundamental step of the probabilistic modeling. To those input parameters where there is a lack of information of the $pdf(\mu_i, \sigma_i)$, engineering judgment based on a conservative assumption on the accuracy of the data will be needed. For instance, if an input parameter is assumed to have an accuracy of $\pm a$ and no additional information is known about its uncertainty, a uniform *pdf* can be assumed and the corresponding standard deviation of this parameter will be $\pm\frac{1}{\sqrt{3}}a$.

Some input parameters can be left as deterministic, if their sensitivity and uncertainty is known to be not important in the outputs of the model, thus resulting in the probabilistic model $\tilde{\Theta}(\boldsymbol{x}^{det}, \boldsymbol{x}^{sto}) \equiv \tilde{\Theta}(\boldsymbol{x})$. An important feature of the probabilistic modeling is its ability to handle stochastic geometric parameters as well. In the present model the geometrical parameters (e.g. pebble bed thickness, cooling channel cross section, test box dimensions, etc.) have not been considered stochastic. However, it can be helpful in design stages where an optimization of the geometry is required: a probabilistic model considering these uncertain geometrical parameters, as well as other non-geometrical model inputs, can be set up and optimization procedures based on screening methods or multi-objective optimization algorithms (genetic algorithms or nonlinear programming), can be executed for that purpose instead of usual heuristic procedures.

Once the probabilistic model $\tilde{\Theta}(\boldsymbol{x})$ is defined, a computational Design of Experiments (DoE) is performed. In this computational DoE, a group of design points is selected from the model inputs space $\boldsymbol{x}$ and the model responses are calculated at these points. These design points are used in a further step to construct a response surface meta-model $g(\boldsymbol{x})$ that approximates the phenomena of the original probabilistic finite element model $\tilde{\Theta}$ by means of an interpolation scheme. For the selection of the design points the following algorithms are available in ANSYS DesignXplorer: Central Composite DoE (Montgomery, 1991), Box-Behnken DoE (Box and Behnken, 1960), Optimal Space-Filling DoE (Husslage et al., 2006), Sparse Grid Initialization (Beena and Ganguli, 2010), Latin Hypercube Sampling DoE (McKay et al., 1979) or a Custom DoE.

The response surface is generated by using the response points obtained from the computational DoE. Several methods are available here as well for the user: full quadratic (2$^{\text{nd}}$ order) polynomial regression (Montgomery, 1991), Gaussian process modeling (Sacks et al., 1989), non-parametric regression (Christensen, 2001), neural network (Hajela and Berke, 1991) and sparse grid regression (Beena and Ganguli, 2010). The selection of the DoE scheme affects the availability of response surface methods. For instance, if an optimal space-filling DoE is chosen, a reduced group of response points will be generated, hence allowing only Kriging interpolation algorithms; for the construction of a response surface by polynomial interpolation, fractional factorial DoE like the central composite or the Box-Behnken DoE are to be used; similarly, sparse grid initialization allows only response surfaces by sparse grid regression.

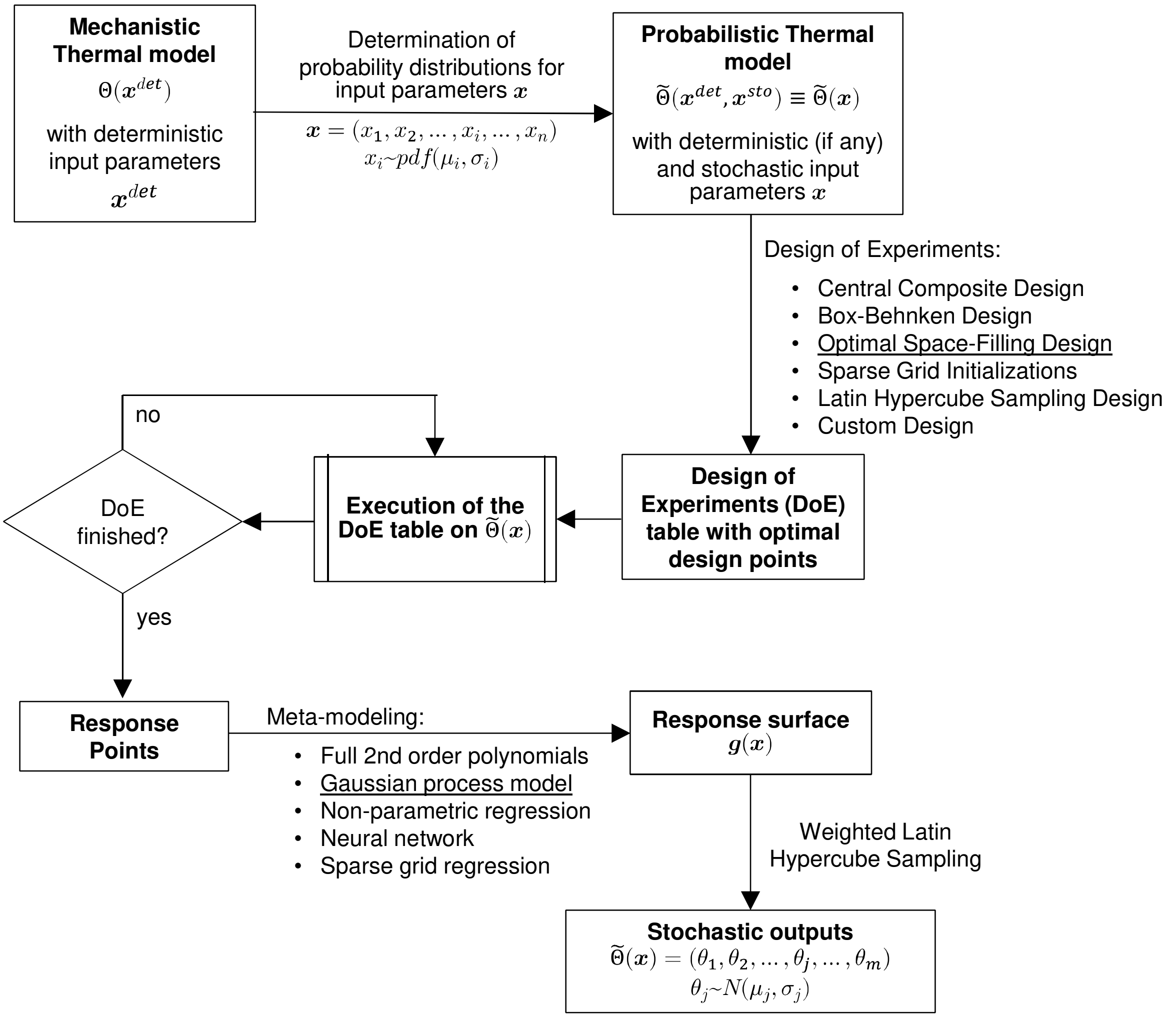

Figure 6.1: Flow chart of a FEM probabilistic analysis. The process has 3 cornerstones: (1) the identification of relevant stochastic input parameters and association of probability density functions (*pdf*) to them, (2) definition of a Design of Experiments and its execution and (3) construction of a response surface meta-model that replaces the probabilistic model to perform "low-cost"[19] stochastic simulations with it. The underlined options have been chosen and applied for the probabilistic thermal model of PREMUX in ANSYS with the DesignXplorer module.

6.2.1 Optimal-space filling Design of Experiments

In order to select the design points that will be solved deterministically and used for the construction of the response surface, an Optimal Space-Filling (OSF) DoE with maximum entropy algorithm (Shewry and Wynn, 2006) has been favored over other methods. As reported by Bursztyn and Steinberg (2006), space-filling algorithms based on entropy or maximum distance criterion yield better space filling results than other designs. This DoE type has the additional advantage of requiring less number of design points for the construction of a response surface in comparison with the classic fractional designs like the classics Central Composite (CCD) or Box-Behnken Designs, reducing the computational time for the construction of the

---

[19] Term after Allen et al. (2003; 2000).

computational DoE table (Figure 6.1). This is because the number of design points needed for a CCD scheme in order to build later a full quadratic response surface grows exponentially as the number of input parameters increases ($2^{N-f} + 2N + 1$, where N is the number of design points and f the fraction of the CCD), while this growth is only quadratic $\frac{(N+2)(N+1)}{2}$ for an OSF algorithm aimed at building the an analog response surface by means of Kriging interpolation.

The OSF algorithm is a variant of the Latin Hypercube Sampling (LHS) design. In its simplest statement (McKay et al., 1979), a k-dimensional LHS design is a mesh of N^k positions, where each k-factor of each independent variable is divided in N-levels equally spaced. Here, only one point is placed in each level in such a way that no point shares the same level for each independent variable. The points are generated randomly but with the restriction that the correlations among the independent variables are $\leq 5\%$, i.e. weakly dependent. The OSF is obtained by adding a post-processing to the LHD, so that the distances between the points are maximized by a maximum entropy algorithm. The resulting design then maximizes the Shannon information of the computational experiment (Shewry and Wynn, 2006).

6.2.2 Gaussian process response surface meta-modelling

For the response surface approximation of the thermal model $\tilde{\Theta}(\boldsymbol{x})$ developed in this Chapter, a Gaussian process meta-model $g(\boldsymbol{x})$ based on Kriging interpolation has been chosen, so that $\tilde{\Theta}(\boldsymbol{x}) \cong g(\boldsymbol{x})$ with enough precision within a defined domain. As stated before, the selection of an optimal-space filling computational DoE with maximum entropy option reduces the number of design points available for the construction of the response surface, thus making it not suitable for the use of classic polynomial interpolation meta-models based on least squares. On the other side, Kriging interpolation algorithms can be used with the chosen computational DoE. The Kriging meta-model is constructed with a polynomial part and departures from that (Sacks et al., 1989):

$$g(\boldsymbol{x}) = \sum_{j=1}^{k} \beta_j f_j(\boldsymbol{x}) + Z(\boldsymbol{x}) \ , \tag{6.1}$$

where $Z(\boldsymbol{x})$ is the realization of a stochastic process with $E[Z(x_i)] = 0, \forall x_i$ and

$$Cov[Z(x_i), Z(x_j)] = \sigma^2 R(x_i, x_j) \ , \tag{6.2}$$

being σ^2 the process variance and $R(x_i, x_j)$ the Gaussian correlation function proposed by Sacks et al. (1989).

The assessment of the precision of the response surface by Kriging interpolation cannot be assessed with a coefficient of determination R^2 as for polynomial regression. This is because the Kriging interpolation algorithm passes through all the design points, yielding always $R^2 = 1$ as a result, provided that the model is not over-constrained. Instead, this assessment is carried by generating additional design points (namely validation points) and comparing the response between $\tilde{\Theta}(\boldsymbol{x})$ and $g(\boldsymbol{x})$.

6.2.3 Weighted Latin Hypercube Sampling of the stochastic outputs

For the stochastic sampling of the outputs using the response surface obtained through Kriging meta-modeling as described in the last Section, a modified version of the LHS, namely Weighted LHS (ANSYS®, 2012), has been performed. This algorithm shares basically the principles of LHS, but the probability of occurrence of sampling points far from the *pdf* mean is higher than for the LHS algorithm. This allows taking into account these points without necessitating very large sample sizes as it happens in the case of the LHS.

6.3 Model assumptions and simplifications

The number of design points needed for the construction of the meta-model grows exponentially, or quadratically for an OSF scheme at best, with the number of stochastic input parameters in the probabilistic model. As the execution of the computational DoE table implies an individual computation with the finite element model for each design point, if the number of input parameters is too large, the procedure may become excessively time consuming, if not impractical, especially if the finite element model is complex. Hence, in order to ease the execution of the computational DoE, several assumptions and simplifications have been done to the finite element model.

Figure 5.11-top left of Section 5.7 shows the CAD model of PREMUX with all its elements (with the exception of the thermal insulation for the sake of a better graphical representation), which envelopes the test box and the inlet and outlet pipes. Due to the poor thermal conductivity of the Li_4SiO_4 pebble bed and the shorter dimension of the pebble bed in the z-axis than in the other axes, it is assumed that the heat flux in the pebble bed in the z-axis is negligible and the vector mostly flows on the xy-plane. This approximation is assumed to be valid at least in the region around the longitudinal midplane of the PREMUX test box, which also includes the PREMUX measurement plane. This assumption allows simplifying the thermal evaluation of PREMUX by only analyzing the slice of the test section highlighted in Figure 5.11-top left.

The resulting geometry after the extraction of the slice has been imported into ANSYS 14.5 via DesignXplorer module (Figure 6.2.). The lateral boundary faces of the model affected with a heat flux symmetry condition (zero heat flux through this surface), so as to represent the assumed negligible heat flux through them. The air coolant heat flow and mass transport in the cooling channels #4 and #10 is simplified by a 1D fluid line element (so-called *FLUID116*[20] element type). Despite this simplification, the element can take into account the convective heat transfer between the fluid and the cooling channels walls by means of well-established empirical

---

[20] A FLUID116 finite element is defined in the ANSYS code as a 1D coupled thermal-fluid line element with 2 nodes and 2 optional additional nodes, able to conduct heat and fluid mass transport. Convection is accounted by means of the 2 additional nodes and their associated convection surfaces (ANSYS®, 2013).

correlations. The heater cables and thermocouples are represented as homogeneous solids without considering their internal structure.

Next Sections 6.4 and 6.5 aim at listing and describe in detail all input data of the model. These input data have been divided into two groups: material properties and boundary conditions input data. After determining the expected values and the accuracy or uncertainty of each one in Section 6.4, a decision on which ones are assumed to be stochastic and which remain deterministic is done in Section 6.5. As stated in the beginning of this Section, this is done order to reduce the number of design points in the computational DoE, thus improving the overall computation time of the probabilistic simulation.

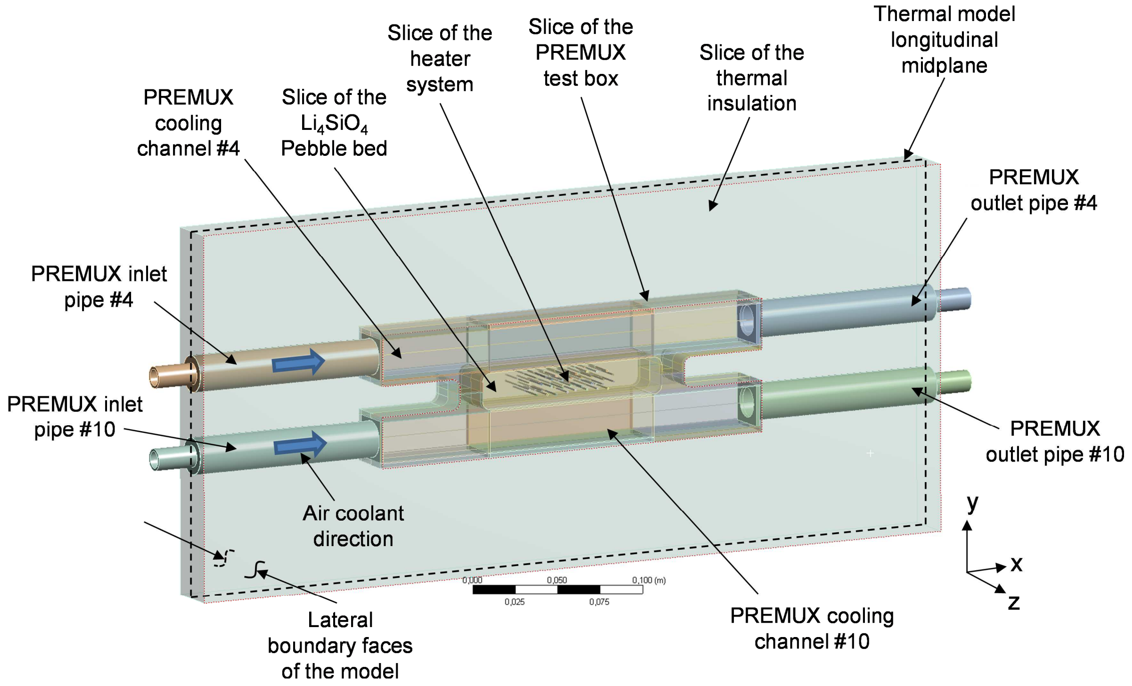

Figure 6.2: Thermal probabilistic CAD model of PREMUX imported into ANSYS Workbench via DesignXplorer.

6.4 Model input data: material properties

6.4.1 Test box steel, Li_4SiO_4 pebble bed and thermal insulation properties

The thermal conductivity database of the P92 structural steel of the PREMUX test box is provided by Richardot et al. (2000). These values are given with a high accuracy (<1%).

As already introduced in Section 6.1, the thermal conductivity of the breeder functional material is given by the expression of Reimann et al. (2002a) in Eqn. (4.2). However, these values show a higher uncertainty, which is unfortunately not expressly given by the authors. However, a comprehensive review of the main breeder material pebble materials performed by Abou-Sena (2005) shows that the accuracy of such data is not worse than 10%.

The ASTM C553-13 standard (2013) database has been employed for the value of the thermal conductivity of the mineral fiber blanket, with a given accuracy better than 10% (see Table 6.3).

6.4.2 Air coolant properties

The density of the (dry) air is determined with the ideal gas law (Clapeyron, 1834) considering it a perfect gas and knowing that the relative molar mass is 28.965 $kg/kmol$ (Dixon, 2007). The specific thermal capacity at constant pressure $c_{p,air}$ is given by (Dixon, 2007):

$$c_{p,air} = 1002.5 + 275 \times 10^{-6}(T - 200)^2 \; J/kg\,K \ , \tag{6.3}$$

with an accuracy of 0.1% from -70 °C to 180 °C and $T \; in \; K$.

For the thermal conductivity, the following simplified expression from Dixon (2007) has been used:

$$k_{air} = 0.02624 \left(\frac{T}{300}\right)^{0.8646} \; W/(m \; K) \ , \tag{6.4}$$

with a reported accuracy of 1% between -30 °C and 230 °C. The dynamic viscosity is given by the Sutherland's formula (Sutherland, 1893) with a negligible accuracy for engineering purposes:

$$\mu_{air} = \lambda \frac{T^{3/2}}{T + C} \; N \; s/m^2 \ , \tag{6.5}$$

where $\lambda = 1.458 \times 10^{-6} \; Pa \; s/\sqrt{K}$ and $C = 110.4 \; K$ (Dixon, 2007).

6.5 Model input data: boundary conditions

6.5.1 Heat generation from the heater system

The ohmic resistance of the heater's H_i hot part at room temperature $R_{hot,0}^{H_i}$ is required for the calculation of the heat generation $G_{hot}^{H_i}$ deployed in the pebble bed. Although the line resistance of each heater part (hot $r_{hot,0}^{H_i}$ and cold $r_{cold,0}^{H_i}$) at room temperature is stated with a certain accuracy in the technical specifications described in Section 3.3.1, it is more convenient to measure them directly in order to have a value with less uncertainty than the given one in the specifications. However, this measurement is only possible for the total resistance of each heater, $R_{tot,0}^{H_i}$. Given the length of the cold part $L_{cold}^{H_i}$ of a heater H_i, the total resistance of the hot part at room temperature is calculated as:

$$R_{hot,0}^{H_i} = R_{tot,0}^{H_i} - r_{cold,0}^{H_i} L_{cold}^{H_i} \ . \tag{6.6}$$

As $R_{hot,0}^{H_i} \gg r_{cold,0}^{H_i} L_{cold}^{H_i}$ and the relative uncertainties of $r_{cold,0}^{H_i}$ and $R_{tot,0}^{H_i}$ are lower than that for $R_{hot,0}^{H_i}$, the value of $R_{hot,0}^{H_i}$ determined by the data reduction equation of Eqn. (6.6) has a lower uncertainty than the one given by the specifications, which is translated into a less uncertainty of the heat generation in each heater H_i hot part.

Recalling the geometrical parameters of each heater (hot part length $L^{H_i}_{hot}$, cold part length $L^{H_i}_{cold}$ and heaters diameter D^{H_i}) and the current I^{H_i}, the heat generation of each heater hot part H_i at room temperature is calculated as:

$$G^{H_i}_{hot,0} = \frac{(I^{H_i})^2\left(R^{H_i}_{tot,0} - r^{H_i}_{cold,0}L^{H_i}_{cold}\right)}{\frac{\pi(D^{H_i})^2}{4}L^{H_i}_{hot}} \,. \tag{6.7}$$

The measured values of the total resistance of each of the 3 heaters are summarized in Table 3.1 of Section 3.3.1. Taking into account these values, Table 6.1 summarizes the nominal values of $G^{H_i}_{hot,0}$ depending on the nominal current I^{H_i} used in each power level (VHI, HI, MED, LO and VLO).

Table 6.1: Heat generation values $G^{H_i}_{hot}$ and total deployed in the Li_4SiO_4 pebble bed in each heater H_i hot part, as function of the operating scenario (“VHI”, “HI”, “MED”, “LO” and “VLO”).

Operating scenario	Heater 1		Heater 2		Heater 3	
	I^{H_1} [A]	$G^{H_1}_{hot,0}$ [W/m³]	I^{H_2} [A]	$G^{H_2}_{hot}$ [W/m³]	I^{H_3} [A]	$G^{H_3}_{hot,0}$ [W/m³]
VHI	5.164	$3.69 \cdot 10^8$	4.940	$3.64 \cdot 10^8$	2.072	$3.73 \cdot 10^8$
HI	4.676	$3.03 \cdot 10^8$	4.472	$2.99 \cdot 10^8$	1.878	$3.06 \cdot 10^8$
MED	4.230	$2.48 \cdot 10^8$	4.045	$2.44 \cdot 10^8$	1.697	$2.50 \cdot 10^8$
LO	3.447	$1.64 \cdot 10^8$	3.308	$1.63 \cdot 10^8$	1.386	$1.67 \cdot 10^8$
VLO	2.435	$0.82 \cdot 10^8$	2.380	$0.82 \cdot 10^8$	0.979	$0.83 \cdot 10^8$

To determine the combined standard uncertainty associated to $G^{H_i}_{hot,0}$, the TSM for the propagation of the uncertainty in a data reduction equation has been applied as described in Section 4.2.3: given the data reduction equation of Eqn. (6.7), and assuming that the uncertainties associated to the variables $R^{H_i}_{tot,0}$, $r^{H_i}_{cold,0}$, $L^{H_i}_{cold}$ and $L^{H_i}_{hot}$ (i.e. $u_{R^{H_i}_{tot,0}}$, $u_{r^{H_i}_{cold,0}}$, $u_{L^{H_i}_{cold}}$, $u_{L^{H_i}_{hot}}$ respectively) are the significant sources of uncertainty (therefore neglecting the uncertainty of I^{H_i} and D^{H_i} due to their higher accuracy with respect to the others) the combined standard uncertainty $u_{G^{H_i}_{hot,0}}$ associated to $G^{H_i}_{hot,0}$ is determined as:

$$u_{G^{H_i}_{hot,0}} = \\ = \sqrt{\frac{\partial G^{H_i}_{hot,0}}{\partial r^{H_i}_{cold,0}}\left(u_{r^{H_i}_{cold,0}}\right)^2 + \frac{\partial G^{H_i}_{hot,0}}{\partial R^{H_i}_{tot,0}}\left(u_{R^{H_i}_{tot,0}}\right)^2 + \frac{\partial G^{H_i}_{hot,0}}{\partial L^{H_i}_{cold}}\left(u_{L^{H_i}_{cold}}\right)^2 + \frac{\partial G^{H_i}_{hot,0}}{\partial L^{H_i}_{hot}}\left(u_{L^{H_i}_{hot}}\right)} \tag{6.8}$$

The uncertainties $u_{R^{H_i}_{tot,0}}$, $u_{r^{H_i}_{cold,0}}$, $u_{L^{H_i}_{cold}}$, $u_{L^{H_i}_{hot}}$ are calculated taking into account their parent distributions, following the guidelines of the ISO/IEC Guide 98-3:2008 (2008): while a Gaussian distribution is assumed for $u_{R^{H_i}_{tot,0}}$, rectangular distributions are considered for $u_{r^{H_i}_{cold,0}}$, $u_{L^{H_i}_{cold}}$ and $u_{L^{H_i}_{hot}}$, taking into account their accuracy specifications given by the manufacturer.

Applying the aforementioned procedure, the following values are determined for the expanded uncertainties of $G_{hot,0}^{H_i}$: $U_{G_{hot,0}^{H_1}} \approx U_{G_{hot,0}^{H_2}} = 5.82\%$ and $U_{G_{hot,0}^{H_3}} = 9.52\%$.

The resistivity of the Nichrome 80/20 increases with the temperature and so does the heat generation. To take into account this effect, the temperature resistance factors F_T of Table 6.2 for Nichrome[21] have been applied to the heat generation at room temperature $G_{hot,0}^{H_i}$. The accuracy of F_T is notably better than that for $G_{hot,0}^{H_i}$ and therefore its uncertainty is neglected.

Table 6.2: Table of correction factor F_T for the resistivity of Nichrome 80/20 as function of the tempearture.

Correction	Temperature [°C]										
factor	20	100	200	300	400	500	600	700	800	900	1000
$\boldsymbol{F_T}$	1.000	1.006	1.015	1.028	1.045	1.065	1.068	1.057	1.051	1.052	1.062

6.5.2 Air coolant inlet temperature and mass flow

The uncertainties of these values have been calculated using the methods defined in Section 4.2. The measured inlet temperature of the air coolant has been $T_{in,air} = (19.1 \pm 1.31)\ °C$ and the mass flow, $\dot{m}_{air} = (2.97 \pm 0.30) \cdot 10^{-3}\ kg/s$ (both with coverage factor 2).

6.5.3 Thermal contact conductance between pebble bed and test box walls

The thermal contact conductance between the heaters / thermocouples and the neighboring pebble bed has been assumed to be perfect, meaning that these inserted elements are considered to be a constitutive part of the pebble bed from the point of view of the thermal conductivity. This assumption is supported from the fact that these inserted elements have a cross-sectional diameter of 1 *mm,* while the Li_4SiO_4 pebble sizes range from 0.25 *mm* to 0.60 *mm.* As both have curvatures of the same order of magnitude, the local packing factor around the inserted elements is not expected to differ much from the pebble bed bulk therefore the heater and thermocouples are not expected to locally modify the effective thermal conductivity of the pebble bed sensibly.

On the other side, the thermal contact conductance between the pebble bed and the test box walls, $TCC_{St\leftrightarrow Li_4SiO_4}$, is expected to be not perfect, as the curvatures between these two objects are very different. In this region the pebbles line up with the test box walls, resulting in a local increase of voids, thus reducing the packing factor and producing a non-negligible thermal contact resistance between both objects. For this type of contact, the Yagi and Kunii (1960) model has been used with the constants indicated by Reimann et al. (2005):

---

[21] Data from *MatWeb:* `http://www.matweb.com`

$$TCC_{St\leftrightarrow Li_4SiO_4} = 2577 + 4.327T - 8.91 \cdot 10^{-4}T^2 \ , \tag{6.9}$$

with T expressed in *°C.*

Empirical results are very scarce to assess the accuracy of the expression in Eqn. (6.9). Only Dalle Donne and Sordon (1990) have a few experimental results that they are compared with the Yagi and Kunii model. These authors state that their empirical observations fitted with the model within ±30% for all cases. Similar work for Li_2TiO_3 pebbles (Abou-Sena et al., 2009) indicate that an accuracy of at least ±30% is common for such experimental data, hence such value has been assumed for the expanded uncertainty of this parameter.

6.5.4 Heat transfer coefficient between air coolant and inlet/outlet pipes

The averaged convective heat transfer coefficient between the inlet and outlet pipes and the air coolant is calculated as:

$$\bar{h}_{air} = \overline{Nu}_{D_h}^{Gn} \frac{k_{air}}{D_h} \ , \tag{6.10}$$

where $\overline{Nu}_{D_h}^{Gn}$ is the averaged Nusselt number determined with the Gnielinski correlation (1976):

$$\overline{Nu}_{D_h}^{Gn} = \frac{(f/8)\left(Re_{D_h} - 1000\right)Pr}{1 + 12.7\sqrt{f/8}\left(Pr^{2/3} - 1\right)} \ . \tag{6.11}$$

In the expression above, Re_{D_h} is the Reynolds number related to hydraulic diameter D_h, which in this case coincides with the inner diameter of the pipes ($\emptyset_{in}$=18 mm), *Pr* is the Prandlt number and *f* is the friction factor, which for smooth pipes is given by:

$$f = \frac{1}{\left(1.82 \log Re_{D_h} - 1.64\right)^2} \ , \tag{6.12}$$

The Gnielinski correlation is valid for $2300 < Re_{D_h} < 5 \cdot 10^6$ and $0.5 < Pr < 200$ with an accuracy better than 10%. Eqn. (6.11) assumes small variations in the physical properties of the fluid in the region under study, which is the case for the inlet and outlet pipes. In the case that these variations are large, the $\overline{Nu}_{D_h}^{Gn}$ has to be corrected. Petukhov (1970) proposed the following correction of $\overline{Nu}_{D_h}^{Gn}$ for large variations of the physical values in gases:

$$\overline{Nu}_{D_h}^{Gn} = \overline{Nu}_{D_h}^{Gn}|_{T_b} \left(\frac{T_b}{T_w}\right)^n \ , where\ n = \begin{cases} 0.47 & for\ T_w > T_b \\ 0 & for\ T_w < T_b \end{cases} \tag{6.13}$$

being $\overline{Nu}_{D_h}^{Gn}|_{T_b}$ the Nusselt number calculated with the Gnielinski correlation evaluated at the fluid's bulk temperature T_b and wall's temperature T_w. The correction applies provided that $0.27 < (T_b/T_w) < 2.7$, where T_b/T_w is to be expressed in degrees Kelvin.

Eqn. (5.88) in Section 5.7.1 has been implemented in the probabilistic model for the calculation of the heat transfer coefficient between the coolant air and the cooling channels h_{air} in PREMUX. The accuracy of the expression above depends on the accuracy of $\overline{Nu}_{D_h}^{Gn}$, which is at least better than 10% as stated before, and of Φ, which is better than 10% as seen in Section 5.7.1. However, a value of 20% is assumed for the expanded uncertainty of the heat transfer coefficient obtained with the expression above for the sake of conservatism. Such a conservative value should take into account additional uncertainty of the experimental data and the fact of using one source of data for the fitting, despite being representative, as indicated by Jiji (2006).

6.5.5 Heat transfer coefficient between the PREMUX test box thermal insulation and the ambient air

Free convection between the thermal insulation of the PREMUX test box and the surrounding air occurs during operation. In order to take into account this heat transfer mechanism, the 1D correlation of the Nusselt number for natural convection for prismatic bodies $\left(\overline{Nu}_L^{Sp}\right)$ after Sparrow and Stretton (1985) has been used under the assumption that the PREMUX test box, together with the thermal insulation, can be approximated to a prism of dimensions $L_p = 0.5\ m$, $H_p = 0.25\ m$ and $W_p = 0.25$ (Figure 6.3):

$$\overline{Nu}_L^{Sp} = 5.748 + 0.752\left(\frac{Ra}{f_4(Pr)}\right)^{0.252} , \tag{6.14}$$

$$f_4(Pr) = \left[1 - \left(\frac{0.492}{Pr}\right)^{\frac{9}{16}}\right]^{\frac{16}{9}} , \tag{6.15}$$

and where Ra is the Rayleigh number, which is calculated as:

$$Ra = \frac{g\beta_{th}}{\nu\alpha}(T_s - T_\infty)L_p^3 . \tag{6.16}$$

In Eqn. (5.88), g is the gravity acceleration ($g = 9.81\ m/s^2$), β is the thermal expansion coefficient, which is $1/T_\infty$ for ideal gases ($\beta_{th} = 0.0035$ in the case of air at 15 °C), ν is the dynamic viscosity ($\nu = 9.594 \cdot 10^{-6}$ for ambient air at 0.1 MPa and 15 °C), α is the thermal diffusivity ($\alpha = 1.275 \cdot 10^{-5}$ for ambient air at 0.1 MPa and 15 °C), T_s is the surface temperature of the thermal insulation and T_∞ is the ambient temperature ($T_\infty \approx 15\ °C$) and L_c is a characteristic length, which in the case of natural convection for prisms is defined by Sparrow and Stretton (1985) as:

$$L_c = \sqrt{\pi}\frac{A_{tot}}{\sqrt{4A_{proj}}} = 1.567\ m . \tag{6.17}$$

In the expression above, A_{tot} is the total area of the prism ($A_{tot} = 0.625\ m^2$) and A_{proj} is the projected area of the prism on the ground, $A_{proj} = L \times W = 0.125\ m^2$.

With the aforementioned data, the natural convection coefficient is calculated as:

$$\bar{h}_{nat} = \overline{Nu}_{D_h}^{Sp}\frac{k_{air}}{L_c} . \tag{6.18}$$

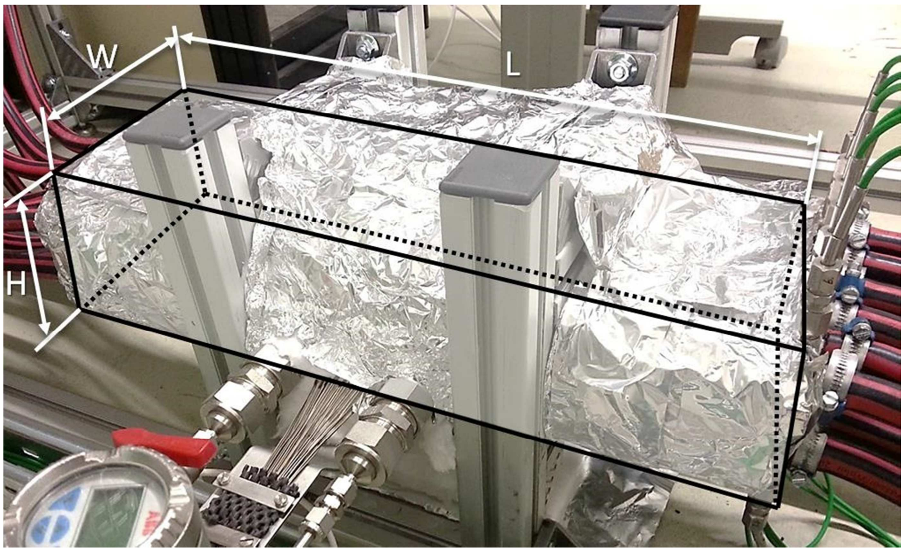

Figure 6.3: Approximation of the PREMUX test box to a prism of dimensions $L = 0.5\ m$, $H = 0.25\ m$ and $W = 0.25\ m$ for the calculation of the heat transfer coefficient for natural convection of a prism.

Sparrow and Stretton (1985) report a maximum deviation of less than 10% with this correlation. However, a more conservative expanded uncertainty of 20% is considered in the determination of $\bar{h}_{nat}$, taking into account the observation of Jiji (2006).

6.6 Summary of model inputs and selection of the stochastic data

A detailed description of every input data required for the probabilistic model has been given in the last section. However, not all the model's input variables are wanted to be stochastic: some input variables have a reduced sensitivity and uncertainty with respect to the rest and can be neglected, reducing the number of design points to compute.

Table 6.3 lists the model input data determined in Section 6.5, stating the accuracy or standard uncertainty of each one and its parent distribution.

The material properties of the steel box and the air coolant are not considered stochastic, as their standard uncertainties are an order of magnitude lower than the rest and analyses have shown that their sensitivity is low. Note the heat transfer coefficient between the air coolant and the inlet and outlet pipes have been considered stochastic in a first calculation (VHI) but discarded after, as it has been found that their contribution to the total sensitivity and uncertainty is only 1%, as it will be shown in Section 6.8.

The first stochastic simulation with VHI conditions has taken into account 15 input parameters, resulting in 136 design points (i.e. simulation runs) after applying an OSF scheme for the computational DoE. Discarding the heat transfer coefficient of the inlet and outlet pipes for other power scenarios (HI, MED, LO and VLO) afterwards has reduced the DoE table almost 60%, resulting in 78 design points. If all input parameters were considered, that would represent a DoE table with 171 design points to be solved.

Table 6.3: Summaray of input data for the probabilistic thermal model. A value in parenthesis indicate that the input datum has been considered stochastic in a first run and deterministic afterwards

Input parameter name	**Label in probabilistic FE analysis**	**Accuracy**	**Parent distributio n**	**Standard uncertainty**	**Considered stochastic?**
Test box steel material properties	Steel box mat. prop.	1% or better	uniform	0.6%	no
Li_4SiO_4 pebble bed material properties	Thermal cond. Li4SiO4	-	normal	10%	yes
Thermal insulation material properties	Thermal cond. insulation	-	normal	10%	yes
Air coolant material properties	Air mat. prop.	1% or better	uniform	0.6%	no
Heat generation heater 1	HGEN heater 1	-	normal	2.9%	yes
Heat generation heater 2	HGEN heater 2	-	normal	2.9%	yes
Heat generation heater 3	HGEN heater 3	-	normal	4.8%	yes
Air coolant inlet temperature	TEMP air inlet	-	normal	3.4%	yes
Thermal contact steel-pebble bed	TCC steel-Li4SiO4	-	normal	15%	yes
Heat transfer coefficient air coolant-inlet pipes	HTC Inlet Pipe CH4 HTC Inlet Pipe CH10	-	normal	10%	no (yes)
Heat transfer coefficient air coolant-outlet pipes	HTC Outlet Pipe CH4 HTC Outlet Pipe CH10	-	normal	10%	no (yes)
Heat transfer coefficient air coolant-cooling channels	HTC cool. channel (corrected)	-	normal	10%	yes
Free convection ambient air-thermal insulation	HTC insulation-air	-	normal	10%	yes
Air coolant mass flow	MFLOW air coolant CH4 MFLOW air coolant CH10	-	normal	5%	yes

6.7 Execution of the probabilistic thermal model

The thermal model described up to now has been implemented in ANSYS Workbench, Version 14.5. A total of 5 stochastic simulation runs have been performed with the probabilistic thermal model in an Intel Core i7-2600K with 4 physical CPUs at 3.4 *GHz*. To each probabilistic run, a heating level corresponding to the 5 scenarios tested in PREMUX (VHI, HI, MED, LO and VLO) has been set up, respectively. For the probabilistic simulation at VHI condition, a total of 136 deterministic steady state thermal simulations have been required for the 15 input data parameters corresponding to each of the 136 design points created in the DoE table. For the HI, MED, LO and VLO power levels, a total of 78 deterministic steady state runs have been performed, after discarding 4 of the 15 input data parameters used in the VHI run, as stated in the previous Section.

After the deterministic runs have been executed, the construction of the meta-model by Kriging interpolation is performed. For the quantification of the goodness of fit, 3 validation points have been randomly chosen for each of the 5 power levels and their steady state thermal response has been compared with the corresponding response with the Kriging meta-modeling, yielding an excellent fitting.

Once the meta-model has been obtained, the stochastic sampling of the outputs is performed with weighted LHS and a sample size of 1000 for each power level, in which the statistics for each observation point (e.g. thermocouple positions in the measurement plane) are computed.

6.8 Results and model validation

The results of the stochastic analyses for the VHI heating power are depicted in Figure 6.4. Also, the results of the simplified, fully-coupled thermo-mechanical analysis of Chapter 5 have been added to these results for a complete comparison with the probabilistic model and the PREMUX experimental results. The uncertainty bands of the probabilistic model and of PREMUX are expressed with a coverage factor 2, representing a 2σ confidence interval.

It can be observed that the uncertainty band of the probabilistic model overlaps the one of the experimental results with a p-value of more than 0.05 in almost all cases, confirming the null hypothesis of the equal means of the probabilistic model and the PREMUX experiment.

Only the temperature measurement of the thermocouple B2.41, which corresponds to the temperature of the most outer thermocouple of the heater block 2, falls clearly outside the confidence interval of the model, being significantly lower than the predicted value. As it has been stated in Section 4.3.3, this significant deviation from the predicted temperature suggests a movement of this thermocouple outwards with respect to the center of the pebble bed during the runs. The stiffening of the heating wires by adding more spacing plates in order to reduce the free heating wire length between supports is therefore highly recommended in order to avoid such wire displacements in the pebble bed in future similar assemblies.

The results for the rest of the heating power levels performed in PREMUX (namely HI, MED, LO and VLO) are reported in the Appendix B.

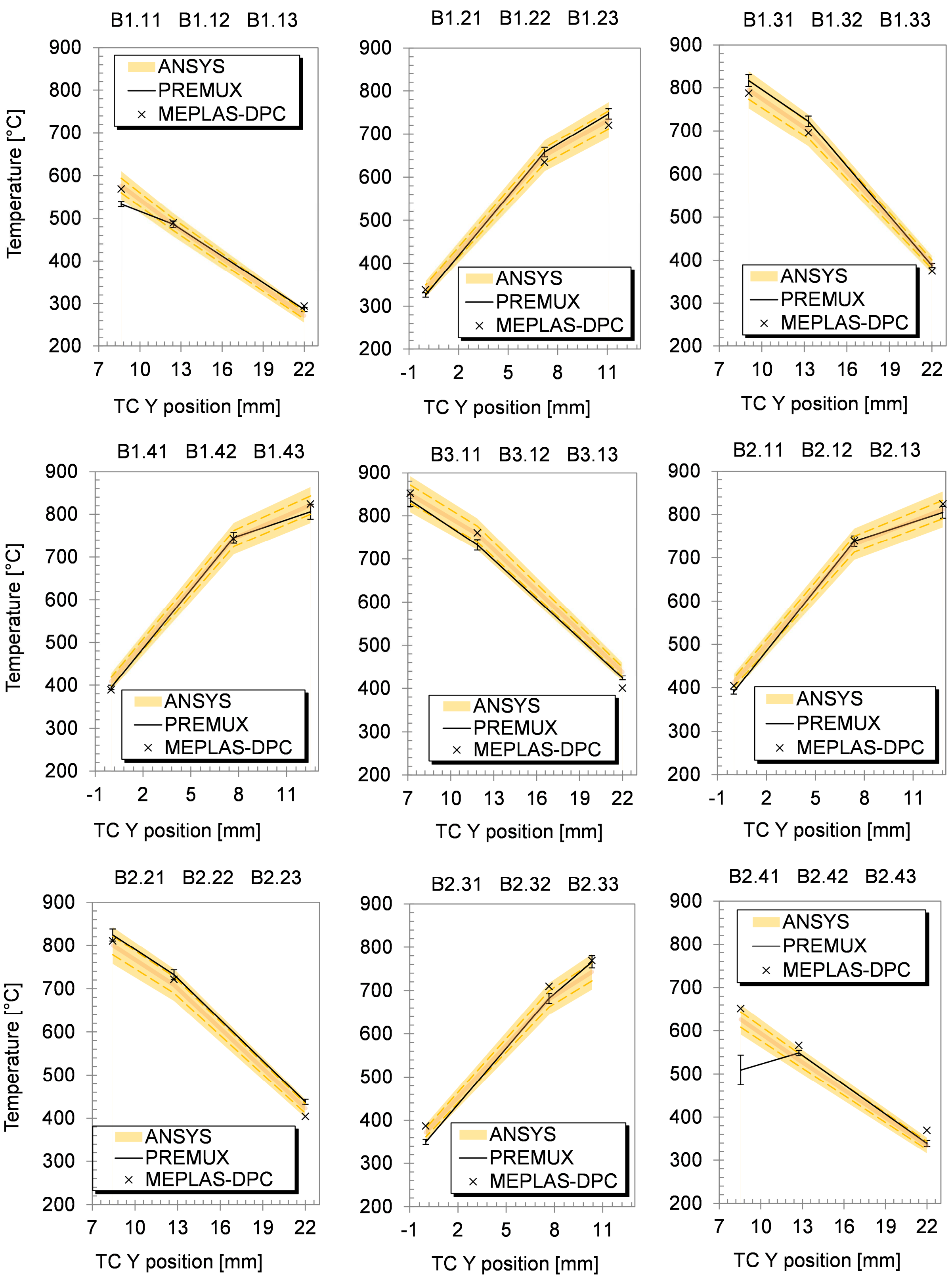

Figure 6.4: Comparison between the predicted steady state temperatures of the Li_4SiO_4 pebble bed with the ANSYS probabilistic thermal model, as well as with the MEPLAS-DPC model and PREMUX at the VHI power level. For the finite element results, the solid line represents the average, the dashed lines depict $\pm\sigma$ and the whole uncertainty band depicts $\pm 2\sigma$.

Figure 6.5 from left to right depicts the air coolant output temperature in the cooling channel #4 and #10 from VHI to VLO power levels, respectively. An agreement between experimental and model values is here observed as well (p-value > 0.05).

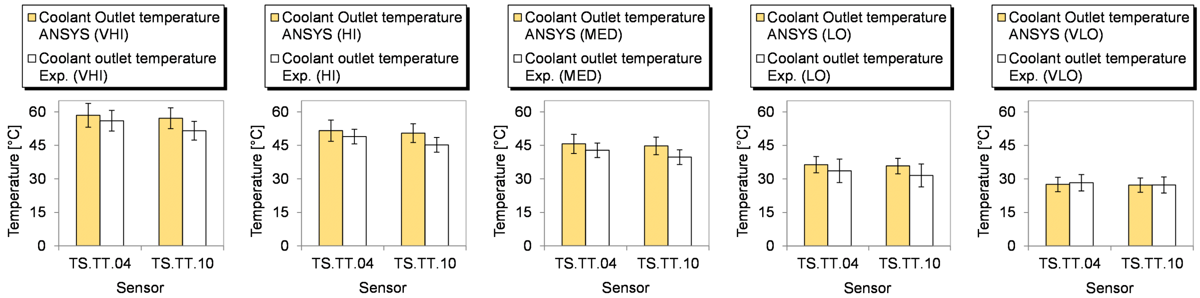

Figure 6.5: Comparison of the predicted steady state temperatures of the outlet air coolant between ANSYS and the PREMUX experimental results. From left to right: VHI, HI, MED, LO, and VLO power levels. The uncertainty bars represents a 95% confidence interval (coverage factor 2).

The related literature about the validation of finite element models is abundant in the area of the design and development of fusion blanket components. However, it lacks of a formal statistical procedure that proves the level of agreement of a model in terms of the statistical power of the corresponding inference test proving the hypothesis of “good agreement”. In this work, a statistical quantification of the model validation is proposed by plotting the measured T^{Exp} vs. predicted T^{ANS} temperatures together with the regression line $T^{ANS} = a\, T^{Exp}$ (Figure 6.6).

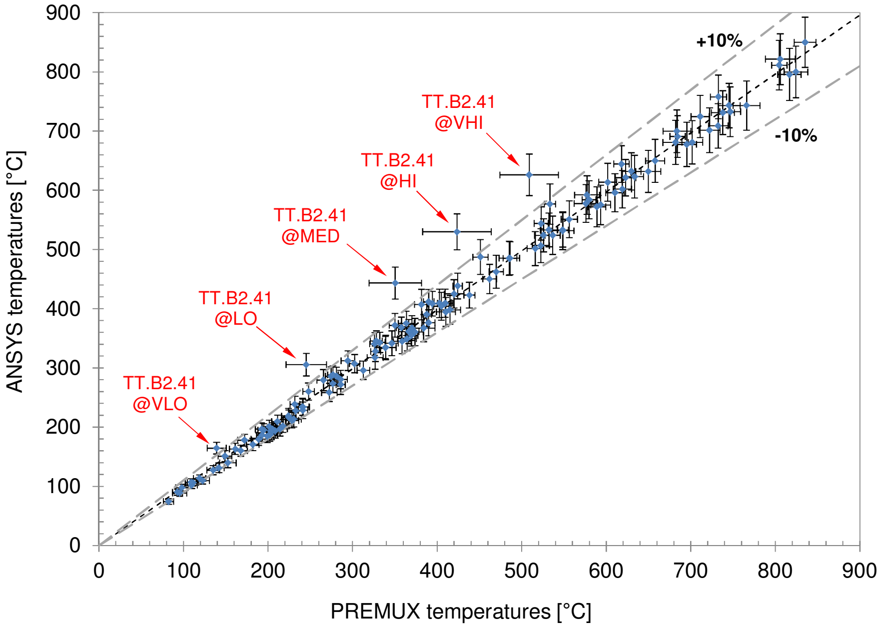

Figure 6.6: Statistical validation of the probabilistic thermal model of PREMUX. Plot of the predicted Li_4SiO_4 pebble bed temperature (T^{ANS}) vs. the temperature measurements obtained in the PREMUX (T^{Exp}), along with the regression line $T^{ANS} = a\, T^{Exp}$, where $a = 1.001 \pm 0.008$ (95% confidence interval). It can be concluded that the model agrees with the experimental results with a significance of less than 5%. The dashed lines serve as an indication of the $\pm 10\%$ with respect to the $T^{ANS} = T^{Exp}$ line.

The slope of the fitting line is computed together with its 95% confidence interval. In the case of the probabilistic thermal model developed here, the slope of the regression line is $a = 1.001$, with a 95% confidence interval $(0.993, 1.009)$. Therefore, it is concluded that the probabilistic model agrees with the experimental results with a significance level $\leq 5\%$. The 5 highlighted temperature measurements in Figure 6.6 that deviates significantly from the regression line correspond to the ones measured by the thermocouple B2.41, as observed before.

The adjusted goodness of fit of the validation regression line is R^2-adj= 99.8%, with a RMSE $= 20.65$ °C. In order to generalize and evaluate the model's accuracy, a RMSE% has been defined that is relative to the measured mean temperature of the Li_4SiO_4 pebble bed, which is 371.5 °C, in the range of the 5 power levels performed in the experimental campaign. This yields to a RMSE% of 5.56%.

6.9 Stochastic sensitivity analysis

In order to quantify the sensitivity of the model inputs to the outputs, the partial rank correlation (Hamby, 1995) method has been applied. This method calculates the Spearman's rank-order correlation coefficient of two variable ranks R and S as:

$$r_S = \frac{\sum_{i=1}^{n_S} (R_i - \overline{R})(S_i - \bar{S})}{\sqrt{\sum_{i=1}^{n_S} (R_i - \overline{R})^2} \sqrt{\sum_{i=1}^{n_S} (S_i - \bar{S})^2}} \, , \tag{6.19}$$

where R_i and S_i are the ranks of the variables r_i and s_i that belong to the set of observations $\{r_1, \ldots, r_{n_S}\}^T$ and $\{s_1, \ldots, s_{n_S}\}^T$, respectively and where $\overline{R}$ and $\bar{S}$ are the mean of these ranks.

The rank-order correlation coefficient r_S takes then values in the interval $[-1,1]$ and gives an indication of the relative strength of the variation of an output S against variations of the input R. As the set of model inputs (i.e. observations) is finite and has been obtained from random sampling, the rank-order correlation coefficient is itself a stochastic variable, whose significance is to be assessed with the statistic:

$$t = r_S \sqrt{\frac{n_S - 2}{1 - {r_S}^2}} \, , \tag{6.20}$$

in a t-Student distribution with 0 mean and $\upsilon = n_S - 2$.

For each power level, a sample size of $n_S = 500$ has been used for the determination of the Spearman rank-order correlation coefficients. This sample size is a trade-off between computation time and accuracy of the statistical inference tests. The significance level of the rank-orders have been set to $p < 0.05$.

The results of the sensitivity study for the heating power VHI are depicted in Figure 6.7. Here, a table with the Spearman rank-order correlation coefficients of each model input parameter is depicted (top) and their relative (%) contribution to the outputs (the temperature measurements) are tabulated (bottom). The same report for the rest of the power levels (HI, MED, LO and VLO) is given in Appendix C.

For all power levels it can be generalized that the most sensitive input parameters to the temperature predictions of the Li_4SiO_4 pebble bed are: (1) the heat generation of the 3 heaters, (2) the thermal conductivity of the pebble bed and (3) the heat transfer coefficient in the PREMUX test box cooling channels. These 5 model inputs, out of 15 input parameters in the VHI power and 11 for the rest of the power levels, represent at least 80% of the total sensitivity of each pebble bed temperature.

In each figure, it is observed that the temperature predictions of the thermocouple*s* on the heater cable *h* (B*h.p*1) and in the pebble bed (B*h.p*2) at each position *p* are most sensitive to the heat generation of the heaters (~40% ÷ 50%), the pebble bed thermal conductivity (~30% ÷ 40%) and to the heat transfer coefficient in the cooling channel (~10% ÷ 20%). On the other side, the influence of the heat transfer coefficient of the cooling channels on the temperature predictions on the test box walls (B*h.p*3) is here twice higher (~20% ÷ 30%) and close to the effect of heat generation of the heaters (~30% ÷ 40%). In this case, the thermal conductivity of the pebble bed is less sensitive (< 10%).

As for the other input parameters, the thermal contact conductance between the steel box and the pebble bed represents only a maximum of 6% of total sensitivity of the temperature estimations at the box walls (B*h.p*3) and it is negligible elsewhere. The sensitivity contribution of the inlet temperature of the air coolant increases moderately as the power level decreases: when tested at VHI its sensitivity represents 0% at B*h.p*1 and B*h.p*2 locations and ~5% at B*h.p*3, while for VLO it represents ~7% at B*h.p*1 and B*h.p*2 locations and ~13% at B*h.p*3. The air coolant mass flow is even less sensitive and represents a maximum of ~3% at the B*h.p*3 locations and it is negligible elsewhere.

The contribution of the heat transfer coefficients at the inlet and outlet pipes has been found to be of a maximum of 1% at the B*h.p*3 and negligible in other locations when it has been tested at VHI. Due to this reduced influence, they have not been considered for the stochastic analyses at the other power levels. The thermal conductivity of the thermal insulation and the free convection between this insulation and the still air at room temperature represents as well about 2% of the total sensitivity at the B*h.p*3 and they are negligible elsewhere. However, these 2 input parameters have been taken into account in the probabilistic analysis for all power levels, as they did not significantly increase the total computation time.

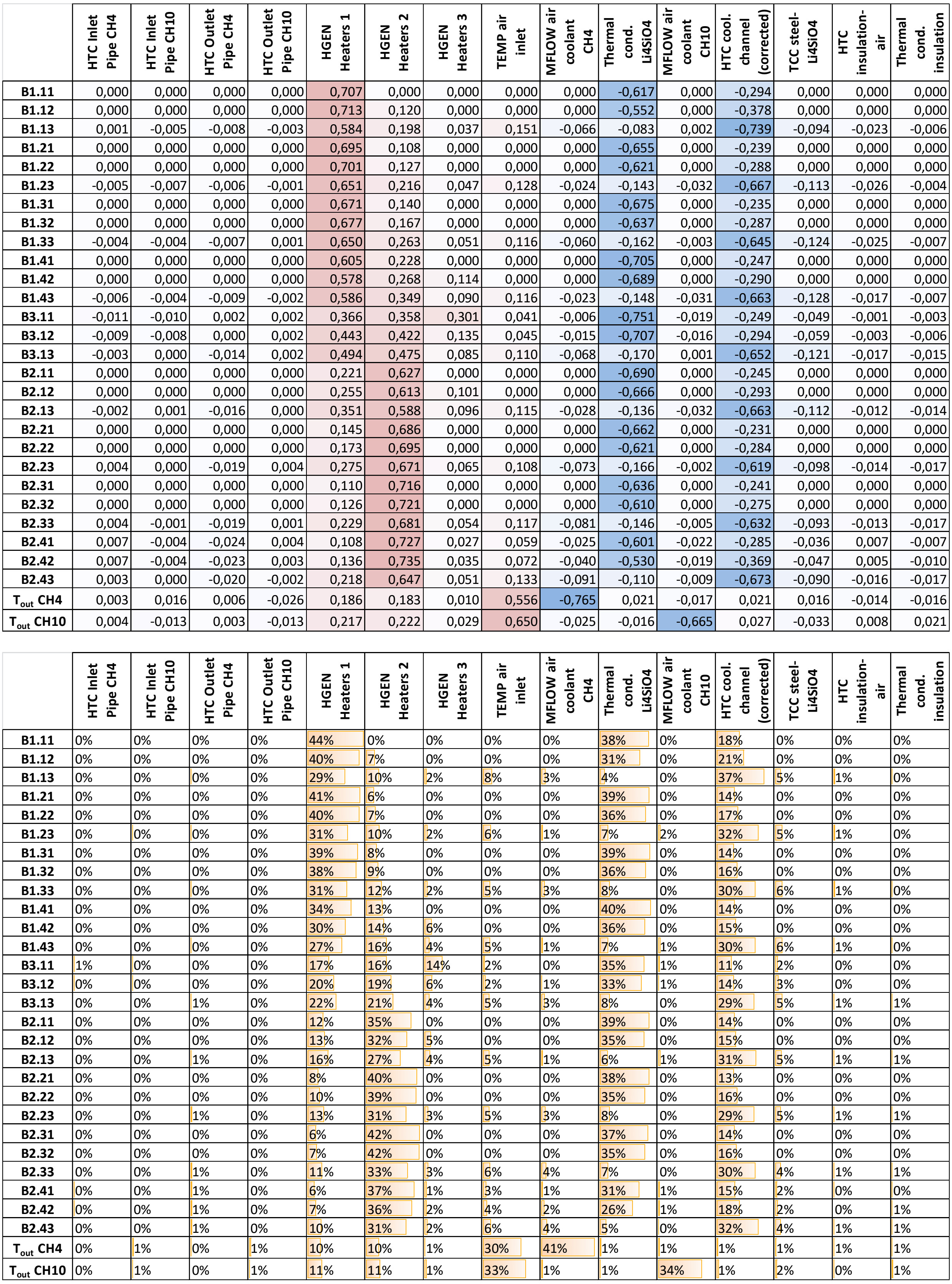

	HTC Inlet Pipe CH4	HTC Inlet Pipe CH10	HTC Outlet Pipe CH4	HTC Outlet Pipe CH10	HGEN Heaters 1	HGEN Heaters 2	HGEN Heaters 3	TEMP air inlet	MFLOW air coolant CH4	Thermal cond. Li4SiO4	MFLOW air coolant CH10	HTC cool. channel (corrected)	TCC steel-Li4SiO4	HTC insulation-air	Thermal cond. insulation
B1.11	0,000	0,000	0,000	0,000	0,707	0,000	0,000	0,000	0,000	-0,617	0,000	-0,294	0,000	0,000	0,000
B1.12	0,000	0,000	0,000	0,000	0,713	0,120	0,000	0,000	0,000	-0,552	0,000	-0,378	0,000	0,000	0,000
B1.13	0,001	-0,005	-0,008	-0,003	0,584	0,198	0,037	0,151	-0,066	-0,083	0,002	-0,739	-0,094	-0,023	-0,006
B1.21	0,000	0,000	0,000	0,000	0,695	0,108	0,000	0,000	0,000	-0,655	0,000	-0,239	0,000	0,000	0,000
B1.22	0,000	0,000	0,000	0,000	0,701	0,127	0,000	0,000	0,000	-0,621	0,000	-0,288	0,000	0,000	0,000
B1.23	-0,005	-0,007	-0,006	-0,001	0,651	0,216	0,047	0,128	-0,024	-0,143	-0,032	-0,667	-0,113	-0,026	-0,004
B1.31	0,000	0,000	0,000	0,000	0,671	0,140	0,000	0,000	0,000	-0,675	0,000	-0,235	0,000	0,000	0,000
B1.32	0,000	0,000	0,000	0,000	0,677	0,167	0,000	0,000	0,000	-0,637	0,000	-0,287	0,000	0,000	0,000
B1.33	-0,004	-0,004	-0,007	0,001	0,650	0,263	0,051	0,116	-0,060	-0,162	-0,003	-0,645	-0,124	-0,025	-0,007
B1.41	0,000	0,000	0,000	0,000	0,605	0,228	0,000	0,000	0,000	-0,705	0,000	-0,247	0,000	0,000	0,000
B1.42	0,000	0,000	0,000	0,000	0,578	0,268	0,114	0,000	0,000	-0,689	0,000	-0,290	0,000	0,000	0,000
B1.43	-0,006	-0,004	-0,009	-0,002	0,586	0,349	0,090	0,116	-0,023	-0,148	-0,031	-0,663	-0,128	-0,017	-0,007
B3.11	-0,011	-0,010	0,002	0,002	0,366	0,358	0,301	0,041	-0,006	-0,751	-0,019	-0,249	-0,049	-0,001	-0,003
B3.12	-0,009	-0,008	0,000	0,002	0,443	0,422	0,135	0,045	-0,015	-0,707	-0,016	-0,294	-0,059	-0,003	-0,006
B3.13	-0,003	0,000	-0,014	0,002	0,494	0,475	0,085	0,110	-0,068	-0,170	0,001	-0,652	-0,121	-0,017	-0,015
B2.11	0,000	0,000	0,000	0,000	0,221	0,627	0,000	0,000	0,000	-0,690	0,000	-0,245	0,000	0,000	0,000
B2.12	0,000	0,000	0,000	0,000	0,255	0,613	0,101	0,000	0,000	-0,666	0,000	-0,293	0,000	0,000	0,000
B2.13	-0,002	0,001	-0,016	0,000	0,351	0,588	0,096	0,115	-0,028	-0,136	-0,032	-0,663	-0,112	-0,012	-0,014
B2.21	0,000	0,000	0,000	0,000	0,145	0,686	0,000	0,000	0,000	-0,662	0,000	-0,231	0,000	0,000	0,000
B2.22	0,000	0,000	0,000	0,000	0,173	0,695	0,000	0,000	0,000	-0,621	0,000	-0,284	0,000	0,000	0,000
B2.23	0,004	0,000	-0,019	0,004	0,275	0,671	0,065	0,108	-0,073	-0,166	-0,002	-0,619	-0,098	-0,014	-0,017
B2.31	0,000	0,000	0,000	0,000	0,110	0,716	0,000	0,000	0,000	-0,636	0,000	-0,241	0,000	0,000	0,000
B2.32	0,000	0,000	0,000	0,000	0,126	0,721	0,000	0,000	0,000	-0,610	0,000	-0,275	0,000	0,000	0,000
B2.33	0,004	-0,001	-0,019	0,001	0,229	0,681	0,054	0,117	-0,081	-0,146	-0,005	-0,632	-0,093	-0,013	-0,017
B2.41	0,007	-0,004	-0,024	0,004	0,108	0,727	0,027	0,059	-0,025	-0,601	-0,022	-0,285	-0,036	0,007	-0,007
B2.42	0,007	-0,004	-0,023	0,003	0,136	0,735	0,035	0,072	-0,040	-0,530	-0,019	-0,369	-0,047	0,005	-0,010
B2.43	0,003	0,000	-0,020	-0,002	0,218	0,647	0,051	0,133	-0,091	-0,110	-0,009	-0,673	-0,090	-0,016	-0,017
T_{out} CH4	0,003	0,016	0,006	-0,026	0,186	0,183	0,010	0,556	-0,765	0,021	-0,017	0,021	0,016	-0,014	-0,016
T_{out} CH10	0,004	-0,013	0,003	-0,013	0,217	0,222	0,029	0,650	-0,025	-0,016	-0,665	0,027	-0,033	0,008	0,021

	HTC Inlet Pipe CH4	HTC Inlet Pipe CH10	HTC Outlet Pipe CH4	HTC Outlet Pipe CH10	HGEN Heaters 1	HGEN Heaters 2	HGEN Heaters 3	TEMP air inlet	MFLOW air coolant CH4	Thermal cond. Li4SiO4	MFLOW air coolant CH10	HTC cool. channel (corrected)	TCC steel-Li4SiO4	HTC insulation-air	Thermal cond. insulation
B1.11	0%	0%	0%	0%	44%	0%	0%	0%	0%	38%	0%	18%	0%	0%	0%
B1.12	0%	0%	0%	0%	40%	7%	0%	0%	0%	31%	0%	21%	0%	0%	0%
B1.13	0%	0%	0%	0%	29%	10%	2%	8%	3%	4%	0%	37%	5%	1%	0%
B1.21	0%	0%	0%	0%	41%	6%	0%	0%	0%	39%	0%	14%	0%	0%	0%
B1.22	0%	0%	0%	0%	40%	7%	0%	0%	0%	36%	0%	17%	0%	0%	0%
B1.23	0%	0%	0%	0%	31%	10%	2%	6%	1%	7%	2%	32%	5%	1%	0%
B1.31	0%	0%	0%	0%	39%	8%	0%	0%	0%	39%	0%	14%	0%	0%	0%
B1.32	0%	0%	0%	0%	38%	9%	0%	0%	0%	36%	0%	16%	0%	0%	0%
B1.33	0%	0%	0%	0%	31%	12%	2%	5%	3%	8%	0%	30%	6%	1%	0%
B1.41	0%	0%	0%	0%	34%	13%	0%	0%	0%	40%	0%	14%	0%	0%	0%
B1.42	0%	0%	0%	0%	30%	14%	6%	0%	0%	36%	0%	15%	0%	0%	0%
B1.43	0%	0%	0%	0%	27%	16%	4%	5%	1%	7%	1%	30%	6%	1%	0%
B3.11	1%	0%	0%	0%	17%	16%	14%	2%	0%	35%	1%	11%	2%	0%	0%
B3.12	0%	0%	0%	0%	20%	19%	6%	2%	1%	33%	1%	14%	3%	0%	0%
B3.13	0%	0%	1%	0%	22%	21%	4%	5%	3%	8%	0%	29%	5%	1%	1%
B2.11	0%	0%	0%	0%	12%	35%	0%	0%	0%	39%	0%	14%	0%	0%	0%
B2.12	0%	0%	0%	0%	13%	32%	5%	0%	0%	35%	0%	15%	0%	0%	0%
B2.13	0%	0%	1%	0%	16%	27%	4%	5%	1%	6%	1%	31%	5%	1%	1%
B2.21	0%	0%	0%	0%	8%	40%	0%	0%	0%	38%	0%	13%	0%	0%	0%
B2.22	0%	0%	0%	0%	10%	39%	0%	0%	0%	35%	0%	16%	0%	0%	0%
B2.23	0%	0%	1%	0%	13%	31%	3%	5%	3%	8%	0%	29%	5%	1%	1%
B2.31	0%	0%	0%	0%	6%	42%	0%	0%	0%	37%	0%	14%	0%	0%	0%
B2.32	0%	0%	0%	0%	7%	42%	0%	0%	0%	35%	0%	16%	0%	0%	0%
B2.33	0%	0%	1%	0%	11%	33%	3%	6%	4%	7%	0%	30%	4%	1%	1%
B2.41	0%	0%	1%	0%	6%	37%	1%	3%	1%	31%	1%	15%	2%	0%	0%
B2.42	0%	0%	1%	0%	7%	36%	2%	4%	2%	26%	1%	18%	2%	0%	1%
B2.43	0%	0%	1%	0%	10%	31%	2%	6%	4%	5%	0%	32%	4%	1%	1%
T_{out} CH4	0%	1%	0%	1%	10%	10%	1%	30%	41%	1%	1%	1%	1%	1%	1%
T_{out} CH10	0%	1%	0%	1%	11%	11%	1%	33%	1%	1%	34%	1%	2%	0%	1%

Figure 6.7: Sensitivity analysis of 15 model parameters to the output variables, i.e. pebble bed and outlet coolant temperatures, for the VHI power level. Top table: Spearman Rank-Order correlation coefficients. Bottom table: % contribution of each model parameter to the output variables.

Chapter 7

Conclusion and outlook

7.1 Conclusions

A strategy for the closed validation of the thermo-mechanical functionality of pebble beds for HCPB breeding blankets is presented. The strategy followed consists of providing appropriate testing and numerical predictive tools for a comprehensive and formal validation of these components in a fusion reactor.

Motivated by the need for accurately reproducing the space-depending neutronic volumetric heating of pebble beds in out-of-pile experiments, firstly an advanced heater system based on a hexagonal matrix of parallel heater wires has been designed, developed and constructed. This new heater concept differs from the traditional plate heaters with respect to three key aspects. First, it can capture 2$^{\text{nd}}$ order temperature gradients in the radial and toroidal direction. The existence of several layers of heating sources in both directions permits also the installation of a set of thermocouples, which can capture temperature maps with enough resolution to be reconstructed by biharmonic spline interpolation and to identify the nonlinear thermal gradients. Second, the small wire diameter of the heater is of the same order of magnitude than the smallest pebble and, therefore, the wires can be seen as "linear pebbles". This results in a reduced intrusion in the pebble bed, which has been confirmed by the negligible influence of the heaters in the pebble bed packing factor, as well as by the in-situ effective thermal conductivity tests at temperatures close to room temperature, which have agreed well with the ones reported in the literature without the presence of the heater system. And third, the low thermal inertia of the heater system has proven perform correctly the relatively fast ramp-up power transients during an ITER-like pulse.

As a proof-of-concept, the heater has been integrated in a pre-test experimental set-up (PREMUX), representing a prototypic region of the Li_4SiO_4 pebble bed in the HCPB Breeder Unit. Steady state at 5 power level and transient runs have been performed in PREMUX. It has been found that the steady state runs are self-similar, allowing the treatment of these runs in a generic way by means of a single dimensionless temperature distribution. On the other side, there have been no significant differences between the temperatures at the top and bottom interface layer between the steel box and the pebble bed. Therefore it is concluded that the potential gap formation, if any, after repeated thermal cycling of the pebble bed along its whole operational power level range does not have a noticeable effect in the temperature distribution. This reveals the robust behavior of the temperature fields in the functional materials in the Breeder Unit. Additionally, it has been observed that the purge gas pressure has no significant influence in the temperature distribution in the range between 2 *bar* and 4 *bar*.

As for the provision of numerical tools, a simplified 2D fully coupled thermo-mechanical model in steady-state conditions has been implemented firstly in the ANSYS code, continuing Gan's work (2008) in ABAQUS. The basic features of the model are the nonlinear elasticity and Drucker-Prager Cap plasticity. The wall-heat transfer has been modeled using available temperature dependent empirical correlations. The thermo-mechanical model has been implemented by using the standard and optimized material routines of the code. However, a multi elastic-plastic algorithm (referred to as MEPLAS) is required in the solution routine in order to be able to reproduce the nonlinear elasticity and thermal conductivity as function also of the stress-state. A first validation of the model with the available literature on oedometric tests at different temperatures has shown a good agreement. A 2D thermo-mechanical model of PREMUX has been then built in ANSYS using the MEPLAS algorithmand the predicted temperature distribution has shown as well a good agreement with the experimental results in PREMUX. The predicted hydrostatic pressure and the von Mises stress in the Li_4SiO_4 pebble bed are relatively small. Only peaks of 2.5 *MPa* for the hydrostatic pressure and of 2 *MPa* for the von-Mises stresses are formed on the surface of the heaters. Therefore, this values suggests a very low pebble cracking, which has been confirmed by a post-mortem analysis of the decommissioned pebbles after the tests and where only 2.7 w.t.% are pebble fragments and dust. Also, the analysis of PREMUX has shown that the maximum temperature at the pebble bed-wall interface is relatively low (less than 400 °C), therefore radiation could be neglected if a more sophisticated wall-heat transfer model is to be implemented in the future. To be observed is that the pebble bed stresses have a pure thermal origin, i.e. are driven by the thermal expansion difference between the pebble bed and the steel container, and not by the application of an external force.

In order to formally qualify the thermal performance of the pebble beds in a HCPB Breeder Unit, a probabilistic finite element modeling approach is proposed as a complementary provision for the numerical tools. This probabilistic approach is based on the replacement of the finite element model by an appropriate response functions built with the design points resulting from a computational Design of Experiments. The probabilistic model outputs are then obtained as a result of a stochastic sampling on the response surface. As an application example, a thermal model representing PREMUX has been built with the DesignXplorer module in ANSYS and the experimental results have been used as benchmark data for the validation routine. As a validation metric, the slope of the regression analysis between the experimental data and the stochastic model outputs is proposed. The results of the analysis reveal that the probabilistic model and the experimental results agree 1:1 on a confidence level of 95%. This probabilistic approach allows not only the quantification of the model agreement with available experimental results, but also the execution of stochastic sensitivity studies. Here variations of a model input variable against the outputs are treated as well in a probabilistic way and statistical inference tests are applied to a test statistic to identify the significant model input variables.

7.2 Outlook and future work

With the positive development of a modular, low intrusive heater concept and its proof of concept in the experimental campaign in PREMUX, together with the given fabrication route of a quasi-real scale of the component, the natural continuation of the present work is the design, development and construction of a full-scale HCPB TBM Breeder Unit mock-up and its thermo-mechanical testing. A high temperature He-loop facility is planned to be available in the near-future (Ghidersa et al., 2013), opening the door to an accurate representation of the coolant gas in this component, allowing the test of the mock-up with neither further assumptions nor simplifications in this regard.

As the primary aim of the out-of-pile test will be to validate the thermo-mechanical functionality of a HCPB TBM Breeder Unit, it may not be necessary to implement a fully relevant system of pebble beds. Instead, the problematic Be may be replaced, for instance, by a copper alloy as a substitute material for the neutron multiplier pebble bed. Here, it will be essential to achieve a good characterization of the substitute material before a decision on the construction of the experiment is taken. However, a preliminary assessment of Cu-Zn alloy has shown its potential.

From the point of view of the pebble bed modeling and the probabilistic FE modeling approach of breeding blankets, the following next research lines can be envisaged:

1. With a minor modification of the algorithm, MEPLAS can be run taking into account time integration effects, i.e. transient analyses. The goal here will be to reproduce also the time evolution of the thermo-mechanics of the pebble beds during a power pulse of ITER or DEMO, in order to take into account transient effects and the dynamics of the thermo-mechanical cycling of the pebble bed, with especial emphasis in the possible gap formation issue.
2. If transient behavior is enabled (previous point 1) and a reactor power pulse is to be reproduced, implementation of an enhanced wall treatment for the heat transfer will be mandatory so as to reproduce the possible loss of contact of the pebble bed with the wall. Always considering cost-efficient simulations as a primary goal, the enhanced wall-heat transfer treatment may only need to take into account the purge gas thermal conductivity, as the relatively low temperatures in that region may allow neglecting radiation effects. Even if some assumptions, linearizations and/or simplifications have to be assumed, care has to be taken to obtain expressions only as function of the local temperature, trying to avoid dependencies from the pebble bed geometry, stress-strain field or other variables that require complex multi-field coupling.
3. As it has been mentioned in the previous Section, the pebble bed stresses are thermally induced due to the confined thermal expansion of the pebble beds in their steel containers. Should the Young modulus and the thermal conductivity be able to be expressed as a function of the thermal expansion difference between the steel box and the pebble beds instead of the stress fields, those two material properties will become only a

function of the temperature field, thus decoupling the thermal and mechanical fields and greatly reducing the complexity of the computations. Therefore, research should be performed in order to further decouple the problem of the nonlinear elasticity and the thermal conductivity from the stress-strain fields. If that can be achieved, there will be no need for a routine like in MEPLAS, and fully default element formulations will be sufficient to reproduce the basic thermo-mechanics of the pebble beds. Moreover, fully-coupled schemes will be able to be replaced by sequential thermal-structural simulations.

4. The complexity reduction that will follow after a successful uncoupling of the elasticity law and the thermal conductivity from the stress-state may lead to the ability of performing 3D computations with small and medium geometries, which are recommended to take into account thermo-mechanical physics and details that are not reflected in a 2D model.

5. If points 1 to 4 are achieved, it is recommended to use of ANSYS default material routines in order to include creep effects in the pebble beds. The implementation of the creep material properties with the default ANSYS material definitions is straightforward, robust should not strongly penalize the code execution time.

6. Also, depending on the degree of simplification reached, the deterministic thermo-mechanical model could be enhanced to include probabilistic data, as shown in Chapter 6. This will permit taking into account the uncertainties of some key model parameters, especially on the material properties of the pebble bed where little information is available. The probabilistic approach will serve as well to quantify the agreement of such thermo-mechanical model with the data available from a full-scale mock-up of the HCPB Breeder Unit, as well as to gain a better understanding of the effects of the uncertainties on key characteristics of the system (e.g. material properties leading to different gap formation) in the thermal field of the pebble beds.

References

ABAQUS®, 2011. *Theory reference*. Version 6.11.

Abdou, M.A., 1982. *Tritium breeding in fusion reactors*. Report ANL/PP/TM-165. Argonne, Illinois: Fusion Power Program Argonne National Laboratory.

Abdou, M.A. et al., 2015. Blanket/first wall challenges and required R&D on the pathway to DEMO. *Fusion Engineering and Design*, pp.2-43.

Abou-Sena, A., Löbbecke, B., von der Weth, A. & Knitter, R., 2011. Effect of post welding heat treatment of the HCPB TBM on Eurofer and lithium orthosilicate pebbles. *Fusion Engineering and Design*, pp.2254-57.

Abou-Sena, A., Ying, A. & Abdou, M., 2005. Effective thermal conductivity of lithium ceramic pebble beds for fusion blankets: a review. *Fusion Science and Technology*, pp.1094-100.

Abou-Sena, A., Ying, A. & Abdou, M., 2009. Experimental measurements of the interface thermal conductance of a lithium metatitanate pebble bed. *Fusion Science and Technology*, pp.206-10.

AD 2000-Merkblatt HP 30:2003-01, 2003. *Durchführung von Druckprüfungen*. Essen: Verband der Technischen Überwachungs-Vereine e.V.

Agrawal, D.K., 1998. Microwave processing of ceramics. *Current Opinion in Solid State and Materials Science*, pp.480-85.

Akiyama, Y., 1991. *Design Technology of Fusion Reactors*. Singapore: Wolrd Scientific Publishing Co. Pte. Ltd.

Allen, T.T., Bernshteyn, M.A. & Kabiri-Bamoradian, K., 2003. Constructing Meta-Models for Computer Experiments. *Journal of Quality Technology*, pp.264-74.

Allen, T.T. & Yu, L., 2002. Low-cost response surface methods from simulation optimization. *Quality and Reliability Engineering International*, pp.5-17.

Allen, T., Yu, L. & Bernshteyn, M., 2000. Low-cost response surface methods applied to the design of plastic fasteners. *Quality engineering*, pp.583-91.

Anderko, K., Schäfer, L. & Materna-Morris, E., 1991. Effect of the δ-ferrite phase on the impact properties of martensitic chromium steels. *Journal of Nuclear Materials*, pp.492-95.

Andersson, P. & Bäckström, G., 1976. Thermal conductivity of solids under pressure by the transient hot wire mthod. *Review of Scientific Instruments*, pp.205-09.

ANSYS®, 2012. Design Exploration User Guide.

ANSYS®, 2013. *ANSYS Theory Reference.* 145th ed.

ASTM Standard C553-13, 2013. *Standard specification for mineral fiber blanket thermal insulation for commercial and industrial applications.* West Conshohocken, PA: ASTM Internaitonal.

Aubert, P. et al., 2011. Low activation steels welding with PWHT and coating for ITER test blanket modules and DEMO. *Journal of Nuclear Materials*, pp.156-62.

Autorité de Súreté Nucléaire, 2005. *Arrêté du 12 décembre 2005 relatif aux équipements sous pression nucléaires (ESPN).* Paris: ASN.

Azizov, E.A., 2012. Tokamaks: from A. D. Sakharov to the present (the 60-year history of tokamaks). *Physics-Uspekhi*, pp.190-203.

Baughn, J.W., Hoffman, M.A., Takahashi, R.K. & Launder, B.E., 1984. Local Heat Transfer Downstream of an Abrupt Expansion in a Circular Channel With Constant Wall Heat Flux. *ASME Journal of Heat Transfer*, pp.789-96.

Beena, P. & Ganguli, R., 2010. Response surface approximation using sparse grid design. *international Journal of Computational and Applied Mathematics*, pp.459-78.

Blackwell, J.H., 1954. A transient-flow method for determination of thermal constants of insulating materials in bulk, part I-theory. *Journal of Applied Physics*, pp.137-44.

Boccaccini, L.V. et al., 2011. Present status of the conceptual design of the EU test blanket systems. *Fusion Engineering and Design*, pp.478-83.

Boccaccini, L.V. et al., 2005. *Design Description Document for the European Helium Cooled Pebble Bed (HCPB) Test Blanket Modules.* DDD2005-EU-HCPB. Karlsruhe: Forschungszentrum Karlsruhe.

Boccaccini, L.V. et al., 2002. Strategy for the blanket testing in ITER. *Fusion Engineering and Design*, pp.423-29.

Boccaccini, L.V. et al., 2004. Materials and design of the European DEMO blankets. *Journal of Nuclear Materials*, pp.148-55.

Boccaccini, L.V. et al., 2009. The EU TBM systems: Design and development programme. *Fusion Engineering and Design*, pp.333-37.

Boccaccini, L.V. et al., 2006. The European test blanket module systems: Design and integration in ITER. *Fusion Engineering and Design*, pp.407-14.

Boelter, L.M.K., Cherry, V.H., Johnson, H.A. & Martinelli, R.C., 1965. *Heat transfer notes.* New York: McGraw-Hill.

Bolton, M.D., 1986. The strength and dilatancy of sands. *Géotechnique*, pp.65-78.

Box, G.E.P. & Behnken, D.W., 1960. Some new three level designs for the study of quantitative variables. *Technometrics*, pp.455-75.

Buckingham, E., 1914. On physically similar systems; illustrations of the use of dimensional equations. *Physical Review*, pp.345-76.

Bühler, L., 1998. FZKA 6093 *A simple model for the elasticity of granular materials in fusion breeding blankets.* Technical Report. Karlsruhe Institute of Technology.

Bühler, L., 2002. FZKA 6561 *Continuum models for pebble beds in fusion blankets.* Internal report. Karlsruhe Institute of Technology.

Bursztyn, D. & Steinberg, D.M., 2006. Comparison of designs for computer experiments. *Journal of Statistical Planning and Inference*, pp.1103-19.

Carslaw, H.S. & Jaeger, J.C., 1959. *Conduction of Heat in Solids.* 2nd ed. Oxford, UK: Oxford University Press.

Çengel, Y.A. & Cimbala, J.M., 2006. Chapter 8: Flow in pipes. In *Fluid mechanics : fundamentals and applications.* 1st ed. New York: MacGraw-Hill. Ch. 8. pp.321-98.

Chen, Y., Fischer, U., Pereslavtsev, P. & Wasastjerna, F., 2003. *The EU Power Plant Conceptual Study - Neutronic design analyses for near term and advanced reactor models.* Scientific Report FZKA 6763. Karlsruhe: Karlsruhe Institute of Technology.

Christensen, R., 2001. *Advanced linear modeling: multivariate, time series, and spatial data; nonparametric regression and response surface maximization.* 2nd ed. Albuquerque, New Mexico, USA: Springer.

Chuyanov, V.A. & ITER Test Blanket Working Group, 2002. ITER Test Blanket Working Group activities: a summary, recommendations and conclusions. *Fusion Engineering and Design*, pp.273-81.

Cismondi, F., Kecskés, S. & Aiello, G., 2011. HCPB TBM thermo mechanical design: Assessment with respect codes and standards and DEMO relevancy. *Fusion Engineering and Design*, pp.2228-32.

Cismondi, F. et al., 2009. Design update, therma and fluid dynamic analyses of the EU-HCPB TBM in vertical arrangement. *Fusion Engineering and Design*, pp.607-12.

Cismondi, F. et al., 2010. Preliminary thermal design and related DEMO relevancy of the EU-HCPB TBM in vertical arrangement. *Fusion Engineering and Design*, pp.2040-44.

Cismondi, F. et al., 2012. The fundamental role of fluid dynamic analyses in the design of the solid EU Test Blanket Module. *Fusion Enigneering and Design*, pp.1123-29.

Cismondi, F. & Neuberger, H., 2009. *Main design parameters choice for the HCPB IN TBM BU and related level of DEMO relevancy.* Technical Note TG02-T-12-D1. Karlsruhe Institute of Technology.

Clapeyron, E., 1834. Mémoire sur la puissance motrice de la chaleur. *Journal de l'École Polytechnique*, pp.159-90.

Coleman, H.W. & Steele, W.G., 2009. *Experimentation, validation, and uncertainty analysis for engineers.* 3rd ed. Hoboken, New Yersey, USA: John Wiley & Sons.

Coube, O., 1998. *Modelling and numerical simulation of powder die compaction with consideration of cracking.* PhD Thesis. Fraunhofer.

Coulomb, C. A., 1773. In memories de Mathematique et de Physique. *Academie Royal des Sciences par divers sans*, pp.343-82.

Dalle Donne, M. et al., 1991. *KfK contribution to the development of DEMO-relevant test blankets for NET/ITER. Pt. 2: BOT helium cooled solid breeder blanket.* Report KFK-4928. Karlsruhe: Kernforschungszentrum Karlsruhe GmbH.

Dalle Donne, M. et al., 1994. European DEMO BOT solid breeder blanket. Karlsruhe, 1994. Proceedings of the 18th Symposium on Fusion Technology (SOFT).

Dalle Donne, M., Goraieb, A., Piazza, G. & Sordon, G., 2000. Measurements of the effective thermal conductivity of a Li4SiO4 pebble bed. *Fusion Engineering and Design*, pp.513–19.

Dalle Donne, M. & Sordon, G., 1990. Heat transfer in pebble beds for fusion blankets. *Fusion Technology.*

D'Auria, F. & Galassi, G.M., 1998. Code validation and uncertainties in system thermalhydraulics. *Progress in Nuclear Energy*, pp.175-216.

D'Auria, F. & Mazzantini, O., 2011. The best estimate plus uncertainty challenge in the current licencing process of present reactors. *Science and Technology of Nuclear Installations*, 2011, pp.1-9.

Dean, G. & Crocker, L., 2001. Measurement Good Practice Guide No. 48 *The use of Finite Element methods for design with adhesives.* Guide. Teddington, Middlesex, United Kingdom: National Physical Laboratory.

Dell'Orco, G. et al., 2006. Progress in the benchmark exercise for analyzing the lithiate breeder pebble bed thermo-mechanical behavior. *Fusion Engineering and Design*, pp.169-74.

Dell'Orco, G. et al., 2007. A constitutive model for the thermo-mechanical behaviour of fusion-relevant pebble beds and its application to the simulation of HELICA mock-up experimental results. *Fusion Engineering and Design*, pp.2366-74.

Di Maio , P.A., Giammusso, R. & Vella, G., 2010. On the hyperporous non-linear elasticity model for fusion-relevant pebble beds. *Fusion Engineering and Design*, pp.1234-44.

Di Maio, P.A. et al., 2008. Experimental tests and thermo-mechanical analyses on the HEXCALIBER mock-up. *Fusion Engineering and Design*, pp.1287-93.

DIN EN ISO 8573-1:2010, 2010. *Druckluft für allgemeine Anwendung - Teil 1: Verunreinigungen und Qualitätsklassen.* Berlin: Deutsches Institut für Normung e.V.

DIN EN ISO Standard 13919-1:1996-09, 1996. *Elektronen- und Laserstrahl-Schweißverbindungen Leitfaden für Bewertungsgruppen für Unregelmäßigkeiten.* Berlin: Deutsches Institut für Norming e.V.

DIN EN ISO Standard 286-1:2010-11, 2010. Geometrische Produktspezifikation (GPS) - ISO-Toleranzsystem für Längenmaße - Teil 1: Grundlagen für Toleranzen, Abmaße und Passungen (ISO 286-1:2010). Berlin, 2010. Deutsches Institut für Normung e.V.

DIN EN ISO Standard 8894-1:2010, 2010. *Feuerfeste Werkstoffe - Bestimmung der Wärmeleitfähigkeit - Teil 1: Heißdrahtverfahren (Kreuzverfahren und Wiederstandthermometer-Verfahren) (ISO 8894-1:2010).* Berlin: Deutsches Institut für Normung e.V.

DIN EN Standard 1011-7:2004-10, 2004. *Schweißen - Empfehlungen zum Schweißen metallischer Werkstoffe - Teil 7: Elektronenstrahlschweißen.* Berlin: Deutsches Institut für Normung e.V. Deutsches Institut für Normung e.V.

DIN Standard 1343:1990-01, 1990. *Referenzzustand, Normzustand, Normvolumen; Begriffe und Werte.* Berlin. Deutsches Institut für Normung e.V.

Dixon, J.C., 2007. *The schock absorver handbook.* 2nd ed. John Wiley & Sons.

Drucker, D. C., Gibson, R. E & Henkel, D. J., 1955. Soil Mechanics and Work Hardening Theories of Plasticity. *Proceedings ASCE*, p.Paper 798.

Drucker, D.C., 1957. Nonr-562(20)/2 *A definition of stable inelastic material.* Technical Report. Brown University.

Drucker, D.C. & Prager, W., 1952. Soil Mechanics and Plastic Analysis or Limit Design. *Quarterly of Applied Mechanics*, pp.157-65.

Eddington, A.S., 1920. The internal constitution of the stars. *The Observatory*, pp.341-58.

EFDA, 2005. EFDA-RP-RE-5.0 *A conceptual study of commercial fusion power plants.* Report. European Commission.

Einstein, A., 1905. Ist die Trägheit eines Körpers von seinem Energieinhalt abhängig? *Annalen der Physik*, pp.639-41.

Enoeda, M. et al., 2006. Overview of design and R&D of test blankets in Japan. *Fusion Engineering and Design*, pp.415-24.

Enoeda, M. et al., 1998. Effective thermal conductivity measurements of the binary pebble beds by hot wire method for the breeding blanket. *Fusion Technology*, pp.877-81.

Erfling, H.-D. & Grüneisen, E., 1942. Annalen der Physik. pp.89-99.

Federici, et al., 2015. Overview of the design approach and optimization of R&D activities towards an EU DEMO. *Fusion Engineering and Design.*

Federici, G., Raffray, R. & Abdou, M.A., 1989. Tritium modeling of experimental results for lithium-metasilicate in the LISA-1 experiment. *Advances in Ceramics - Fabrication and Properties of Lithium Ceramics II*, pp.329-44.

Federici, G., Wu, C.H., Raffray, A.R. & Billone, M.C., 1992. Modeling of tritium release from ceramic breeders: Status and some implications for next-step devices. *Journal of Nuclear Materials*, pp.1-31.

Feng, K.M. et al., 2006. Preliminary design for a China ITER test blanket module. *Fusion Engineering and Design*, pp.1219-24.

Fischer, U. et al., 2015. Neutronics requirements for a DEMO fusion power plant. *Fusion Engineering and Design*, p.In Press.

Fossum, A.F. & Brannon, R.M., 2004. SAND2004-3226 *The Sandia Geomodel: Theory and User's Guide*. Report. Sandia National Laboratories.

Fossum, A.F. & Fredrich, J.T., 2000. Cap plasticity models and compactive and dilatant pre-failure deformation. *4th North American Rock Mechanics Symposium.*

Foster, M.P. & Evans, A.N., 2008. An evaluation of interpolation techniques for reconstructing ionospheric TEC maps. *IEEE Transactions on Geoscience nd Remote Sensing*, pp.2153-64.

Foster, C.D., Regueiro, R.A., Fossum, A.F. & Borja, R.I., 2005. Implicit numerical integration of a three-invariant, isotropic/kinematic hardening cap plasticity model for geomaterials. *International Journal of Numerical and Analytical Methods in Geomechanics*, pp.5109-38.

Gan, Y., 2008. *Thermo-mechanics of pebble beds in fusion blankets.* PhD Thesis. Karlsruhe Institute of Technology.

Gan, Y. et al., 2014. Thermal discrete element analysis of EU solid breeder blanket subjected to neutron irradiation. *Fusion Science and Technology*, pp.83-90.

Gan, Y. & Kamlah, M., 2007a. Identification of material parameters of a thermo-mechanical model for pebble beds in fusion blankets. *Fusion Engineering and Design*, pp.189-206.

Gan, Y. & Kamlah, M., 2007b. FUSION Nr. 312 *Thermo-mechanical analyses of HELICA and HEXCALIBER mock-up experiments.* Internal Report. Karlsruhe Institute of Technology.

Gan, Y., Kamlah, M. & Reimann, J., 2010. Computer simulation of packing structure on pebble beds. *Fusion Engineering and Design*, pp.1782-87.

Gan, Y., Kamlah, M., Rizzi, G. & Boccaccini, L.V., 2007c. FUSION Nr. 297 *Validation of a thermo-mechanical model for ceramic breeder and beryllium pebble beds.* Internal Report. Karlsruhe Institute of Technology.

Ghidersa, B.E., Jin, X., Rieth, M. & Ionescu-Bujor, M., 2013. KATHELO: A new high heat flux component testing facility. *Fusion Engineering and Design*, pp.854-57.

Giancarli, L.M. et al., 2012. Overview of the ITER TBM Program. *Fusion Engineering and Design*, pp.395-402.

Giancarli, L. et al., 2006. Breeding Blanket Modules testing in ITER: An international program on the way to DEMO. *Fusion Engineering and Design*, pp.393-405.

Gnielinski, V., 1976. New equations for heat and mass transfer in turbulent pipe and channel flow. *International Chemical Engineering*, pp.359-68.

Gurson, A.L., 1977. Continuum theory of ductile rupture by void nucleation and growth: Part I - Yield criteria and flow rules for porous ductile media. *Journal of Engineering Materials and Technology*, pp.2-15.

Hajela, P. & Berke, L., 1991. Neurobiological computational models in structural analysis and design. *Computers & structures*, pp.657-67.

Hamby, D.M., 1995. A comparison of sensitivity analysis techniques. *Health Physics*, pp.195-204.

Han, B., Kim, Y. & Him, C.H., 2006. Optimal configuration of neutron reflector in He-cooled molten Li blanket. *Fusion Engineering and Design*, pp.729-32.

Hermsmeyer, S. et al., 2003a. Revision of the EU helium cooled pebble bed blanket for DEMO. In *20th IEEE/NPSS Symposium on Fusion Engineering.*, 2003a.

Hermsmeyer, S. et al., 2006. *European DEMO helium cooled pebble bed (HCPB) blanket concept designed for modular segmentation.* Final Report TW3-TTBB-001-D2. Karlsruhe Institute of Technology.

Hermsmeyer, S. et al., 2001. An improved European helium cooled pebble bed blanket. *Fusion Engineering and Design*, pp.689-93.

Hermsmeyer, S., Malang, S., Fischer, U. & Gordeev, S., 2003b. Lay-out of the He-cooled solid breeder model B in the European power plant conceptual study. *Fusion Engineering and Design*, pp.281-87.

Hernández, F., Cismondi, F. & Kiss, B., 2011a. Design cycle of a Breeder Unit mock-up for the Helium Cooled Pebble Bed Test Blanket Module (HCPB-TBM) for ITER. In *European Nuclear Young Generation Forum 2011.* Prague, 2011a. International Youth Nuclear Congress.

Hernández, F., Cismondi, F. & Kiss, B., 2011b. Fluid dynamic and thermal analyses of a HCPB TBM breeder unit mock-up. *Fusion Engineering and Design*, pp.2278-81.

Hernández, F., Cismondi, F. & Kiss, B., 2012. Thermo-mechanical analyses and assessment with respect to the design codes and standards of the HCPB-TBM breeder unit. *Fusion Engineering and Design*, pp.1111-17.

Hernández, F., Kolb, M., Annabattula, R. & von der Weth, A., 2014. Construction of PREMUX and preliminary experimental results, as preparation for the HCPB breeder unit mock-up testing. *Fusion Engineering and Design*, pp.1257-62.

Hernández, F. et al., 2013. Set-up of a pre-test mock-up experiment in preparation for the HCPB breeder unit mock-up experimental campaign. *Fusion Engineering and Design*, pp.2378-83.

Hernández, F. et al., 2014. Manufacturing pre-qualification of a Short Breeder Unit Mock-up (SHOBU) as part of the roadmap towards the out-of-pile validation of a full scale Helium Cooled Pebble Bed Breeder Unit. In *28th Szmposium on Fusion Technology*. San Sebastián, 2014.

Hofer, D. & Kamlah, M., 2005. Drucker-Prager-Cap creep modelling of pebble beds in fusion blankets. *Fusion Engineering and Design*, pp.105-17.

Husslage, B., Rennen, G., van Dam, E.R. & den Hertog, D., 2006. ISSN 0924-7815 *Space-filling Latin Hypercube designs for computer experiments*. Discussion Paper. Tilburg, The Nederlands: Tilburg University.

IAEA, 2008. *Best estimate safety analysis for Nuclear Power Plants*. Technical Report. Vienna, Austria: IAEA Safety Reports Series no.52.

ISO/IEC Guide 98-3:2008, 2008. ISBN 92-67-10188-9 *Guide to the expression of uncertainty in measurement*. Guide. Joint Committee for Guides in Metrology.

ITER Documentation, 2004. *DDD1.6 Blanket - 1.1 Engineering Description*. Design Description Document.

ITER EDA, 2000. *ITER EDA Documentation series No.19: Technical Basis for the ITER-FEAT outline report*. Report A0 GDRD 2 01-07-13 R 1.0. Vienna: IAEA.

Jiji, L.M., 2006. *Heat convection*. New York, NY, USA: Springer-Verlag Berlin Heidelberg.

JIS Standard R 2616:2001, 2001. *Testing method for thermal conductivity of insulating fire bricks*. Japanese Standards Association.

Jong, C., 2006. With ANSYS towards fusion power generation. In *2006 International ANSYS Conference*. Pittsburgh, 2006. 2006 International ANSYS Conference.

Kaname, I., 2010. ITER on the road to fusion energy. *Nuclear Fusion*, pp.1-10.

Kawamura, H. et al., 2004. Present status of beryllide R&D as neutron multiplier. *Journal of Nuclear Materials*, pp.112-18.

Kazi, S.N., Togun, H. & Sadeghinezhad, E., 2012. Heat transfer to separation flow in heat exchangers. In Kazi, S.N. *An overview of heat transfer phenomena*. Kuala Lumpur, Malaysia. pp.498-526.

Kim, K. & Lee, Y., 1994. Prediction of turbulent heat transfer downstream of an abrupt pipe expansion. *Korean Society of MEchanical Engineers*, pp.248-54.

Kirillov, I.R., Shatalov, G.E., Strebkov, Y.S. & the RF TBM Team, 2005. RF TBMs for ITER tests. *Fusion Engineering and Design*, pp.425-32.

Kiss, B., 2009. *CFD analysis of temperature distribution in the BU*. Internal Report. Budapest: Budapest University of Technology and Economics.

Kiss, B., 2010. *Investigation of temperature distribution in sub-components of BU in case of different mass flows*. Internal Report. Budapest: Budapest University of Technology and Economics.

KIT-INR, 2010. *Experimentelle Anlagen: L-STAR*. [Online] Available at: http://www.inr.kit.edu/256.php [Accessed 27 August 2013].

KIT-INR, 2010. *L-STAR Water Cooling System Handbook*. Karlsruhe Institut.

KIT-INR, 2015. *Experimental facilities and measurement techniques for gas cooling research and technology at INR*. [Online] Available at: http://www.inr.kit.edu/130.php [Accessed 5 April 2015].

Knitter, R., Alm, B. & Roth, G., 2007. Crystallisation and microstructure of lithium orthosilicate pebbles. *Journal of Nuclear Materials*, pp.1387–92.

Knitter, R. et al., 2011. *Development / Qualification / Procurement Plan for Ceramic Breeder Pebbles*. F4E-2009-GRT-030 Task-1 Final Report (0-D4). Karlsruhe: Karlsruhe Institute of Technology.

Kolb, M., 2016. *Personal communication*.

Krasnorutskyi, S. et al., 2014. Qualification of electron beam welding for the production of a Breeder Unit of the HCPB TBM for ITER. In *Proceedings of the 67th IIW Annual Assembly & International Conference*. Seoul, 2014.

Kwast, H. et al., 1994. The behaviour of ceramic breeder materials with respect to tritium release and pellet/pebble mechanical integrity. *Journal of Nuclear Materials*, pp.1010-14.

Kwast, H. et al., 1990. Comparison of the tritium residence times of various ceramic breeder materials irradiated in EXOTIC experiments 4 and 5. In *16th Symposium on Fusion Technology (SOFT)*. London, UK, 1990.

Lade, P.V., 1988a. Effects of voids and volume changes on the behaviour of frictional materials. *International Journal for Numerical and Analytical Methods in Geomechanics*, pp.351-70.

Lade, P.V. & Kim, K.M., 1988b. Single hardening constitutive model for frictional materials. *Computers nd Geotechnics*, pp.33-47.

Lasher, W.C. & Taulbee, D.B., 1992. On the computation of turbulent backstep flow. *International Journal of Heat and Fluid Flow*, pp.30-40.

Lawson, J.D., 1957. Some criteria for a power producing thermonuclear reactor. *Proceedings of the Physical Society*, pp.6-10.

Lee, D.H., Lee, J.S., Park, H.J. & Kim, M.K., 2011. Experimental and numerical study of heat transfer downstream of an axisymmetric abrupt expansion and in cavity of a circular tube. *Journal od Mechanical Science and Technology*, pp.395-401.

Lindau, R. et al., 2005. Present development stataus of EUROFER and ODS-EUROFER for application in blanket concepts. *Fusion Engineering and Design*, pp.989-96.

Lo Frano, R. & Aquaro, D., 2014. Preliminary experimental evaluation of thermal conductivity of ceramic pebble beds. *Journal of Physics: Conference Series*.

Magnani, E., Gabriel, F. & Boccaccini, L.V., 2009. *Technical contour of HCPB DEMO and proposal list of figure of merits as target for the TBM experiments*. Technical Note TG06-T-31.3-D1. Karlsruhe Institute of Technology.

Maisonnier, D. et al., 2005. *A conceptual study of commercial fusion power plants (PPCS)*. EFDA-RP-RE-5.0. European Fusion Development Agreement (EFDA).

Maisonnier, D. et al., 2006. DEMO and fusion power plant conceptual studies in Europe. *Fusion Engineering and Design*, pp.1123-30.

Majumdar, S. & Smith, P., 1998. Treatment of irradiation effects in structural design criteria for fusion reactors. *Fusion Engineering and Design*, pp.25-30.

Materna-Morris, E., 1990. The development of dendritic carbides in a dual-phase martensitic/ferritic steel. *Scanning Microscopy*, pp.287-96.

McGeary, R.K., 1961. Mechanical packing of spherical pebbles. *Journal of the American Ceramic Society*, pp.513-22.

McKay, M.D., Beckman, R.J. & Conover, W.J., 1979. A comparison of three methods for selecting values of input variables in the analysis of output from a computer code. *Technometrics*, pp.239-45.

Miller, A.I., 2001. Heavy water: A manufacturer's guide for the hydrogen century. *Canadian Nuclear Society Bulletin*, pp.1-14.

Miller, R.L. & Krakowski, R.A., 1981. LA-8978-MS *The Modular Stellarator Fusion Reactor concept*. Los Alamos, New Mexico: Los Alamos National Laboratory Los Alamos National Laboratory.

Mondal, A., Agrawal, D.L. & Upadhyaya, A., 2009. Microwave heating of pure copper powder with varying particle size and porosity. *Journal of Microwave Power and Electromagnetic Energy*, pp.5-10.

Montgomery, D.C., 1991. *Design and analysis of experiments.* New York: Wiley.

Moscardini, M., Pupeschi, S. & Aquaro, D., 2013. Thermal Analyses of the Breeder Unit of the Helium Cooled Pebble Bed Test Blanket Module. In *22nd International Conference Nuclear Energy for New Europe (NENE).* Bled, Slovenia, 2013.

National Physical Laboratory, 1995. *Kaye&Laby. Tables of Physical & Chemical Constants. Chapter 4, Section 4.7, Subsect. 4.7.4 Nuclear Fusion.* [Online] Available at: http://www.kayelaby.npl.co.uk/atomic_and_nuclear_physics/4_7/4_7_4.html [Accessed 08 February 2015].

Németh, J., Hernández, F. & Zeile, C., 2012. *Thermal FEM analysis for HCPB-TBM Breeder Unit mock-up test.* Internal Report. Karlsruhe: Karlsruhe Institute of Technology.

Neuberger, H. et al., 2014. Overview on ITER and DEMO blanket fabrication activities of the KIT INR and related frameworks. In *Proceedings of the 28th Symposium on Fusion Technology.* San Sebastián, 2014.

Neuberger, H., von der Weth, A. & Rey, J., 2011. KIT induced activities to support fabrication, assembly and qualification of technology for the HCPB-TBM. *Fusion Engineering and Design*, pp.2039-42.

Neuberger, H. & Zeile, C., 2009. *Analysis of preliminary configuration options for the HCPB EM TBM breeding zone (Task T11).* Deliverable. Karlsruhe Institute of Technology.

Nix, G.H., Lower, G.W., Vachon, R.I. & Tanger, G.E., 1967. Direct determination of thermal diffusivity and conductivity with refined line-source technique. In Heller, G. *Progress in Aeronautics and Astronautics: Thermophysics of Spacecraft and Planetary Bodies.* New York: Academic Press. pp.865-78.

Nobel Lectures, 1966. Chemistry 1922-1941. *Elsevier Publishing Company.*

Norajitra, P., Piel, D., Reimann, G. & Ruprecht, R., 2001. The first HEBLO experiments based on the EU HCPB blanket concept. *Fusion Engineering and Design*, pp.623-27.

OECD:NEA, 1998. *Report on the uncertainty methods study.* Report NEA/CSNI(97)35/Volume 1. Organization for Economic Co-operation and Development.

OECD:NEA, 2005. Origins of the uncertainty and methods. In D'Auria, F., Glaeser, H. & Schultz, R., eds. *Evaluation of Uncertainties in relation to severe accidents and Level-2 probabilistic safety analysis, Workshop Proceedings.* Aix-en-Provence, France, 2005. OECD:NEA.

Okabe, A., Boots, B., Sugihara, K. & Nok Chiu, S., 2000. *Spatial tessellations: Concepts and applications of voronoi diagrams.* 2nd ed. West Sussex, UK: John Wiley & Sons Ltd.

Pavier, E., 1998. *Caracterisation du comportement d'une poudre de fer pour le procedé de compression en matrice.* PhD Thesis. Institut National Polytechnique de Grenoble.

Pelessone, D., 1989. GA-C19579 *A modified formulation of the Cap Model.* Gulf Atomic Report. Prepared for the Defense Nuclear Agency under contract DNA-001086-C-0277.

Pereslavtsev, P. et al., 2010. Neutronic analysis of the HCPB TBM in ITER utilizing an advanced integral approach. *Fusion Engineering and Design*, pp.1653-58.

Petersen, H., 1970. *The properties of helium: Density, specific heats, viscosity, and thermal conductivity at pressures from 100 bar and from room temperature to about 1800 K.* Risö Report No. 224. Danish Atomic Energy Commission, Research Stablishment Risö.

Petukhov, B.S., 1970. Heat transfer and friction in turbulent pipe flow with variable physical properties. *Advances in heat transfer*, pp.504-64.

Piazza, G. et al., 2001b. Behaviour of ceramic breeder materials in long time annealing experiments. *Fusion Engineering and Design*, pp.653-59.

Proust, E. et al., 1991. Solid breeder balnket design and tritium breeding. *Fusion Engineering and Design*, pp.73-84.

Raeder, J. et al., 2016. ISBN 978-3-944161-70-9 *Review of the safety concept for fusion reactor concepts and transferability of the nuclear fission regulation to potential fusion power plants.* GRS - 389. Gesellschaft für Anlagen- und Reaktorsicherheit (GRS) gGmbH.

Rajendra Kumar, E. et al., 2008. Preliminary design of Indian Test Blanket Module for ITER. *Fusion Engineering and Design*, pp.1169-72.

RCC-MR, 2007. *Design and construction for mechanical components of FBR nuclear islands (RCC-MR).* Paris: AFCEN.

RCC-MRx, 2012. *Design and construction rules for mechanical components of nuclear installations (RCC-MRx).* Paris: AFCEN.

Red-Horse, J., Paez, T.L., Field, R.V. & Romero, V., 2000. *Nondeterministic analysis of mechanical systems.* Report. Sandia National Laboratories.

Reh, S., Beley, J.D., Mukherjee, S. & Khor, E.H., 2006. Probabilistic finite element analysis using ANSYS. *Structural Safety*, pp.17-43.

Reimann, J. et al., 2000. Thermomechanical behaviour of ceramic breeder and beryllium pebble beds. *Fusion Engineering and Design*, pp.643-49.

Reimann, J., Boccaccini, L., Enoeda, M. & Ying, A.Y., 2002b. Thermomechanics of solid breeder and Be pebble bed materials. *Fusion Engineering and Design*, pp.319-31.

Reimann, J. & Hermsmeyer, S., 2002a. Thermal conductivity of compressed ceramic breeder pebble beds. *Fusion Engineering and Design*, pp.345-51.

Reimann, J. et al., 2006a. TW5-TTBB-006 D1+D2 *Production and characterization of breeder and multiplier materials in support of the HELICA and HEXCALIBER experiments.* Technical report.

Reimann, J., Knitter, R. & Piazza, G., 2005. TW5-TTBB-006 *Final report on new compilation of the material data base and the material assessment report.* Final Report. Karlsruhe Institute of Technology.

Reimann, J. & Müller, S., 1998. First experiments on the thermomechanical behaviour of Li4SiO4 pebble beds. *Fusion Technology*, pp.1337-40.

Reimann, J., Piazza, G. & Harsch, H., 2006b. Thermal conductivity of compressed beryllium pebble beds. *Fusion Engineering and Design*, pp.449-54.

Reimann, J., Pieritz, R.A. & Rolli, R., 2006. Topology of compressed pebble beds. *Fusion Engineering and Design*, pp.653-58.

Rey, J., Filsinger, D., Ihli, T. & Polixa, C., 2008. Manufacturing aspects in the design of the breeder unit for helium cooled pebble bed blankets. *Fusion Engineering and Design*, pp.1258-62.

Ricapito, I., Ciampichetti, A., Agostini, P. & Benamati, G., 2008. Tritium processing systems for the helium cooled pebble bed test blanket module. *Fusion Engineering and Design*, pp.1461-65.

Richardot, D., Vaillant, J.C., Arbab, A. & Bendick, W., 2000. *The T92/P92 book.* Vallourec & Mannesmann tubes.

Riera, M. D., 1999. *Comportamiento elastoplástico de compactos Pulvimetalúrgicos.* PhD Thesis. Barcelona: Universitat Politècnica de Catalunya.

Rieth, M. et al., 2006. TW4-TTMS-004 D1 *Design limits of welded EUROFER components.* Internal Report. Karlsruhe: Karlsruhe Institute of Technology.

Rieth, M. & Rey, J., 2009. Specific welds for test blanket modules. *Journal of Nuclear Materials*, pp.471-74.

Romanelli, F. et al., 2012. A roadmap to the realization of fusion energy. In *1st IAEA DEMO Programme Workshop.* Los Angeles, 15-18 October, 2012.

Roy, C.J. & Oberkampf, W.L., 2011. A comprehensive framework for verification, validation, and uncertainty quantification in cientific computing. *Computer Methods in Applied Mechanics and Engineering*, pp.2131-44.

Ruatto, P. & Boccaccini, L.V., 1998. Ferromagnetic in-vessel components in ITER: electromagnetic analysis of the European HCPB Test Blanket Module. *Fusion Technology*, pp.1247-50.

Sacks, J., Welch, W.J., Mitchell, T.J. & Wynn, H.P., 1989. Design and analysis of computer experiments. *Statistical science*, pp.409-35.

Salavy, J.-F. et al., 2009. Ferritic-Martensitic steel Test Blanket Modules: Status and future needs for design criteria requirements and fabrication validation. *Journal of Nuclear Materials*, pp.922-26.

Sandler, I.S., DiMaggio, F.L. & Baladi, G.Y., 1976. A generalized Cap model with mixed hardening. *Journal of the Geotechnical Engineering Division*, pp.683-99.

Sandler, I.S. & Pucik, T.A., 1993. AD-A266 342 *Non-uniqueness in dynamic rate-independent non-associated plasticity.* Technical Report. Defense Nuclear Agency.

Sandler, I.S. & Rubin, D., 1979. An algorithm and a modular subroutine for the Cap model. *International Journal for Numerical and Analytical Methods in Geomechanics*, pp.173-86.

Sandwell, D.T., 1987. Biharmonic spline interpolation of GEOS-3 and SEASAT altimeter data. *Geophyisical Research Letters*, pp.139-42.

Schwer, L.E. & Murray, Y.D., 1994. A three-invariant smooth Cap model with mixed hardening. *International Journal for Numerical and Analytical Methods in Geomechanics*, pp.657-88.

Shatalov, G., 2001. DEMO Blanket testing in ITER. Influence on reaching DEMO. *Fusion Engineering and Design*, pp.39-46.

Shewry, M.C. & Wynn, H.P., 2006. Maximum entropy sampling. *journal of Applied Statistics*, pp.165-70.

Siekmann, H.E. & Thamsen, P.U., 2009. *Strömungslehre für den Maschinenbau.* 2nd ed. Berlin: Springer Berlin Heidelberg.

Sparrow, E.M. & Stretton, A.J., 1985. Natural convection from variously oriented cubes and from other bodies of unity aspect ratio. *International Journal of Heat and Mass Transfer*, pp.741-52.

Spitzer, L.J., 1954. NYO-6047; PM-S-14 *Problems of the Stellarator as a usefull power source.* US: Princeton University.

Spitzer, L.J., 1958. The Stellarator concept. *Physics of Fluids*, pp.181-96.

Stieglitz, R., 2009a. Einführung in die Fusionstechnologie (I). In *Fusionstechnologie A*. Karlsruhe: KIT Campus Süd lecture.

Stieglitz, R., 2009b. Einführung in die Fusionstechnologie (II). In *Fusionstechnologie A*. Karlsruhe: KIT Campus Süd lecture.

Sutherland, W., 1893. The viscosity of gases and molecular force. *Philosofical Magazine Series 5.*

Swan, C.C. & Seo, Y.-K., 1999. Limit state analysis of earthen slopes using dual continuum/FEM approaches. *International Journal of Numerical and Analytical Methods in Geomechanics*, pp.1359-71.

Tavassoli, F., 2013. Eurofer steel, development to full code qualification. *Procedia Engineering*, pp.300-08.

Tavassoli, A.-A.F. et al., 2004. Materials design data for reduced activation martensitic steel type EUROFER. *Journal of Nuclear Materials*, pp.257-62.

Taylor, B.N. & Kuyatt, C.E., 1994. *Guidelines for evaluating and expressing the uncertainty of NIST measurement results*. Technical Report. Washington, DC: U.S. Goverment Printing Office National Institute of Standards and Technology.

The National Academies, 2011. *Interim Report - Status of the Study "An assessment of the prospects for inertial fusion energy"*. Report. Washington, DC: The National Academies Press National Research Council.

THERMOCOAX, 1998. *How to choose your THERMOCOAX heating element?* [Online] Available at: http://www.thermocoax.com/pdf/E013_9_HE_English.pdf [Accessed 25 November 2011].

Tucker, J., Zhang, C., Ying, A. & Abdou, M., 2013. Further development of continuum FEM simulation for ceramic breeder pebble bed unit thermomechanics. In *25th Symposium on Fusion Engineering (SOFE)*. San Francisco, 2013. 25th Symposium on Fusion Engineering (SOFE).

Ullman, D.G., 2010. Chapter 5: Planning for Design. In *The Mechanical Design Process*. 4th ed. New York, NY: McGraw-Hill. pp.111-42.

Uo, K., 1961. The confinement of plasma by the Heliotron magnetic field. *Journal of the Physical Society of Japan*, pp.1380-95.

van der Laan, J.G. et al., 2002. Test-element assembly and loading parameters for the in-pile test of HCPB ceramic pebble beds. *Fusion Engineering and Design*, pp.383-90.

van der Laan, J.G. et al., 2000. Design analyses and pre-tests for the irradiation of HCPB pebble-bed assemblies. *Fusion Engineering and Design*, pp.909-18.

van Til, S., Federov, A.V. & Magielsen, A.J., 2012. Study of ceramic pebble beds in Post Irradiation Examination of the Pebble Bed Assemblies irradiation experiment. *Fusion Engineering and Design*, pp.885-89.

VDI-Richtlinie 2230 T1, 2003. *Systematische Berechnung hochbeanspruchter Schraubenverbindungen. Zylindrische Einschraubenverbindungen.* VDI Norm. Düsseldorf: Verein Deutscher Ingenieure.

Vella, G. et al., 2001. Modelling of the thermal-mechanical behaviour of a single size beryllium pebble bed. *Fusion Engineering and Design*, pp.635-40.

Vladimirov, P. et al., 2011. *Development / Qualification / Procurement Plan for Be pebble materials.* F4E-2009-GRT-030 Task-2 Final Report (0-D4). Karlsruhe: Karlsruhe Institute of Technology.

von Mises, R., 1913. Mechanik der festen Körper im plastisch deformablen Zustand. *Göttin. Nachr. Math. Phys.*, pp.582-92.

Watson, D.F., 1992. *Contouring: A guide to the analysis and display of spatial data.* 1st ed. Oxford, UK: Pergamon Press.

Watson, D.F. & Philip, G.M., 1984. Triangle based interpolation. *Mathematical Geology*, pp.779-95.

Wobig, H. & Rehker, S., 1972. A Stellarator coil system without helical windings. *Proceedings of the 7th Symposium on Fusion Technology*, pp.345-57.

Woche, H., Specht, E. & Schmidt, J., 2005. Local heat transfer in tubes after sudden change of diameter. *Chemical Engineering & Technology*, pp.677-83.

Woodruff, S., 2004. An overview of Tokamak alternatives in the US Fusion Program with the aim of fostering concept innovation. *Journal of Fusion Energy*, pp.27-40.

Wu, H.-C., 2005. *Continuum Mechanics and Plasticity.* Chapman & Hall/CRC Press.

Xia, K. & Masud, A., 2006. A new stablished finite-element method embedded with a cap model for the analysis of granular materials. *Journal of Engineering Mechanics*, pp.250-59.

Xu, Z. et al., 2006. *Development of a DEMO Helium Cooled Pebble Bed (HCPB) Breeder Unit featured in flat plates with meandering channels.* Scientific Report FZKA 7181. Karlsruhe: Karlsruhe Institute of Technology.

Yagi, S. & Kunii, D., 1960. Studies on heat transfer near wall surface in packed beds. *American Institute of Chemical Engineers*, pp.97-104.

Yap, C.R., 1989. *Turbulent heat and momentum transfer in recirculating and impinging flows.* PhD Thesis. The University of Manchester, Institute of Science and Technology.

Ying, A. et al., 2006. An overview of US ITER test blanket module program. *Fusion Engineering and Design*, pp.433-41.

Yoshikawa, N., 2010. Fundamentals and applications of microwave heating of metals. *Journal of Microwave Power and Electromagnetic Energy*, pp.4-13.

Zohm, H., 2010. On the minimum size of DEMO. *Fusion Science and Technology*, pp.613-24.

Appendix

Appendix A

Manufacturing of a Short Breeder Unit mockup, as demonstration of the fabrication route of a Breeder Unit

After the consecution of a reference design for the manufacturing of a HCPB Breeder Unit (Section 2.2.1), the fabrication feasibility of this reference design is demonstrated with the assembly of the so-called *Short Breeder Unit* (SHOBU) mock-up, which is presented in this Appendix. This mock-up is fully relevant to a HCPB Breeder Unit in terms of fabrication and the manufacturing technologies planned for it (Rey et al., 2008) are first applied to SHOBU, with special attention to the definition and execution of each of its welding groups. The realization of the SHOBU mock-up has been performed in the frame of the grant BMBF 03 FUS0011, funded by the government of Germany (Neuberger et al., 2014).

A.1 Bill of materials and relevancy of SHOBU with respect to a HCPB Breeder Unit

The SHOBU mock-up (Figure A.1) is formed by 14 different components and 45 parts in total grouped in 11 welding groups. The material used for most of the parts is EUROFER97, while some have been fabricated with P92.

The mock-up consists of two differentiated sectors: (1) the sub-assembly corresponding to the relevant HCPB Breeder Unit mock-up and (2) the components aimed at representing the interfaces between the HCPB TBM Box and the HCPB Breeder Unit, which are mainly the "TBM Manifold" plates, the "Coolant Pipes" and a "Frame" representing the welding interface between the HCPB Breeder Unit and the "BU Backplate".

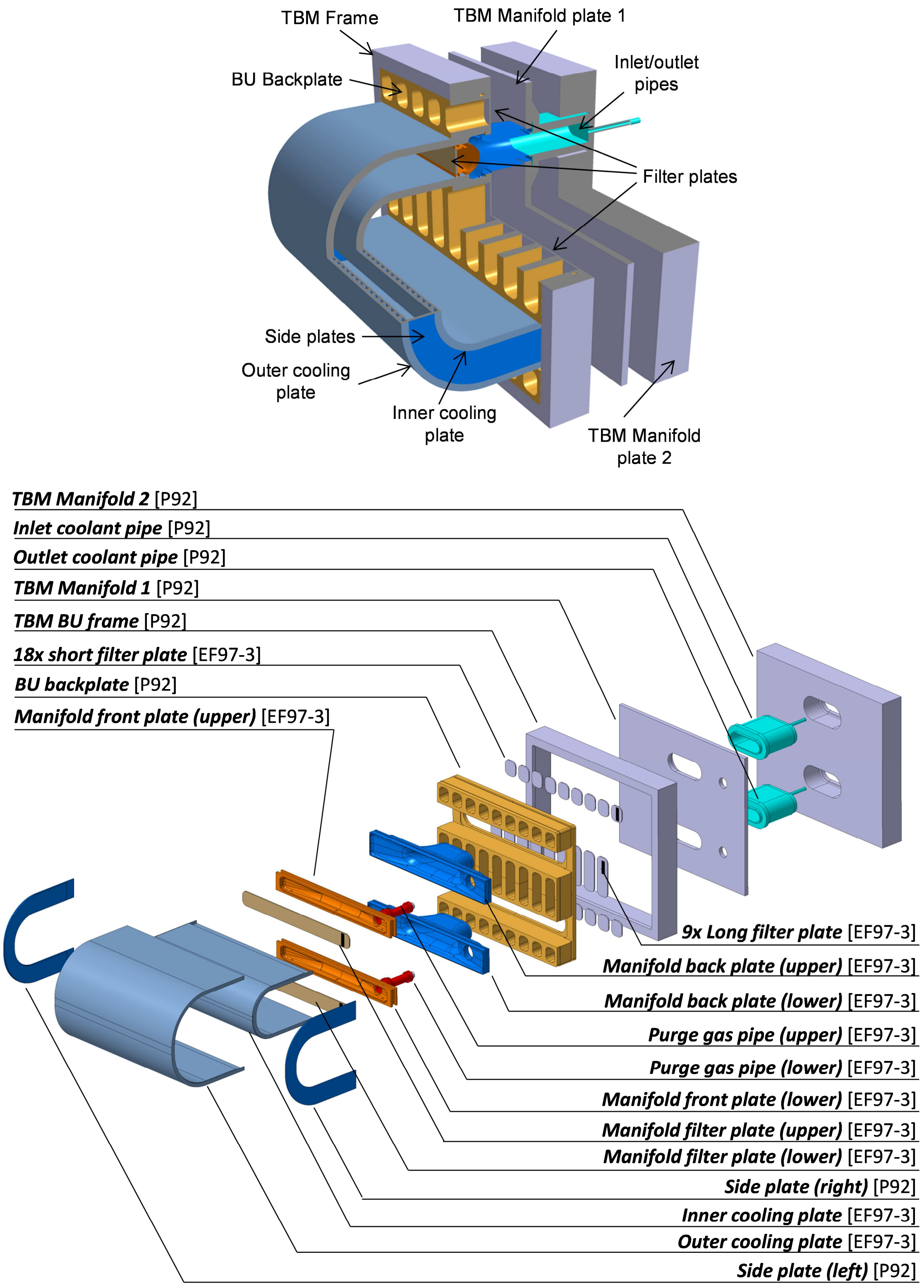

Figure A.1: The Short Breeder Unit mock-up “SHOBU” (Hernández et al., 2014). Top: CAD picture with a 3D cut-off of a quarter of the mock-up. Bottom: Exploded view of the SHOBU assembly.

As it can be observed in Figure A.1, the cooling plates of SHOBU are considerably shorter than in the reference design. While this design modification does not affect the manufacturing relevance of the SHOBU mock-up with respect to a HCPB Breeder Unit, it has been necessary as the qualification of the manufacturing of the full-scale cooling plates has been performed in the frame of a parallel project (F4E OPE 305 Lot 3 grant, see Neuberger et al., 2014). After the successful pre-qualification of SHOBU and the full-scale cooling plates it is foreseen to manufacture a HCPB Breeder Unit mock-up combining the know-how gathered from both projects, as the rest of the manufacturing aspects of SHOBU (single part manufacturing, welding seams and assembly sequence) are relevant to the reference design.

A.1.1 Assembly sequence of SHOBU

The assembly of the SHOBU mock-up has been divided into 11 welding groups (WG, Figure A.2). The groups WG1 to WG7 form the equivalent to a HCPB Breeder Unit.

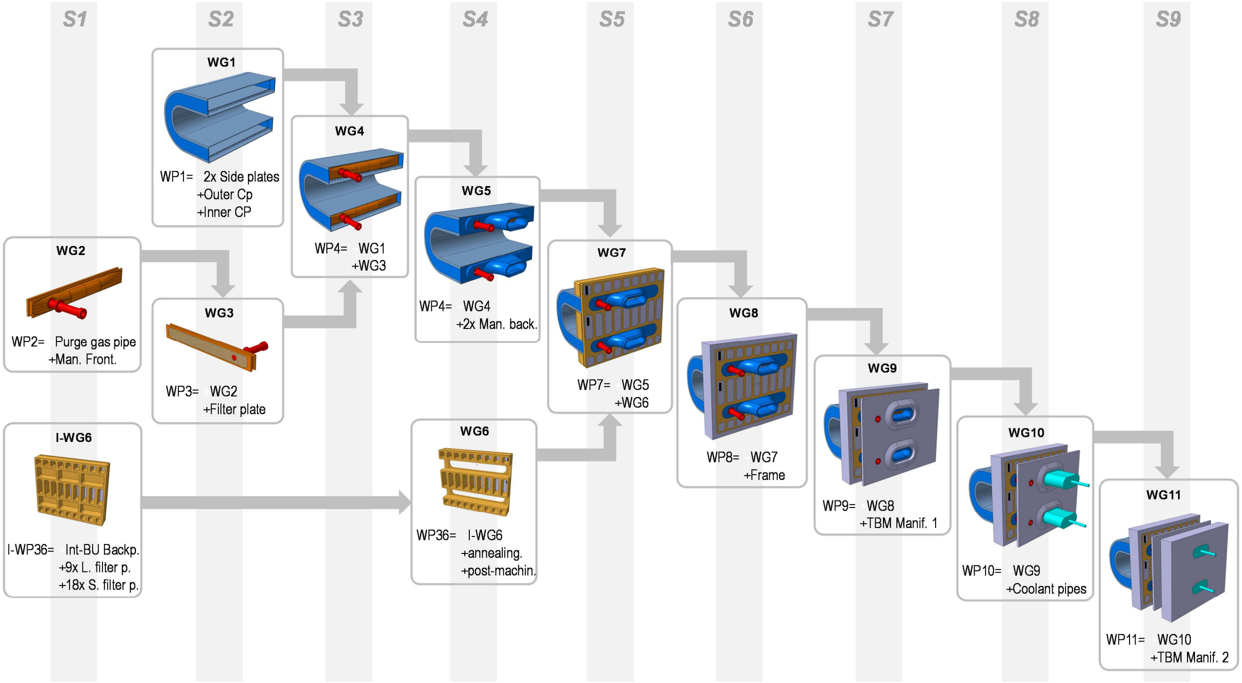

Figure A.2: Assembly sequence of SHOBU (Hernández et al., 2014). Gantt-like chart of the 11 welding groups (WG), 1 intermediate welding group (I-WG6) and the 9 assembly stages. The resulting WG7 in stage S5 represents a complete relevant HCPB Breeder Unit mock-up. S6 mimics the insertion and welding of the relevant HCPB Breeder Unit to the HCPB TBM Box. Stages S7 to S9 imitates the insertion and welding of the “Coolant Pipes” and the “TBM Manifold” plates, completing the assembly of the HCPB TBM.

The addition of the groups WG8 to WG11 in the mock-up demonstrate the feasibility of the HCPB Breeder Unit integration in the HCPB TBM Box by imitating the insertion and welding of the relevant HCPB Breeder Unit and subsequent completion of the HCPB TBM Box assembly by welding the equivalent TBM Manifold plates and the and helium cooling interface pipes (the “Coolant Pipes”). 9 assembly stages (S1 to S9) have been identified in the process and are depicted in the Gantt-like chart of Figure A.2: Assembly sequence of SHOBU . Gantt-like chart of the 11 welding groups (WG), 1 intermediate welding group (I-WG6) and the 9 assembly stages. The resulting WG7 in stage S5 represents a complete relevant HCPB Breeder Unit mock-up. S6 mimics the insertion and welding of the relevant HCPB Breeder Unit to the HCPB TBM Box. Stages S7 to S9 imitates the insertion and welding of the “Coolant Pipes” and the “TBM Manifold” plates, completing the assembly of the HCPB TBM.

Some welding groups up to WG7 can be parallelized. However, it has been identified that the WG6 is a critical path in the SHOBU assembly, and therefore for the future HCPB Breeder Unit mock-up, as this sub-assembly comprises multiple manufacturing steps (manufacturing of an intermediate “BU Backplate” and welding of 27 filter plates, a heat treatment and post-machining to obtain the final WG6.

The SHOBU mock-up is the first assembled of its kind and, in view of simplicity, it does not include the breeder Li_4SiO_4 pebble bed. The assembly sequence shown in Figure A.2 takes into account the fact that the volume formed in WG1 between the cooling plates and the side plates must be filled with this breeder material in the HCPB Breeder Unit. This volume is closed by the assembly of the WG3. Therefore, the assembly sequence of SHOBU is also relevant to that in the HCPB Breeder Unit. As it is described in Section 3.2.4, a 2-stage heat treatment must be performed after the completion of the SHOBU (or the HCPB Breeder Unit) assembly, so as to reduce the hardness of the welds and bring the mechanical properties at least to a 80 % of the base material (EUROFER97). Although temperatures of 1050 °C are required during this heat treatment, the presence of the Li_4SiO_4 pebble bed in the assembly is not a concern and the material properties of the breeder material, as well as the chemical compatibility between this pebble bed and the EUROFER97 steel are not affected, as reported by Abou-Sena (2011).

A.1.2 Manufacturing technologies of the single parts of SHOBU

Manifold system: CNC-3D machining

Due to its complex geometry, the so-called *manifold system* formed by the “Manifold front plate” and the “Manifold back plate” requires Computer Numerical Controlled 3-dimensional machining (CNC-3D). The CATIA V5-CAD files corresponding to these parts obtained after the design cycle are converted into “stl” files and released to a qualified workshop, which performs the programming of the CNC-3D machines. The components are given a medium tolerance class (DIN EN ISO Standard 286-1:2010-11, 2010), but special attention is taken to fulfill the condition of a maximum gap of 0.1 *mm* between parts in order to ensure their weldability with the chosen joining technology (EBW, Section 3.2.4).

Cooling plates: wire cutting by spark erosion, chemical cleaning, cold forming and electron beam micro-drilling

As stated in Section 3.2.1, the manufacturing of the full scale cooling plates have been qualified in parallel with SHOBU due to their length, which is not a standard in the industry. However, the cooling plates in SHOBU share the same manufacturing process. These plates require 6 steps:

(1) Execution of 30 “start holes” of Ø1.6 mm each on a billet plate of EUROFER97 by electrical discharge drilling;

(2) Wire cutting of the cooling channels around the start holes: an electrode is inserted in the start holes produced in the previous step and produces the shape of the $(2.6 \times 4.5) mm$ cooling channels' cross-section by spark erosion;

(3) Extraction of the 5 mm thick cooling plate from the billet plate by wire cutting the contour by spark erosion;

(4) Chemical cleaning of the resulting cooling plate in order to eliminate Cu and Zn byproducts deposed on the surfaces after the spark erosion process, as they jeopardize the quality of the electron bean weld;

(5) Bending of the cooling plates by a 2 step 90° bending process to achieve the inner radii of 25 mm and 50 mm in the inner and outer cooling plates, respectively;

(6) A 2-step heat treatment of the cooling plates in order to eliminate the inner stresses produced during the bending process of the plates and to recover at least 80% of the initial mechanical properties of the steel.

The cooling plates of the HCPB Breeder Unit shall have an additional step in order to produce micro-holes of $\varnothing 0.2$ mm on the ribs between cooling channels (Figure A.3 right). These micro-holes are performed in order to allow the He purge gas to penetrate the cooling plates and flow from the Be into the Li_4SiO_4 pebble bed during the operation.

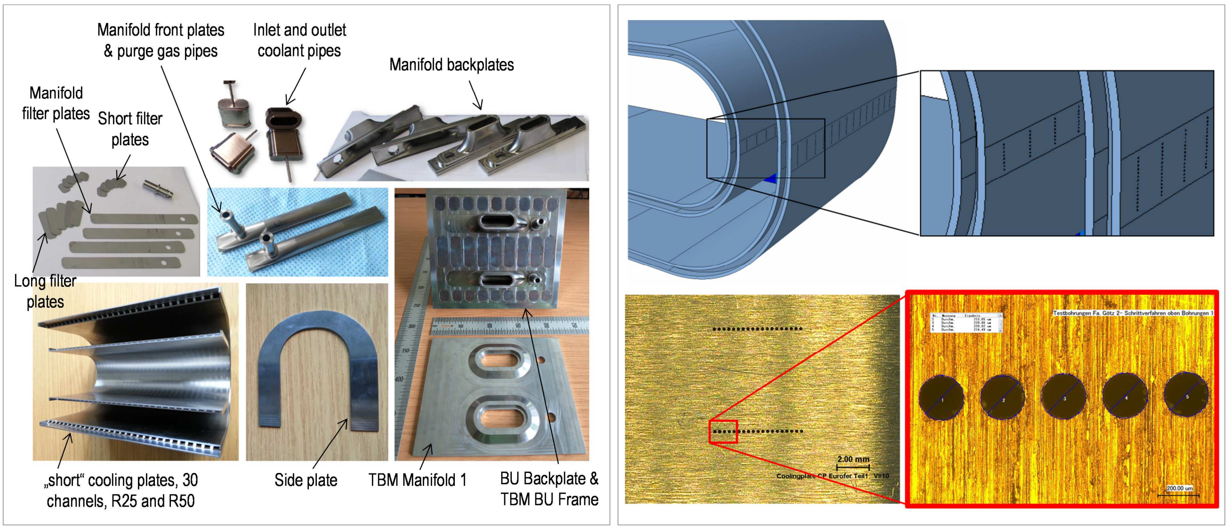

Figure A.3: Manufacturing of single parts of SHOBU (left) and detail of the purge gas micro-holes performed in the ribs between the cooling channels of the cooling plates (Hernández et al., 2014).

These micro-holes have not been performed in the cooling plates of SHOBU as they do not affect the relevancy of the assembly in terms of fabrication. Preliminary tests show the manufacturing feasibility of such micro-holes by electrical discharge sink erosion drilling (Figure A.3 right). Additional fabrication experiments have shown that this step could be performed before the forming of the plates, without damaging the micro-holes by the bending process. However, more fabrication tests are required to qualify the suitability of this fabrication sequence with relevant cooling plate's dimensions.

For the cold forming of the cooling plates of SHOBU, a customized bending tool has been developed in collaboration with the *Institut für Umformtechnik* (IFU) of the University of Stuttgart (Germany) and the *Forschungsgesellschaft Umformtechnik mbH* (FGU) in the frame of the grant BMBF 03 FUS0011 (Neuberger et al., 2014) This collaboration has been extended in the frame of the previously mentioned F4E OPE 305 Lot 3 grant for the production of full scale inner cooling plates.

Filter plates: electron-beam micro-drilling

Filter plates are required in the "Front Manifold Plate" and in the "BU Backplate" as per reference design in the HCPB Breeder Unit. These filter plates allow the flow of the purge gas into the Breeder Unit cell retaining the pebbles in the breeder zone cuboid. As the minimum size of the pebbles found in its distribution is Ø0.2 *mm*, the diameter of these micro-holes has been set to 0.15 *mm.*

This filter plates are performed by electron beam (EB) drilling. A 1.3 *mm* raw EUROFER97 plate is placed in a vacuum chamber and a high speed EB gun shots at the plate, perforating it with an hexagonal pattern.

A.1.3 Joining technology: electron beam welding, detailed design of the joints and execution of the welding assembly

The HCPB Breeder Unit is considered to be a complex welding assembly due to the large amount of parts, sub-assemblies involved and the presence of narrow welding seams, some of them as small as 2 mm in the area of the manifold system. These narrow welding seams performed in relatively small parts the dissipation of the heat during the welding a challenging task. Moreover, a low distortion is required in order to ensure the successful assembly of the welding groups together and the HCPB Breeder Unit itself in the corresponding HCPB TBM Box welding interface (represented in SHOBU by the "BU Frame part"). A high degree of automatization in the process and high welding speeds are as well wanted, in order to facilitate a future industrialization of the components with low assembly times. Therefore, the EBW technique has been selected as the joining technology for the HCPB Breeder Unit, due to its high energy density combined with a low heat input, maintaining a low distortion in the welded parts. Furthermore, the process can be highly automatized, allowing multiple welding pools or pre-heating beams, if needed. EBW has been successfully applied for the welding assembly of the SHOBU mock-up.

In the frame of the BMBF 03 FUS0011 program, a collaboration with the *Institut of Füge- und Schweißtechnik* (IFS, University of Braunschweig, Germany) and with the industrial partner *pro-beam AG* has been started with the goal of investigating preliminary welding procedure specifications and appropriate welding parameters and their execution in SHOBU.

In an initial phase, welding probes of 5 relevant welding situations, corresponding to the welding groups WG6, WG4, WG5, WG7 and WG8, have been manufactured by KIT (Figure

A.4) and adequate EB-welding parameters have been investigated by IFS. The resulting welds have been qualified according to two requirements:

(1) The fulfillment of the highest quality class according to the EN ISO 13919-1 norm, which corresponds to a class “B” (DIN EN ISO Standard 13919-1:1996-09, 1996);

(2) The mechanical properties of the welds (tensile and toughness) shall be not less than 80% of the base material.

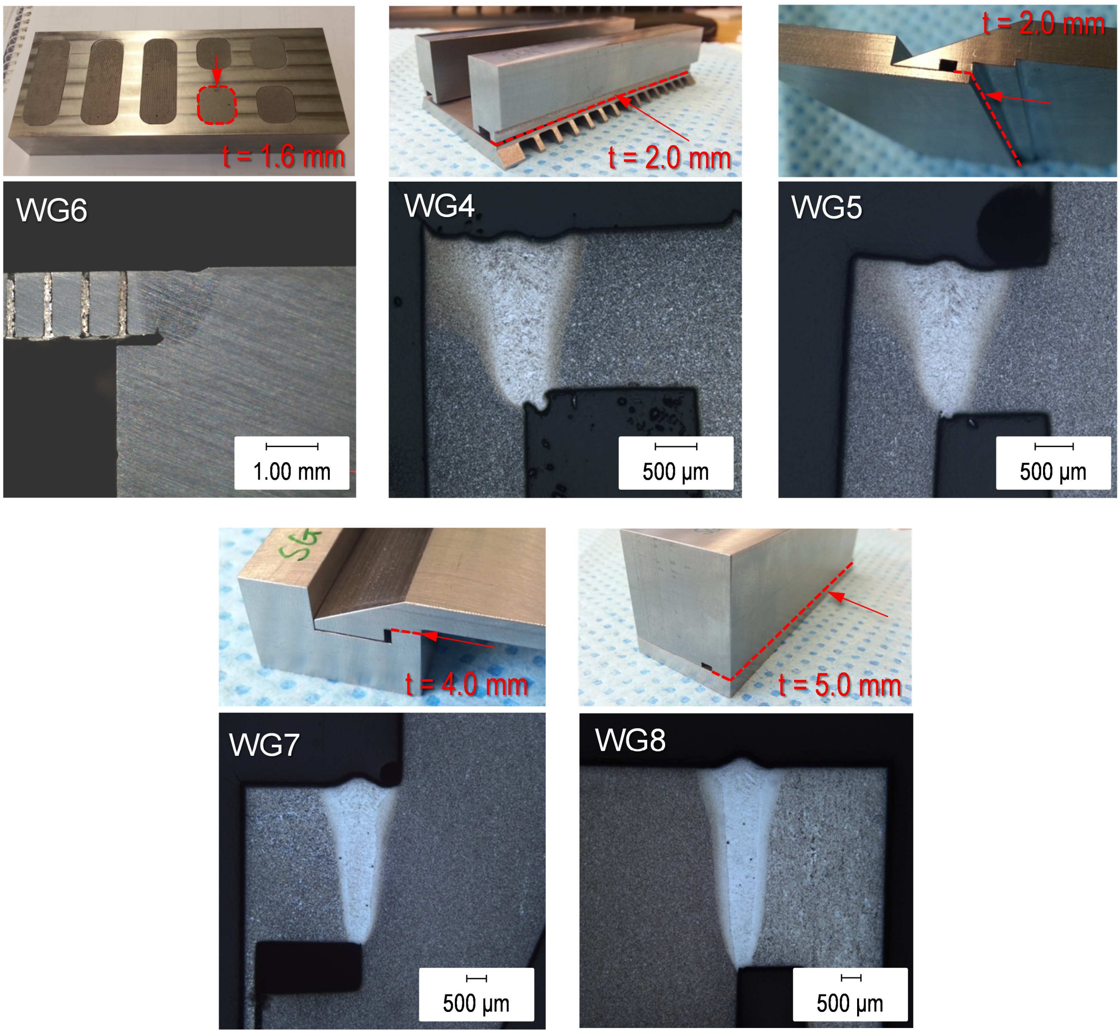

Figure A.4: Welding experiments perfomred to 5 characteristic welding situations in SHOBU, corresponding to the welding groups WG6, WG4, WG5, WG7, WG8. The *t* in each of the 5 pictures indicate the welding thickness. The qualification of the welds have been performed by Krasnorutsky et al. (2014) according to the DIN EN ISO 13919-1 norm. All the welds have reached a class “B” in the aforementioned standard, which corresponds to the highest rating, as required in the defined quality standards for SHOBU. The resulting welding parameters have been applied to the SHOBU mock-up.

Local modifications of the geometry of the reference design of the HCPB Breeder Unit have been applied to follow recommendations regarding the geometry of the welding seams for better welding results with EBW technique (DIN EN Standard 1011-7:2004-10, 2004).

After the qualification of the welding probes, Krasnorutskyi et al. (2014) conclude that high weld speeds ($\geq 25\ mm/s$) are beneficial to keep a low concavity of the weld bead and a low convexity of the weld root, which are the pivotal parameters for the assessment of the welds in the DIN EN ISO 13919-1 norm. However, speeds between 10 mm/s and 15 mm/s are preferred to keep a low content on δ-ferrite in the welds. The relatively soft δ-ferrite phase is, although in a low percentage, part of the microstructure of the EUROFER97, which is mainly composed by a matrix of tempered martensite within previously formed austenitic grains. During the cooling of this steel (e.g. during the cooling after a welding pass), dendritic martensite carbide precipitates ($M_{23}C_6$) in the interface grain boundary of δ–ferrite and the martensite matrix (Materna-Morris, 1990). Anderko et al. (1991) reports that these precipitates may be the cause for the decrease of the impact toughness and the increase of the ductile to brittle transition temperature if the presence of δ–ferrite is more than 2-3%. Hence, it is desired to minimize the presence of δ–ferrite grains in EUROFER97. Krasnorutskyi et al. (2014) reports that speeds of 25 mm/s lead still to a content of less than 1% content of δ–ferrite. Therefore, the welding speed has been kept at 25 mm/s as a trade-off between low δ–ferrite content and correct weld bead and root geometries. This has resulted to a class "B" rating of all the welds according to the DIN EN ISO 13919-1 norm.

The hardness of the welds, which gives an indication of the tensile and toughness mechanical properties, has been found to be $400 - 450$ HV1 (Krasnorutski et al., 2014), a result that agrees with the one of Rieth and Rey (2009). A 2-stage PWHT is then required to lower these values to the range of $320 - 340$ HV1, after Aubert et al. (2011) and Rieth and Rey (2009). According to these authors, although these values of the hardness are higher than those for the base material, the impact toughness and tensile strength properties of the weld are still acceptable.

In Figure A.4 micro-pores can be observed in the weld throat for the WG7 and WG8. However, their occurrence is very low, they do not form clusters (appear in an isolated manner) and their size is small ($\leq 100\ \mu m$) in comparison to the weld throat, thus not influencing negatively in the final qualification of the weld seam, as reported by Krasnorutskyi et al. (2014).

After obtaining qualified welding procedure specifications for the 5 characteristic welding situations, they have been applied to SHOBU in IFS (Figure A.5), utilizing an EB welding rig from *Pro-beam AG,* with chamber volume of 2.6 m^3. Figure A.5-bottom shows the correct assembly and EB-welding of the WG7 of SHOBU, which corresponds to the manufacturing equivalent of a HCPB Breeder Unit mock-up.

A.1.4 Acceptance tests of the SHOBU mock-up

The RCC-MR code is the one selected one for ITER, whose appendix A18 covers the ESPN order (Autorité de Súreté Nucléaire, 2005) to comply with the French nuclear regulations on pressure vessel equipment. The RCC-MR 2007 code have been complemented with the ITER SDC-IC, which covers specific damage modes under irradiation not covered by the RCC-MR 2007 code (Tavassoli et al., 2004; Majumdar & Smith, 1998).

Figure A.5: Welding Group WG5 (top left) and WG6 (top right) with augmented views (middle) and finished assembly (bottom left and right). Despite the multiple sub-assemblies in WG7 or the multiple welding seams in WG6, the order of magnitude O of the distortions δ is very low ($O(\delta) \approx 10^{-1}\ mm$), allowing a successful assembly.

After the completion of SHOBU, a pressure test at room temperature and a pressure $p_{RT} = 16\ MPa$ is required as per AD2000 (AD 2000-Merkblatt HP 30:2003-01, 2003), a standard that is in line with the Pressure Directive Equipment required in ITER, as the RCC-MR code. This test pressure results from applying a factor $f = 2$ to the operating pressure $p_{550°C} = 8\ MPa$ of the HCPB Breeder Unit at its maximum operating temperature (550 °C). In this way, the equivalent stress during the operation in ITER is conservatively reproduced at room temperature by applying $p_{RT} = f \times p_{550°C}$. Despite this strategy of KIT is a very conservative calculation, as it is an upper limit of the qualification level from all European pressure test standards, it aims at demonstrating that the welding assembly of SHOBU in KIT is a reliable component, in view of relevance to design codes like the new RCC-MRx code used for ITER (RCC-MRx, 2012).

After the successful conclusion of this test, a leak tightness test is also required as per RCC-MR:2007 Section RMC7400 (RCC-MR, 2007). This test shall proof that the maximum leakage rate of the mock-up is less than 10^{-9} $mbar\ l\ s^{-1}$, as required in ITER (waiting for completion of welding assembly for pressure and leak tightness tests)

Appendix B

Results of the stochastic thermal analysis for heating powers other than VHI

B.1 Stochastic analysis results for the heating power HI, MED, LO and VLO

The stochastic analysis described and performed in Chapter 6 has been completed for all of the rest of the defined heating power levels in PREMUX, namely HI, MED, LO and VLO. These are reported in the following pages.

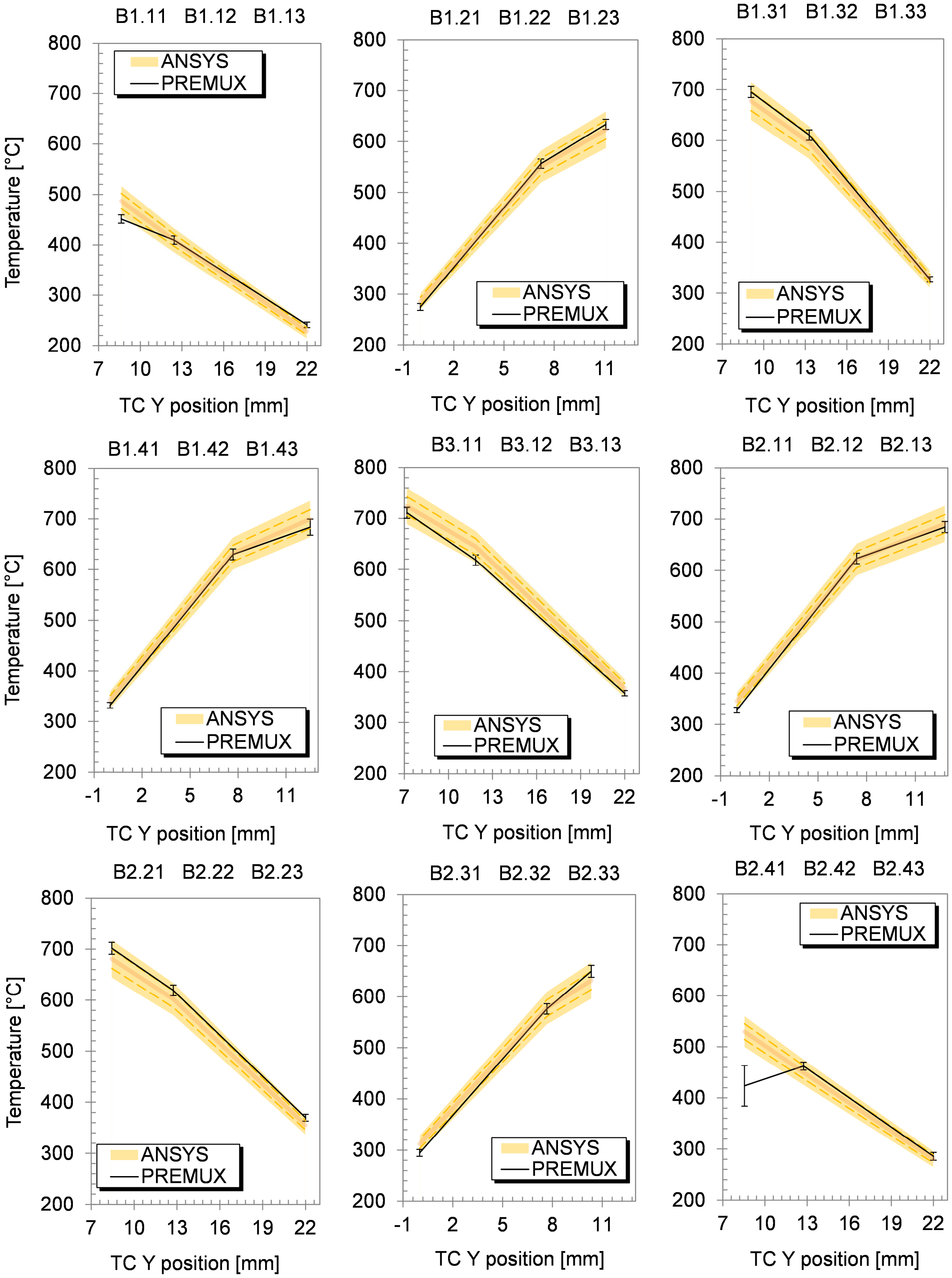

Figure B.1: Comparison between the predicted steady state temperatures of the Li_4SiO_4 pebble bed with ANSYS and with PREMUX at the HI power level. For the finite element results, the solid line represents the average, the dashed lines depict $\pm\sigma$ and the whole uncertainty band depicts $\pm2\sigma$.

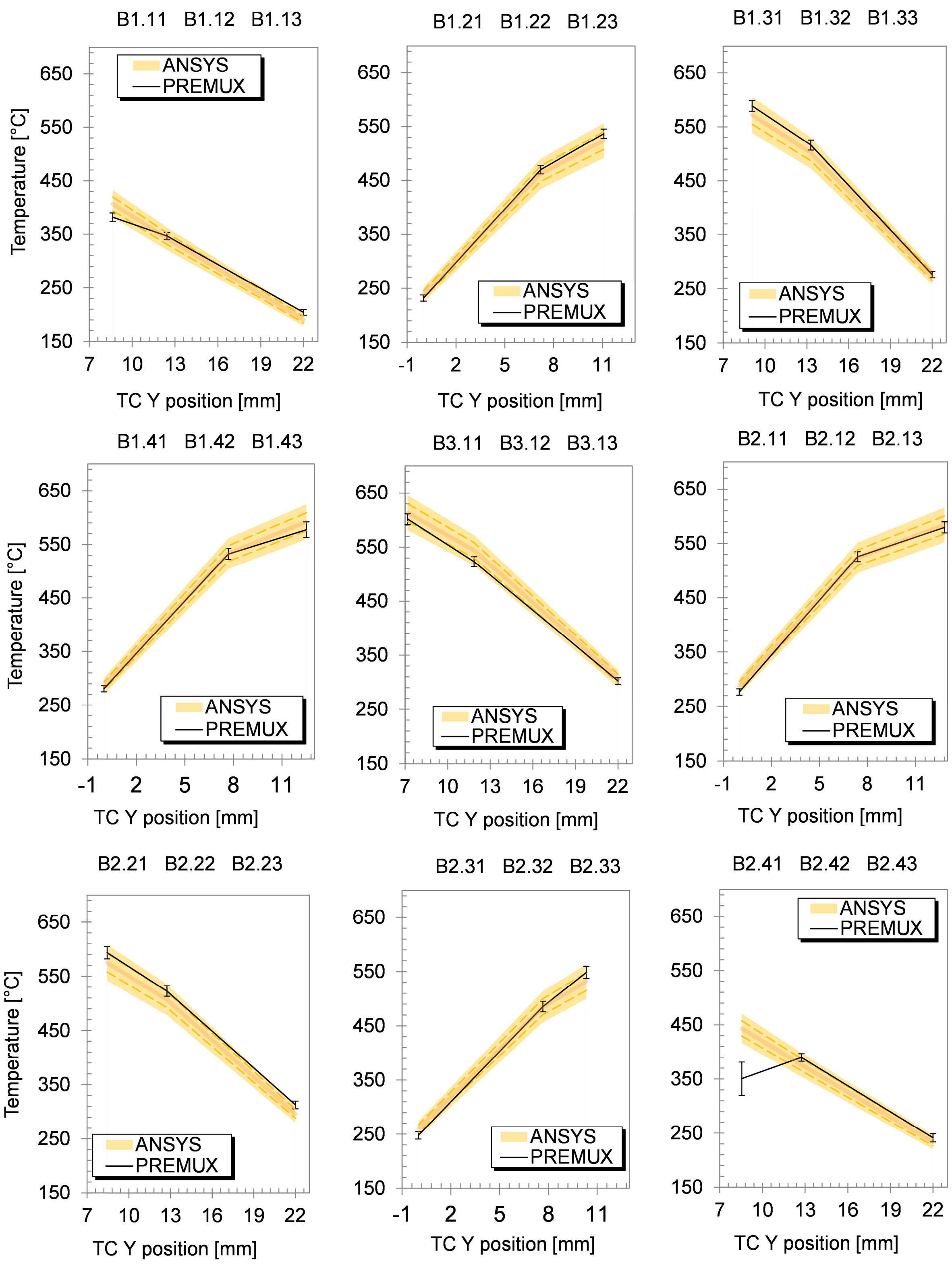

Figure B.2: Comparison between the predicted steady state temperatures of the Li_4SiO_4 pebble bed with ANSYS and with PREMUX at the MED power level. For the finite element results, the solid line represents the average, the dashed lines depict $\pm\sigma$ and the whole uncertainty band depicts $\pm 2\sigma$.

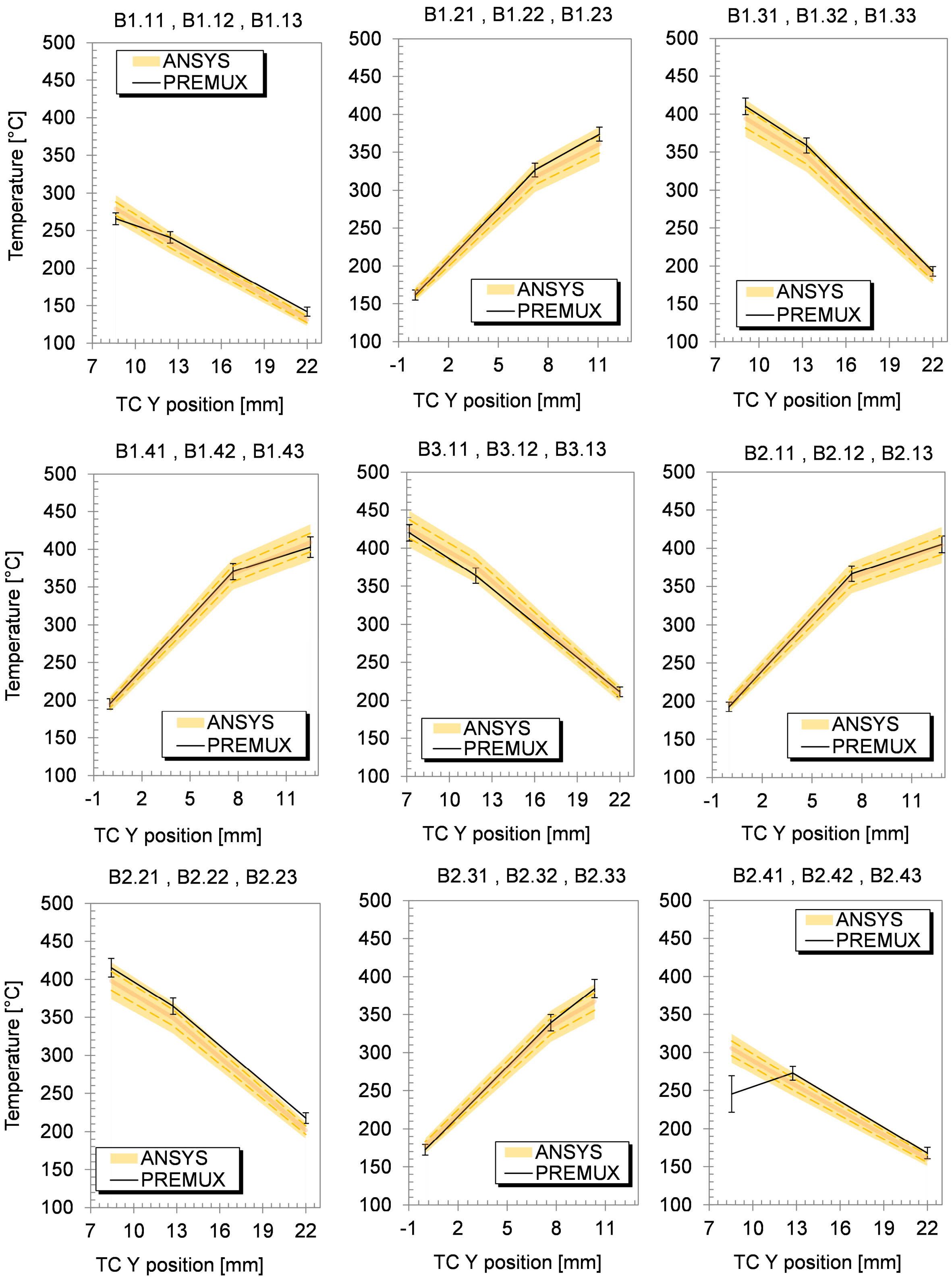

Figure B.3: Comparison between the predicted steady state temperatures of the Li_4SiO_4 pebble bed with ANSYS and with PREMUX at the LO power level. For the finite element results, the solid line represents the average, the dashed lines depict $\pm\sigma$ and the whole uncertainty band depicts $\pm 2\sigma$.

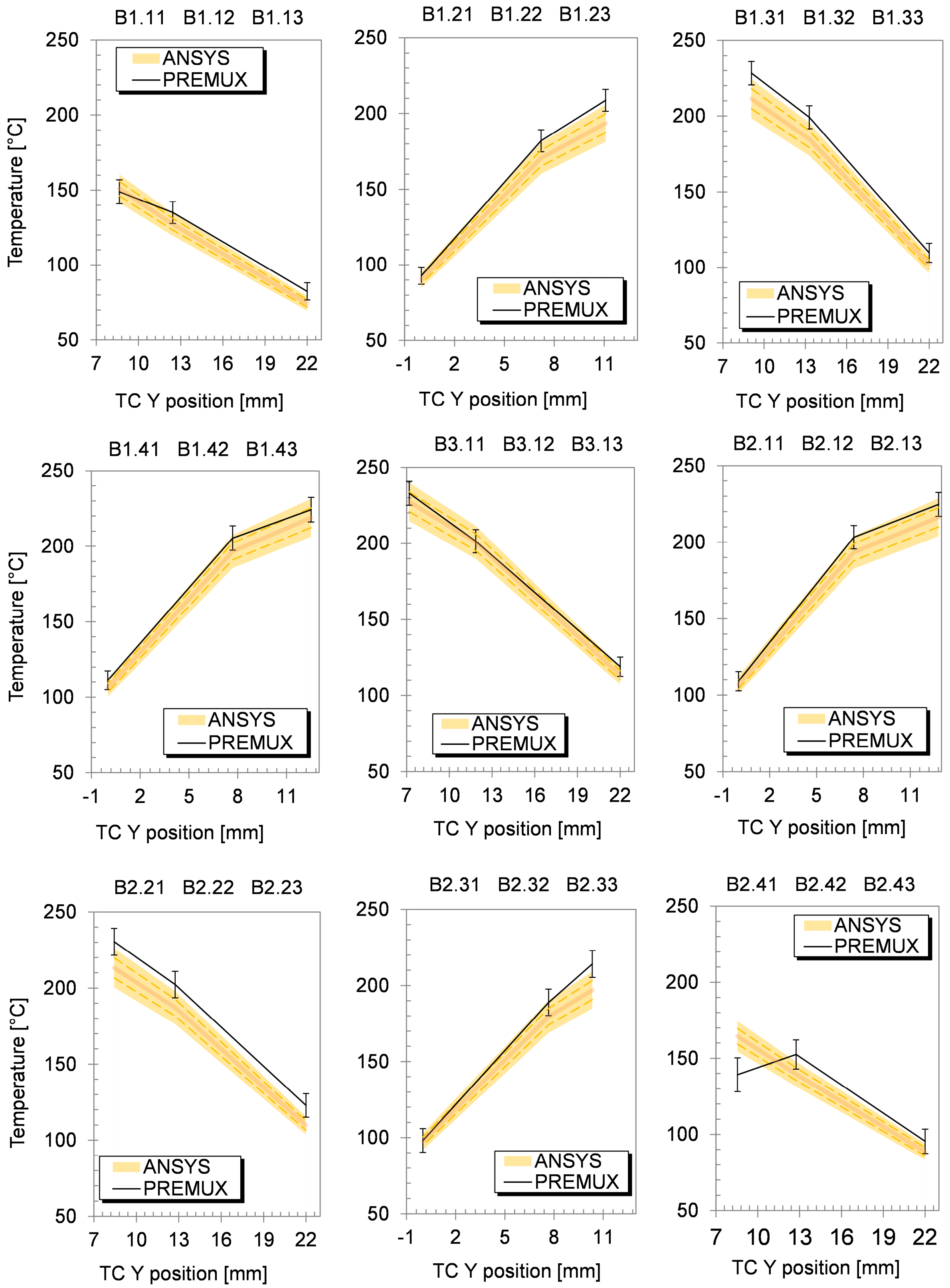

Figure B.4: Comparison between the predicted steady state temperatures of the Li_4SiO_4 pebble bed with ANSYS and with PREMUX at the VLO power level. For the finite element results, the solid line represents the average, the dashed lines depict $\pm\sigma$ and the whole uncertainty band depicts $\pm 2\sigma$.

Appendix C

Results of the stochastic sensitivity analysis for heating powers other than VHI

C.1 Stochastic sensitivity analysis results for the heating power HI, MED, LO and VLO

The stochastic sensitivity analysis described and performed in Chapter 6 has been completed for all of the rest of the defined heating power levels in PREMUX, namely HI, MED, LO and VLO. These are reported in the following pages.

	HGEN Heaters 1	HGEN Heaters 2	HGEN Heaters 3	TEMP air inlet	MFLOW air coolant CH4	Thermal cond. Li4SiO4	MFLOW air coolant CH10	HTC cool. channel (corrected)	TCC steel-Li4SiO4	HTC insulation-air	Thermal cond. insulation
B1.11	0,715	0,105	0,000	0,102	0,000	-0,620	0,000	-0,271	0,000	0,000	0,000
B1.12	0,720	0,132	0,000	0,128	0,000	-0,556	0,000	-0,352	0,000	0,000	0,000
B1.13	0,582	0,215	0,015	0,230	-0,066	-0,083	-0,012	-0,719	-0,080	0,012	-0,018
B1.21	0,703	0,110	0,000	0,000	0,000	-0,657	0,000	-0,217	0,000	0,000	0,000
B1.22	0,711	0,130	0,000	0,000	0,000	-0,623	0,000	-0,264	0,000	0,000	0,000
B1.23	0,643	0,235	0,028	0,205	-0,023	-0,122	-0,042	-0,655	-0,118	0,012	-0,021
B1.31	0,682	0,140	0,000	0,000	0,000	-0,674	0,000	-0,212	0,000	0,000	0,000
B1.32	0,689	0,169	0,000	0,000	0,000	-0,637	0,000	-0,265	0,000	0,000	0,000
B1.33	0,645	0,279	0,030	0,188	-0,062	-0,144	-0,010	-0,635	-0,120	0,012	-0,018
B1.41	0,618	0,222	0,000	0,000	0,000	-0,703	0,000	-0,228	0,000	0,000	0,000
B1.42	0,591	0,266	0,103	0,000	0,000	-0,686	0,000	-0,271	0,000	0,000	0,000
B1.43	0,581	0,363	0,065	0,187	-0,018	-0,133	-0,043	-0,652	-0,129	0,015	-0,014
B3.11	0,375	0,349	0,301	0,065	-0,010	-0,750	-0,006	-0,233	-0,062	0,008	0,000
B3.12	0,454	0,419	0,126	0,080	-0,016	-0,703	-0,008	-0,283	-0,069	0,014	0,001
B3.13	0,489	0,486	0,059	0,176	-0,053	-0,150	-0,009	-0,647	-0,129	0,020	-0,005
B2.11	0,227	0,630	0,000	0,000	0,000	-0,679	0,000	-0,250	0,000	0,000	0,000
B2.12	0,261	0,617	0,000	0,000	0,000	-0,655	0,000	-0,293	0,000	0,000	0,000
B2.13	0,347	0,596	0,064	0,183	-0,008	-0,112	-0,046	-0,660	-0,118	0,025	0,001
B2.21	0,151	0,689	0,031	0,064	0,000	-0,650	-0,017	-0,240	-0,053	0,021	0,016
B2.22	0,179	0,695	0,037	0,079	-0,006	-0,611	-0,014	-0,292	-0,062	0,023	0,017
B2.23	0,272	0,673	0,037	0,171	-0,047	-0,132	-0,011	-0,626	-0,113	0,028	0,008
B2.31	0,119	0,714	0,013	0,067	-0,004	-0,627	-0,018	-0,250	-0,047	0,022	0,018
B2.32	0,133	0,719	0,018	0,079	-0,003	-0,600	-0,020	-0,286	-0,053	0,023	0,018
B2.33	0,228	0,675	0,031	0,188	-0,010	-0,104	-0,052	-0,647	-0,106	0,030	0,007
B2.41	0,117	0,726	0,010	0,085	-0,007	-0,591	-0,023	-0,296	-0,044	0,022	0,018
B2.42	0,143	0,734	0,015	0,111	-0,018	-0,520	-0,022	-0,375	-0,053	0,025	0,018
B2.43	0,215	0,647	0,021	0,200	-0,065	-0,082	-0,020	-0,680	-0,079	0,030	0,008
T_{out} CH4	0,174	0,163	0,018	0,649	-0,703	-0,004	-0,020	0,000	0,024	0,017	-0,027
T_{out} CH10	0,216	0,192	0,022	0,723	-0,030	-0,002	-0,606	0,005	0,010	0,017	-0,018

	HGEN Heaters 1	HGEN Heaters 2	HGEN Heaters 3	TEMP air inlet	MFLOW air coolant CH4	Thermal cond. Li4SiO4	MFLOW air coolant CH10	HTC cool. channel (corrected)	TCC steel-Li4SiO4	HTC insulation-air	Thermal cond. insulation
B1.11	39%	6%	0%	6%	0%	34%	0%	15%	0%	0%	0%
B1.12	38%	7%	0%	7%	0%	29%	0%	19%	0%	0%	0%
B1.13	29%	11%	1%	11%	3%	4%	1%	35%	4%	1%	1%
B1.21	42%	7%	0%	0%	0%	39%	0%	13%	0%	0%	0%
B1.22	41%	8%	0%	0%	0%	36%	0%	15%	0%	0%	0%
B1.23	31%	11%	1%	10%	1%	6%	2%	31%	6%	1%	1%
B1.31	40%	8%	0%	0%	0%	39%	0%	12%	0%	0%	0%
B1.32	39%	10%	0%	0%	0%	36%	0%	15%	0%	0%	0%
B1.33	30%	13%	1%	9%	3%	7%	0%	30%	6%	1%	1%
B1.41	35%	13%	0%	0%	0%	40%	0%	13%	0%	0%	0%
B1.42	31%	14%	5%	0%	0%	36%	0%	14%	0%	0%	0%
B1.43	26%	16%	3%	8%	1%	6%	2%	30%	6%	1%	1%
B3.11	17%	16%	14%	3%	0%	35%	0%	11%	3%	0%	0%
B3.12	21%	19%	6%	4%	1%	32%	0%	13%	3%	1%	0%
B3.13	22%	22%	3%	8%	2%	7%	0%	29%	6%	1%	0%
B2.11	13%	35%	0%	0%	0%	38%	0%	14%	0%	0%	0%
B2.12	14%	34%	0%	0%	0%	36%	0%	16%	0%	0%	0%
B2.13	16%	28%	3%	8%	0%	5%	2%	31%	5%	1%	0%
B2.21	8%	36%	2%	3%	0%	34%	1%	12%	3%	1%	1%
B2.22	9%	34%	2%	4%	0%	30%	1%	14%	3%	1%	1%
B2.23	13%	32%	2%	8%	2%	6%	1%	30%	5%	1%	0%
B2.31	6%	38%	1%	4%	0%	33%	1%	13%	2%	1%	1%
B2.32	7%	37%	1%	4%	0%	31%	1%	15%	3%	1%	1%
B2.33	11%	32%	1%	9%	0%	5%	3%	31%	5%	1%	0%
B2.41	6%	37%	1%	4%	0%	30%	1%	15%	2%	1%	1%
B2.42	7%	36%	1%	5%	1%	26%	1%	18%	3%	1%	1%
B2.43	11%	32%	1%	10%	3%	4%	1%	33%	4%	1%	0%
T_{out} CH4	10%	9%	1%	36%	39%	0%	1%	0%	1%	1%	1%
T_{out} CH10	12%	10%	1%	39%	2%	0%	33%	0%	1%	1%	1%

Figure C.1: Sensitivity analysis of 11 model parameters to the output variables, i.e. pebble bed and outlet coolant temperatures, for the HI power level. Top table: Spearman Rank-Order correlation coefficients. Bottom table: % contribution of each model parameter to the output variables.

	HGEN Heaters 1	HGEN Heaters 2	HGEN Heaters 3	TEMP air inlet	MFLOW air coolant CH4	Thermal cond. Li4SiO4	MFLOW air coolant CH10	HTC cool. channel (corrected)	TCC steel-Li4SiO4	HTC insulation-air	Thermal cond. insulation
B1.11	0,711	0,109	0,000	0,120	0,000	-0,622	0,000	-0,269	0,000	0,000	0,000
B1.12	0,714	0,136	0,000	0,148	0,000	-0,561	0,000	-0,347	0,000	0,000	0,000
B1.13	0,585	0,219	0,016	0,267	-0,065	-0,109	-0,014	-0,700	-0,081	0,014	-0,020
B1.21	0,700	0,113	0,000	0,000	0,000	-0,659	0,000	-0,216	0,000	0,000	0,000
B1.22	0,705	0,134	0,000	0,109	0,000	-0,628	0,000	-0,260	0,000	0,000	0,000
B1.23	0,644	0,239	0,030	0,236	-0,024	-0,152	-0,040	-0,637	-0,120	0,013	-0,023
B1.31	0,678	0,144	0,000	0,000	0,000	-0,677	0,000	-0,212	0,000	0,000	0,000
B1.32	0,683	0,172	0,000	0,103	0,000	-0,642	0,000	-0,260	0,000	0,000	0,000
B1.33	0,645	0,283	0,032	0,218	-0,059	-0,174	-0,010	-0,616	-0,122	0,013	-0,018
B1.41	0,613	0,225	0,000	0,000	0,000	-0,706	0,000	-0,226	0,000	0,000	0,000
B1.42	0,587	0,268	0,101	0,000	0,000	-0,690	0,000	-0,266	0,000	0,000	0,000
B1.43	0,583	0,367	0,067	0,216	-0,017	-0,166	-0,041	-0,631	-0,131	0,016	-0,017
B3.11	0,377	0,351	0,291	0,077	-0,010	-0,752	-0,006	-0,230	-0,063	0,010	0,000
B3.12	0,452	0,418	0,124	0,094	-0,015	-0,706	-0,007	-0,278	-0,069	0,016	0,000
B3.13	0,492	0,488	0,061	0,206	-0,051	-0,183	-0,011	-0,626	-0,130	0,023	-0,006
B2.11	0,230	0,624	0,000	0,000	0,000	-0,683	0,000	-0,248	0,000	0,000	0,000
B2.12	0,264	0,611	0,000	0,000	0,000	-0,661	0,000	-0,288	0,000	0,000	0,000
B2.13	0,351	0,598	0,067	0,212	-0,007	-0,146	-0,043	-0,640	-0,121	0,028	0,000
B2.21	0,156	0,683	0,031	0,077	0,000	-0,655	-0,016	-0,237	-0,054	0,022	0,016
B2.22	0,182	0,689	0,037	0,093	-0,007	-0,617	-0,014	-0,287	-0,064	0,024	0,017
B2.23	0,277	0,672	0,040	0,200	-0,046	-0,166	-0,012	-0,607	-0,116	0,030	0,008
B2.31	0,124	0,710	0,015	0,081	-0,004	-0,630	-0,018	-0,247	-0,049	0,022	0,018
B2.32	0,139	0,714	0,019	0,093	-0,003	-0,605	-0,020	-0,282	-0,054	0,023	0,018
B2.33	0,232	0,675	0,034	0,217	-0,009	-0,136	-0,051	-0,629	-0,108	0,031	0,006
B2.41	0,122	0,722	0,012	0,101	-0,007	-0,593	-0,022	-0,293	-0,045	0,023	0,018
B2.42	0,147	0,729	0,017	0,128	-0,017	-0,527	-0,021	-0,367	-0,054	0,027	0,017
B2.43	0,221	0,650	0,024	0,231	-0,062	-0,111	-0,020	-0,661	-0,079	0,030	0,008
T_{out} CH4	0,169	0,157	0,020	0,726	-0,628	-0,017	-0,020	-0,009	0,022	0,016	-0,022
T_{out} CH10	0,203	0,178	0,021	0,790	-0,027	-0,017	-0,530	-0,002	0,009	0,016	-0,017

	HGEN Heaters 1	HGEN Heaters 2	HGEN Heaters 3	TEMP air inlet	MFLOW air coolant CH4	Thermal cond. Li4SiO4	MFLOW air coolant CH10	HTC cool. channel (corrected)	TCC steel-Li4SiO4	HTC insulation-air	Thermal cond. insulation
B1.11	39%	6%	0%	7%	0%	34%	0%	15%	0%	0%	0%
B1.12	37%	7%	0%	8%	0%	29%	0%	18%	0%	0%	0%
B1.13	28%	10%	1%	13%	3%	5%	1%	33%	4%	1%	1%
B1.21	41%	7%	0%	0%	0%	39%	0%	13%	0%	0%	0%
B1.22	38%	7%	0%	6%	0%	34%	0%	14%	0%	0%	0%
B1.23	30%	11%	1%	11%	1%	7%	2%	30%	6%	1%	1%
B1.31	40%	8%	0%	0%	0%	40%	0%	12%	0%	0%	0%
B1.32	37%	9%	0%	6%	0%	34%	0%	14%	0%	0%	0%
B1.33	29%	13%	1%	10%	3%	8%	0%	28%	6%	1%	1%
B1.41	35%	13%	0%	0%	0%	40%	0%	13%	0%	0%	0%
B1.42	31%	14%	5%	0%	0%	36%	0%	14%	0%	0%	0%
B1.43	26%	16%	3%	10%	1%	7%	2%	28%	6%	1%	1%
B3.11	17%	16%	13%	4%	0%	35%	0%	11%	3%	0%	0%
B3.12	21%	19%	6%	4%	1%	32%	0%	13%	3%	1%	0%
B3.13	22%	21%	3%	9%	2%	8%	0%	27%	6%	1%	0%
B2.11	13%	35%	0%	0%	0%	38%	0%	14%	0%	0%	0%
B2.12	14%	33%	0%	0%	0%	36%	0%	16%	0%	0%	0%
B2.13	16%	27%	3%	10%	0%	7%	2%	29%	5%	1%	0%
B2.21	8%	35%	2%	4%	0%	34%	1%	12%	3%	1%	1%
B2.22	9%	34%	2%	5%	0%	30%	1%	14%	3%	1%	1%
B2.23	13%	31%	2%	9%	2%	8%	1%	28%	5%	1%	0%
B2.31	6%	37%	1%	4%	0%	33%	1%	13%	3%	1%	1%
B2.32	7%	36%	1%	5%	0%	31%	1%	14%	3%	1%	1%
B2.33	11%	32%	2%	10%	0%	6%	2%	30%	5%	1%	0%
B2.41	6%	37%	1%	5%	0%	30%	1%	15%	2%	1%	1%
B2.42	7%	36%	1%	6%	1%	26%	1%	18%	3%	1%	1%
B2.43	11%	31%	1%	11%	3%	5%	1%	32%	4%	1%	0%
T_{out} CH4	9%	9%	1%	40%	35%	1%	1%	0%	1%	1%	1%
T_{out} CH10	11%	10%	1%	44%	1%	1%	29%	0%	1%	1%	1%

Figure C.2: Sensitivity analysis of 11 model parameters to the output variables, i.e. pebble bed and outlet coolant temperatures, for the MED power level. Top table: Spearman Rank-Order correlation coefficients. Bottom table: % contribution of each model parameter to the output variables.

	HGEN Heaters 1	HGEN Heaters 2	HGEN Heaters 3	TEMP air inlet	MFLOW air coolant CH4	Thermal cond. Li4SiO4	MFLOW air coolant CH10	HTC cool. channel (corrected)	TCC steel-Li4SiO4	HTC insulation-air	Thermal cond. insulation
B1.11	0,703	0,108	0,000	0,170	0,000	-0,623	0,000	-0,262	0,000	0,000	0,000
B1.12	0,704	0,136	0,000	0,211	0,000	-0,560	0,000	-0,338	0,000	0,000	0,000
B1.13	0,565	0,215	0,022	0,381	-0,064	-0,114	-0,015	-0,665	-0,079	0,014	-0,020
B1.21	0,694	0,114	0,000	0,131	0,000	-0,661	0,000	-0,211	0,000	0,000	0,000
B1.22	0,699	0,134	0,000	0,154	0,000	-0,629	0,000	-0,254	0,000	0,000	0,000
B1.23	0,628	0,237	0,034	0,332	-0,022	-0,158	-0,043	-0,609	-0,122	0,013	-0,022
B1.31	0,672	0,145	0,000	0,122	0,000	-0,679	0,000	-0,207	0,000	0,000	0,000
B1.32	0,675	0,174	0,000	0,146	0,000	-0,645	0,000	-0,253	0,000	0,000	0,000
B1.33	0,631	0,280	0,036	0,304	-0,056	-0,185	-0,013	-0,593	-0,126	0,014	-0,018
B1.41	0,605	0,227	0,000	0,122	0,000	-0,709	0,000	-0,219	0,000	0,000	0,000
B1.42	0,579	0,268	0,103	0,139	0,000	-0,692	0,000	-0,259	0,000	0,000	0,000
B1.43	0,572	0,362	0,071	0,305	-0,017	-0,180	-0,043	-0,604	-0,134	0,018	-0,016
B3.11	0,374	0,350	0,289	0,115	-0,009	-0,752	-0,006	-0,224	-0,065	0,011	0,000
B3.12	0,446	0,416	0,124	0,136	-0,013	-0,708	-0,008	-0,268	-0,073	0,015	0,000
B3.13	0,483	0,481	0,065	0,291	-0,046	-0,200	-0,012	-0,599	-0,134	0,023	-0,006
B2.11	0,228	0,618	0,000	0,113	0,000	-0,686	0,000	-0,240	0,000	0,000	0,000
B2.12	0,261	0,603	0,000	0,134	0,000	-0,665	0,000	-0,278	0,000	0,000	0,000
B2.13	0,344	0,588	0,071	0,302	-0,005	-0,162	-0,045	-0,612	-0,123	0,029	0,001
B2.21	0,155	0,678	0,034	0,110	0,001	-0,657	-0,018	-0,230	-0,056	0,020	0,017
B2.22	0,183	0,683	0,040	0,131	-0,006	-0,620	-0,015	-0,277	-0,064	0,022	0,018
B2.23	0,272	0,660	0,043	0,281	-0,042	-0,178	-0,013	-0,586	-0,120	0,031	0,010
B2.31	0,123	0,704	0,017	0,116	-0,001	-0,632	-0,018	-0,241	-0,051	0,022	0,018
B2.32	0,139	0,709	0,021	0,133	-0,001	-0,607	-0,020	-0,273	-0,055	0,023	0,018
B2.33	0,228	0,662	0,037	0,307	-0,007	-0,146	-0,051	-0,604	-0,111	0,031	0,005
B2.41	0,121	0,716	0,013	0,146	-0,006	-0,594	-0,022	-0,286	-0,044	0,024	0,017
B2.42	0,146	0,721	0,018	0,186	-0,015	-0,529	-0,021	-0,356	-0,054	0,027	0,016
B2.43	0,217	0,634	0,030	0,332	-0,058	-0,120	-0,019	-0,634	-0,079	0,031	0,006
T_{out} CH4	0,133	0,123	0,019	0,855	-0,471	-0,016	-0,012	-0,009	0,023	0,011	-0,016
T_{out} CH10	0,156	0,130	0,017	0,895	-0,021	-0,020	-0,380	-0,005	0,014	0,008	-0,016

	HGEN Heaters 1	HGEN Heaters 2	HGEN Heaters 3	TEMP air inlet	MFLOW air coolant CH4	Thermal cond. Li4SiO4	MFLOW air coolant CH10	HTC cool. channel (corrected)	TCC steel-Li4SiO4	HTC insulation-air	Thermal cond. insulation
B1.11	38%	6%	0%	9%	0%	33%	0%	14%	0%	0%	0%
B1.12	36%	7%	0%	11%	0%	29%	0%	17%	0%	0%	0%
B1.13	26%	10%	1%	18%	3%	5%	1%	31%	4%	1%	1%
B1.21	38%	6%	0%	7%	0%	36%	0%	12%	0%	0%	0%
B1.22	37%	7%	0%	8%	0%	34%	0%	14%	0%	0%	0%
B1.23	28%	11%	2%	15%	1%	7%	2%	27%	5%	1%	1%
B1.31	37%	8%	0%	7%	0%	37%	0%	11%	0%	0%	0%
B1.32	36%	9%	0%	8%	0%	34%	0%	13%	0%	0%	0%
B1.33	28%	12%	2%	13%	2%	8%	1%	26%	6%	1%	1%
B1.41	32%	12%	0%	6%	0%	38%	0%	12%	0%	0%	0%
B1.42	28%	13%	5%	7%	0%	34%	0%	13%	0%	0%	0%
B1.43	25%	16%	3%	13%	1%	8%	2%	26%	6%	1%	1%
B3.11	17%	16%	13%	5%	0%	34%	0%	10%	3%	0%	0%
B3.12	20%	19%	6%	6%	1%	32%	0%	12%	3%	1%	0%
B3.13	21%	21%	3%	12%	2%	9%	1%	26%	6%	1%	0%
B2.11	12%	33%	0%	6%	0%	36%	0%	13%	0%	0%	0%
B2.12	13%	31%	0%	7%	0%	34%	0%	14%	0%	0%	0%
B2.13	15%	26%	3%	13%	0%	7%	2%	27%	5%	1%	0%
B2.21	8%	34%	2%	6%	0%	33%	1%	12%	3%	1%	1%
B2.22	9%	33%	2%	6%	0%	30%	1%	13%	3%	1%	1%
B2.23	12%	30%	2%	13%	2%	8%	1%	26%	5%	1%	0%
B2.31	6%	36%	1%	6%	0%	33%	1%	12%	3%	1%	1%
B2.32	7%	35%	1%	7%	0%	30%	1%	14%	3%	1%	1%
B2.33	10%	30%	2%	14%	0%	7%	2%	28%	5%	1%	0%
B2.41	6%	36%	1%	7%	0%	30%	1%	14%	2%	1%	1%
B2.42	7%	34%	1%	9%	1%	25%	1%	17%	3%	1%	1%
B2.43	10%	29%	1%	15%	3%	6%	1%	29%	4%	1%	0%
T_{out} CH4	8%	7%	1%	51%	28%	1%	1%	1%	1%	1%	1%
T_{out} CH10	9%	8%	1%	54%	1%	1%	23%	0%	1%	1%	1%

Figure C.3: Sensitivity analysis of 11 model parameters to the output variables, i.e. pebble bed and outlet coolant temperatures, for the LO power level. Top table: Spearman Rank-Order correlation coefficients. Bottom table: % contribution of each model parameter to the output variables.

	HGEN Heaters 1	HGEN Heaters 2	HGEN Heaters 3	TEMP air inlet	MFLOW air coolant CH4	Thermal cond. Li4SiO4	MFLOW air coolant CH10	HTC cool. channel (corrected)	TCC steel-Li4SiO4	HTC insulation-air	Thermal cond. insulation
B1.11	0,682	0,000	0,000	0,314	0,000	-0,600	0,000	-0,246	0,000	0,000	0,000
B1.12	0,671	0,121	0,000	0,388	0,000	-0,526	0,000	-0,312	0,000	0,000	0,000
B1.13	0,467	0,179	0,024	0,644	-0,051	-0,080	-0,020	-0,553	-0,060	0,012	-0,017
B1.21	0,683	0,102	0,000	0,243	0,000	-0,646	0,000	-0,201	0,000	0,000	0,000
B1.22	0,682	0,122	0,000	0,286	0,000	-0,610	0,000	-0,241	0,000	0,000	0,000
B1.23	0,542	0,203	0,036	0,579	-0,019	-0,122	-0,042	-0,530	-0,104	0,013	-0,022
B1.31	0,663	0,135	0,000	0,226	0,000	-0,667	0,000	-0,196	0,000	0,000	0,000
B1.32	0,662	0,163	0,000	0,270	0,000	-0,626	0,000	-0,242	0,000	0,000	0,000
B1.33	0,559	0,246	0,038	0,538	-0,049	-0,148	-0,017	-0,527	-0,116	0,015	-0,019
B1.41	0,600	0,217	0,000	0,226	0,000	-0,695	0,000	-0,210	0,000	0,000	0,000
B1.42	0,570	0,256	0,000	0,263	0,000	-0,673	0,000	-0,246	0,000	0,000	0,000
B1.43	0,504	0,320	0,070	0,540	-0,016	-0,141	-0,044	-0,537	-0,122	0,018	-0,016
B3.11	0,363	0,339	0,288	0,215	-0,008	-0,743	-0,006	-0,216	-0,063	0,012	0,000
B3.12	0,437	0,400	0,121	0,261	-0,011	-0,691	-0,006	-0,258	-0,072	0,016	-0,002
B3.13	0,433	0,429	0,062	0,523	-0,045	-0,156	-0,015	-0,537	-0,123	0,023	-0,008
B2.11	0,223	0,607	0,000	0,221	0,000	-0,674	0,000	-0,230	0,000	0,000	0,000
B2.12	0,250	0,591	0,000	0,260	0,000	-0,647	0,000	-0,266	0,000	0,000	0,000
B2.13	0,307	0,517	0,068	0,538	-0,008	-0,124	-0,046	-0,545	-0,110	0,026	-0,001
B2.21	0,145	0,668	0,032	0,212	0,004	-0,646	-0,015	-0,222	-0,054	0,021	0,016
B2.22	0,173	0,666	0,040	0,261	-0,002	-0,603	-0,014	-0,268	-0,065	0,026	0,015
B2.23	0,243	0,589	0,044	0,515	-0,041	-0,140	-0,016	-0,527	-0,110	0,029	0,007
B2.31	0,114	0,692	0,017	0,228	0,002	-0,620	-0,017	-0,231	-0,046	0,021	0,015
B2.32	0,128	0,692	0,020	0,261	0,001	-0,589	-0,019	-0,263	-0,053	0,025	0,013
B2.33	0,203	0,577	0,038	0,549	-0,013	-0,108	-0,050	-0,534	-0,097	0,028	0,003
B2.41	0,113	0,695	0,013	0,282	-0,003	-0,576	-0,022	-0,273	-0,040	0,025	0,013
B2.42	0,135	0,687	0,023	0,353	-0,014	-0,499	-0,020	-0,340	-0,048	0,030	0,012
B2.43	0,191	0,542	0,030	0,581	-0,060	-0,086	-0,024	-0,550	-0,064	0,027	0,002
T_{out} CH4	0,081	0,062	0,010	0,958	-0,263	-0,008	-0,002	-0,004	0,018	0,001	-0,020
T_{out} CH10	0,087	0,067	0,009	0,972	-0,010	-0,010	-0,194	-0,003	0,016	-0,002	-0,018

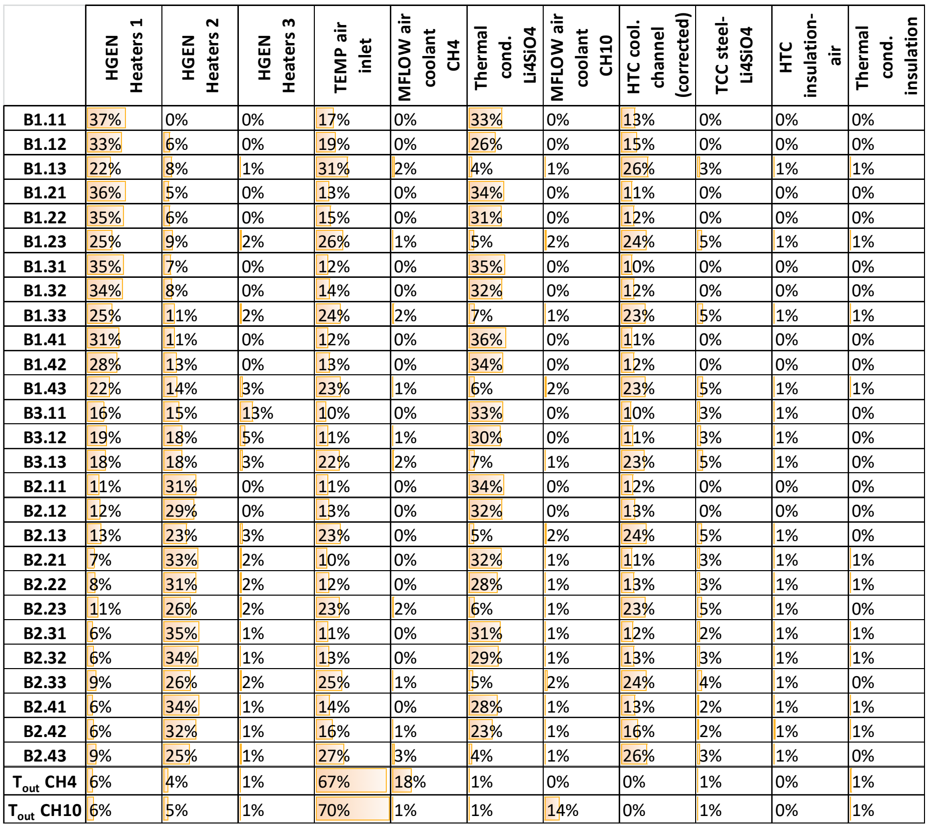

	HGEN Heaters 1	HGEN Heaters 2	HGEN Heaters 3	TEMP air inlet	MFLOW air coolant CH4	Thermal cond. Li4SiO4	MFLOW air coolant CH10	HTC cool. channel (corrected)	TCC steel-Li4SiO4	HTC insulation-air	Thermal cond. insulation
B1.11	37%	0%	0%	17%	0%	33%	0%	13%	0%	0%	0%
B1.12	33%	6%	0%	19%	0%	26%	0%	15%	0%	0%	0%
B1.13	22%	8%	1%	31%	2%	4%	1%	26%	3%	1%	1%
B1.21	36%	5%	0%	13%	0%	34%	0%	11%	0%	0%	0%
B1.22	35%	6%	0%	15%	0%	31%	0%	12%	0%	0%	0%
B1.23	25%	9%	2%	26%	1%	5%	2%	24%	5%	1%	1%
B1.31	35%	7%	0%	12%	0%	35%	0%	10%	0%	0%	0%
B1.32	34%	8%	0%	14%	0%	32%	0%	12%	0%	0%	0%
B1.33	25%	11%	2%	24%	2%	7%	1%	23%	5%	1%	1%
B1.41	31%	11%	0%	12%	0%	36%	0%	11%	0%	0%	0%
B1.42	28%	13%	0%	13%	0%	34%	0%	12%	0%	0%	0%
B1.43	22%	14%	3%	23%	1%	6%	2%	23%	5%	1%	1%
B3.11	16%	15%	13%	10%	0%	33%	0%	10%	3%	1%	0%
B3.12	19%	18%	5%	11%	1%	30%	0%	11%	3%	1%	0%
B3.13	18%	18%	3%	22%	2%	7%	1%	23%	5%	1%	0%
B2.11	11%	31%	0%	11%	0%	34%	0%	12%	0%	0%	0%
B2.12	12%	29%	0%	13%	0%	32%	0%	13%	0%	0%	0%
B2.13	13%	23%	3%	23%	0%	5%	2%	24%	5%	1%	0%
B2.21	7%	33%	2%	10%	0%	32%	1%	11%	3%	1%	1%
B2.22	8%	31%	2%	12%	0%	28%	1%	13%	3%	1%	1%
B2.23	11%	26%	2%	23%	2%	6%	1%	23%	5%	1%	0%
B2.31	6%	35%	1%	11%	0%	31%	1%	12%	2%	1%	1%
B2.32	6%	34%	1%	13%	0%	29%	1%	13%	3%	1%	1%
B2.33	9%	26%	2%	25%	1%	5%	2%	24%	4%	1%	0%
B2.41	6%	34%	1%	14%	0%	28%	1%	13%	2%	1%	1%
B2.42	6%	32%	1%	16%	1%	23%	1%	16%	2%	1%	1%
B2.43	9%	25%	1%	27%	3%	4%	1%	26%	3%	1%	0%
T_{out} CH4	6%	4%	1%	67%	18%	1%	0%	0%	1%	0%	1%
T_{out} CH10	6%	5%	1%	70%	1%	1%	14%	0%	1%	0%	1%

Figure C.4: Sensitivity analysis of 11 model parameters to the output variables, i.e. pebble bed and outlet coolant temperatures, for the VLO power level. Top table: Spearman Rank-Order correlation coefficients. Bottom table: % contribution of each model parameter to the output variables.

Appendix D

Thermal map reconstruction by spline interpolation

D.1 Biharmonic spline interpolation

For a better visualization of the temperature data acquired in PREMUX, the pebble bed temperature distribution has been reconstructed by means of biharmonic spline interpolation. This interpolation method is based on the biharmonic equation (Sandwell, 1987):

$$\nabla^4 w(\boldsymbol{x}) = \sum_{j=1}^{N} \alpha_j \delta(\boldsymbol{x} - \boldsymbol{x}_j) \ , \tag{D.1}$$

where $\boldsymbol{x}$ is an arbitrary position in $\mathbb{R}^{m}$**,** $\boldsymbol{x}_j$ is the jth of the N data points available (assuming non-homogeneous spaced “point forces” where the m-dimensional spline has to pass through), α_j is the parameter representing a strength force at $\boldsymbol{x}_j$, and $\delta(\boldsymbol{x} - \boldsymbol{x}_j)$ is an appropriate function. The general solution of Eqn. (D.1) is:

$$w(\boldsymbol{x}) = \sum_{j=1}^{N} \alpha_j \phi_m(\boldsymbol{x} - \boldsymbol{x}_j) \ , \tag{D.2}$$

and imposing that

$$w(\boldsymbol{x}_i) = \sum_{j=1}^{N} \alpha_j \phi_m(\boldsymbol{x}_i - \boldsymbol{x}_j) \, , \forall i \colon 1 \leq i \leq N \ , \tag{D.3}$$

The parameters α_j are obtained by solving the linear system of equations that result from the conditions in Eqn. (D.3). For m=2 dimensions as in the case of the measurement plane in PREMUX, $\phi_m = \phi_2$ takes the form of the Green’s point force biharmonic function:

$$\phi_2 = \|\boldsymbol{x}\|^{\mathbf{2}} ln(\|\boldsymbol{x}\| - 1), \forall i \colon 1 \leq i \leq N \ , \tag{D.4}$$

The biharmonic spline interpolation is available as a subroutine in Labview and it has been implemented in the PREMUX Control View. The interpolation scheme is fast enough to be run in real time in the Control Toolbox, provided that the number of locations to interpolate is not very large. As an example, the biharmonic interpolation has run smoothly interpolating a grid of 55 × 35 points at a sample rate of 500 *ms.*

Acknowledgements

Firstly, I would like to express my sincere gratitude to my mentors, Prof. Dr. Robert Stieglitz and Prof. Dr. Marc Kamlah for giving me the opportunity to perform this doctoral work at the Institute of Neutron Physics and Reactor Technology (INR) in KIT, for their priceless knowledge and guidance during the whole duration of this research. Also, I would like to thank Prof. Dr. Hans Jürgen Seifert for accepting being the Chairman over the defense of my thesis.

Besides my mentors, I am really grateful to my colleagues of the Design, Analysis and Fabrication department (DAF) in INR. In particular I am thankful to Dr. Lorenzo Virgilio Boccaccini and Dr. Ivan Alessio Maione for their support and their valuable comments and suggestions to my work, especially during the last stage of the research. Likewise, I would like to specially thank Dr. Fabio Cismondi for his unconditional support and encouraging me to pursue this doctoral work. Also, I am extremely grateful to Mr. Matthias Kolb, Dr. Christian Zeile, Mr. Heiko Neuberger and Mr. Jörg Rey for their priceless and countless fruitful technical discussions, as well as for the excellent working atmosphere that they provided. I am also obliged to Peter Freiner for his key support with the different logistics, as well as his encouragement.

I am very grateful to Dr. Yixiang Gang, Dr. Ratna Annabattula and Dr. Jörg Reimann for their valuable support and help with the theoretical background. Also, I would like to thank Dr. Milica Ilic, Dr. Bradut-Eugen Ghidersa, Dr. Frederik Arbeiter, Dr. Axel von der Weth, Dr. Angela Jianu, Dr. Ali Abou-Sena, Mr. Simone Pupeschi, Mr. Georg Schlindwein and Mr. Andre Kunze for the invaluable discussions on the experimental part, as well as to Mr. Oliver Bitz for his additional support on the mock-ups drawings.

I would like to convey also a special thanks to the INR workshop, in particular to Mr. Uwe Haefner, Mr. Rupert Schmidt, Mr. Norbert Prothmann and Mr. Oliver Albrecht for their commitment and excellent work in the construction of the experimental apparatus. Likewise, I am grateful to the KIT TEC for their professionalism and their great work in the construction of the mock-ups, in particular to Mr. Hardy Ritz, Mr. Stefan Dichiser, Mr. Joachim Konrad, Mr. Stephen Fischer, Mr. Patrick Brecht and Mr. Sven Linke.

Last but not least I would like to thank my family and in particular my parents and my wife, for their unconditional support, patience and invaluable encouragement throughout the entire journey of this research work and the writing of this thesis.